

Effect of Strain Aging on Mechanical Properties of Microalloyed (X70) UOE Steel Pipes

by

Jun Ma

A thesis submitted in partial fulfillment of the requirements for the degree of

Master of Science

in

Materials Engineering

Department of Chemical and Materials Engineering
University of Alberta

© Jun Ma, 2016

Abstract

Strain aging of microalloyed steel pipes, manufactured for oil and gas transmission, can occur during the anti-corrosion fusion bonded epoxy coating process (180°C - 250°C) and/or during long term storage or use. The primary mechanism of strain aging involves the segregation of interstitial solute carbon/or nitrogen atoms to mobile dislocations and subsequent locking of these dislocations. The aging process is influenced by many factors including aging temperature and time, steel composition/microstructure (as defined by the C/Nb ratio), position through the pipe wall thickness (i.e., inner diameter, center line or outer diameter) and imposed plastic strain. In this work, a Box-Behnken statistical design is conducted to determine the relationship between both longitudinal and transverse tensile properties (yield strength, ultimate tensile strength and yield to tensile strength ratio) and the aging variables mentioned above. Using the statistical software Minitab Academic (version 17), quadratic equations and response surfaces correlating the significant aging variables with changes in the longitudinal and transverse mechanical properties of the steel pipes are developed. The effect of strain aging on micro-hardness and Charpy impact toughness is also investigated in this study. Additionally, the effect of macro location in the UOE pipe (i.e., circumferential location at 90° or 180° relative to the weld) on the response to strain aging is assessed.

It is found that a transition from continuous to discontinuous yielding, featured by the upper yield point followed by Luders strain, occurs for several types of steels due to strain aging. Aging temperature, C/Nb ratio and through thickness position (or imposed pre-strain) are statistically significant in determining most longitudinal and transverse

tensile properties. The change in micro-hardness correlates linearly with the change in the yield strength. The effect of strain aging for the test conditions studied on Charpy impact toughness of the steel is relatively small. The changes in the yield strength and yield to tensile ratio are affected by the microstructural features of the steels, where greater changes are observed with the microstructure with smaller grain size and lower volume percentage of pearlite. The effects of through wall thickness position and imposed plastic strain on strain aging are relatively complex because of the generation and interaction between dislocations due to pipe forming and/or artificial plastic deformation. The aging response observed at 90° relative to the weld does not correlate well with the aging response observed at 180° relative to the weld. This suggests that strain history differences incurred during the UOE pipe forming process influences the strain aging response of the pipe.

Acknowledgements

I would like to acknowledge and thank my supervisors Dr. Hani Henein and Dr. Douglas Ivey for their invaluable guidance and support. I would also like to thank Dr. J. Barry Wiskel for his advice and counsel throughout the duration of my research project.

I would like to thank my group members in the Advanced Materials and Processing Laboratory (AMPL) for helping me solve technical issues in this project. Special thanks to Jonas Valloton for helping me with EBSD analysis. Thanks to Nathan Gerein and Shihong Xu for their help with SEM analysis. Special thanks also to Laurie Collins, Muhammad Rashid and Jon Jackson of EVRAZ NA Inc., Regina for helping me with tensile testing and Charpy testing.

I would like to extend my thanks to EVRAZ NA Inc., Enbridge, Trans-Canada Pipeline, UT Quality and Alliance Pipelines for their financial sponsorship of this work along with the Natural Sciences and Engineering Research Council (NSERC) of Canada.

Last but not least, I would like to give my special thanks to my parents and my friends for their constant encouragement. I could not have completed this work without all of them.

Table of Contents

Abstract	ii
Acknowledgements	iv
List of Tables	ix
List of Figures	xii
List of Symbols and Acronyms	xxi
Chapter 1 Introduction	1
Chapter 2 Literature Review	3
2.1 Processing of Microalloyed X70 UOE Pipeline Steel	3
2.1.1 TMCP of Microalloyed Steel.....	3
2.1.2 X70 Steel.....	6
2.1.3 UOE Pipe Forming	8
2.1.4 Thermal Process on Line Pipes.....	9
2.2 Mechanical Properties of Microalloyed Steels.....	11
2.2.1 Tensile Properties.....	11
2.2.2 Hardness.....	13
2.2.3 Charpy V-notch Impact Toughness	14
2.3 Strain Aging of Steels	15
2.3.1 Strain Aging Mechanism	15
2.3.2 Strain Aging for Different Types of Steels.....	22
2.3.3 Methods to Improve Resistance to Strain Aging	26
2.3.4 Cumulative Strain Aging Effect of All Thermal Events.....	28
2.4 Design of Experiments	29
2.4.1 Factorial Experiments	30
2.4.2 Response Surface Methodology	31
2.4.3 Analysis of Variance.....	33
2.5 Summary	35
Chapter 3 Materials and Experimental Methods	36
3.1 Steels Studied.....	36
3.2 Sample Preparation	37
3.2.1 Tensile Samples	37
3.2.2 Charpy V-notch Samples	40

3.2.3	Metallographic Samples.....	41
3.3	Design of Experiments	41
3.3.1	Box-Behnken Design – Variables and Levels	42
3.3.2	Non Box-Behnken Design	43
3.4	Heat Treatment.....	43
3.5	Mechanical Testing	44
3.5.1	Tensile Testing.....	44
3.5.2	Vickers Hardness Testing	47
3.5.3	Charpy Testing.....	48
3.6	Microstructural Characterization.....	48
3.6.1	Grain Size Measurement.....	49
3.6.2	Volume Fraction of Microconstituents	52
Chapter 4	Mechanical Properties	54
4.1	Longitudinal Tensile Properties	54
4.1.1	Longitudinal Tensile Properties of As-received Steels.....	54
4.1.2	Quantitative Analysis of Longitudinal Tensile Properties Affected by Aging	56
4.1.3	Strain Hardening Exponent of Longitudinal Samples	65
4.2	Transverse Tensile Properties	66
4.2.1	Transverse Tensile Properties of As-received Steels.....	67
4.2.2	Transverse Tensile Properties of Pre-strained Steels.....	67
4.2.3	Transverse Tensile Curves of Strain-aged Steels.....	68
4.2.4	Quantitative Analysis (4-factor BBD) of Transverse Tensile Properties Affected by Strain-aging.....	69
4.2.5	Quantitative Analysis (3-factor BBD) of Transverse Tensile Properties of Steel A Affected by Strain-aging.....	76
4.2.6	Strain Hardening Exponent of Transverse Samples	79
4.3	Micro-hardness.....	80
4.3.1	Micro-hardness of As-received and Aged Steel A	80
4.3.2	Micro-hardness of As-received and Aged Steel B.....	81
4.3.3	Micro-hardness of As-received and Aged Steel C.....	81
4.4	Charpy Impact Toughness.....	82
4.5	Summary of the Effect of Strain Aging on Mechanical Properties.....	84

Chapter 5	Microstructure Analysis	86
5.1	OM and SEM Analysis	86
5.2	Grain Size Measurement	89
5.2.1	Interception Method	89
5.2.2	EBSD Map Method	90
5.3	Volume Fraction of Microconstituents	93
Chapter 6	Discussion	95
6.1	Effect of Aging Temperature	95
6.1.1	Effect of Aging Temperature on ΔYS	95
6.1.2	Effect of Aging Temperature on ΔUTS	99
6.1.3	Effect of Aging Temperature on $\Delta YS/TS$	100
6.1.4	Effect of Aging Temperature on ΔHV	102
6.1.5	Effect of Aging Temperature on CVN Toughness	102
6.2	Effect of Aging Time	102
6.3	Effect of Position	104
6.3.1	Effect of Position on ΔYS	104
6.3.2	Effect of Position on ΔUTS	105
6.3.3	Effect of Position on $\Delta YS/TS$	106
6.3.4	Effect of Position on ΔHV	106
6.4	Effect of Pre-strain	107
6.4.1	Effect of Pre-strain on ΔYS	108
6.4.2	Effect of Pre-strain on ΔUTS	111
6.4.3	Effect of Pre-strain on $\Delta YS/TS$	113
6.5	Effect of Microstructure	114
6.5.1	Effect of Microstructure on ΔYS	114
6.5.2	Effect of Microstructure on ΔUTS	118
6.5.3	Effect of Microstructure on $\Delta YS/TS$	119
6.5.4	Effect of Microstructure on ΔHV	119
6.6	Effect of Sample Direction	120
Chapter 7	Conclusions, Recommendations and Future Work	123
7.1	Conclusions	123
7.2	Industrial Application	124

7.3 Recommendations and Future Work.....	125
Reference	126
Appendix A Mechanical Property Results.....	i
Appendix A.1 Tensile Properties	i
Appendix A.2 Micro-hardness	viii
Appendix A.3 CVN Impact Toughness	ix
Appendix B Microstructure Analysis.....	x
Appendix C Full ANOVA Tables for Box-Behnken Designs	xiv

List of Tables

Table 2-1 Amount of Carbon Required to Produce Yield Point [5]	18
Table 2-2 Number of Runs Required by 3^k Factorial Designs and Three - Level Box- Behnken Designs	33
Table 2-3 ANOVA Table of 3-factor BBD for Δ YS of Steel A	33
Table 3-1 Nominal X70 UOE Pipeline Steel Specifications	37
Table 3-2 Dimensions of Rectangular Tensile Specimen.....	38
Table 3-3 Dimensions of Cylindrical Tensile Samples	39
Table 3-4 Dimensions of Half-size Charpy V-notch Specimens.....	40
Table 3-5 Strain Aging Variables and Levels for BBD – Longitudinal Tensile Properties	42
Table 3-6 Strain Aging Variables and Levels for BBD – Transverse Tensile Properties	42
Table 3-7 Guidelines for Grid Size Selection [104]	52
Table 4-1 Four-factor BBD Test Matrix and Results for Longitudinal Tensile Properties	57
Table 4-2 Reduced ANOVA Table of 4-factor BBD for Δ YS of Longitudinal Samples.	58
Table 4-3 Reduced ANOVA Table of 4-factor BBD for Δ UTS of Longitudinal Samples	61
Table 4-4 Reduced ANOVA Data of 4-factor BBD for Δ YS/TS of Longitudinal Samples	63
Table 4-5 Four-factor BBD Test Matrix and Results for Transverse Samples.....	70
Table 4-6 Reduced ANOVA Table of 4-factor BBD for Δ YS of Transverse Samples....	71
Table 4-7 Reduced ANOVA Table of 4-factor BBD for Δ UTS of Transverse Samples .	73
Table 4-8 Reduced ANOVA Table of 4-factor BBD for Δ YS/TS of Transverse Samples	75

Table 4-9 Three-factor BBD Test Matrix and Results for Transverse Steel A	77
Table 4-10 Reduced ANOVA Table of 3-factor BBD for Δ YS of Transverse Steel A ...	78
Table 4-11 Statistically Significant Aging Variables Affecting Tensile Properties	84
Table 5-1 Average Grain Size of As-received Steel A, B and C Located 90° to the Weld Measured by Circular Intercept method using OM Images	89
Table 5-2 Average Grain Size of As-received Steel A, B and C at ID, CL and OD Positions Located 90° to the Weld Measured using EBSD Maps.....	91
Table 5-3 Measured Volume Percentage of Phases for As-received Steel A, B and C Located 90° to the Weld.....	94
Table A-1 Summary of As-received Tensile Test Results.....	i
Table A-2 Summary of Aged Tensile Test Results	ii
Table A-3 As-received and Pre-strained Tensile Properties.....	viii
Table A-4 Micro-hardness of As-received and Aged Steel A	viii
Table A-5 Micro-hardness of As-received and Aged Steel B	viii
Table A-6 Micro-hardness of As-received and Aged Steel C	ix
Table A-7 Absorbed Energy for Steel A Charpy Samples from the ID Position	ix
Table A-8 Absorbed Energy for Steel A Charpy Samples from the OD Position.....	ix
Table C-9 Full ANOVA Table of 4-factor BBD for Δ YS of Longitudinal Samples	xiv
Table C-10 Full ANOVA Table of 4-factor BBD for Δ UTS of Longitudinal Samples ...	xv
Table C-11 Full ANOVA Table of 4-factor BBD for Δ YS/TS of Longitudinal Samples	xv
Table C-12 Full ANOVA Table of 4-factor BBD for Δ YS of Transverse Samples.....	xvi
Table C-13 Full ANOVA Table of 4-factor BBD for Δ UTS of Transverse Samples	xvii
Table C-14 Full ANOVA Table of 4-factor BBD for Δ YS/TS of Transverse Samples .	xvii
Table C-15 Full ANOVA Table of 3-factor BBD for Δ YS of Transverse Steel A	xviii

Table C-16 Full ANOVA Table of 3-factor BBD for ΔY_S of Transverse Steel B xviii

List of Figures

Figure 2.1 Schematic of different stages in TMCP and corresponding changes in the microstructure [20].	4
Figure 2.2 Microstructure transformation controlled by TMCP [20].	4
Figure 2.3 Scanning electron microscopy (SEM) secondary electron (SE) images of Nb-microalloyed steel processed at a low cooling rate: (a) low and (b) high magnification [27].	5
Figure 2.4 SEM SE images of Nb-microalloyed steel processed at an intermediate cooling rate: (a) intermediate and (b) high magnification [27].	6
Figure 2.5 SEM SE images of Nb-microalloyed steel processed at high cooling rate: (a) low and (b) high magnification [27].	6
Figure 2.6 SEM SE images of X60 and X70 steel in the longitudinal section [29].	7
Figure 2.7 SEM SE images of fracture surfaces of CTOD test specimens with SEM, 500X [29].	8
Figure 2.8 Schematic of UOE pipe forming process [31].	8
Figure 2.9 Photographs of (a) U-press, (b)-(c) O-press and (d) expansion [1].	9
Figure 2.10 Schematic of FBE coating process [33].	10
Figure 2.11 Thermal profile of a 32'' OD, 25.5 mm WT C-Mn steel line pipe during the FBE coating application process [34].	11
Figure 2.12 Typical stress-strain behavior for a metal showing elastic and plastic deformations. The yield strength is defined using the 0.2% strain offset method [35].	12
Figure 2.13 Vickers hardness measurement [38].	14
Figure 2.14 Schematic of Charpy impact tester [39].	15
Figure 2.15 Stress-strain curve of uniformly annealed mild steel [42].	16
Figure 2.16 A carbon atom at the base of an edge dislocation [5].	17

Figure 2.17 Schematic representation of the effect of strain aging on the stress-strain curve for HSLA steels.	17
Figure 2.18 Solute carbon distribution in steel pipe and composition profile of carbon along A-B [68].....	21
Figure 2.19 Solute carbon distribution in coated pipe and composition profile of carbon along A-B [68].....	21
Figure 2.20 TEM in-situ heating experiment of coarse ferrite in #372 steel pipe (a) before heating, (b) at 150°C, (c) isothermally held for 3 minutes at 250°C, (d) isothermally held for 5 minutes at 250°C, (e) isothermally held for 10 minutes at 250°C and (f) isothermally held for 30 minutes at 250°C [68]. ..	22
Figure 2.21 Elongation for (1) X80 initial pipe, (2) X80 pipe after aging at 150°C and (3) X80 pipe after aging at 250°C [74].	24
Figure 2.22 Engineering stress-strain curves for XOM1 line pipe aged in the Gleeble™ subject to equivalent thermal cycles per Equation 2.4 [34].	29
Figure 2.23 Yield strength as a function of actual aging time for various aging temperatures [34].....	29
Figure 2.24 General DOE process.	30
Figure 2.25 Schematic of 2 ³ plus centers design.	32
Figure 2.26 Comparison between (a) 3 ³ factorial design and (b) three-factor and three-level Box-Behnken design.....	32
Figure 3.1 Sample locations related to the weld of Steel A, B, C.	36
Figure 3.2 Schematic of a rectangular tensile specimen.....	37
Figure 3.3 Positions of rectangular tensile specimens in a pipe.	38
Figure 3.4 Schematic of a cylindrical tensile specimen.....	39
Figure 3.5 Position of a cylindrical tensile specimen in a pipe.	39
Figure 3.6 Further grinding of a cylindrical sample.	39
Figure 3.7 Standard half-size Charpy V-notch specimens.....	40

Figure 3.8 Position of Charpy specimens in a pipe.	40
Figure 3.9 Longitudinal surface (a) and transverse surface (b) of mounted samples.	41
Figure 3.10 Salt bath furnace attached with a thermocouple.	43
Figure 3.11 Longitudinal tensile specimens heat treatment for 15 minutes at: (a) 175°C, (b) 215°C, (c) 255°C, (d) 350°C and (e) 300°C.	44
Figure 3.12 Positions of marked gage length section for (a) rectangular and (b) cylindrical specimens.	45
Figure 3.13 Stress-strain curve for an as-received longitudinal A1 sample.	46
Figure 3.14 Pre-straining curves for transverse Steel A1 exhibiting a permanent tensile strain of (a) 1.7% and (b) 3.4%.	47
Figure 3.15 Vickers hardness indents on a mounted sample.	47
Figure 3.16 Measurement of an indent by Vickers hardness tester.	48
Figure 3.17 Circle overlay for grain size measurement of a Steel C1 sample from the CL position.	49
Figure 3.18 Formation of EBSD pattern. Electrons from a divergent source incident on crystal planes at the Bragg angle are diffracted into a pair of cones to form Kikuchi bands in the diffraction pattern [108].	50
Figure 3.19 A map of Euler angle triplets for Steel C1 at the CL position in the longitudinal direction.	51
Figure 3.20 EBSD misorientation map for Steel B1 at the CL position showing grains with high-angle ($\geq 15^\circ$) grain boundaries.	52
Figure 3.21 Grid overlay for volume percentage of microconstituents measurement of a Steel C1 sample from the CL position.	53
Figure 4.1 Longitudinal stress-strain curves from the CL position at the (a) 90° and (b) 180° location for as-received Steel A, B and C.	54
Figure 4.2 YS of as-received steels from the ID, CL and OD positions.	55
Figure 4.3 UTS of as-received steels from the ID, CL and OD positions.	55

Figure 4.4 YS/TS of as-received steels from the ID, CL and OD positions.....	56
Figure 4.5 Parity plots for Δ YS at the 90° location using (a) BBD data (Table 4-1) and (b) additional aging test data.....	59
Figure 4.6 Response surface plots for (a) Δ YS vs. P and C/Nb, T=255°C and (b) Δ YS vs. P and T, C/Nb=1.2.....	59
Figure 4.7 Parity plot for Δ YS of longitudinal steel samples measured at the 180° location vs. Equation 4.1.....	60
Figure 4.8 Parity plots for Δ UTS at the 90° location using a) BBD data (Table 4-1) and b) additional aging data.....	61
Figure 4.9 Response surface for Δ UTS vs. P and T, C/Nb = 1.2.....	62
Figure 4.10 Parity plot for Δ UTS at the 180° location vs. Equation 4.2.....	62
Figure 4.11 Parity plot for Δ YS/TS at the 90° location using a) BBD data (Table 4-1) and b) additional aging data.....	64
Figure 4.12 Response surface for Δ YS/TS vs. C/Nb and P.....	64
Figure 4.13 Parity plot for Δ YS/TS at the 180° location vs Equation 4.3.....	65
Figure 4.14 Strain hardening exponents for Steel A1 in the longitudinal orientation.....	65
Figure 4.15 Strain hardening exponents for Steel B1 in the longitudinal orientation.....	66
Figure 4.16 Strain hardening exponents for Steel C1 in the longitudinal orientation.....	66
Figure 4.17 Transverse stress-strain curves for as-received pipe samples from the CL position for Steel A, B and C.....	67
Figure 4.18 Transverse stress-strain curves for as-received, 1.7% pre-strained and 3.4% pre-strained samples from the CL position of Steel A.....	68
Figure 4.19 (a) YS, (b) UTS and (c) YS/TS for as-received, 1.7% pre-strained and 3.4% pre-strained transverse samples from the CL position of Steel A, B and C..	68
Figure 4.20 Transverse stress-strain curves for 1.7% pre-strained and subsequently aged at 255°C for 5 minutes samples for (a) Steel A, (b) Steel B and (c) Steel C.	69

Figure 4.21 Parity plots based on Equation 4.4 for ΔYS of transverse samples using (a) BBD data and (b) additional aging test data.....	72
Figure 4.22 Response surface plots for transverse samples for a) ΔYS vs. C/Nb and T, $\epsilon = 1.7\%$ and b) ΔYS vs. C/Nb and ϵ , T = 255°C.	72
Figure 4.23 Parity plots based on Equation 4.5 for ΔUTS of transverse samples using a) BBD data and b) additional aging test data.	74
Figure 4.24 Response surface plots of transverse samples for a) ΔUTS vs. C/Nb and T, $\epsilon = 1.7\%$ and b) ΔUTS vs. C/Nb and ϵ , T = 255°C.....	74
Figure 4.25 Parity plots based on Equation 4.6 for $\Delta YS/TS$ of transverse samples using a) BBD data and b) additional aging test data.	76
Figure 4.26 Response surface plots of transverse samples for a) $\Delta YS/TS$ vs. C/Nb and T, $\epsilon = 1.7\%$ and b) $\Delta YS/TS$ vs. C/Nb and ϵ , T = 255°C.....	76
Figure 4.27 Parity plots based on Equation 4.7 for ΔYS of transverse Steel A samples using (a) BBD data and (b) additional aging test data.	78
Figure 4.28 Response surface plots of transverse Steel A samples for (a) ΔYS vs. T and t, $\epsilon = 1.7\%$ and (b) ΔYS vs. T and ϵ , t = 5 min.....	79
Figure 4.29 Strain hardening exponent for as-received and pre-strained transverse samples from Steel A, B and C.	80
Figure 4.30 Micro-hardness of as-received and aged Steel A samples. The error bars in the figure represent the standard deviation on 20 measurements taken per sample.....	81
Figure 4.31 Micro-hardness of as-received and aged Steel B samples. The error bars in the figure represent the standard deviation on 20 measurements taken per sample.....	81
Figure 4.32 Micro-hardness of as-received and aged Steel C samples. The error bars in the figure represent the standard deviation on 20 measurements taken per sample.....	82
Figure 4.33 Absorbed energy of as-received and aged (a) at 215°C for 5 min, (b) at 255°C for 5 min and (c) at 255°C for 25 min Steel A samples from the ID position. The error bars in the figure represent the standard deviation on 5 measurements taken per sample.	83

Figure 4.34 Absorbed energy of as-received and aged (a) at 215°C for 5 min, (b) at 255°C for 5 min and (c) at 255°C for 25 min Steel A samples from the OD position. The error bars in the figure represent the standard deviation on 5 measurements taken per sample.	84
Figure 5.1 OM images of longitudinal surface (Figure 3.9a) for Steel A, B, C located 90° to the weld at the ID, CL and OD positions.	87
Figure 5.2 SEM SE images for Steel A at the CL position.	87
Figure 5.3 SEM SE images for Steel B at the CL position.	88
Figure 5.4 SEM SE images for Steel C at the CL position.	88
Figure 5.5 Grain size for as-received steels located 90° to the weld measured by circular interception method using OM images. The error bars in the figure represent the standard deviation on five measurements taken per sample.	90
Figure 5.6 EBSD maps for Steel A, B and C at the ID, CL and OD positions.	91
Figure 5.7 Area percentage of grain size for Steel A located 90° to the weld from ID, CL and OD positions.	92
Figure 5.8 Area percentage of grain size for Steel B located 90° to the weld from ID, CL and OD positions.	92
Figure 5.9 Area percentage of grain size for Steel C located 90° to the weld from ID, CL and OD positions.	93
Figure 6.1 Diffusion distance of C atoms for each tested temperature and time combinations estimated using Equation 6.1 and Equation 6.2.	96
Figure 6.2 Stress-strain curves for as-received and aged longitudinal Steel A samples from the ID position.	97
Figure 6.3 Plot of diffusion ratio vs. temperature for Steel A at the (a) ID and OD positions and (b) CL position.	97
Figure 6.4 Distribution percentages of MS (means of squares) for different variables affecting ΔYS for a) longitudinal and b) transverse samples.	98
Figure 6.5 Stress-strain curves for 1.7% pre-strained and subsequently aged transverse Steel A samples.	99

Figure 6.6 Distribution percentages of MS (means of squares) for different variables affecting Δ UTS for (a) longitudinal and (b) transverse samples.	100
Figure 6.7 Change in YS and UTS after aging (at 255°C for 25 min) for steels located 90° relative to the weld at the ID, CL and OD positions.	100
Figure 6.8 Plot of Δ YS vs. Δ YS/TS for all steels located 90° relative to the weld.	101
Figure 6.9 Distribution percentages of MS (means of squares) for different variables affecting Δ YS/TS of transverse steel samples.	101
Figure 6.10 Yield strength for Steel A1, B1 and C1, at different through wall thickness positions, aged at 255°C for 5 minutes and 25 minutes.	103
Figure 6.11 Distribution percentages of MS for different variables affecting Δ YS of Steel A in the transverse direction.	103
Figure 6.12 Plot of Δ YS vs. position for Steel A1, B1 and C1 aged at 255°C.	105
Figure 6.13 Plot of Δ UTS vs. position for Steel A1, B1 and C1.	105
Figure 6.14 Plot of Δ YS/TS vs. position for Steel A1, B1 and C1 aged at 255°C.	106
Figure 6.15 Plot of Δ HV vs. position for Steel A1, B1 and C1 aged at 255°C.	107
Figure 6.16 Plots of Δ YS vs. Δ HV for steels (located 90° to the weld) aged at 255°C.	107
Figure 6.17 Contour plot of Δ YS vs. T and ϵ for Steel A (t = 5 min).	108
Figure 6.18 Contour plot of Δ YS vs. T and ϵ for Steel B (t = 5 min).	109
Figure 6.19 Plot of Δ YS vs. pre-strain for Steel A aged at 215°C.	109
Figure 6.20 Plot of Δ YS vs. pre-strain for Steel C aged at 215°C.	110
Figure 6.21 Strain hardening exponent for transverse samples of Steel A, B and C samples at the CL position.	111
Figure 6.22 (a) Response surface plot and (b) contour plot of Δ UTS as a function of aging temperature and pre-strain for Steel A aged for 5 min.	112
Figure 6.23 (a) Response surface plot and (b) contour plot of Δ UTS as a function of aging temperature and pre-strain for Steel B aged for 5 min.	112

Figure 6.24 Plot of ΔUTS vs. pre-strain for Steel C aged at 215°C.	112
Figure 6.25 (a) Response surface plot and (b) contour plot of $\Delta YS/TS$ as a function of aging temperature and pre-strain for Steel A aged for 5 min.	113
Figure 6.26 (a) Response surface plot and (b) contour plot of $\Delta YS/TS$ as a function of aging temperature and pre-strain for Steel B aged for 5 min.	113
Figure 6.27 Plot of $\Delta YS/TS$ vs. pre-strain for Steel C aged at 215°C.	114
Figure 6.28 Plot of ΔYS for longitudinal samples aged at different temperatures vs. grain size.	115
Figure 6.29 Measured volume percentage of pearlite for Steel A, B and C at OD, CL and ID positions located 90° to the weld.	116
Figure 6.30 Estimated free carbon content for Steel A, B and C at the OD, CL and ID positions located 90° to the weld.	116
Figure 6.31 Stress-strain curves for Steel B: (a) longitudinal samples at the ID position and (b) transverse, 1.7% pre-strained samples.	117
Figure 6.32 Stress-strain curves for Steel C: (a) longitudinal samples at the ID position and (b) transverse, 1.7% pre-strained samples.	117
Figure 6.33 Plot of ΔUTS for longitudinal samples aged at different temperatures vs. grain size.	118
Figure 6.34 Plot of $\Delta YS/TS$ for longitudinal steel samples aged at different temperatures vs. grain size.	119
Figure 6.35 Plot of ΔHV due to aging at 255°C for steels from the 90° location vs. grain size.	120
Figure 6.36 Average ΔYS for longitudinal and transverse steel samples from the CL position aged at 215°C.	121
Figure 6.37 Average ΔYS for longitudinal steel samples from the OD position and transverse 1.70% pre-strained steel samples aged at 215°C.	122
Figure 0.1 YS vs. aging conditions for Steel A1.	iv
Figure 0.2 YS vs. aging conditions for Steel B1.	iv

Figure 0.3 YS vs. aging conditions for Steel C1.....	v
Figure 0.4 YS vs. aging conditions for Steel A2.	v
Figure 0.5 YS vs. aging conditions for Steel B2.....	vi
Figure 0.6 YS vs. aging conditions for Steel C2.....	vi
Figure 0.7 $\lg\sigma_T$ vs. $\lg\epsilon_T$ for longitudinal as-received Steel A1 (as-received, CL position).	vii
Figure 0.8 Strain hardening exponents for Steel A2, B2 and C2, in the longitudinal orientation, at the ID, CL and OD positions.....	vii
Figure 0.9 OM images of the transverse surface (Figure 3.9b) for Steel A, B, C located 90° to the weld at the ID, CL and OD positions.	x
Figure 0.10 OM images of the longitudinal surface (Figure 3.9b) for Steel A: a) from the ID position at the 90° location; b) from the ID position at the 180° location; c) from the CL position at the 90° location; d) from the CL position at the 180° location.	xi
Figure 0.11 OM images of the longitudinal surface (Figure 3.9b) for Steel B: a) from the ID position at the 90° location; b) from the ID position at the 180° location; c) from the CL position at the 90° location; d) from the CL position at the 180° location.	xi
Figure 0.12 OM images of the longitudinal surface (Figure 3.9b) for Steel C: a) from the ID position at the 90° location; b) from the ID position at the 180° location; c) from the CL position at the 90° location; d) from the CL position at the 180° location.	xii
Figure 0.13 Measured average grain size for Steel A, B and C from the CL position located 90° and 180° to the weld.....	xii
Figure 0.14 Measured volume fraction of microconstituents for Steel A, B and C from the CL position located 90° and 180° to the weld.....	xiii

List of Symbols and Acronyms

Symbol/Abbreviation	Description	Unit
%El	Percentage of Elongation at Break	
Adj MS	Adjusted Mean of Squares	
Adj SS	Adjusted Sum of Squares	
AF	Acicular Ferrite	
Al	Aluminum	
ANOVA	Analysis of Variance	
API	American Petroleum Institute	
APT	Atom Probe Tomography	
B	Boron	
BBD	Box-Behnken Design	
BCC	Body-Centered Cubic	
C	Carbon	
Ca	Calcium	
Cr	Chromium	
CL	Center Line	
CR	Cooling Rate	°C/s
CT	Coiling Temperature	K
CTOD	Crack Tip Opening Displacement	mm
Cu	Copper	
CVN	Charpy V-Notch (energy)	J
DBTT	Ductile-Brittle Transition Temperature	°C
DF	Degree of Freedom	
DOE	Design of Experiments	
EBSD	Electron Back-scatter Diffraction	
ERW	Electric Resistance Welding	
F/α	Ferrite	
FBE	Fusion Bonded Epoxy	
Fe	Iron	
HSLA	High Strength Low Alloy	
ID	Inner Diameter	mm
K	Strength Coefficient	
Mn	Manganese	
Mo	Molybdenum	
MS	Mean of Square	
N	Nitrogen	
n	Strain Hardening Exponent	
Nb	Niobium	
Ni	Nickel	
O	Oxygen	
OD	Outer Diameter	mm

OM	Optical Microscope(y)	
OVAT	One Variable at a Time	
P	Pearlite	
Q	Activation Energy	kJ/mol
Q&T	Quenched and Tempered	
RSM	Response Surface Methodology	
S	Sulfur	
SAW	Submerged-arc welding	
SE	Secondary electron	
SEM	Scanning Electron Microscope(y)	
SIA-V	Solute Interstitial Atom-Vacancy	
SMYS	Specific Minimum Yield Strength	ksi
SS	Sum of Square	
TEM	Transmission Electron Microscopy	
Ti	Titanium	
TMCP	Thermo-Mechanically Controlled Processing	
UOE	Uing, Oing and Expanding	
UTS	Ultimate Tensile Strength	MPa
V	Vanadium	
YS/TS	Yield to Tensile Strength Ratio	
YS	Yield Strength	MPa
Zr	Zirconium	
γ	Austenite	
ϵ	Engineering Strain	mm/mm
ϵ_T	True Strain	mm/mm
σ	Engineering Stress	MPa
σ_T	True Stress	MPa

Chapter 1 Introduction

Grade X70 (specified minimum yield strength equal to 70 ksi or 480 MPa) steel pipes manufactured by the UOE process [1] [2], spiral forming or electric resistance welding (ERW) [3] have been widely used in the long distance transmission of water, oil, natural gas, etc. Following pipe making, strain aging of the steel occurs due to the application of a fusion bonded epoxy (FBE) coating (typically applied at temperatures ranging from 180°C to 250°C for 5 to 10 minutes), as well as long term outdoor storage (especially in the summer).

Significant longitudinal strain can be imposed on pipelines because of ground movement (e.g., permafrost melting, landslides, subsidence, seismic activity, water crossing, etc.) during pipeline operation. Transverse strain on a pipeline can also arise as a result of plastic bending deformation during pipe forming (e.g., UOE process). In the most simplistic case, the inner diameter (ID) or outer diameter (OD) of the pipe will experience the largest strain while the center line (CL) will experience negligible plastic strain. However, the magnitude and complexity of the plastic strain depends on both the pipe diameter and the forming conditions used [4]. Thus, both longitudinal and transverse mechanical properties of a pipe are important for design purposes. An understanding of the longitudinal and transverse pipe properties and how these properties will change with the aging process is important in geotechnical strain based design and stress based design of pipelines.

The fundamental mechanism for strain aging of steels, first developed by Cottrell and Bilby [5] [6], involves the diffusion of interstitial C and/or N atoms to mobile dislocations and subsequent locking of these dislocations. In microalloyed steels, dislocations distort the lattice and produce residual stress fields in the structure. The internal stresses can be relieved by interstitial atoms (such as C and N) segregating along the dislocations [7]. Strain aging primarily manifests itself as a return of the upper yield point and an increase in yield strength (YS). Other mechanical properties [4] [8] [9] including ultimate tensile strength (UTS), yield to tensile ratio (YS/TS), strain hardening exponent (n), hardness and impact toughness are also influenced by strain aging. It has been found that factors that affect strain aging phenomenon include aging temperature (T), aging time (t), plastic strain (i.e., generation and interaction of dislocations), chemical composition and microstructural features of the steels [10] [11] [12] [13] [14] [15]. However, the effects of such factors on the mechanical properties of steels were not quantified in previous research.

In this work, the effects of aging temperature, time, through wall thickness position, macro location (relative to the weld) and steel composition (via the C/Nb ratio) on the longitudinal and transverse mechanical properties of three different uncoated X70 UOE

pipes are studied. The Box-Behnken design (BBD) [16] is used to design the aging tests and the response surface methodology (RSM) [16] is developed to produce a quadratic response of different variables along with the interactions between them. The quadratic response surface model has the form:

$$Y = \beta_o + \sum_{i=1}^n \beta_i \cdot x_i + \sum_{i=1}^n \beta_{ii} \cdot x_i^2 + \sum_{i=1}^n \sum_{j<i}^n \beta_{ij} \cdot x_i \cdot x_j \quad (1.1)$$

where Y is the dependent variable of interest (i.e., the change in each tensile property), x_i and x_j represent the independent variables and β_o , β_i , β_{ii} and β_{ij} are the constant, linear, quadratic and interaction terms, respectively. An empirical quadratic equation is developed using the statistical software Minitab 17 to generate test matrices for the BBD, to quantify the influence of the statistically significant strain aging factors on the changes in tensile properties and to plot 3D response surfaces for the models.

Furthermore, the microstructures of all the three steels from different through wall thickness positions (i.e., ID, CL and OD) are observed using optical microscopy (OM) and scanning electron microscopy (SEM). The average grain sizes of different steel samples are measured using the intercept method based on OM images and grain size distributions are obtained using EBSD maps. Volume fractions of microconstituents are measured using the grid overlay method based on OM images. Qualitative and quantitative microstructure analyses are conducted to study the fundamentals behind the changes in mechanical properties due to strain aging, in terms of microstructural features

This thesis is divided into seven chapters. The literature review in Chapter 2 presents an introduction to the tested materials, previous research on strain aging in steels and an introduction to the methodology used in this work – design of experiments (DOE). The detailed information of the materials examined (three types of microalloyed X70 UOE pipe steels) and the experimental methods and procedures are described in Chapter 3. Chapter 4 presents the summarized experimental results obtained from mechanical property measurements (i.e., tensile testing, Charpy V-notch testing and Vickers microhardness testing). Microstructure analyses including metallographic microstructure observation and quantitative analysis (grain size measurement and microconstituent volume fraction measurement) are presented in Chapter 5. Discussion of the results in Chapter 4 and Chapter 5 can be found in Chapter 6, while conclusions along with recommendations are summarized in Chapter 7.

Chapter 2 Literature Review

The literature review begins with an introduction to processing methods and mechanical properties of the X70 UOE pipeline steel, which is used as the experimental material in this work. This is followed by a review of previous work on strain aging in steels. A review of the design of experiments (DOE) is also presented in this chapter.

2.1 Processing of Microalloyed X70 UOE Pipeline Steel

High-strength low-alloy (HSLA) steels have been extensively applied in bridges, suspension components, building structures, vehicles, tubular components, rails and off-shore industries because of their higher strength-to-weight ratios than conventional low carbon steels. HSLA steels have carbon contents between 0.05 and 0.25 wt% to retain formability and weldability and they contained manganese (Mn) content up to 2.0 wt%. Other small additions of alloying elements include nitrogen (N), niobium (Nb), titanium (Ti), vanadium (V), molybdenum (Mo), copper (Cu), nickel (Ni) and chromium (Cr) for strengthening. Some steels also include zirconium (Zr), calcium (Ca) and rare earth elements for sulfide-inclusion shape control to enhance formability [17]. Microalloyed steel is one type of HSLA steel which contains very small amount of Nb, Ti and V for grain size refinement and precipitation hardening [18]. Despite the low level of alloying, the alloying elements contribute to remarkably higher levels of strength and toughness.

This section begins with an introduction to steel processing techniques (TMCP), along with an introduction to grade X70 steel pipes. This is followed by a description of UOE pipe forming procedures and subsequent thermal history of steel pipes during the anti-corrosion coating process. In addition, some important mechanical properties of microalloyed steels are introduced.

2.1.1 TMCP of Microalloyed Steel

Thermomechanical control process (TMCP) is a widely used technology for improving the strength and toughness of steel plates. TMCP provides control of the microstructure, phase transformations and rolling, and helps overcome issues related to the addition of alloying elements and conventional heat treatment. TMCP includes five stages, namely reheating, rough rolling, finish rolling, accelerated cooling and coiling [19] [20]. The first four stages are shown in Figure 2.1.

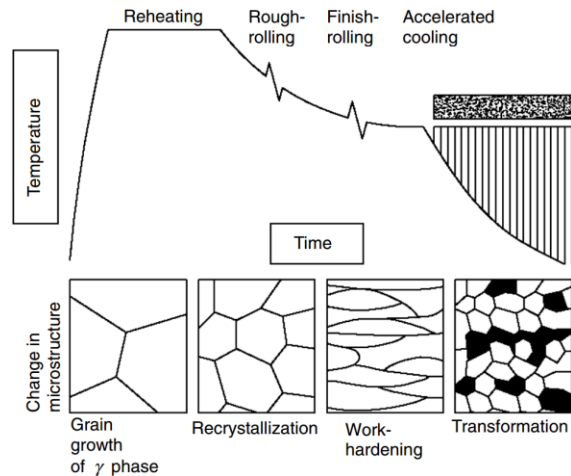


Figure 2.1 Schematic of different stages in TMCP and corresponding changes in the microstructure [20].

Initially, the steel is reheated to a relatively high temperature (1100-1300°C) and stays at this temperature for enough time to form a uniform austenite phase and dissolve precipitates [21]. The required temperature during homogenization is selected primarily based on the chemical composition of steel and equilibrium solution temperature for precipitates. After the reheating treatment, the cast slab is rough rolled to produce semi-finished products. At temperatures above non-recrystallization temperature and below 1200°C, austenite grain size refinement is achieved after several static and dynamic recrystallization cycles [22]. Afterwards, finish rolling is conducted by deforming the plate at temperatures between the austenite (γ) to ferrite (α) transformation temperature and non-recrystallization temperature. This rolling process changes the austenite grain from equiaxed to an elongated shape [23] at relatively lower temperature, at which ferrite phase coarsening is effectively impeded. After rolling, the steel strip is rapidly cooled at cooling rates (CR) between 10 to 30°C/s to a coiling temperature (CT) using a water spray on the run-out table [24]. In this stage, the desired microstructure transformation can be accomplished by adjusting CR and CT, as is illustrated in Figure 2.2. As CR varies through the thickness of the plate, different microstructural features can be observed at different positions.

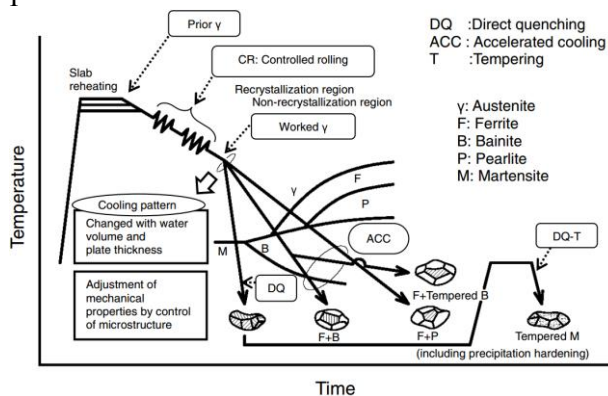


Figure 2.2 Microstructure transformation controlled by TMCP [20].

Finally, the steel strip is coiled for the purpose of introducing strain-induced precipitation and strengthening the steel [25]. Precipitates of desired size can be formed by increasing the dislocation density and increasing precipitation kinetics.

Thus, microstructure evolution is controlled by adjusting the processing parameters during different stages in TMCP. Compared with conventional technology, lower homogenization temperatures and finish rolling temperatures [26] and accelerated cooling are used, so that finer ferrite grains can be obtained with TMCP.

Shanmugam et al. [27] compared the microstructures of Nb-microalloyed steels produced by different cooling rates (the cooling rates are not specified due to proprietary reasons). They found that at conventional or low cooling rates, the microstructure mainly consisted of polygonal ferrite-pearlite, as is shown in Figure 2.3. In Figure 2.4, it is shown that an intermediate cooling rate gave rise to the formation of degenerated pearlite and bainitic ferrite together with conventional ferrite-pearlite. At higher cooling rates (used for TMCP), the microstructure primarily consisted of bainitic ferrite (Figure 2.5) and a good strength-toughness combination was achieved.

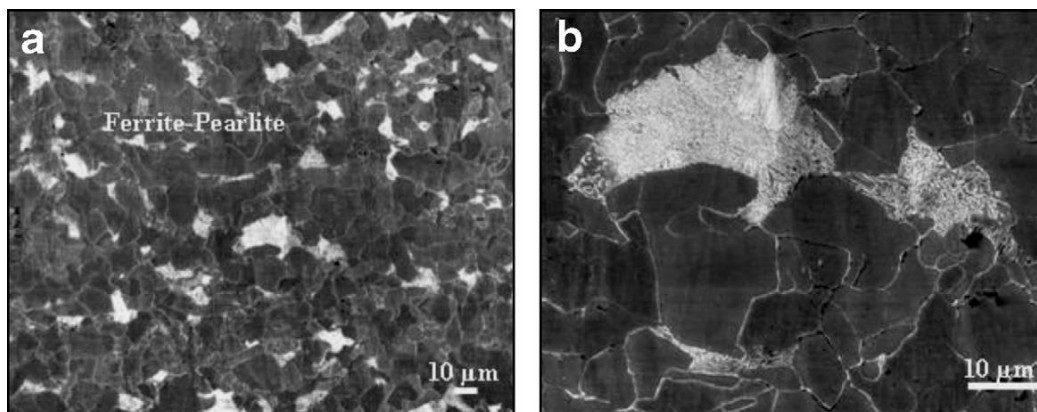


Figure 2.3 Scanning electron microscopy (SEM) secondary electron (SE) images of Nb-microalloyed steel processed at a low cooling rate: (a) low and (b) high magnification [27].

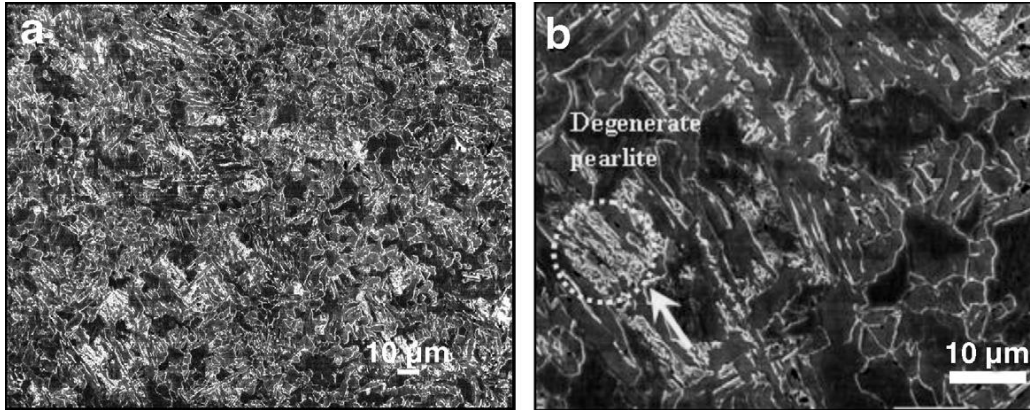


Figure 2.4 SEM SE images of Nb-microalloyed steel processed at an intermediate cooling rate: (a) intermediate and (b) high magnification [27].

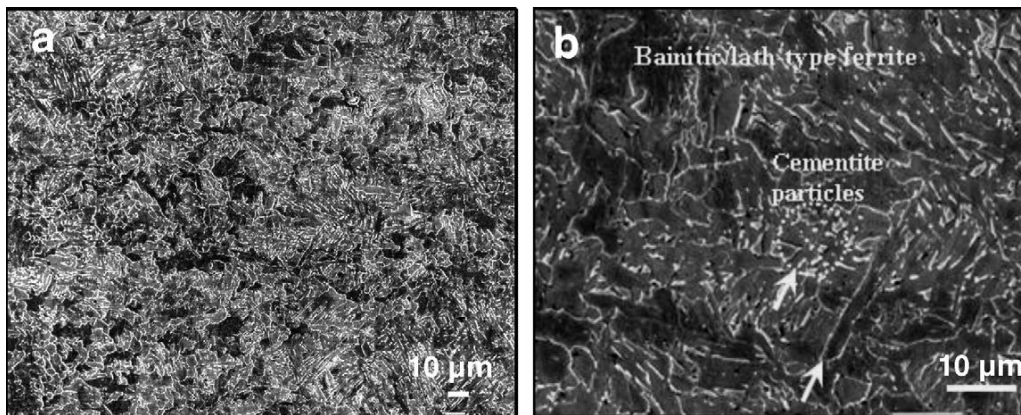


Figure 2.5 SEM SE images of Nb-microalloyed steel processed at high cooling rate: (a) low and (b) high magnification [27].

Since microalloyed steels manufactured by TMCP are not quenched and tempered, they are not susceptible to quench cracking and do not need to be stress relieved. TMCP can produce mechanical properties similar to quenched and tempered (Q&T) steels using controlling cooling. The machinability of microalloyed steel is better than that for Q&T steel because of its ferrite-pearlite or bainitic ferrite microstructure.

2.1.2 X70 Steel

The American Petroleum Institute (API) SPEC 5L specification gives the standard for pipes used in transporting water, gas and oil in the natural oil and gas industries. The standard covers welded and seamless pipes, including plain-end, bell-end and through-the-flowline pipes, as well as pipes with ends prepared for use with special coupling.

API 5L X grades cover X42, X46, X52, X56, X60, X65, X70, X80, etc. The two digits following the “X” indicate the minimum yield strength (in ksi) of pipes produced for each

grade. Grade X70 means a minimum yield strength of 70 ksi (485 MPa) and a minimum ultimate tensile strength of 82 ksi (570 MPa).

Grade X70 steel line pipe, manufactured by the UOE process, spiral forming or electric resistance welding (ERW), has been widely used in the long distance transmission of oil and gas [28]. Godefroid et al. [29] compared the microstructure and mechanical properties of X60 and X70 pipeline steels and verified the safe replacement of old X60 steel by modern X70 steel. The X70 steel was tested to be more preferable for pipeline projects because of its better mechanical resistance (manifested by higher yield strength, ultimate tensile strength and hardness), without loss of ductility, fracture toughness and fatigue resistance. The improvement of comprehensive mechanical properties was attributed to TMCP for X70, compared with traditional hot rolling and normalizing operations for X60 steel. TMCP provided easier control of rolling parameters, such as reheating temperature, rough and finishing rolling temperature, degree of rolling deformation and coiling temperature. SEM metallographic images (Figure 2.6) showed smaller grain sizes and the presence of bainite in the X70 steel. Figure 2.7 indicates the ductile behavior for both X60 and X70 steels. The images of fracture surface were obtained after crack tip opening displacement (CTOD) testing.

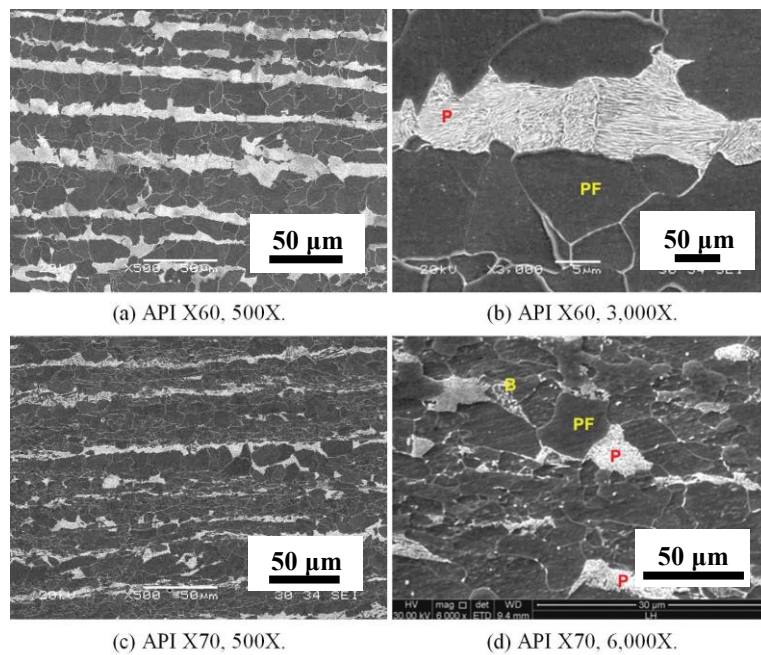


Figure 2.6 SEM SE images of X60 and X70 steel in the longitudinal section [29].

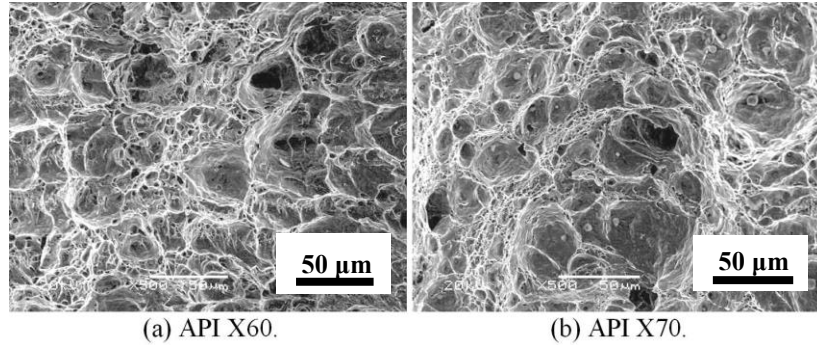


Figure 2.7 SEM SE images of fracture surfaces of CTOD test specimens with SEM, 500X [29].

Based on the API SPEC 5L standard [30], a lower level of carbon content in X70 steel is compensated by the minor addition of alloying elements. Also, the API standard gives lower maximum S and P contents, minimizing the formation of inclusions (elongated MnS particles) and segregation (P segregation to grain boundaries during austenization) and preventing the embrittlement phenomena in the X70 steel. Therefore, X70 steel manufactured using TMCP is widely used in pipeline industry.

2.1.3 UOE Pipe Forming

The UOE forming process is an effective approach for manufacturing submerged-arc welding (SAW) pipes with large diameter, thick wall and high strength. A whole UOE process comprises successive stages of crimping, U-forming, O-forming, joining, welding and expanding. Figure 2.8 schematically shows the typical process of forming a UOE pipe.

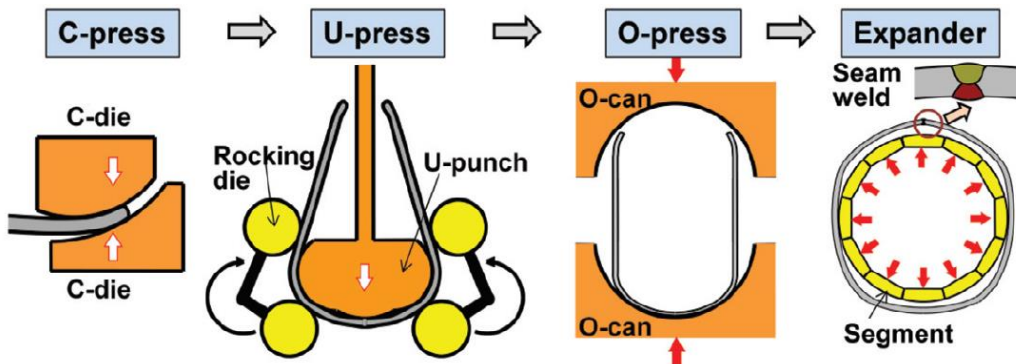


Figure 2.8 Schematic of UOE pipe forming process [31].

During the crimping stage, the longitudinal edge of steel plate is trimmed to obtain appropriate welding bevels, and then bent by involute-shape tools (e.g.; C-die). After that, the plate is transferred to the U-press, where the plate is bent by moving the U-punch down. The entire punch is bent through three-point bending. The U-punch stops when the plate contacts the anvils set at a predetermined height. Then the U-punch is held in place

and the side rollers move inwards to make the final position of the straight arms of the U-shaped plate nearly vertical.

Subsequently, the plate or “skelp” is conveyed to the O-press using two semi-circular stiff dies (also called O-cans). The two ends of the open-seam are joined by actuating the top die down to force the skelp into a nearly circular shape. The O-press finishes by forcing the dies further together and generating a net compressive strain ranging from 0.1% to 0.2% [32]. Followed by the O-press, the pipe seam is welded firstly on the inside joined and then on the outside. Before the pipe is expanded, extensive ultrasonic testing is conducted on the weld.

The expansion process (also called E process) is finished by an internal mandrel consisting of 8, 10 or 12 segments. The hydraulically actuated mandrel expands a length of $\frac{1}{2}$ to 1 diameter, which depends on the wall thickness. The E process improves the roundness of the pipe and gives the desired final size of the pipe. Typically, the pipe should be expanded 0.8-1.3% from its diameter after the O-step. Figure 2.9 gives actual photographs of the U-press, O-press and expansion processes.



Figure 2.9 Photographs of (a) U-press, (b)-(c) O-press and (d) expansion [1].

2.1.4 Thermal Process on Line Pipes

Fusion bonded epoxy (FBE) powder coatings have been widely used for anti-corrosion protection in pipeline construction. Figure 2.10 gives the procedure for a typical FBE coating process.

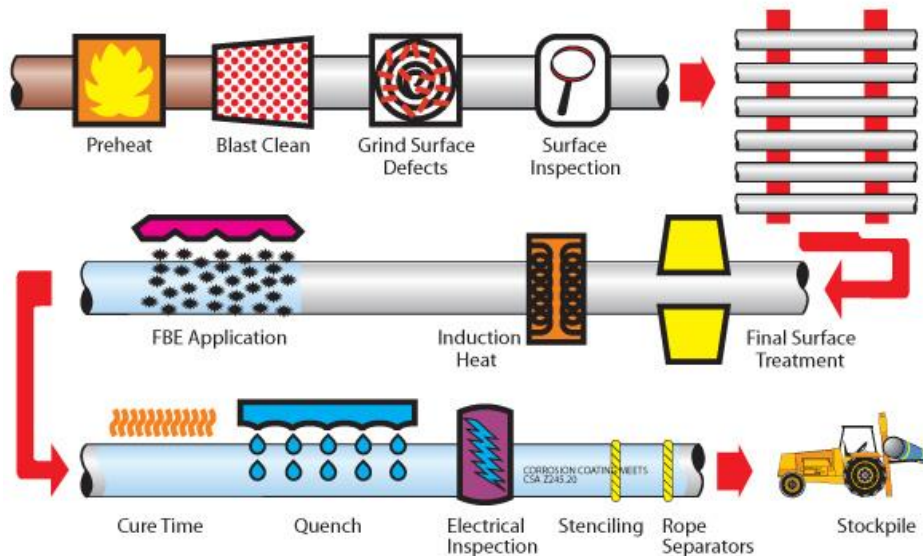


Figure 2.10 Schematic of FBE coating process [33].

Firstly, solvent cleaning is commonly applied for removing grease and oil contamination. Then blast cleaning is used for removing rust, scale, slats, etc., from the surface and producing a rough surface. During the blast cleaning process, abrasives including aluminum oxide, steel shot, steel grit, coal slag, garnet, etc. are forced onto the pipe surface by using compressed air (610 to 760 kPa).

After surface preparation, the cleaned metal part is heated to the recommended FBE powder application temperature using induction or oven heating. The pipe passes through a high frequency alternating current magnetic field, in which the steel part is heated to the required FBE coating temperature (typically in the range of 180 to 250°C). At such high temperatures, the powder melts and transforms into liquid that flows onto the pipe surface, forming a “fluidization bed”. The fluidized powder is sprayed onto the hot surface by using an electrostatic spray gun that provides powder particles with positive charge. When the pipe is rotating in its longitudinal axis, spraying lances travel from one end to the other end of the heated pipe so that the surface of pipe is coated thoroughly. The molten powder will become a solid coating and bond with the pipe surface. Complete curing can be accomplished by the residual heat on the steel, or by the help of additional heating resources.

Strain aging occurs during the anti-corrosion coating process at temperatures ranging from 180 to 250°C. An example of thermal history of line pipe during the FBE coating process is shown in Figure 2.11.

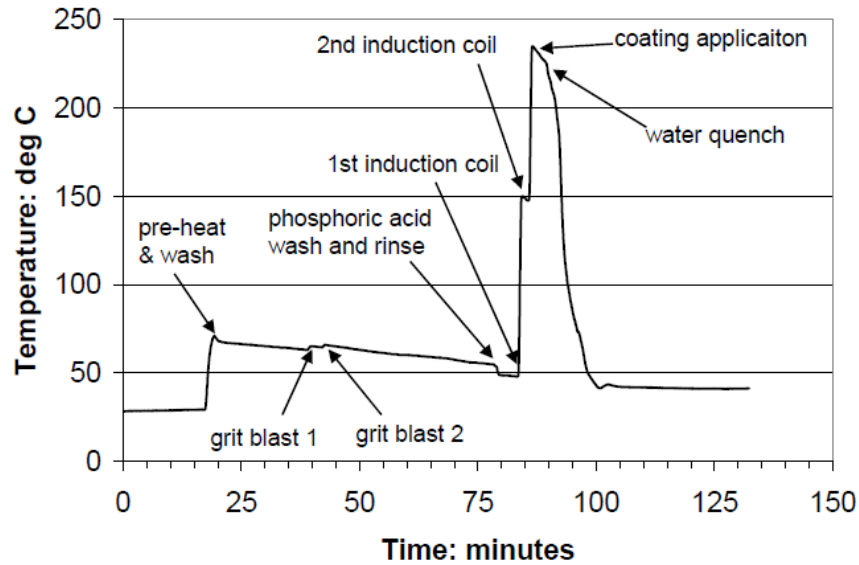


Figure 2.11 Thermal profile of a 32'' OD, 25.5 mm WT C-Mn steel line pipe during the FBE coating application process [34].

2.2 Mechanical Properties of Microalloyed Steels

The mechanical properties (i.e., tensile properties, impact toughness and hardness) of microalloyed steels are introduced in this section.

2.2.1 Tensile Properties

Tensile properties (such as yield strength, ultimate tensile strength, yield to tensile strength ratio, ductility and strain hardening exponent) of materials are the mechanical properties measured from tensile curves (i.e., stress-strain curves) through tensile testing.

2.2.1.1 Yield Strength (YS)

The yield strength of a certain type of material is defined as the stress at which the material begins to deform plastically. Once the yield strength has been exceeded, some fraction of the deformation will be permanent and non-reversible. Since the yield strength (or yield point) represents the upper limit to forces than can be applied without deformation, it is one of the most important mechanical properties considered for steel pipe design. Specific Minimum Yield Strength (SMYS), an indication of the minimum stress in steel that will cause plastic deformation, is commonly used for designing steel pipes in the oil and gas industry.

Precisely determining the yield strength value is difficult because of the variations in the stress-strain curves exhibited by real materials. For most metallic materials, the yield strength is commonly determined by the offset yield point. As shown in Figure 2.12, a

straight line is constructed parallel to the elastic portion of the stress-strain curve at some specific strain offset, usually 0.2%. The stress corresponding to the intersection of this line and the stress-strain curve is defined as the yield strength.

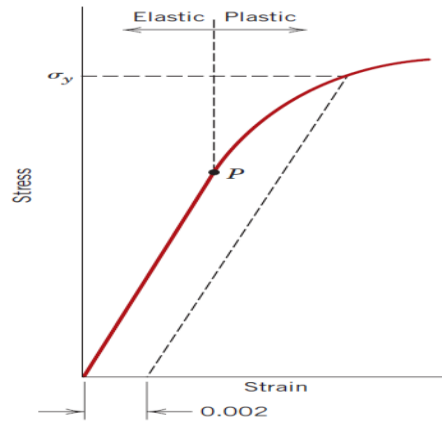


Figure 2.12 Typical stress-strain behavior for a metal showing elastic and plastic deformations. The yield strength is defined using the 0.2% strain offset method [35].

However, some materials have a nonlinear elastic region. The usual practice is to define the yield strength as the stress required to produce some amount of strain (e.g., $\epsilon = 0.5\%$). Welded pipelines are one of the few structures subject to plastic strains during their installation (e.g., laying of sub-sea pipelines (design strain $\approx 0.8\%$) or soil movement in onshore pipelines (design strain $\approx 0.5\%$)). The yield strength of pipeline steels in this project is determined using the stress corresponding to 0.5% elongation.

2.2.1.2 Ultimate Tensile Strength (UTS)

After yielding, the stress necessary to continue plastic deformation in metals increases to a maximum, and then decreases to the eventual fracture. Ultimate tensile strength is the maximum engineering stress that a material can withstand while being stretched before breaking. Some brittle materials break very sharply without plastic deformation. UTS is rarely used in the design of ductile materials (including most metals), but it is important in brittle materials (like ceramics).

2.2.1.3 Yield-to-Tensile Strength Ratio (YS/TS)

The yield strength to ultimate tensile strength ratio reflects the strain hardening response of materials and has been recognized as an important parameter in material specification and selection, structural design and integrity assessment [36]. Generally, a low YS/TS ratio is considered to provide high capacity for plastic deformation and to enhance the margin of safety against failure.

2.2.1.4 Ductility

Ductility is a measurement of the degree of plastic deformation that has been sustained at fracture. It can be expressed quantitatively as percent elongation – the increase in the gage length measured after the specimen fracture within the gage length [37].

2.2.1.5 Strain Hardening Exponent (n)

The stress flow curve of most metals in the region of uniform plastic deformation can be expressed by a simple power curve relation as follows:

$$\sigma_T = K \cdot \varepsilon_T^n \quad (2.1)$$

where σ_T is the true stress acting on the material, ε_T is the true strain, n is the strain hardening exponent and K is the strength coefficient. A log-log plot of true stress and true strain (from the yield point to the maximum load) results in a straight line and the slope of the line represents n . The value of n ranges from 0 (perfectly plastic solid) to 1 (100% elastic solid). Most metals have an n value between 0.1 and 0.5.

The strain hardening exponent determines how the metal behaves when it is work hardened. Materials having higher n values have better formability than those with lower n values. As metals work harden, their remaining capacity for work hardening decreases. Thus, the strain hardening exponent of materials can be used as an indicator of dislocation density.

2.2.2 Hardness

Hardness is a measure of resistance of metal to plastic deformation, usually by indentation. Thus, the hardness of material is measured by hardness tests, in which a pointed or rounded indenter is pressed into a surface under a substantially static load. The indentation hardness values are determined by measuring the critical dimensions of an indentation left by a loaded indenter of specific dimensions.

Hardness measurements can be classified into macro- and micro-scale based on the forces applied and displacements obtained. Macro-hardness measurement is a quick and simple method of obtaining mechanical property data for the bulk material from a small sample. However, when concerned with surface properties, the macro-indentation depth would be too large relative to the surface-scale features. Micro-hardness is determined by forcing a smaller indenter (e.g., Vickers or Knoop indenter) into the surface of the material. The indentations are usually so small that they must be measured with a microscope. Vickers hardness, one of the standard methods used for micro-hardness measurement, is calculated from the size of an impression produced under load by a pyramid-shaped diamond indenter, as is shown in Figure 2.13.

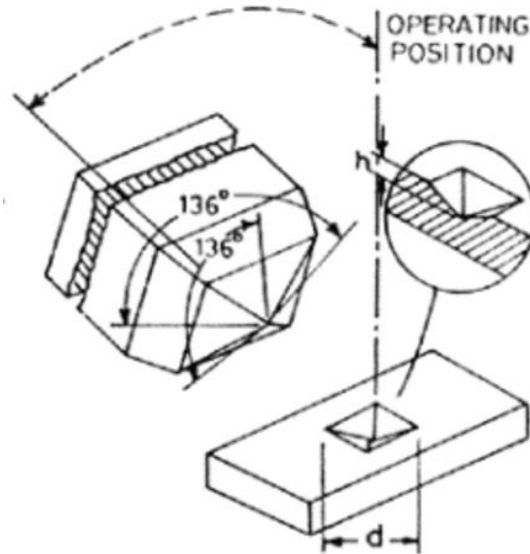


Figure 2.13 Vickers hardness measurement [38].

2.2.3 Charpy V-notch Impact Toughness

Toughness is a mechanical property that is indicative of a material's resistance to fracture when a crack or other stress-concentrating defect is present [34]. Fracture toughness can be defined as the ability of a material to absorb energy and plastically deform before fracturing.

Charpy V-notch (CVN) testing is most commonly used for measuring the impact toughness. The specimens are machined into a V-notch shape as a point of stress concentration. As shown in Figure 2.14, the load on a specimen is applied as an impact blow from a weighted pendulum hammer released from a cocked position (H). Upon release, a knife edge mounted on the pendulum strikes and fractures the specimen at the notch. The pendulum continues to swing and rises to a maximum height (h) lower than H . The absorbed energy (i.e., impact toughness) is computed from the difference between H and h .

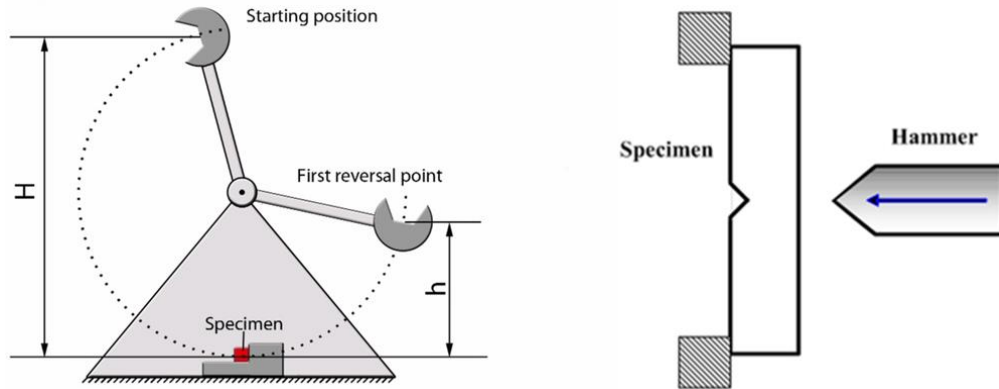


Figure 2.14 Schematic of Charpy impact tester [39].

2.3 Strain Aging of Steels

Aging is a commonly used heat treatment technique that contributes to higher strength of steels. Interstitial atoms and fine precipitates produced by changes in solid solubility with temperature act as obstacles to the motion of dislocations and thereby increase the yield strength and tensile strength of steels [40]. In this work, the focus is on strain aging, when steels are strained and then aged at low temperatures (normally lower than 300°C). Strain aging primarily manifests itself as an increase in yield strength and a return of the upper yield point [41].

This section begins with research on strain aging in the early years (before the 1940's), when the widely accepted mechanism of strain aging had not been established. This is followed by an introduction to the strain aging mechanism and a summary of research on the effect of strain aging on the mechanical properties of different types of steels. Furthermore, efforts to find ways to retard the strain aging process are summarized. In addition, the method for estimating the cumulative effect of strain aging during a series of thermal events is introduced in the last section.

2.3.1 Strain Aging Mechanism

When mild steels are deformed in tension, the stress-strain curve is irregular [42], as shown in Figure 2.15. When the elastic limit is reached, a remarkable amount of stretching suddenly appears at constant stress, the value of which is equal to or lower than the initial elastic limit. The stress on the yield plateau shows some irregular fluctuations because plastic deformation occurring in this stage is concentrated in discrete narrow zones called Luders bands or Hartmann lines (named after Luders [43] [44] in 1860 and Hartmann [43] [45] in 1896), which propagate along the specimen as the specimen is stretched. Luders' lines on specimens of mild steels, strained in tension, are inclined at approximately 50° to the axis of pulling direction [45]. The bands are visible due to a depression in surface orientation caused by plastic deformation within the bands. It was

believed that the direction of the bands was determined by the geometry of the specimen and the applied stress [46].

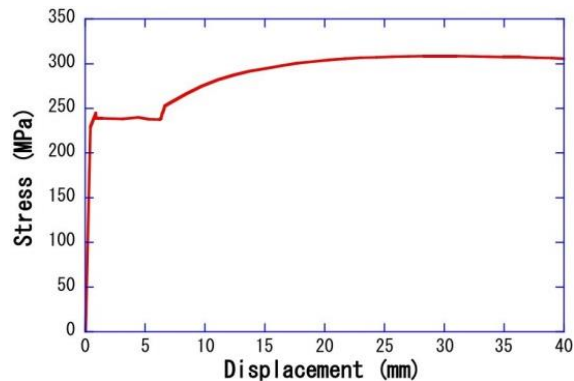


Figure 2.15 Stress-strain curve of uniformly annealed mild steel [42].

Compared with mild steel, the plateau-type of yielding (also called discontinuous yielding) is not frequently shown in unaged medium carbon steels and alloy steels [44], where the steels are strengthened by alloying elements. In 1879, Martens reported that discontinuous yielding appeared after the metals had been strained and experienced low-temperature aging treatment. This is generally regarded as the first discovery of strain aging.

The mechanism for strain aging of iron involving the segregation of free C atoms along dislocations to form Cottrell atmospheres (named after Cottrell [47] in 1948) was developed by Cottrell and Bilby [5] in 1949. Cottrell's mechanism was founded based on Snoek's [48] finding that low temperature annealing followed by cold working eliminated the elastic-after-effect [49] caused by mobile C or N atoms in solution of α -iron. Snoek believed that the annealing treatment caused solute atoms to be bound by stress fields produced by strain hardening. Cottrell interpreted the sources of the stress fields as dislocations and conducted further study on carbon atmospheres in α -iron.

Cottrell and Bilby proposed that in body-centered cubic (BCC) materials, like iron, foreign interstitial atoms distorted the lattice and produced residual stress fields around the atoms. The stresses could be relieved by interstitial atoms (such as C and N) diffusing towards dislocations, which have a more open structure at their core [50], as shown in Figure 2.16.

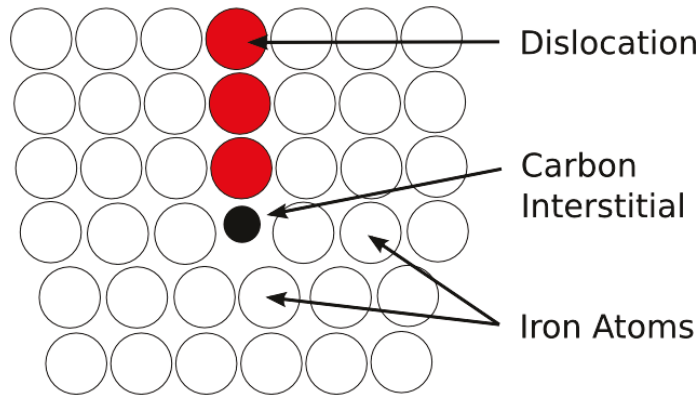


Figure 2.16 A carbon atom at the base of an edge dislocation [5].

When mobile dislocations surrounded by Cottrell atmospheres are locked by free C atoms, these dislocations are not able to escape from the atmosphere if the applied force is small and the C atoms then migrate with the dislocations. By this means, the yield stress of iron is increased by the locking effect. However, if a sufficiently large force is applied to the material, the dislocations can be torn from their atmospheres and become highly mobile, generating rapid plastic flow under a lower stress. This is the reason for the upper yield point followed by a yield plateau at lower yield point (Figure 2.17).

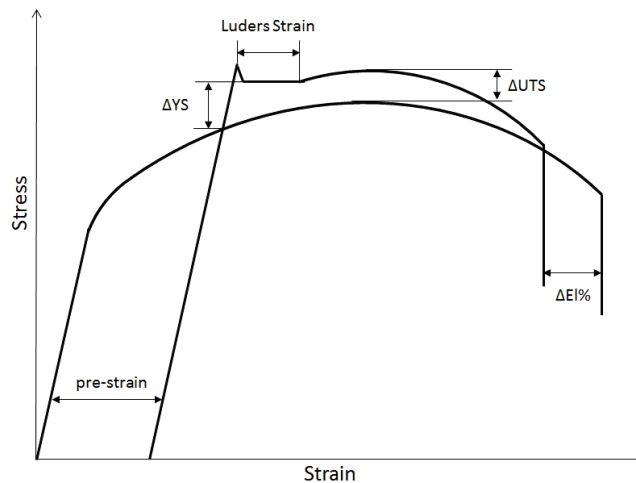


Figure 2.17 Schematic representation of the effect of strain aging on the stress-strain curve for HSLA steels.

Cottrell's mechanism has been widely accepted as the primary mechanism of strain aging. He distinguished strain aging from another type of age hardening caused by the motion of dislocations impeded by strain fields of precipitates. Under suitable situations, both age hardening types could co-exist in the same material. Cottrell also found that the amount of C required to provide atmospheres for all dislocations in a crystal structure was extremely small. Table 2-1 below gives the results based on the hypothesis that every dislocation has one C atom per half-plane of atoms.

Table 2-1 Amount of Carbon Required to Produce Yield Point [5]

Dislocation Density (lines/cm ²)		10 ¹²	10 ⁸
Wt% of C Absorbed in Dislocations	Full Yield Point	0.01	<0.0001
	No Yield Point	0.001	<0.0001

Based on Cottrell's study on the migration of free C atoms towards dislocations and Bilby's [51] effort on estimating the interaction energy between edge/screw dislocations and solute atoms that led to a spherical distortion of the lattice, Hall [52] further analyzed Bilby's grain-boundary theory on strain aging. It was known that if dislocations in a ferrite matrix approached a grain boundary (the region with a higher yield stress than the matrix), they would pile up along the grain boundary until stress concentration led the film to yield. Deformation occurred when dislocations were transferred to the next grain. Hall explained that when the Luders band covered the entire gage length of a mild steel sample, all the grain boundaries were weakened and broken down. If the sample was aged afterwards, the grain boundaries began to heal around the grains by the diffusion of C and N, resulting in an increase in yield stress. After aging for a long enough period of time, an increasing number of boundaries would be repaired to their original state. Thus, deformation resulting from higher yield stress must occur again by generating the secondary Luders bands. However, the healing of grain boundary mechanism proposed by Hall could not explain why strain aging also occurred in single crystals.

In 1955, Cochardt et al. [53] extended Cottrell and Bilby's theory of dislocation locking. Cottrell and Bilby estimated that when a dislocation was surrounded by a saturated carbon atmosphere, its strain energy was reduced by about 10%. However, Vreeland and Wood [54] interpreted data on delayed yield in steel and reported that the energy reduction was only a few tenths of one percent. Cochardt ascribed Cottrell's error in calculation to his simplified assumption that carbon atoms only segregated near edge dislocations. As Nabarro [55] pointed out, free carbon atoms also diffuse to screw dislocations. In Cochardt's study, the interaction energy between impurity atoms and both edge and screw dislocations was estimated using the observed crystallographic relations between the dislocation lines, slip planes and the lattice. The dilation and shear strain associated with carbon atoms in α -iron was estimated assuming that a unit cell containing a carbon atom was deformed tetragonally as in martensite [56] [57]. It was found that for both edge and screw dislocations, the maximum interaction energy was about 0.75 eV, higher than the 0.5 eV calculated by Mott [58] in 1952. Therefore, Cochardt believed that there should be a limitation to the number of carbon atoms that could migrate to a dislocation because a decrease in strain energy could not be achieved with the segregation of too many carbon atoms. Considering the elastic strain energy close to a dislocation, the results showed that the saturation concentration near a dislocation was approximately 6 at%. When a screw dislocation is surrounded by a saturated carbon atmosphere, the decrease in strain energy amounted to 20%, almost twice as much as that for an edge dislocation.

Nabarro [55] pointed out that three kinds of solute redistribution occurred during the strain-aging process: 1) stress induced ordering of carbon atoms among possible sets of interstitial sites [48]; 2) diffusion of carbon to form a dislocation atmosphere; 3) precipitation of iron carbide particles. Dislocation atmosphere formation was considered as the most important one that led to the return of upper yield point and an increase in the yield strength. Carbide precipitation that occurred in the latter aging stage mainly contributed to an increase in UTS and a decrease in ductility [59]. In 1959, Wilson and Russell [60] observed an increase in yield stress of a prestrained steel that was aged at 20°C for over 15 hours. Room temperature was used to slow down the strain aging process. Based on the Cottrell-Bilby equation [5], the estimated dislocation density was too low for the existing carbon content to raise the yield stress. So they predicted that during the initial stages, strain aging mainly resulted from atomic jumps between neighboring lattice sites, which could occur more rapidly than atom segregation, even at low temperatures. This assumption was supported by tensile testing results for quenched low carbon steel with higher dislocation density. Although the low carbon content did not contribute to the appearance of the upper yield point by forming Cottrell atmospheres, discontinuous yielding was also exhibited during continuous straining at a low strain rate. Wilson and Russell believed that stress induced ordering of carbon was responsible for this phenomenon.

The third mechanism (precipitation hardening) was also supported by Wilson and Russell [61] (1960). Their study provided a clear separation of the contributions to the increase in yield stress made by Cottrell atmosphere formation (second mechanism) and precipitation (or cluster formation). Tensile testing was conducted on 4% pre-strained mild steel samples aged at 60°C in an oil bath. Yield point elongation, yield strength, tensile strength and elongation at fracture were measured as a function of aging time. At temperatures as high as 60°C, the first strain aging process was neglected because it occurred in a very short time. It was found that during the first 35 minutes, the yield strength and yield point elongation increased remarkably, while at strains beyond yielding the aging treatment had little effect on the stress-strain relationship. After a sample was aged for over 35 minutes, the yield point elongation remained almost steady with further aging. After aging for over 150 minutes, when the yield strength and flow stress continued to increase slowly, significant changes in UTS and elongation at fracture occurred. Maximum values of UTS were reached when the aging time reached about 10^4 minutes, after which some evidence of over-aging could be observed, such as a decrease in yield strength and UTS and an increase in the elongation at fracture. With electron microscopy examination, they found that even after segregation of about 0.014% solute at 60°C in samples with 4% prestrain, no discrete precipitates could be detected. Fine particles (about 5 nm thick) along dislocations sites were detected after aging at 150°C for several days). This suggested that the particles formed just beyond completion of atmosphere locking were solute clusters. Stable precipitates, however, formed at higher aging temperature for adequate time. In the latter stages of strain aging, continuous solute

segregation led to solute cluster formation or precipitation, resulting in an increase in work hardening ability and a decrease in the ductility of the steel. An additional rise in the yield strength caused by further segregation (after the second stage) was roughly one third of that resulting from primary atmosphere locking [62].

It was believed that yielding was caused by the stress concentration of dislocation pile-ups at grain boundaries. In 1960, Conrad and Schoeck [63] reported their research on the effect of temperature and grain size on the upper and lower yield stress of electrolytic iron. This investigation was based on the Hall-Petch equation [64] for lower yield stress:

$$\sigma_{LY} = \sigma_i + kd^{-1/2} \quad (2.2)$$

where σ_{LY} is the lower yield stress, σ_i is the frictional stress impeding individual dislocations in the pile-up (constant for a given material) [65], k is the strengthening coefficient and d is the average grain diameter. The experimental results indicated that the lower yield stress, associated with strain and grain size (rather than aging temperature), represented the movement of dislocation and did not include thermally activated locking. However, the upper yield stress exhibited stronger temperature dependence, which suggested that it represented the tearing of dislocations from their Cottrell atmospheres. Wilson studied the effect of grain boundaries on strain aging of low-carbon steel [66] [67]. He focused on the grain-size-dependence of the lower yield stress in low-carbon steels and found that k (in the Hall-Petch relationship) could be reduced by rapid cooling from about 400°C and then increased during subsequent aging treatment. By measuring the time required to achieve the return of k , which was much longer than that needed for dislocation locking, he concluded that it was interstitial solute segregation to grain boundaries, rather than locking of dislocations in the interior of grains, that contributed to the increase of k caused by strain aging. In addition, metallographic observations of dislocation distributions during plastic deformation suggested that dislocations were nucleated from high-angle grain boundaries. This finding supported the concept that grain boundaries played important roles as both dislocation barriers and as dislocation sources during discontinuous yielding. The strengthening coefficient was associated with the local stress required to spread yielding across grain-boundaries at a yield point. Thus, when a Cottrell atmosphere was formed completely, new mobile dislocations were generated from grain boundaries. Also, prestraining led to a reduction in the stress required to generate dislocations from the boundary regions. Wilson's study suggested that plastically deformed steels with smaller grain sizes tended to display a higher degree of strain aging.

In summary, it has been generally accepted that the primary mechanism of strain aging involves the diffusion of free C and/or N atoms to mobile dislocations and subsequent locking of these dislocations. This was corroborated by Park et al.'s [68] three-dimension atom probe tomography (3D APT) experiments on uncoated and coated low carbon UOE pipeline steels. As shown in Figure 2.18 and Figure 2.19, inhomogeneous distribution of

carbon was intensified in the coated pipe (0.35 at%) relative to the uncoated pipe (0.14 at%), indicating that strain aging was accelerated by the coating process.

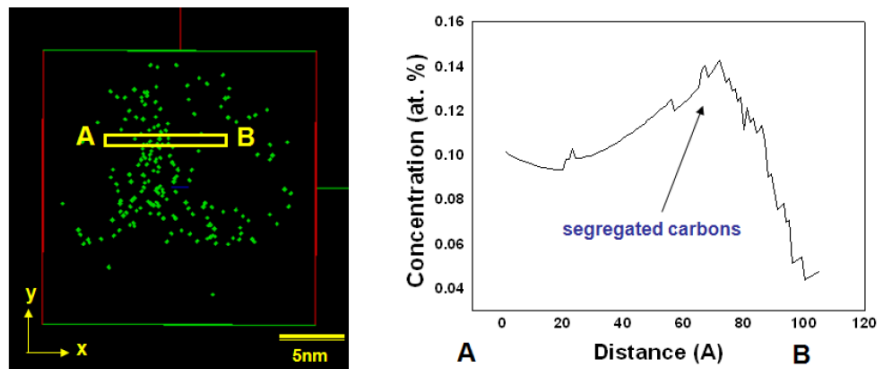


Figure 2.18 Solute carbon distribution in steel pipe and composition profile of carbon along A-B [68].

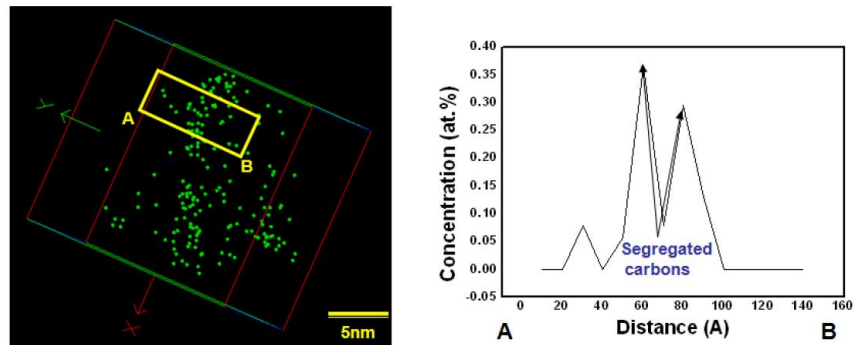


Figure 2.19 Solute carbon distribution in coated pipe and composition profile of carbon along A-B [68].

In-situ transmission electron microscopy (TEM) was conducted by Park to study the dislocations of pipes aged at 250°C for different aging times (from 0 to 30 minutes), as shown in Figure 2.20. The dislocations in the steel pipe did not move or rarely moved. This was an indicator that a change in the dislocation structure is not a major reason for strain aging in pipeline steels.

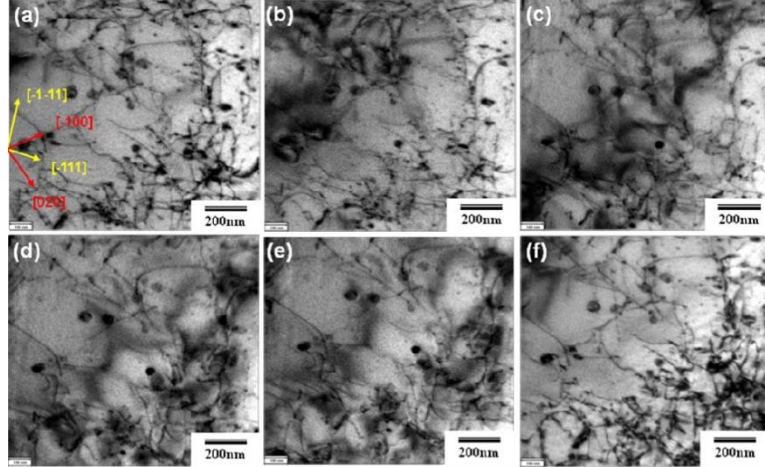


Figure 2.20 TEM in-situ heating experiment of coarse ferrite in #372 steel pipe (a) before heating, (b) at 150°C, (c) isothermally held for 3 minutes at 250°C, (d) isothermally held for 5 minutes at 250°C, (e) isothermally held for 10 minutes at 250°C and (f) isothermally held for 30 minutes at 250°C [68].

The strain aging mechanism (i.e., diffusion and interaction of interstitial carbon atoms with dislocations) in steel has been described by the Equation 2.3 [69].

$$\frac{N(t)}{N_{so}} = \frac{3}{2} \cdot \eta_0 \cdot \lambda \cdot 2 \cdot \left(\frac{\pi}{2}\right)^{1/3} \cdot \left(\frac{A \cdot D}{kT}\right)^{2/3} \cdot t^{2/3} \quad (2.3)$$

where $N(t)$ is the number of dislocations pinned during the aging process, N_{so} is the initial dislocation density, T is the absolute temperature, t is time, η_0 is the initial carbon concentration in solution, λ is the slip distance and A is an interaction parameter. The important variables defined by Equation 2.3 are aging temperature, aging time and the initial dislocation density (i.e., imposed plastic strain). Moreover, Equation 2.3 shows a dependence on the free carbon content (η_0). Although Equation 2.3 describes the mechanism of strain aging, it does not predict the change in mechanical properties incurred during aging.

2.3.2 Strain Aging for Different Types of Steels

Compared with the strain aging phenomena observed for low carbon steels, the effects of aging on the mechanical properties of HSLA steel (especially microalloyed pipeline steel), ultra-low carbon steel, medium carbon steel and dual phase (ferrite/martensite) steel have also been observed and studied.

2.3.2.1 Strain Aging for HSLA Steel

In 1975, Rashid [70] reported his work on the difference in the susceptibility to strain aging between HSLA steel and low carbon steel. Although the chemical compositions of HSLA steels were similar to low-carbon steels, they were stronger because of their smaller grain sizes due to controlled hot rolling and rapid cooling processes, along with

solution and precipitation hardening resulting from minor additions of alloying elements like V, Nb and Ti. Despite the alloying additions, Rashid found that free C or N atoms still existed in HSLA steels because most HSLA steels in the as-rolled condition exhibited discontinuous yielding when they were aged. The stress-strain curves of HSLA steels aged at 205°C indicated their strong susceptibility to strain aging, characterized by increased strength and the presence of an upper yield point and Luders strain. With a series of prestrains (ranging from 0.5% to 20.0%) applied to steel samples, it was found that a maximum ΔYS was observed at lower prestrains (1% and 2%) and ΔYS dropped to a constant value at prestrains greater than 10%. At higher prestrains (over 6%), the upper yield point was followed by an abrupt yield drop and a stress-strain curve which was flat before it dropped. In this condition, strain aging led to the yield strength reaching a value equal to UTS at high prestrain levels. Furthermore, Rashid studied the effect of strain aging at 205°C for 1 hour and 4 hours for both low carbon and HSLA steels. For low carbon steel, the tensile properties of samples aged for 1 hour and 4 hours were almost the same. However, the longer aging treatment made a difference for HSLA steels. It was suggested that the kinetics of strain aging in the HSLA steel was slower than that in low carbon steel. This could be explained by the calculated higher activation energy for diffusion of interstitial solutes in HSLA steel compared with that in low carbon steel [71]. The high activation energy was believed to be caused by interaction between interstitial solutes and elastic strain fields surrounding precipitates in the HSLA steel.

The effect of strain aging on the properties of microalloyed steel pipes was researched by McConnell and Hawbolt [72] in 1979. Impact toughness of two acicular ferrite X70 pipeline steels affected by plastic straining and subsequent aging treatment was studied. One steel (AF1) was semi-killed and contained numerous sulphide stringers, while the other one (AF2) was fully killed and rare earth treated to obtain small, globular and non-directional sulphides. The thermomechanical history was responsible for strain aging because of the manufacture and processing of large diameter pipes. Plastic strain was introduced prior to the welding process when the steel skelp was cold formed to the desired shape. Additional plastic deformation could be introduced by field bending. The plastic strain applied to pipeline steel, combined with the heat from the seam weld, could generate strain age hardening. It was also found that straining and subsequent aging led to a decrease in the toughness and ductility of AF1 and an increase in both properties of AF2. McConnell and Hawbolt believed that the reduction in the toughness was primarily caused by a decrease in the propagation energy, because reduced ductility of the matrix promoted void coalescence in the structure. In contrast, improvement in both ductility and toughness in AF2 was the result of strong nitride formers, such as Al, Ti and Nb. Little strain aging phenomena were obtained because of the lack of free N available to pin dislocations. Precipitation of nitride or carbide compounds was enhanced, which retarded dislocation motion and increased the work hardening rate [73]. This caused necking to occur at higher plastic strains and increase the observed ductility, which was measured by elongation at fracture. Increased strength and ductility of the matrix impeded void coalescence during cracking and enhanced impact toughness. Instrumented

impact testing was also conducted on samples removed from the HAZ of semi-killed spiral welded pipe. The strain aging phenomenon manifested itself as an increase in the yield strength and Rockwell hardness and a decrease in toughness. It was concluded that the strain introduced into the pipe during cold forming, combined with heat generated from the weld, was sufficient to accomplish strain age hardening.

X80 pipes produced by controlled rolling and accelerated cooling, studied by Arabei et al. [74], were found to be considerably susceptible to strain aging at temperatures higher than 150°C. After the plastically deformed ($\epsilon = 2\%$) samples were aged at 200°C for 30 minutes, the strain aging effect was so strong that the lower yield strength reached the UTS and no distinct work hardening was observed. Also, a decrease in the fracture elongation was observed with increasing aging temperature, as shown in Figure 2.21. The severe susceptibility to strain aging was attributed to ultra-small grains ($\approx 2\text{-}3\ \mu\text{m}$) caused by rapid cooling. Grain size refinement facilitated strain aging by increasing dislocation density in the material after the processes in welded-pipe manufacture (including shaping, expansion, etc.).

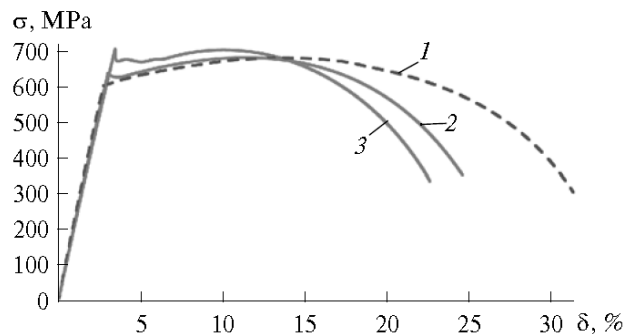


Figure 2.21 Elongation for (1) X80 initial pipe, (2) X80 pipe after aging at 150°C and (3) X80 pipe after aging at 250°C [74].

Liang et al. [15] conducted research on the effect of strain aging on the susceptibility of X100 steel to stress corrosion cracking (SCC). The pipe was originally coated with FBE and under a normal cathodic protection potential of -0.85V. The experimental results showed that an immediate increase in temperature during coating application resulted in strain aging of X100 steel, which was indicated by increased yield strength, decreased fracture elongation and the presence of Luders band during yielding. It was also found that strain aging increased the susceptibility of the steel to SCC, especially at cathodic potential (CP) or more negative potentials. Liang et al. believed that strain aging was able to accelerate hydrogen evolution as well as further permeation into steel, leading to hydrogen-induced SCC of the steel.

In 2008, Yoo et al. [75] reported the strain aging behavior of coated X80/X100 UOE pipes. During the U and O-ing processes, tensile and compressive strain resulting from hoop stress was applied to the inner and outer positions, respectively. During the FBE coating process, the pipe was aged at 200°C to 250°C for several minutes [76]. It was

found that strain aging behavior of the pipe varied with position through the thickness. Strain aging sensitivity increased from the pipe interior to the outside surface. This result was confirmed by Chi et al. [77] five years later. Thus, it was suggested that strain aging resistance of coated pipe decreased with increasing tensile prestrain induced during pipe forming. The strain aging behavior of the whole pipe well corresponded to that of the center line position of the pipe.

2.3.2.2 Strain Aging for Ultra-low Carbon Steel

The strain aging behavior of ultra-low carbon steel (total carbon content of 20 ppm) was studied by De et al. [78] in 1999. It was found that the aging process did not go beyond the Cottrell atmosphere formation stage, because only a slight increase in the yield stress after the first aging stage (stress induced ordering of carbon atoms among possible sets of interstitial sites) was obtained at low prestrains (less than 1%) and high aging temperatures (higher than 140°C). In samples with higher prestrains, solute atoms would contribute only to atmosphere formation and no solute clusters or precipitates were formed for further hardening. This was confirmed by the fact that no precipitates were revealed either in the matrix or along the dislocations by TEM. In ultra-low carbon steels, the increase in yield strength caused by strain aging was independent of the magnitude of pre-strains [79].

Because of the difficulty of quantifying the low amount of carbon during aging, the kinetics of aging was determined by means of measurement of the tensile properties, based on Hartley's [80] modified Cottrell-Billy relationship. The calculated activation energy (Q) for segregation of C to the dislocations was 76.6 ± 2.1 kJ/mol, which was in very good agreement with the value of 75-92 kJ/mol reported in previous research [81]. This suggested an effective way to study the interaction between atoms and dislocations. Measurement of activation energy using the variation of ΔYS with temperature was also conducted by Hammerle et al [82]. Tensile testing was conducted on low carbon steel samples (with prestrain of 6%) aged at 50, 65, 80 and 100°C. The calculated Q value obtained from the slope of the linear relationship was 50.2 ± 1.3 kJ/mol, which is lower than the Q value required to achieve simple diffusion of either C or N atoms to dislocations to form atmospheres. It was suggested that the low Q value was associated with the contribution from the low binding and mobility energies between a C atom and a vacancy in the BCC lattice of iron. Since there were enough vacancies, solute interstitial atom-vacancy (SIA-V) pairs with their greater stability would predominate over single soluble interstitial atoms.

In summary, although the kinetics of strain aging in HSLA steel was slower than that of low carbon steel, due to the addition of alloy elements, an increase in yield strength and hardness and a decrease in ductility and toughness caused by aging were observed. Aging temperature and plastic strain have significant effects on the property changes.

2.3.2.3 Strain Aging for Medium Carbon Steel and Dual Phase Steel

It was reported by Süleyman Gündüz [83] in 2005 that medium carbon microalloyed steels were more susceptible to strain aging than low carbon microalloyed steels, which was characterized by a higher increase in YS and UTS. Moreover, after prestraining and aging treatment, SEM images of fracture surfaces revealed that low carbon steel displayed a dimpled fracture surface (indicator of ductile fracture), while medium carbon steel showed dimples and cleavage facets (indicator of mixed brittle and ductile fracture). Carbon content made a difference in strain aging effect because alloying elements (Al, Ti and V) combined with a considerable amount of carbon atoms, resulting in too few free carbon atoms [5] in low carbon microalloyed steels to accomplish Cottrell atmosphere formation.

Gündüz also tested tensile properties of 5% prestrained medium carbon steels aged at temperatures ranging from 20 to 500°C. The color of the samples changed with increasing temperatures. At the blue brittleness temperature (around 350°C), the highest increase in yield strength and UTS, as well as the highest decrease in fracture elongation, was obtained. This corroborated Dolzhenkov's [84] study on the nature of blue brittleness of steel. The blue oxide film was formed at temperatures where finely dispersed precipitates on dislocations formed. Thus, blue brittleness could be considered as the initial stage of over-aging in microalloyed steels.

In addition to medium carbon and low carbon steels, Gündüz investigated the strain aging behavior of dual phase steels with 20% to 40% martensite volume fractions. Compared with the blue brittleness temperature (about 350°C), the maximum increase in YS and UTS was obtained at only 100°C. Also, a decrease in fracture elongation and a change in the fracture pattern were more obvious than in common low/medium carbon steels. After aging at 250°C, a reduction in YS and UTS, along with an increase in fracture elongation, was observed. Gündüz believed that the over-aging was caused by a tempering effect of martensite and/or coarsening of the precipitates on dislocations. Also, the fact that aging in the dual phase microalloyed steel occurred more slowly than the dual phase carbon steel indicated that nitride and carbide formers (alloying elements) combined with free N and C atoms and retarded formation of dislocation atmospheres.

2.3.3 Methods to Improve Resistance to Strain Aging

Based on the accepted knowledge about the mechanisms of strain aging, researchers have been trying to enhance strain aging resistance by control of heat treatment parameters and addition of alloy elements to the steels.

Souza and Buono [85] studied the effect of Mn, B and C content and coiling temperature on the strain aging resistance of continuously annealed aluminum (Al) killed steels. Al killed steels have high strain aging resistance because of precipitation of N as AlN. The addition of boron (B) removed N atoms from solid solution [86] [87] by forming BN

particles and further improved aging resistance in Al killed steels. Also, an increase in Mn content contributed to the reduction in the amount of C atoms in solid solution [88], because Mn stabilized cementite by retarding its dissolution during the annealing treatment. Souza and Buono found that coiling temperature considerably affected strain aging resistance of B-free Al killed steels. Conversely, for boron added steels, strain aging resistance was promoted due to the addition of B and coiling temperature had little effect on it. Also, an increase in the Mn content of B-free steels led to the same results in B-added steels. This finding supported Strobe's study [89] that AlN particles tended to precipitate on pre-existing MnS particles and that formation of AlN was accelerated with increasing Mn level.

Gater et al. [90] observed better resistance to strain aging in ultra-low carbon strip steels with the addition of V. Gater et al. attributed the decreased susceptibility to strain aging to grain growth (from 9.7-10.3 to 11.5-13.5 μm). The increase in grain size gives rise to a decrease in dislocation density and reduces the pinning effect. Also, based on Rashid's research [71], a fraction of the carbon content was tied up in VC precipitates. Vanadium carbides in the iron lattice can interact with free interstitial carbon atoms and reduce the net rate of carbon diffusion to dislocation cores.

Pereloma et al. [91] investigated the effect of Cr and Mo additions on the strain aging rate of low carbon steel. They found that an increase in Cr content (up to 0.74 wt%) reduced the rate of strain aging in comparison with non-alloyed, low carbon steel, while the addition of Mo accelerated the aging response. This was attributed to the different effect of Cr and Mo on the diffusivity of carbon in the iron matrix. The calculated diffusion activation enthalpy for a Fe-Cr-C alloy was about 4.25 kJ/mol more than that for diffusion in pure Fe-C alloys. Because Cr raised the activation enthalpy for carbon diffusion in iron [92], more cementite was formed in the steel and the free carbon content in ferrite was reduced. In contrast, Mo did not enrich cementite content, so a state of near para-equilibrium existed, leading to an increase in the interstitial carbon content in the matrix. Thus, the addition of Cr was another method for improving the strain aging resistance of low carbon steels.

Yoo et al. [75] found that microstructural constituents made a difference to strain aging resistance. Single γ phase cooled X80 steel pipe had better strain aging resistance than $\gamma+\alpha$ cooled pipe, which was thought to be caused by the formation of finer polygonal ferrite in the single phase cooled steel. This finding suggested that strain aging resistance could be enhanced by reducing the non-recrystallization region and controlling the cooling rate. The revised heat treatment method effectively promoted the formation of polygonal ferrite.

Zhang et al. [93] studied the effect of anti-corrosion coatings on X100 pipeline steels. By increasing the aging temperature from 180°C to 250°C, there was a considerable increase in the strength and YS/TS ratio in longitudinal and transverse directions, a decrease in

uniform elongation in the longitudinal direction, reappearance of the Luders band, a drop in the Charpy impact toughness and a rise in the ductile-brittle transition temperature (DBTT) in the transverse direction. Therefore, Zhang et al, suggested that strain aging resistance of coated pipes could be improved by reducing the coating temperature.

In addition to control of the heat treatment, Koohbor et al. [94] found that strain aging resistance of low carbon steels was enhanced by increasing the rolling speed. By increasing the rolling speed from 43 to 73 rpm, the time required for strain aging rose from 17 days to over 10 months. This was attributed to the occurrence of partial static recrystallization due to the high rolling rate. This led to a decrease in the dislocation density and made strain aging more difficult.

2.3.4 Cumulative Strain Aging Effect of All Thermal Events

Since strain aging of pipes can occur at many stages during pipeline fabrication, including pipe forming, anti-corrosion coating application, girth welding and field joint coating, researchers have been trying to define a simulated heat treatment which reflects the cumulative strain aging effect of all thermal events. Based on classical strain aging theory (segregation of C atoms to dislocations to form atmospheres), Noecker et al. [34] developed an analytical expression that allowed strain aging treatment to be normalized to an equivalent time at an isothermal temperature (250°C).

$$t_{250^{\circ}C} = \frac{250^{\circ}C}{D_{250^{\circ}C}} \left(\frac{D_1 t_1}{T_1} \right) \quad (2.4)$$

where T_1 is a specific aging temperature, t_1 is a specific aging time, D_1 is the diffusion coefficient at T_1 , $D_{250^{\circ}C}$ is the diffusion coefficient at 250°C and $t_{250^{\circ}C}$ is the equivalent aging time at 250°C.

They conducted a series of tensile tests to compare the tensile properties of steels treated at equivalent time and temperature combinations. The aging condition at 200°C for 104 minutes is equivalent to that at 250°C for 15 minutes. However, similar yield strength and UTS values were not achieved through this analytical approach. The expression underestimated the lower temperature aging response, as presented in Figure 2.22 and Figure 2.23. The results indicated that there were limitations in the applicability the equivalent time approach (Equation 2.4). As shown in Figure 2.23, the yield strength for each temperature saturated after some prolonged aging time and the saturation strength seemed to be dependent on the aging temperature. Efforts are still underway to understand the physical origin of temperature dependence of the saturation strength.

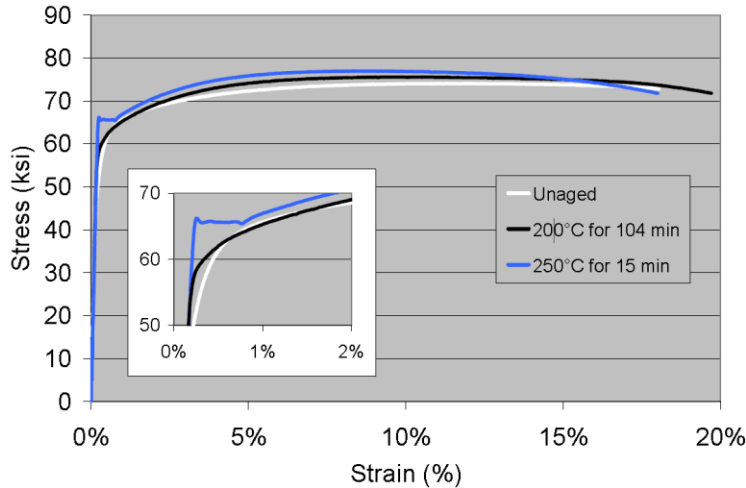


Figure 2.22 Engineering stress-strain curves for XOM1 line pipe aged in the Gleeble™ subject to equivalent thermal cycles per Equation 2.4 [34].

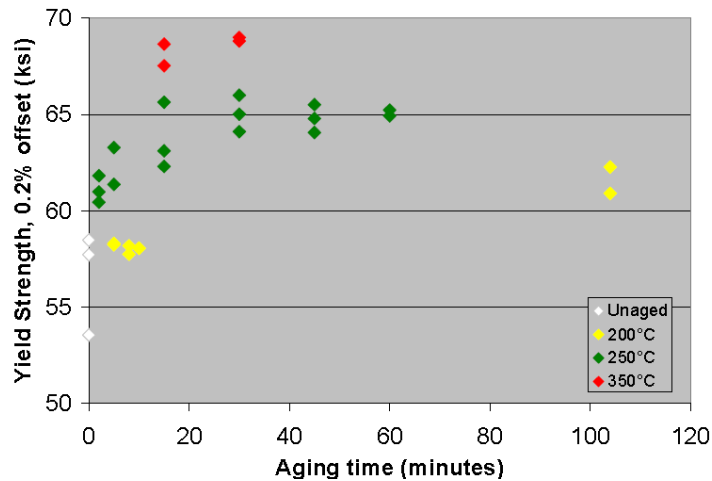


Figure 2.23 Yield strength as a function of actual aging time for various aging temperatures [34].

2.4 Design of Experiments

Design of experiments (DOE), also named experimental design, is a methodology for studying any response that varies as a function of one or more independent variables [16]. Compared with traditional statistical design methods used for studying the effect of only one variable at a time (OVAT), DOE is widely used to tackle complex problems where more than one variable can affect a response and the variables may interact with each other. The purpose of engineering experimentation based on DOE is to explore how to control process inputs so as to produce the desired outputs. By analyzing the cause-and-effect relationships, process inputs can be managed to optimize the output. In DOE, process inputs are usually called variables, predictors or factors and outputs are called responses.

DOE proceeds as illustrated in Figure 2.24. By several cycles of output optimization, better correlations between factors and responses can be achieved.

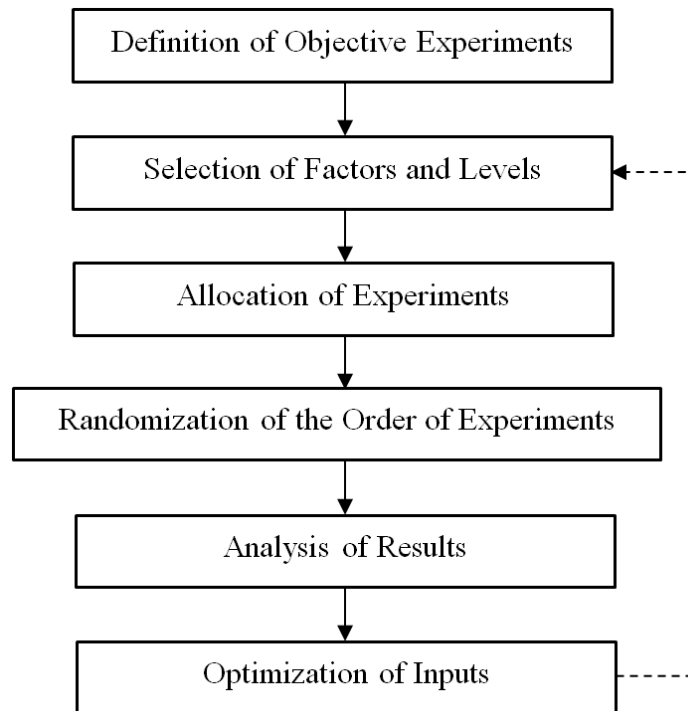


Figure 2.24 General DOE process.

In this section, the most commonly used methods for DOE – factorial experiments and response surface methods - are introduced. In addition, analysis of variance (ANOVA) is used to compare the statistical significance of different variables is introduced.

2.4.1 Factorial Experiments

In DOE, a full factorial experiment (also called fully crossed design), is an experiment which contains at least two factors, each of which consists of discrete possible values (also called “levels” in statistics). A full factorial design includes $a \times b \times c \dots$ designs, where each letter represents the number of levels of a factor, and all the runs are performed in random order. Such a factorial experiment enables investigators to study the effect of each variable as well as their interaction on the response.

2^k factorial experiments, which consist of only two levels of each variable, are one of the simplest and most fundamental factorial experiments; k is the number of variables and 2^k means the number of unique cells or total runs in each replicate of the design. When all the experimental runs are performed in random order, the experiments are able to characterize all the factors in the design and resolve two-order or higher-order interactions.

If the number of experimental runs in a full factorial design is too high to be feasible, a fractional factorial design can be conducted by omitting some of the possible combinations. It only consists of a carefully selected subset of experimental runs of a full factorial design. The subset is selected based on the sparsity of effects principle [95], stating that the responses are affected mainly by a limited number of main effects and lower-order interactions. In two-level factorial experiments, fractional designs are expressed using the notation 2^{k-p} , where k is the number of factors and p is the size of the fraction of the full factorial design.

3^k factorial design can be performed when a factorial experiment is constructed in k variables with each variable appearing at three evenly spaced levels. However, if all possible combinations are involved in the design, a large number of runs are required so that more efficient designs have been developed (such as the Box-Behnken design) by eliminating some of the experiments.

2.4.2 Response Surface Methodology

Response surface methodology (RSM), introduced by Box and Wilson [96] in 1951, is a collection of mathematical and statistical techniques used for modeling and analyzing the relationship between a response of interest and several factors and their interactions [97]. Linear or quadratic empirical equations employed to describe the relationship have the form:

$$Y = \beta_o + \sum_{i=1}^n \beta_i \cdot x_i + \sum_{i=1}^n \beta_{ii} \cdot x_i^2 + \sum_{i=1}^n \sum_{j<i}^n \beta_{ij} \cdot x_i \cdot x_j \quad (2.5)$$

where Y is the dependent variable of interest (e.g., the change in YS), x_i and x_j are the independent variables and β_o , β_i , β_{ii} and β_{ij} are the constant, linear, quadratic and interaction terms, respectively. Two-level factorial designs are not capable of quantifying the curvature in the response [16]. A factor must have at least three levels so as to fit a model that can resolve curvature in the response. Thus, through RSM, center points should be added to the 2^k or 2^{k-p} designs to provide more information about curvature and to increase the number of error degrees of freedom without unbalancing the design. If the low and high coded levels of variables are -1 and +1, the level codes of central points are 0. A 2^3 plus centers design is shown in Figure 2.25.

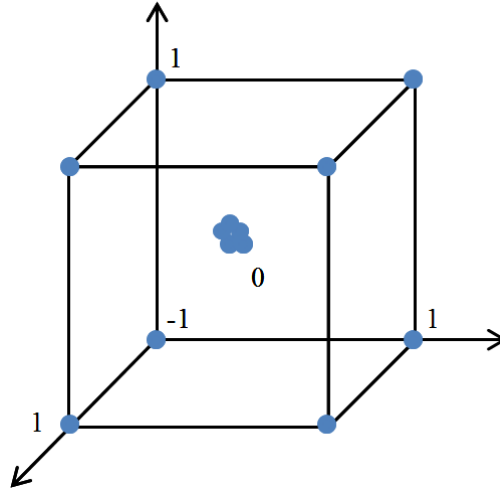


Figure 2.25 Schematic of 2^3 plus centers design.

Box-Behnken design (BBD), a major experimental design for RSM developed by George E. P. Box and Donald Behnken in 1960 [98], requires fewer runs than 3^k full factorial designs. Similar to 3^k designs, Box-Behnken designs can also deliver a full quadratic model containing squared terms and products of two variables. Each factor is placed at one of three equally spaced values coded as -1, 0 and +1, respectively.

Box-Behnken designs are essentially fractions of 3^k factorial designs with replicate experimental runs at center points to preserve the balance of the designs [99]. Figure 2.26 gives a comparison of combinations between a 3^3 design and a three-factor and three-level design. The number of treatment combinations is effectively reduced from 27 to 15 designs. Table 2-2 compares the number of runs of experiments with varying number of factors required by 3^3 designs and Box-Behnken designs. The experimental efficiency is improved with increasing number of factors.

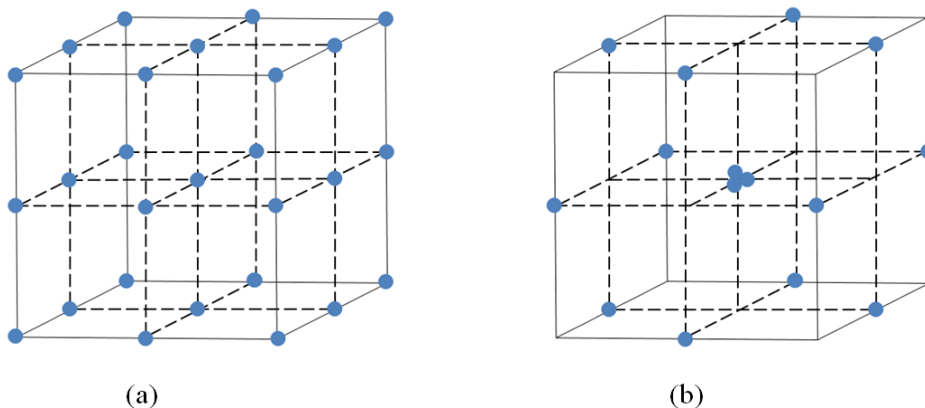


Figure 2.26 Comparison between (a) 3^3 factorial design and (b) three-factor and three-level Box-Behnken design.

Table 2-2 Number of Runs Required by 3^k Factorial Designs and Three – Level Box-Behnken Designs

Number of Factors (k)	3^k Factorial Design	Box-Behnken Design
3	27	15
4	81	27
5	243	46
6	729	54

2.4.3 Analysis of Variance

Analysis of variance (ANOVA) consists of a collection of statistical models used for analyzing the differences among group means and variation between groups. An ANOVA setting provides information of the observed variance in different variables, which are partitioned into components attributed to different variation sources.

In DOE, ANOVAs are widely used in comparing the statistical significance of at least three variables. An ANOVA table can be created with a statistical model, giving the information of the source, DF (degrees of freedom in the source), adjusted SS (sum of squares due to the source), adjusted MS (mean sum of squares due to the source), F-value and P-value, as is shown in an example (Table 2-3). The example is obtained from the experimental results in this work. The response is the Δ YS of the microalloyed steel (X70) UOE pipe samples (named Steel A) and the factors include temperature (T), time (t) and pre-strain (ϵ). The ANOVA table is generated based on a BBD using the software Minitab 17.

Table 2-3 ANOVA Table of 3-factor BBD for Δ YS of Steel A

Source	DF	Adj SS	Adj MS	F-Value	p-Value
Model	9	4164	463	6.6	0.026
Linear	3	2936	979	13.9	0.007
T	1	2679	2679	38.0	0.002
t	1	222	222	3.1	0.137
ϵ	1	36	36	0.5	0.509
Square	3	1173	391	5.5	0.048
T2	1	4	4	0.1	0.826
t2	1	6	6	0.1	0.776
ϵ 2	1	1152	1152	16.3	0.010
Interaction	3	55	18	0.3	0.851
T·t	1	8	8	0.1	0.752
T· ϵ	1	35	35	0.5	0.514
t· ϵ	1	13	13	0.2	0.690
Error	5	353	71		
Lack-of-Fit	3	353	118		
Pure Error	2	0	0		
Total	14	4517			

Source means the source of the variation in the data, including model, error and total. In Box-Behnken designs, the model includes individual variances and their squares and interactions in a quadratic model. Error means the variability within the groups, consisting of pure errors and lack-of-fit.

DF is the number of values in the final calculation of a statistic that are free to vary. It means the number of independent ways by which a dynamic system can move without violating any constraint imposed on it. The DF of each individual variance, its square term and interaction (1) is shown in Table 2-3.

SS represents a measure of variation or deviation from the mean. It is calculated as a summation of the squares of the difference from the mean. In ANOVA, the total SS expresses the total variation attributed to various variables. The adjusted SS is independent of the order in which the factors are entered into the model. The lack-of-fit SS is one of the components of a partition of the sum of squares in an analysis of variance, used in the numerator in an F-test of the null hypothesis that suggests that a proposed model fits well.

MS represent an estimation of population variance, which is calculated by dividing the corresponding SS by DF. In ANOVA, MS can be used to determine whether factors (treatments) are significant. The adjusted mean of squares does not depend on the order the factors are entered into the model.

The F-value of each term is a ratio of mean squares. The numerator is the MS for the term and the denominator is selected such that the expected value of the numerator MS differs from the expected value of the denominator mean square only by the effect of interest. Therefore, a high F-value means that the variation among group means is more than would be expected by chance and, thus, indicates a significant effect.

The p-value is a function of the observed sample results that are used for testing a statistical hypothesis. The p-value is used in the context of null hypothesis testing in order to quantify the idea of statistical significance of evidence. If the p-value is equal to or smaller than a certain significance level, it suggests that the observed data are inconsistent with the assumption that the null hypothesis is true and thus that hypothesis must be rejected. The p-value ranges from 0 to 1. When the p-value is small (usually less than a significance level, like 5% or 1%), the null hypothesis should be rejected and the other hypothesis should be true. Thus, a smaller p-value is an effective indicator for higher significance of a factor in a model.

2.5 Summary

Microalloyed steels manufactured by TMCP are widely used in the pipeline industry because of their improved mechanical properties and reduced cost for manufacture. In particular, X70 steel has been shown to be preferable for manufacturing pipes due to its higher strength (compared with X60 steel manufactured by traditional hot rolling) without loss of ductility and fracture toughness. UOE formed X70 steel pipes experience strain aging during the FBE anti-corrosion coating process, in which the pipes are heated at temperatures ranging from 180°C to 250°C.

Strain aging mainly involves diffusion of interstitial C and/or N atoms to the dislocations in steels. The formation of atom clusters and/or precipitates was also found after aging for a relatively long period (e.g., 150 minutes [61]). Previous research showed that strain aging has remarkable effects on the mechanical properties of microalloyed steels, especially tensile properties, hardness and toughness. Strain aging variables includes aging temperature, time, imposed plastic strain, steel composition and microstructure. However, the effects of these aging variables on mechanical properties have not quantified. In this work, DOE is used to determine the relationship between the property changes and variables. The effect of aging temperature, aging time, through wall thickness position and imposed plastic strain are discussed in Section 6.1, Section 6.2, Section 6.3 and Section 6.4, respectively. The fundamentals behind the changes in mechanical properties due to strain aging are discussed in Section 6.5, in terms of microstructural features. Although the tensile properties of aged longitudinal and transverse samples have been measured in previous research, a comparison between the property changes of samples in both directions has not been made. The changes in the yield strength of longitudinal and transverse tensile samples are compared and discussed in Section 6.6.

Chapter 3 Materials and Experimental Methods

In this chapter, information on the microalloyed steels investigated in this work, including chemical composition and position of steel samples extracted from pipes, is reported. This is followed by sample preparation procedures for mechanical property measurement and microstructure analysis. Then, design of experiments (DOE) performed using statistical software Minitab 17 is introduced. Heat treatments conducted for the steel samples, mechanical testing methods (tensile, micro-hardness and Charpy testing) and microstructure characterization techniques are also presented.

3.1 Steels Studied

Three uncoated X70 UOE pipes (labeled A, B and C) from different manufacturers were used for the strain aging study. The steel samples were extracted from pipes located 90° (marked as 1) and 180° (marked as 2) to the weld (see Figure 3.1). Each steel piece was labeled as A1 (Steel A samples located 90° to the weld), A2 (Steel A samples located 180° to the weld), B1, B2, C1 or C2. The diameter and wall thickness of the pipes, the Mn, Ti and N compositions and the nominal C/Nb wt% ratio for each type of steel are shown in Table 3-1. The C/Nb ratio varies from 0.6 in A to 1.2 in B to 1.8 in C. In contrast, the nominal levels for Mn, Ti and N are similar for all steels. Since the Nb added to the steels can combine with C to form NbC precipitates and/or affect the microstructure of the steels, the C/Nb ratio was used as a variable.

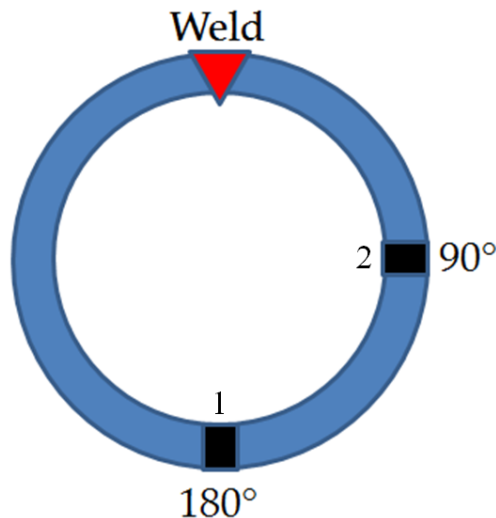


Figure 3.1 Sample locations related to the weld of Steel A, B, C.

Table 3-1 Nominal X70 UOE Pipeline Steel Specifications

Steel	Diameter (mm)	Thickness (mm)	C (wt%)	Nb (wt%)	Mn (wt%)	Ti (wt%)	N (ppm)	C/Nb
A	914	19.1	0.05	0.088	1.60	0.014	40	0.6
B	914	19.0	0.05	0.04	1.65	0.013	40	1.2
C	914	20.4	0.09	0.05	1.59	0.017	<40	1.8

3.2 Sample Preparation

This section introduces the methods for preparing samples for mechanical testing (tensile testing and Charpy testing) and microstructure analysis (OM, SEM and electron backscattered diffraction (EBSD)).

3.2.1 Tensile Samples

Tensile properties of steel samples in both the longitudinal (parallel to the direction of rolling) and transverse (perpendicular to the direction of rolling) directions were studied in this research. Tensile samples extracted in both directions were machined for heat treatment and subsequent tensile testing.

3.2.1.1 Longitudinal Samples

For longitudinal samples, tensile mechanical properties of steels from different positions through the wall thickness (outer diameter (OD), center line (CL) and inner diameter (ID)) and to the weld (90° and 180°) were studied (see Figure 3.3). To make tensile specimens representative of the steel from each position (OD, CL and ID), rectangular specimens with small thickness were used for tensile testing. Specimen dimensions were in accordance with the ASTM standard (ASTM E8/E8M-13a – Standard Test Methods for Tension Testing of Metallic Materials) [100]. A schematic of a subsize sheet-type specimen is shown in Figure 3.2. Detailed dimensions are given in Table 3-2.

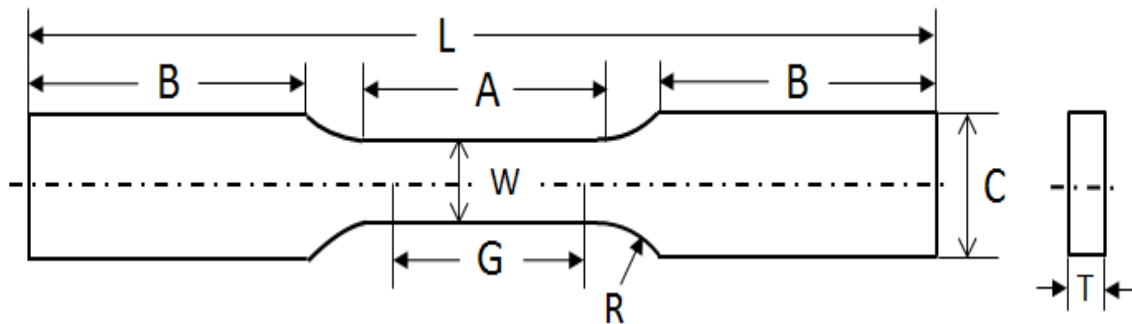


Figure 3.2 Schematic of a rectangular tensile specimen.

Table 3-2 Dimensions of Rectangular Tensile Specimen

Notations (Figure 3.2)	Dimensions (mm)	Tolerance (mm)
G – Gage Length	25.0	± 0.1
W – Width	6.0	± 0.1
T – Thickness	3.0	± 0.1
R – Radius of Fillet	6.0	± 0.5
L – Overall Length	121	± 1
A – Length of Reduced Section	32	± 1
B – Length of Grip Section	40	± 1
C – Width of Grip Section	10	± 1

Subsize specimens ($G = 25$ mm) were manufactured because a large number of tensile bars were required for testing. The length of the grip section (B) value was designed based on the dimensions of cross-heads on the MTS tensile testing machine. The length of the grip section should be long enough to be grabbed tightly. The length of the reduced section (A) selected was the minimum length in ASTM E8/E8M-13a, giving a higher probability for the sample to break close to the middle position of the gage length.

Strips with dimensions 121 mm \times 10 mm \times 20 mm were extracted from the pipes (see Figure 3.1); 3 mm thick steel pieces were extracted from different positions through the thickness and machined into the dog bone shaped tensile specimens (Figure 3.3).

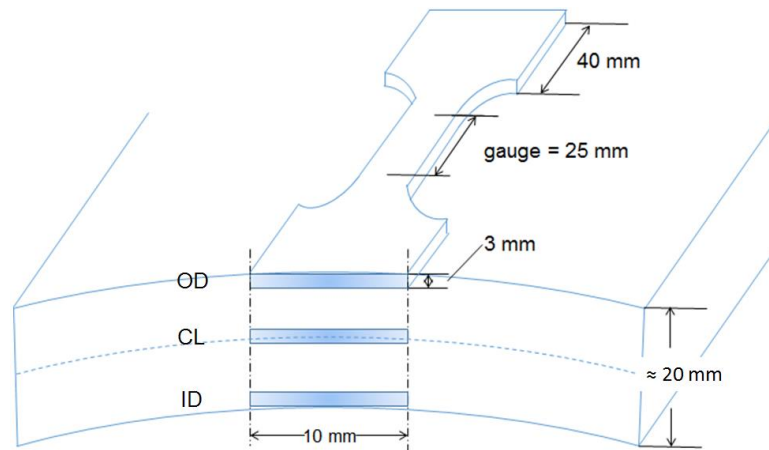


Figure 3.3 Positions of rectangular tensile specimens in a pipe.

3.2.1.2 Transverse Samples

Cylindrical tensile bars in the transverse direction were used for pre-straining and subsequent tensile testing. The samples were only extracted from the pieces of pipes located 180° relative to the weld because of the lack of material for the 90° location. A cylindrical shape was selected because of its uniform deformation after pre-straining. The dimensions were also in compliance with ASTM E8/E8M-13a standard. Figure 3.4 shows a schematic of a round-shape transverse sample. Dimensions of samples are shown in Table 3-3.

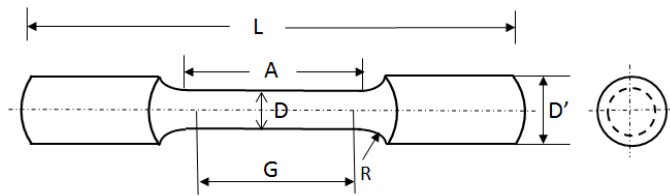


Figure 3.4 Schematic of a cylindrical tensile specimen.

Table 3-3 Dimensions of Cylindrical Tensile Samples

Notations (Figure 3.4)	Dimensions (mm)	Tolerance (mm)
G – Gage Length	24.0	± 0.1
D – Diameter of Reduced Section	6.0	± 0.1
D' – Diameter of Grip Section	9.0	± 0.5
R – Radius of Fillet	6.0	± 0.5
L – Overall Length	122	± 1
A – Length of Reduced Section	30	± 1
B – Length of Grip Section	40	± 1

The G , A and B values were chosen in a similar manner as for the rectangular samples. Specimens were extracted from the mid-thickness of the pipes (Figure 3.5). To ensure that the samples would break in the middle position of the gage length, 0.01-0.02 mm in radius of the steel in the middle was ground away during the machining process, as shown in Figure 3.6.

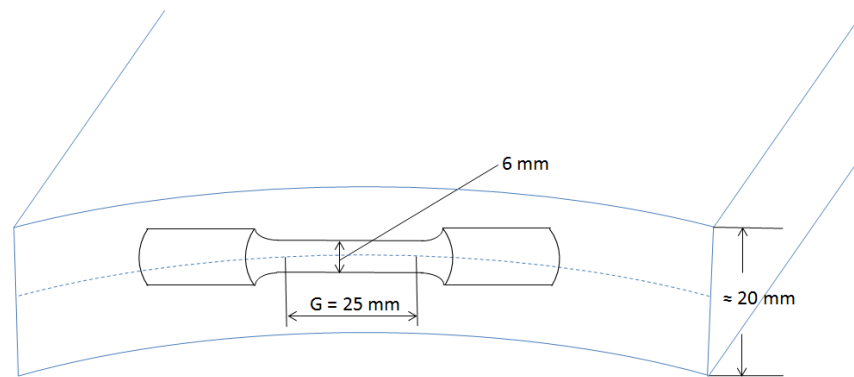


Figure 3.5 Position of a cylindrical tensile specimen in a pipe.

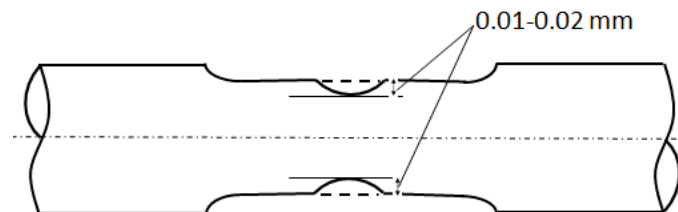


Figure 3.6 Further grinding of a cylindrical sample.

3.2.2 Charpy V-notch Samples

The dimensions of Charpy samples complied with the requirements of the ASTM standard (ASTM E23-05 Standard Test Methods for Notched Bar Impact Testing of Metallic Materials) [101]. Figure 3.7 and Table 3-4 give detailed dimensions of half-size specimens for Charpy tests.

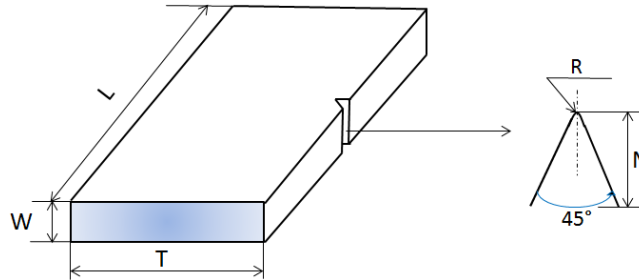


Figure 3.7 Standard half-size Charpy V-notch specimens.

Table 3-4 Dimensions of Half-size Charpy V-notch Specimens

Notations (Figure 3.7)	Dimensions (mm)	Tolerance (mm)
L – Length of Specimen	55	+0, -2.5
T – Thickness of Specimen	10	± 0.05
W – Width of Specimen	5	± 0.05
N – Notch Depth	2	± 0.025
R – Radius of Notch	0.25	± 0.025

Half-size specimens ($W = 5$ mm) were used because they should be thin enough to represent the OD and ID positions relative to the pipes. The positions of the specimens in the pipe are illustrated in Figure 3.8.

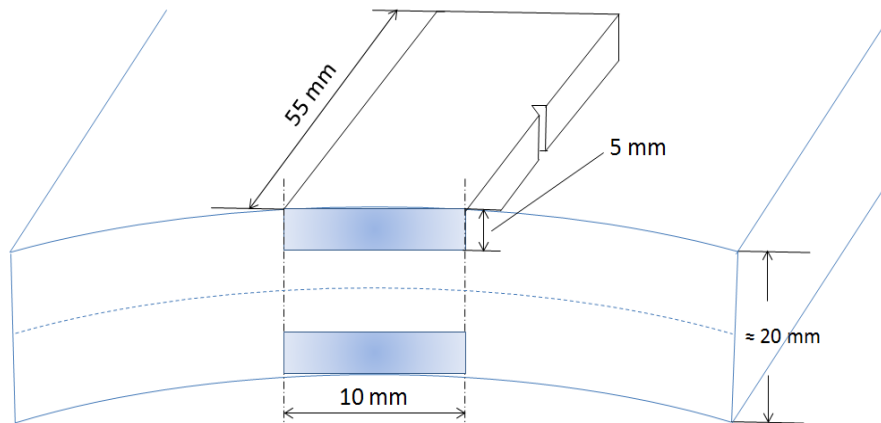


Figure 3.8 Position of Charpy specimens in a pipe.

3.2.3 Metallographic Samples

Samples with dimensions 10 mm × 10 mm × 3 mm were cut (using a precision saw) from grip sections of untested rectangular tensile samples. Longitudinal (10 mm × 10 mm) and transverse (10 mm × 3 mm) surfaces were used for metallographic study. The surfaces of each sample were cleaned and dried prior to mounting. The samples were mounted with mixture of West System 105 Epoxy Resin and 205 Fast Hardener. The mix ratio (105 Resin to 205 Hardener) was 5 to 1 by volume. The mounted specimens are shown schematically in Figure 3.9.

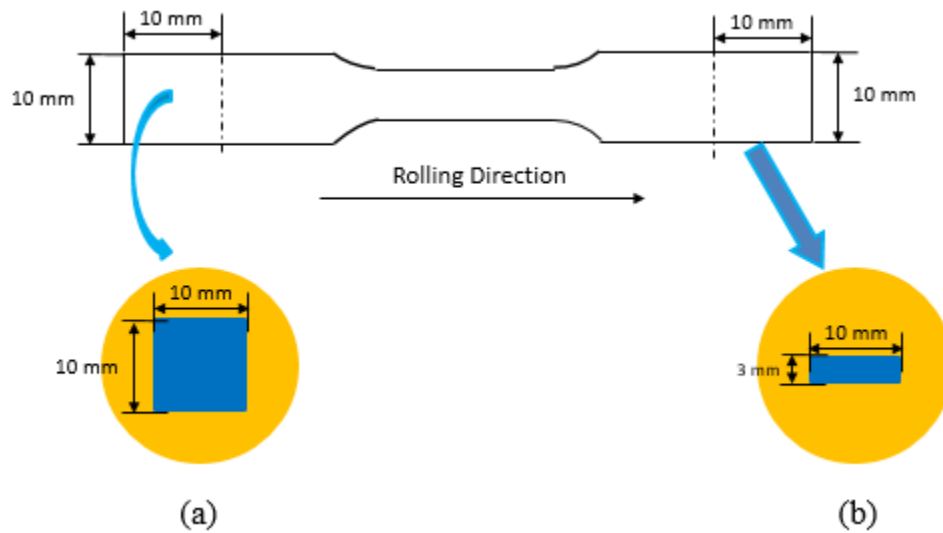


Figure 3.9 Longitudinal surface (a) and transverse surface (b) of mounted samples.

Mounted samples were ground and polished using an auto-polisher (Buehler EcoMet 250). The surfaces were ground using 240, 320, 400 and 800 grit SiC embedded papers sequentially. Afterwards the samples were polished in the sequence of 9 μm , 3 μm and 1 μm polycrystalline diamond suspension. Final polishing was done with 0.05 μm alumina slurry.

Prior to optical microscopy, the exposed surface of the polished samples was etched with 2% (volume fraction) Nital etchant (2% nitric acid + 98% ethanol) at room temperature for 30 s. If hardness testing was to be conducted on a mounted sample prior to metallographic observation, etching was done after the hardness tests (to be discussed in Section 3.5.2).

3.3 Design of Experiments

In this study, a Box-Behnken design (BBD) is performed to design the aging tests and a response surface methodology (RSM) is used to produce a quadratic response of the variables along with the interactions between them. The statistical software Minitab

Academic (version 17) was used to quantify the influence of the statistically significant strain aging factors on the change in mechanical properties and to plot 3D response surfaces for the model.

3.3.1 Box-Behnken Design – Variables and Levels

As mentioned in Section 3.2.1, longitudinal tensile specimens were extracted from different through thickness positions of the pipes. The main strain aging variables and their levels, used in the BBD are shown in Table 3-5. The variables include aging temperature, aging time, position through the thickness (-7.8 mm corresponds to the ID position and +7.8 mm correspond to the OD position) and the C/Nb ratio of each steel. The BBD for longitudinal specimens was performed on those from the location 90° relative to the weld. Since the effects of aging variables on the tensile properties of samples located 90° and 180° relative to the weld are similar, as shown in Appendix A (Table A-2 and Figure 0.1 to Figure 0.6), the BBD was not performed for the 180° location.

Table 3-5 Strain Aging Variables and Levels for BBD – Longitudinal Tensile Properties

Variable	Level		
	-1	0	1
Temperature (°C)	175	215	255
Time (min)	5	15	25
Position (mm)	-7.8	0	7.8
C/Nb	0.6	1.2	1.8

Transverse tensile specimens were extracted from the positions where the gage length section is in the CL position. Artificial pre-strains were imposed on some of the samples to study the effect of the magnitude of pre-strain on strain aging. Instead of the “position”, pre-strain acts as another variable for the BBD. The variables and their levels are shown in Table 3-6.

Table 3-6 Strain Aging Variables and Levels for BBD – Transverse Tensile Properties

Variable	Level		
	-1	0	1
Temperature (°C)	175	215	255
Time (min)	5	15	25
Strain (%)	0	1.7	3.4
C/Nb	0.6	1.2	1.8

3.3.2 Non Box-Behnken Design

Additional aged transverse and longitudinal tensile specimens (not used for BBD) were prepared to verify the response surface models generated from the BBD. The longitudinal samples from the position 180° to the weld were used to assess whether the strain aging model derived at the 90° location was valid at the 180° location.

3.4 Heat Treatment

A salt bath furnace was used for heat treatment because of its rapid heat transfer and excellent temperature uniformity [102]. The upper limit of the furnace temperature was 1000°C. In this work, target temperatures were 175°C, 215°C and 255°C, according to Table 3-5 and Table 3-6. A few additional samples were heat treated at higher temperatures (i.e., 300°C and 350°C). For precise temperature control, a thermocouple was attached to the bath salt in the furnace, as shown in Figure 3.10.



Figure 3.10 Salt bath furnace attached with a thermocouple.

When a target temperature was reached and maintained for 30 minutes, tensile or Charpy samples were completely dipped into bath salt and the cover of the furnace was closed immediately. At the same time, a timer was turned on for time control. Each sample was heat treated (aged) at a target temperature for 5 minutes, 15 minutes or 25 minutes. When the time was complete, the samples were quenched into water and then kept at room temperature in dry conditions, as shown in Figure 3.11.

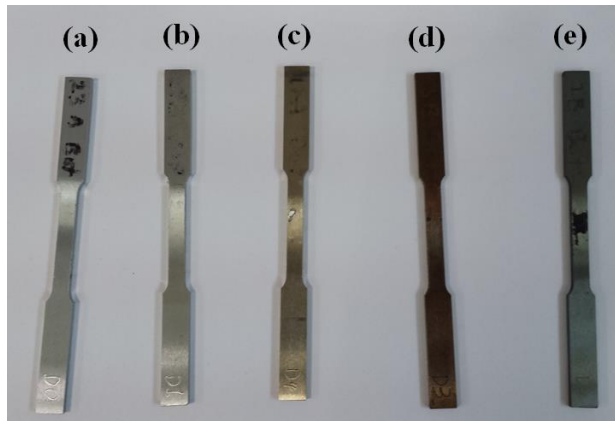


Figure 3.11 Longitudinal tensile specimens heat treatment for 15 minutes at: (a) 175°C, (b) 215°C, (c) 255°C, (d) 350°C and (e) 300°C.

3.5 Mechanical Testing

Mechanical testing methods, including tensile, micro-hardness and Charpy V-notch tests, are described in this section.

3.5.1 Tensile Testing

Prior to tensile testing, the cross section area (A) of each rectangular or cylindrical sample was measured and calculated. The methods for calculating A of rectangular and cylindrical samples are given in Equation 3.1 and Equation 3.2.

$$A = W \cdot T \quad (3.1)$$

$$A = \frac{\pi}{4} D^2 \quad (3.2)$$

where W and T are the width and thickness of the reduced section of a rectangular specimen and D is the diameter of the reduced section of a cylindrical specimen. A Vernier caliper was used to measure W and T at least 3 times for each specimen and the average value was used for the final calculation. The cross section area of cylindrical samples was determined by the diameter (D) of reduced section measured by a micrometer caliper. Since 0.01-0.02 mm in radius of the sample in the middle was ground away during the machining process, the minimum diameter measured around the middle position of the total length was the D value used for calculation.

After cross section area measurement, a 25 mm punch was used to leave marks on the two gage length sections within the reduced section of a rectangular sample. The purpose was to ensure that the fracture was located within at least one marked gage section even if a sample failed near the shoulder. Only one marked gage length section (in the middle of

the reduced section) was used for cylindrical samples, because these samples fractured in the middle. Figure 3.12 shows the positions of marked gage length section.

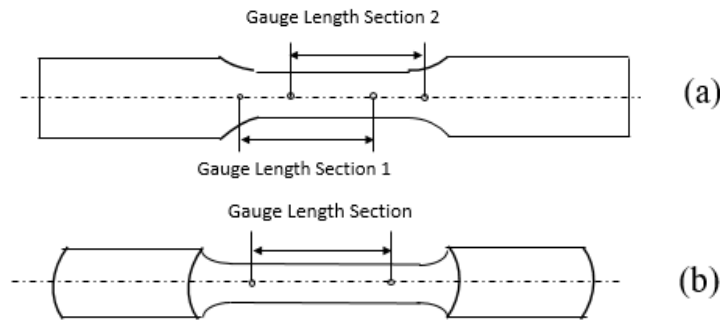


Figure 3.12 Positions of marked gage length section for (a) rectangular and (b) cylindrical specimens.

Tensile testing is conducted using a tensile tester (MTS Electromechanical Universal Testing System). Each specimen was stretched to fracture with a dual strain rate (1.563 or 12.5 mm/min). The lower initial strain rate was used to reveal more detail during yielding, while the increased strain rate was used to improve data collection efficiency. The extensometer gave the displacement (L), which was converted into engineering strain (ϵ) using Equation 3.3, where G is the gage length. The engineering stress (σ) was calculated using the output load (F) divided by the original cross section area Equation 3.4.

$$\epsilon = \frac{L}{G} \quad (3.3)$$

$$\sigma = \frac{F}{A} \quad (3.4)$$

3.5.1.1 Tensile Property Measurement

Tensile properties were calculated after a sample was tested to fracture using the tensile testing machine. Figure 3.13 shows an example of a stress-strain curve, where the engineering stress (of an as-received longitudinal A1 sample) is plotted as a function of engineering strain. After a tensile specimen was elongated to fracture, the tensile properties, including 0.5% elongation yield strength (YS), ultimate tensile strength (UTS), yield to tensile strength ratio (YS/TS) and uniform elongation, were determined.

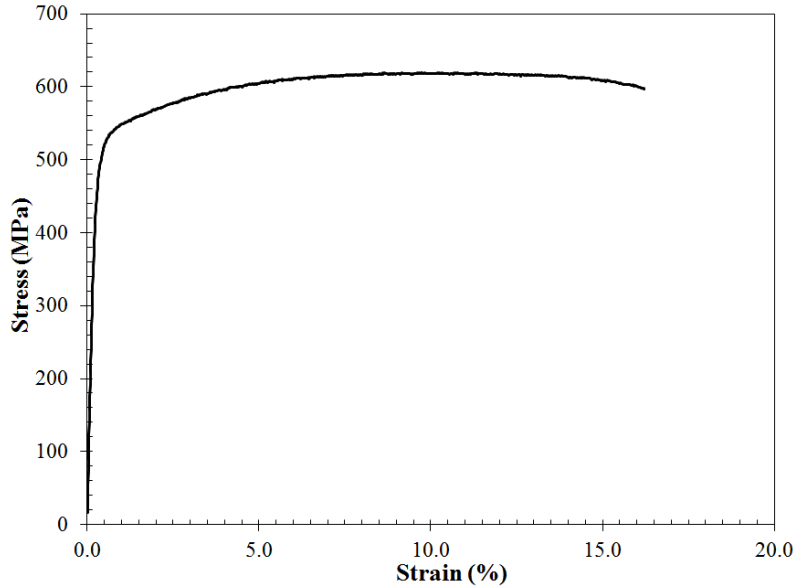


Figure 3.13 Stress-strain curve for an as-received longitudinal A1 sample.

After each specimen was broken into two pieces, the total percent elongation ($\%El$), an indicator of ductility, was determined by removing the fractured specimen from the grips, fitting the broken ends together and measuring the distance between the gage marks (final gage length, G').

$$\%El = \frac{G' - G}{G} \quad (3.5)$$

If the fracture location was within both marked gage length sections in a rectangular sample (i.e., two G' values), the larger one was used for measuring the percentage of elongation because it covered the total elongation at break.

3.5.1.2 Pre-straining

After the initial cross section areas of some transverse specimens (i.e., cylindrical specimens) were measured, the specimens were pre-strained permanently to 1.7% or 3.4% (according to Table 3-6) prior to heat treatment or tensile testing. Since elastic deformation is reversible, the applied strain was higher than permanent strain. After trying a series of applied strain values, it was found that 1.7% and 3.4% permanent strain could be achieved if initial tensile strains of 2.0% or 3.75% were applied to the steels (Steel A, B or C) (Figure 3.14a and Figure 3.14b).

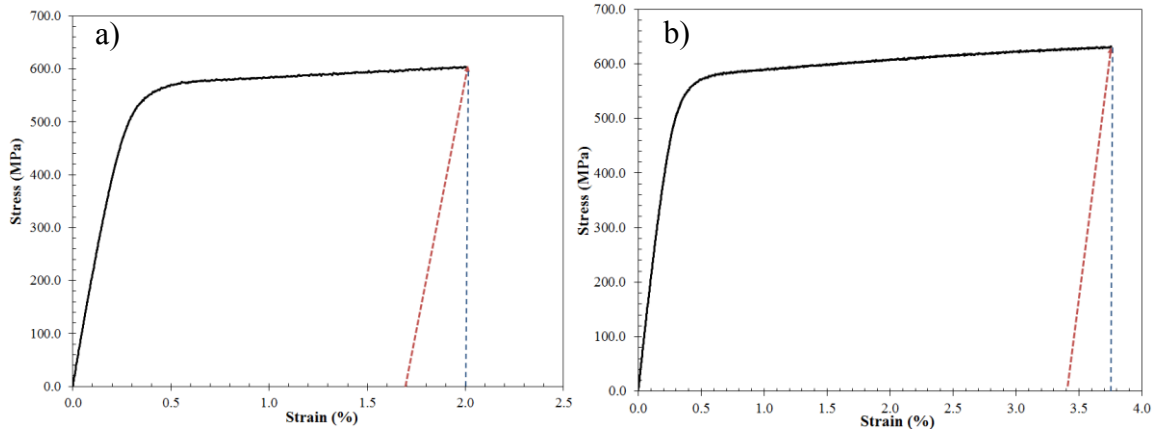


Figure 3.14 Pre-straining curves for transverse Steel A1 exhibiting a permanent tensile strain of (a) 1.7% and (b) 3.4%.

3.5.2 Vickers Hardness Testing

The hardness values from the OD, CL and ID positions of as-received Steel A1, B1 and C1 were measured using a Vickers tester (Wilson HV3100). The Vickers testing method was selected because its hardness measurement is independent of the indenter size and the indenter can be used for all materials irrespective of hardness. Micro-hardness testing was conducted on polished samples using a Vickers hardness indenter with a 0.5 kg load. 24 indents (in a 4×6 matrix) were marked on each sample, as shown in Figure 3.15.

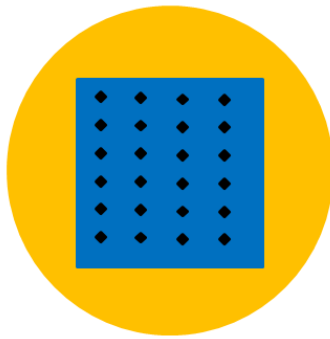


Figure 3.15 Vickers hardness indents on a mounted sample.

A dwell time of 14 seconds was set for each measurement. The sizes (d_1 and d_2) of each indent were measured with an automated Vickers hardness tester (Figure 3.16) and converted to hardness values using the Equation 3.6, where F is the force applied to the diamond (Figure 3.16) in kg-force. The two highest hardness values and the two lowest values were omitted and the average of the remaining 20 measured values was used as the estimated hardness value.

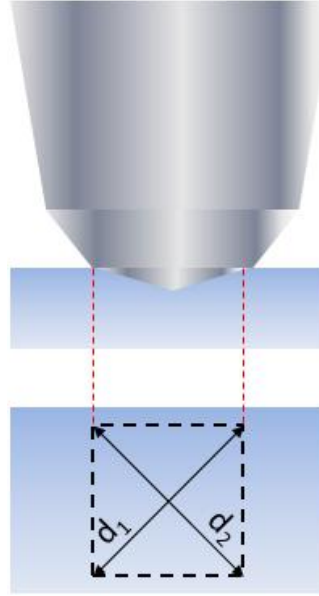


Figure 3.16 Measurement of an indent by Vickers hardness tester.

$$HV = \frac{2 \sin\left(\frac{136^\circ}{2}\right)F}{\left(\frac{d_1+d_2}{2}\right)^2} \quad (3.6)$$

3.5.3 Charpy Testing

The impact toughness of aged Steel A1 was measured through Charpy V-notch testing. Half-size (55 mm × 10 mm × 5 mm) Charpy V-notch impact tests were performed at 5 different temperatures (-60°C, -40°C, -20°C, 0°C and 20°C). A thermocouple was submersed into a bath containing ethanol and dry ice, which was used to obtain lower temperatures. Each specimen was kept at a target temperature for over 10 minutes.

Prior to Charpy testing, the specimens extracted from both OD and ID positions of Steel A1 were heat treated under four different conditions – no heat treatment, 215°C for 5 minutes, 255°C for 5 minutes and 255°C for 25 minutes. For each heat treatment parameter, 3 replications of the Charpy tests were conducted at each temperature. The average and standard deviation were calculated for plotting an absorbed energy versus temperature curve.

3.6 Microstructural Characterization

After the polished samples were etched with 2% Nital, microstructures from the OD, CL and ID positions of as-received Steel A1, A2, B1, B2, C1 and C2 were analyzed using OM (Olympus BX61), SEM (Zeiss Sigma 300 VP-FESEM) and EBSD (Zeiss Sigma FESEM with EDX/EBSD). Quantitative measurements of grain size and microconstituent fraction were undertaken based on ASTM Standards E112-13 [103] and E562-11 [104]. ImageJ software was used to measure the grain size using the circular intercept method

and to estimate the volume fraction of microconstituents. EBSD grain size analysis was performed by detecting changes in crystallographic orientation between neighboring grains of greater than 15° to determine the position of grain boundaries.

3.6.1 Grain Size Measurement

This section begins with grain size measurement based on OM images using the intercept method. This is followed by the EBSD map method used for obtaining grain size distribution.

3.6.1.1 Intercept Method

Grain size measurement was in compliance with ASTM 112-13. After an optical microscope image was opened with ImageJ software (version 1.50i), a circle of known diameter (D) was overlaid on a representative field of the photomicrograph. An example of an optical microscope image is shown in Figure 3.17.

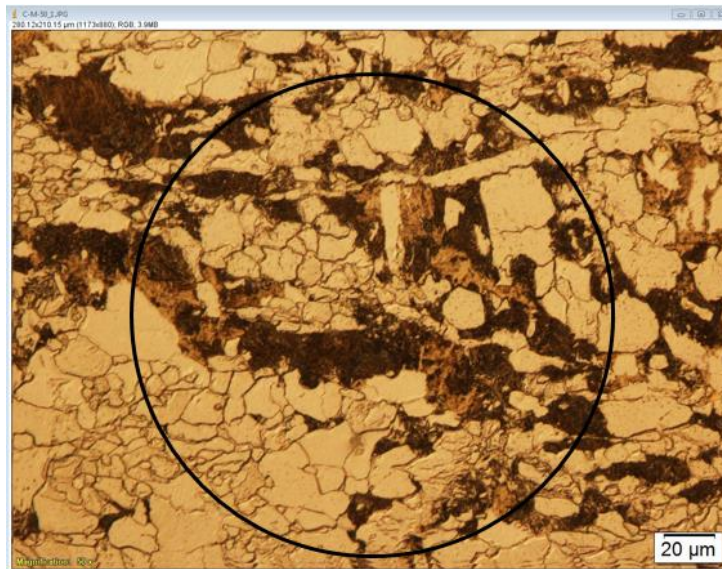


Figure 3.17 Circle overlay for grain size measurement of a Steel C1 sample from the CL position.

The average grain size (GS) was estimated as follows:

$$GS = \frac{\pi D}{N} \quad (3.7)$$

where D is the diameter of the overlaid circle (highlighted in Figure 3.19) and N is the number of the intersections of the circle with grain boundaries. For each sample, grain size measurements were undertaken at 5 locations and the final grain size was the average of the 5 measurements.

3.6.1.2 EBSD Method

EBSD is a technique used to determine the crystallographic orientation of materials. Backscattered electrons are generated because the incident electrons are elastically scattered by the atoms in the solid. A divergent source of electrons can be formed close to the surface of the sample. EBSD is carried out on a flat and highly polished sample tilted 70° from the horizontal. Since some of the incoming electrons are incident on the atomic planes at angles satisfying the Bragg equation [105], these electrons are diffracted in all directions and form a pair of large angle cones corresponding to a specific crystallographic plane. When the diffracted electrons escape the material and collide with the phosphor screen located within the specimen chamber, the different cones give rise to characteristic Kikuchi bands [106] producing an electron backscattered diffraction pattern, as shown in Figure 3.18. Such patterns show the geometry of the lattice planes in the crystal and give direct information about the crystalline structure and crystallographic orientation of the grain from which they originate. By indexing the patterns with a crystallographic database, the different phases and their orientation can then be identified, and thus a map of Euler angle triplets [107] and phase associated with each pixel can be constructed, as shown in Figure 3.19.

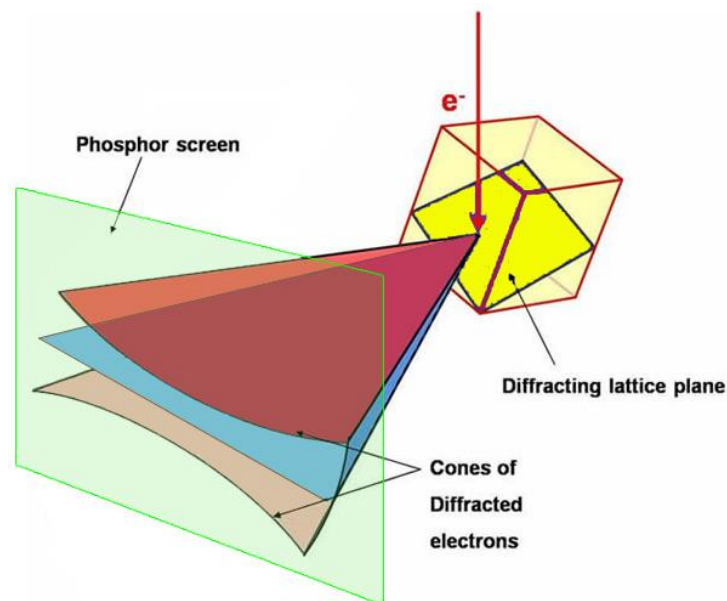


Figure 3.18 Formation of EBSD pattern. Electrons from a divergent source incident on crystal planes at the Bragg angle are diffracted into a pair of cones to form Kikuchi bands in the diffraction pattern [108].

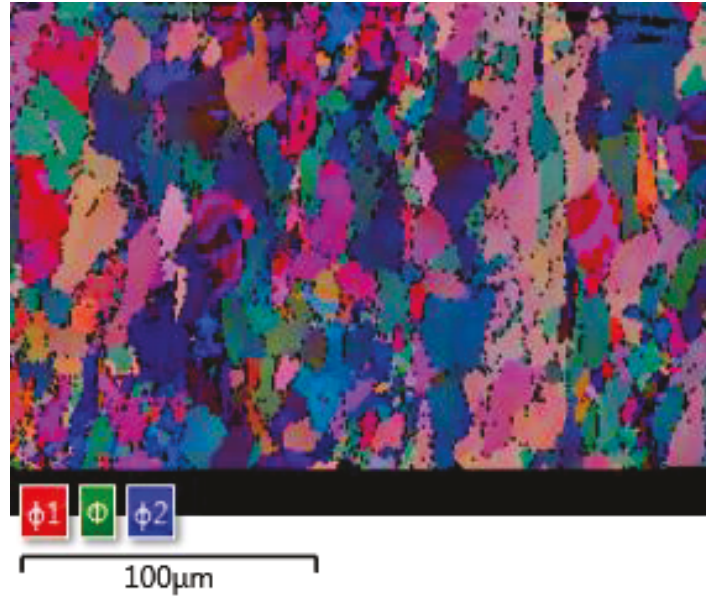


Figure 3.19 A map of Euler angle triplets for Steel C1 at the CL position in the longitudinal direction.

The microscope accelerating voltage influences EBSD performance. The electron beam spread in the sample increases with accelerating voltage and should therefore be kept as low as possible. However, the resolution deteriorates when the voltage is lower than 15 kV and this is believed to be the result of a reduction in pattern quality due to a reduction in the efficiency of the transmission phosphor at lower voltages [110]. In this work, the samples were analyzed using a Zeiss Sigma field-emission (FE) SEM with an appropriate back scattered electron detector at an accelerating voltage of 20 kV and an aperture size of 60 μm .

The time to acquire a data point during a beam scan depends on the time required to obtain an analyzable diffraction pattern. This depends primarily on the material and microscope operating conditions. In this work, the data acquisition time per point on our steel samples, where we typically average the pattern for 2 frames, is 45 ms.

EBSD grain size analysis was conducted using EBSD maps, obtained with EBSD software AZTechKL, that convey visually the basic character of the microstructure with 2D information about grain size and shape. Based on the average grain size measured using OM images, the step size was set as 1 μm . Entire grains were colored by their size relative to the range of grain sizes in the map and, thus, grain boundaries were revealed between map pixels where there was an interpixel change of orientation greater than 15° , (Figure 3.20). EBSD post-processing system CHANNEL 5 was used for grain size measurement. The area of each grain was computed and the grain size (diameter) was determined by assuming a circular shape for each grain.

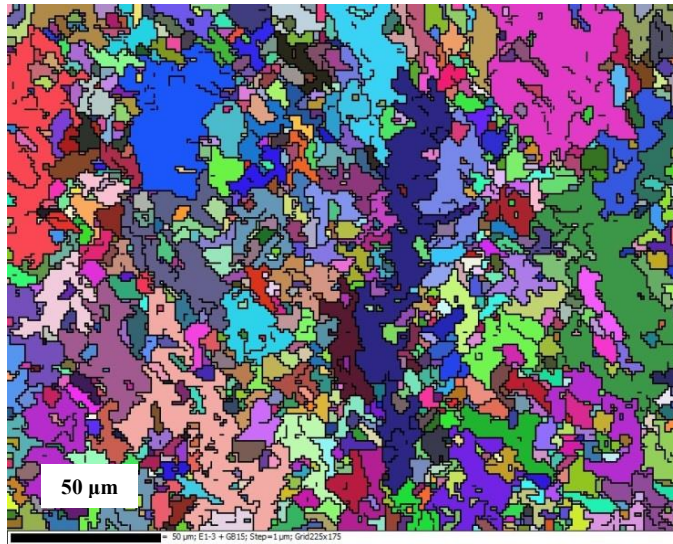


Figure 3.20 EBSD misorientation map for Steel B1 at the CL position showing grains with high-angle ($\geq 15^\circ$) grain boundaries.

3.6.2 Volume Fraction of Microconstituents

SEM analysis was performed using a Zeiss Sigma FESEM. SEM images (magnification of $1k\times$ to $30k\times$) were analyzed to determine the microconstituents in the microstructures of all three steels.

In accordance with ASTM E562-11, quantitative phase analysis was conducted by overlaying a grid of points on optical photomicrographs (magnification of $500\times$). The volume percent of the microconstituents of interest in the micrograph was determined by the fraction of points falling within the corresponding area. The number of points (or the grid size) was determined by a visual estimation of the area fraction of the constituent of interest. The guideline of grid size selection followed Table 3-7. Figure 3.21 gives an example of the grid overlay for volume fraction measurement for a sample from the CL position of as-received Steel C1.

Table 3-7 Guidelines for Grid Size Selection [104]

Visually Estimated Area Fraction (%)	Number of Points
2 – 5	100
5 – 10	49
10 – 20	25
>20	16

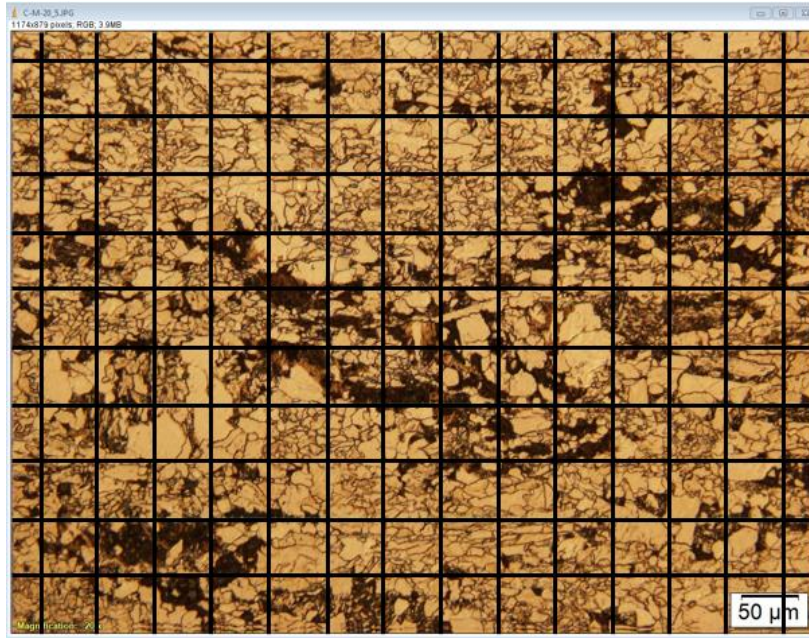


Figure 3.21 Grid overlay for volume percentage of microconstituents measurement of a Steel C1 sample from the CL position.

Chapter 4 Mechanical Properties

The mechanical properties, including tensile properties, micro-hardness and Charpy impact toughness, of as-received and strain aged microalloyed steels were measured and analyzed. Design of experiments was performed to investigate the relationship between these properties and the aging variables.

4.1 Longitudinal Tensile Properties

Tensile properties of the longitudinal samples, including the YS, UTS, YS/TS and strain hardening exponent (n), were obtained from corresponding tensile curves and are presented in this section. Quantitative analysis of the properties affected by aging was undertaken based on the Box-Behnken design (BBD) using the variables and levels in Table 3.5. Empirical equations (represented as quadratic models) were developed to express the changes in each property due to aging as a function of statistically significant aging variables using the software Minitab 17.

4.1.1 Longitudinal Tensile Properties of As-received Steels

The longitudinal tensile curves for Steel A, B and C (extracted from the CL position) located 90° and 180° relative to the weld are shown in Figure 4.1a and Figure 4.1b, respectively. 0.5% total elongation was used to determine the yield stress (marked in Figure 4.1). Steel A and B exhibit similar tensile behavior, while Steel C exhibits slightly different work hardening behavior at low strain values. The difference in yielding is attributed to differences in strain history and microstructure features between the steels (to be discussed in Chapter 6).

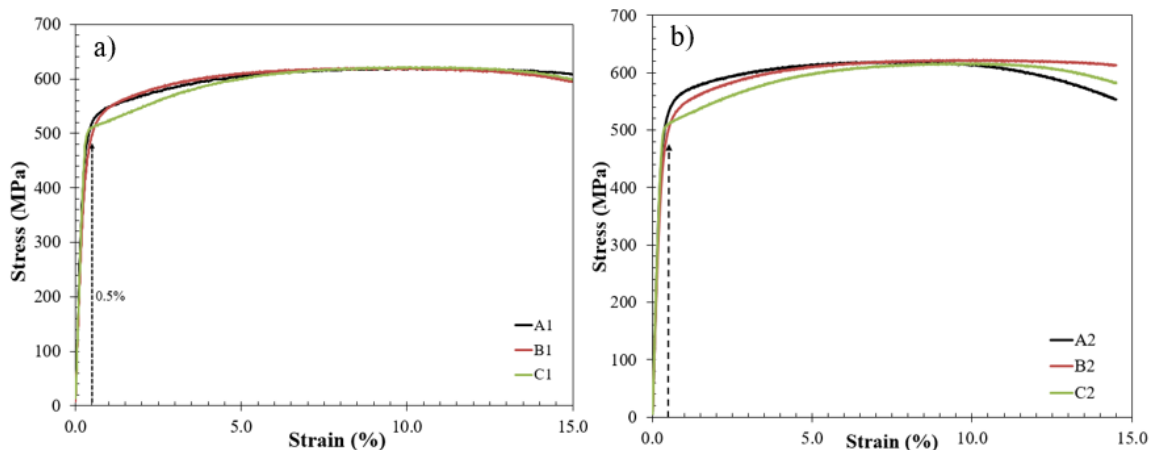


Figure 4.1 Longitudinal stress-strain curves from the CL position at the (a) 90° and (b) 180° location for as-received Steel A, B and C.

The longitudinal yield stress (YS), ultimate tensile strength (UTS) and the yield to tensile strength ratio (YS/TS) for the as-received microalloyed steels at both the 90° and 180°

locations are summarized in Figure 4.2, Figure 4.3 and Figure 4.4, respectively. The tensile properties of Steel A and B are relatively similar through the wall thickness, while Steel C exhibits an obvious difference for the properties at the CL compared with those at the ID and OD.

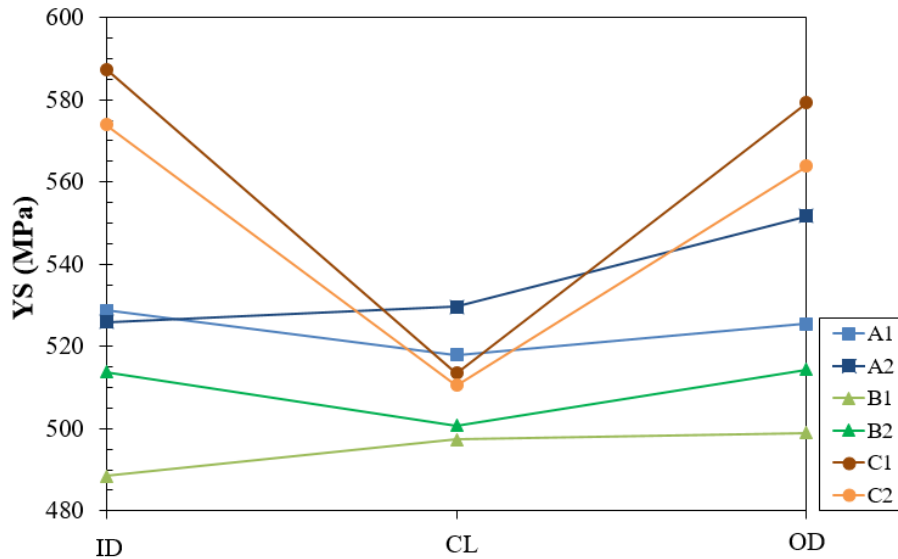


Figure 4.2 YS of as-received steels from the ID, CL and OD positions.

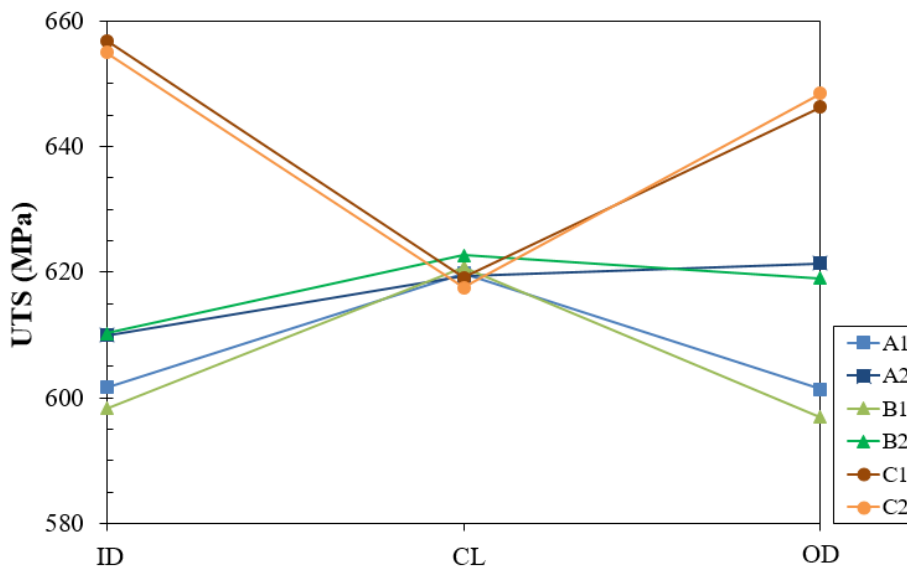


Figure 4.3 UTS of as-received steels from the ID, CL and OD positions.

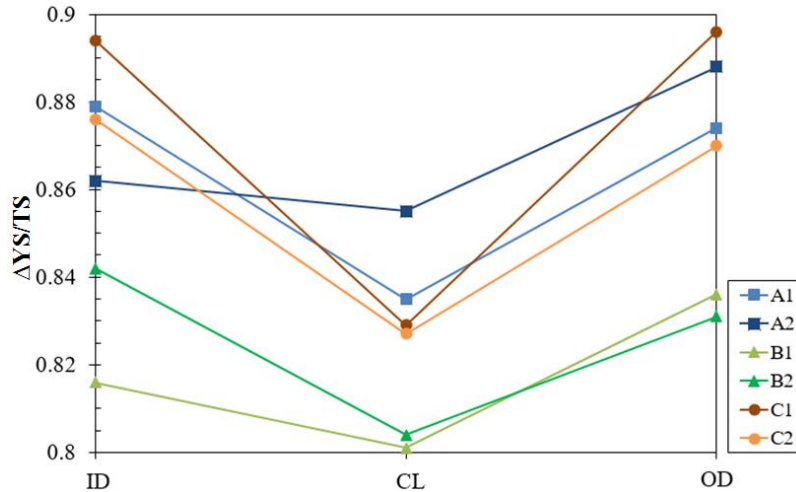


Figure 4.4 YS/TS of as-received steels from the ID, CL and OD positions.

4.1.2 Quantitative Analysis of Longitudinal Tensile Properties Affected by Aging

Table 4-1 summarized all 27 tests (for steels located 90° relative to the weld) undertaken based on the BBD using the variables and levels shown in Table 3-5. Also included in Table 4-1 are the measured changes in the yield stress (ΔYS), ultimate tensile strength (ΔUTS) and the yield to tensile strength ratio ($\Delta YS/TS$) as a result of each aging treatment. The statistical software Minitab 17 was used to develop a quadratic model with an analysis of variance (ANOVA) table. Parity plots were used to assess the overall fit of the empirical equation. Response surfaces were also plotted to show the effect of different variables on each mechanical property change.

Table 4-1 Four-factor BBD Test Matrix and Results for Longitudinal Tensile Properties

Temp	Time	Position	C/Nb	Δ YS (MPa)	Δ UTS (MPa)	Δ YS/TS
0	0	-1	-1	58.8	24.1	0.06
1	0	0	-1	39.2	3.7	0.058
0	-1	0	-1	30.1	4.2	0.043
0	1	0	-1	40.2	8.1	0.054
-1	0	0	-1	19.6	-1.5	0.034
0	0	1	-1	57	21.2	0.062
1	0	-1	0	91.8	29.8	0.125
0	1	-1	0	79.3	24	0.113
0	-1	-1	0	63	34.4	0.072
-1	0	-1	0	58.3	11.6	0.098
0	0	0	0	31.1	4.4	0.044
1	1	0	0	43.3	10.1	0.053
-1	-1	0	0	30.2	-8.2	0.06
1	-1	0	0	42.3	8.4	0.057
0	0	0	0	31.1	4.4	0.044
-1	1	0	0	27.9	0	0.053
0	0	0	0	31.1	4.4	0.044
-1	0	1	0	43.4	-3.5	0.06
0	1	1	0	64.8	14.6	0.062
0	-1	1	0	56	9.5	0.062
1	0	1	0	82.4	53.6	0.042
0	0	-1	1	35.4	15.1	0.032
0	1	0	1	7.9	0.3	0.013
-1	0	0	1	3	3	0.001
0	-1	0	1	6.4	1.8	0.008
1	0	0	1	8.5	1.7	0.012
0	0	1	1	19.7	4.9	0.024

4.1.2.1 Effect of Strain Aging on Δ YS

Based on the information provided in Table 4-1, an ANOVA table indicating the statistical significance of each variable affecting the change in YS, along with the quadratic model, is generated using the statistical software Minitab 17. This is followed by a parity plot used for validating the empirical equation. In addition, response surfaces are plotted to illustrate the effect of statistically significant variables on Δ YS. At the end of this section, the equation is applied to aging testing data for the steel samples located 180° relative to the weld to examine the limitation of the model.

4.1.2.1.1 Δ YS Aging Response - ANOVA Table

The reduced ANOVA data for Δ YS is shown in Table 4-2. In this thesis the term reduced ANOVA is used to indicate that only the independent variables with a significant contribution to the dependent variable are presented. The more complete results are

presented in Appendix C for all analyses. The selected variables, squared terms and combination of variables are those with p-value lower than 0.05, which means that the probability that the effect of the variable is caused by noise is not more than 5%. A low p-value is an indicator for a significant factor affecting the response. Aging temperature, C/Nb ratio and position are statistically significant aging variables for ΔYS . The presence of $(C/Nb)^2$ and P^2 indicates that the response surface for ΔYS is nonlinear over the range of these variables studied in this work. The p-value for aging time was 0.28; hence, it was not considered as a statistically significant variable.

Table 4-2 Reduced ANOVA Table of 4-factor BBD for ΔYS of Longitudinal Samples

Source	DF	SS	MS	F-Value	p-Value	Coefficient
Model	5	14872	2974	47	<0.001	
T	1	1304	1304	21	<0.001	10.4
P	1	1808	1808	28	<0.001	-12.3
C/Nb	1	2241	2241	35	<0.001	-13.7
P^2	1	5489	5489	86	<0.001	29.3
$(C/Nb)^2$	1	2244	2244	35	<0.001	-18.7
Lack-of-Fit	19	1334	70			
Pure Error	2	0	0			
R^2	0.92					

4.1.2.1.2 ΔYS Aging Response – Model

The response surface model for predicting the change in ΔYS resulting from aging is as follows:

$$\Delta YS = 36.1 + 10.4 \cdot T - 12.3 \cdot P - 13.7 \cdot \frac{C}{Nb} + 29.3 \cdot P^2 - 18.7 \cdot \left(\frac{C}{Nb}\right)^2 \quad (4.1)$$

A parity plot (Figure 4.5a) is used to assess the validity of this model by comparing the measured and predicted ΔYS (Equation 4.1). The solid line at 45° represents a 100% match between the measured and predicted data. Qualitatively, these values match each other reasonably well ($R^2 = 0.92$) without the presence of any significant outliers. The lowest value of ΔYS was measured for Steel C from the CL position, while the highest value of ΔYS was measured for Steel B from the ID position. Additional aging test data (also at 90°) was used to generate the parity plot shown in Figure 4.9b. Except for two data points, where the model over predicts the measured data by over 20 MPa, the additional test data fits reasonably well with the model and confirms that the model is valid in predicting strain aging at the 90° location. Similar with the BBD data, Steel C at the CL exhibited the lowest ΔYS and Steel A and B at the ID exhibited the highest ΔYS .

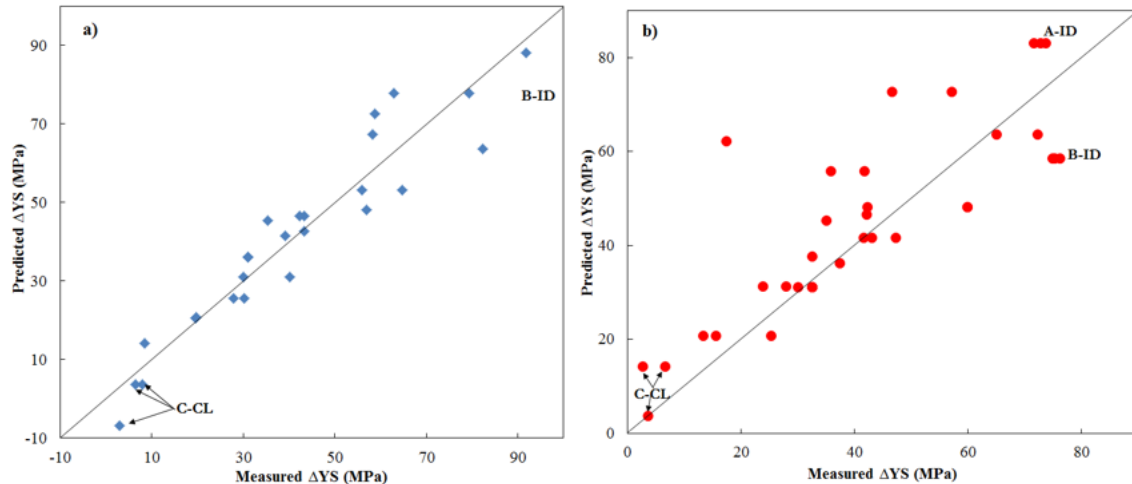


Figure 4.5 Parity plots for ΔYS at the 90° location using (a) BBD data (Table 4-1) and (b) additional aging test data.

4.1.2.1.3 ΔYS Aging Response – Response Surface

Three-dimensional (3D) response surface plots (i.e., plot of Equation 4.1) for ΔYS vs. P and C/Nb and ΔYS vs. P and T are shown in Figure 4.6a and Figure 4.6b, respectively. The graphs were plotted at specific values for the non-plotted variable, as defined in the caption. Figure 4.6a shows that the maximum ΔYS aging response occurs at C/Nb=1.2 (Steel B) at different positions and Steel C (C/Nb=1.8) exhibits a lower overall ΔYS . For each type of steel, the ΔYS is higher at the ID and OD positions than at the CL positions. On examination of Figure 4.6b, ΔYS at all the positions increases with increasing aging temperature.

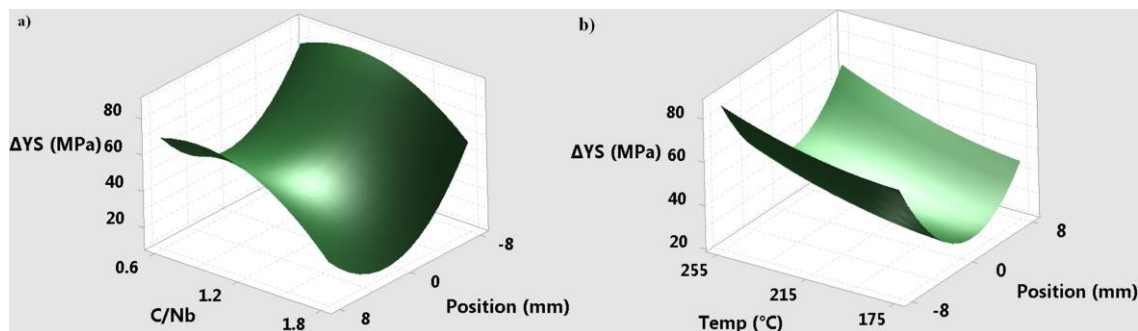


Figure 4.6 Response surface plots for (a) ΔYS vs. P and C/Nb, $T=255^\circ C$ and (b) ΔYS vs. P and T, C/Nb=1.2.

4.1.2.1.4 ΔYS Aging Response – Effect of Location

Equation 4.1 was applied to aging testing data obtained from the steel samples from the 180° location. The parity plot for this location is shown in Figure 4.7. Generally, the predicted data and measured data are not well correlated. There are three points where the model over predicts the measured data by over 40 MPa. The predominance of predicted

Δ YS values above the solid line suggests that the equation generally over predicts the strain aging effect at the 180° location.

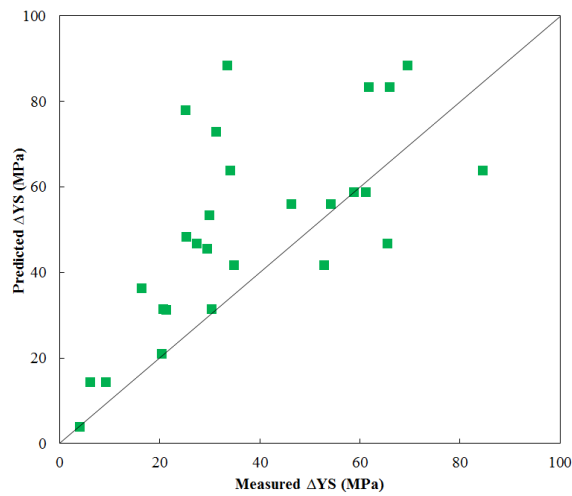


Figure 4.7 Parity plot for Δ YS of longitudinal steel samples measured at the 180° location vs. Equation 4.1.

4.1.2.2 Effect of Strain Aging on Δ UTS

The quantitative analysis method undertaken on the effect of aging variables on Δ UTS for the longitudinal samples is similar to that for Δ YS (Section 4.1.2.1).

4.1.2.2.1 Δ UTS Aging Response – ANOVA Table

The reduced ANOVA data for Δ UTS is shown in Table 4-3. Only the variables, squared terms and combination of variables with a p-value < 0.05 (except for the “P” term whose p-value is 0.164, which is added to make the model hierarchical) are deemed significant and are included in the ANOVA table and response surface model. Without the “P” term in the model, the match between the model and experimental results is much worse ($R^2 < 0.5$). Only aging temperature (T) and position through the thickness (P) are significant variables affecting the Δ UTS value. The presence of the squared term P^2 and the combination term T·P indicates that the response surface for Δ UTS is nonlinear across the range of T and P. The p-value for time and C/Nb ratio are 0.84 and 0.33, respectively; hence, they are not statistically significant in this model.

Table 4-3 Reduced ANOVA Table of 4-factor BBD for Δ UTS of Longitudinal Samples

Source	DF	SS	MS	F-Value	p-Value	Coefficient
Model	4	3354	839	14	<0.001	
T	1	935	935	16	0.001	8.8
P	1	125	125	2	0.164	-3.2
P ²	1	1916	1916	32	<0.001	17.0
T·P	1	378	378	6	0.020	9.7
Lack-of-Fit	20	1322	66			
Pure Error	2	0	0			
R ²	0.72					

4.1.2.2.2 Δ UTS Aging Response – Model

The model for predicting the change in Δ UTS due to aging is as follows:

$$\Delta UTS = 3.0 + 8.8 \cdot T - 3.2 \cdot P + 17.0 \cdot P^2 + 9.7 \cdot T \cdot P \quad (4.2)$$

A parity plot comparing the measured Δ UTS (Table 4-1) and predicted Δ UTS (Equation 4.2), as shown in Figure 4.8a, is used to assess the validity of the model. The measured and predicted values match closely with each other - though not as well as for Δ YS ($R^2 = 0.72$ for Δ UTS vs. $R^2 = 0.92$ for Δ YS) - without the presence of any significant outliers. Similarly, the parity plot with additional aging test data (Figure 4.8b) shows a larger variation between the measured and modeled data with 2 data points where the expression over estimates the measured data by over 20 MPa. The lowest value of Δ YS was measured for the sample from the CL position aged at 175°C, while the highest value of Δ YS was measured for the sample from the OD position aged at 255°C.

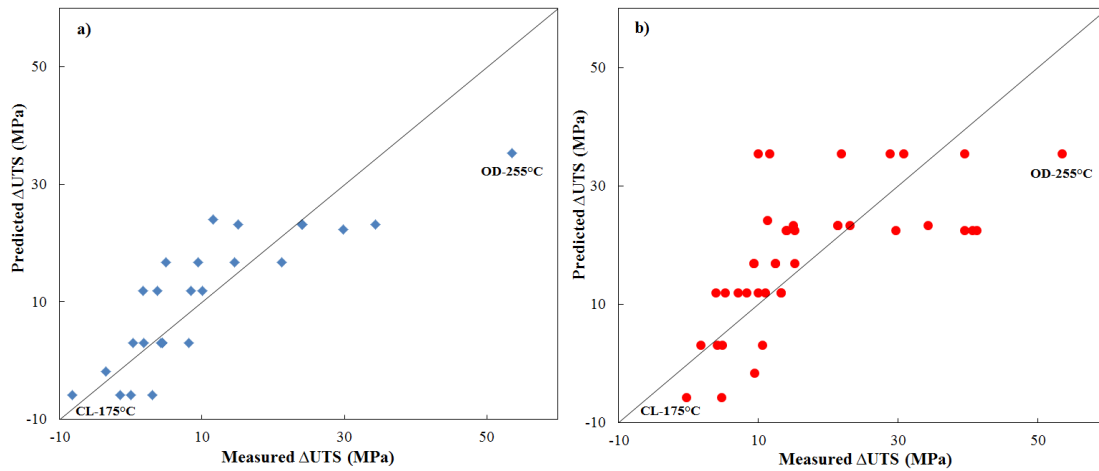


Figure 4.8 Parity plots for Δ UTS at the 90° location using a) BBD data (Table 4-1) and b) additional aging data.

4.1.2.2.3 Δ UTS Aging Response – Response Surface

The response surface plot for Δ UTS as a function of T and P is shown in Figure 4.9. The nonlinear effect of P on Δ UTS is apparent, such that both the ID and OD contribute to larger changes in Δ UTS compared with the CL position. The value of Δ UTS also

increases with increasing T, and this effect is amplified at the OD position (larger P value).

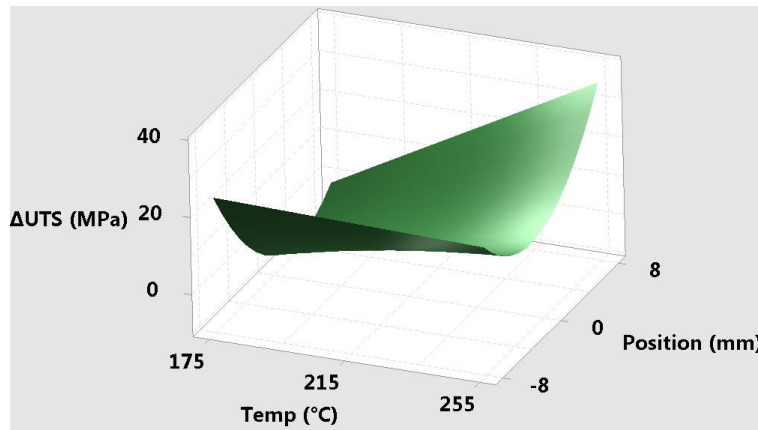


Figure 4.9 Response surface for ΔUTS vs. P and T, C/Nb = 1.2.

4.1.2.2.4 ΔUTS Aging Response – Effect of Location

Equation 4.2 is applied to the aging and testing data taken from the 180° location relative to the weld and the parity plot for this location is presented in Figure 4.10. Generally, the predicted values and the measured data are not well correlated. The predominance of predicted values above the solid line suggests that the empirical equation generally over estimates the effect of strain aging at the 180° location.

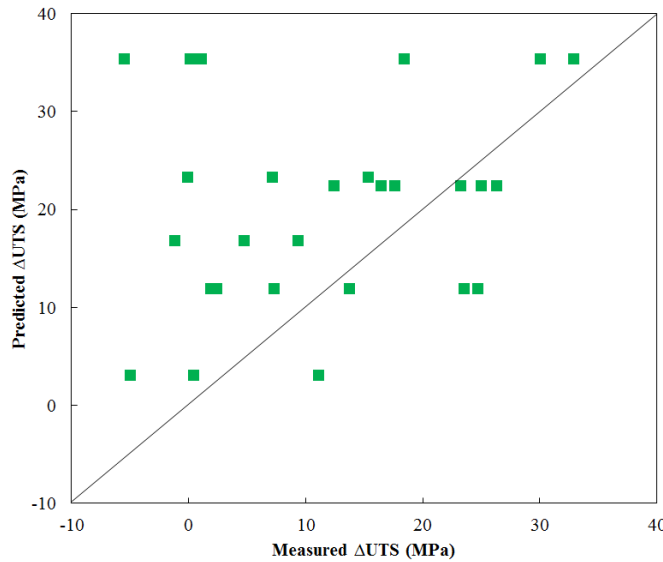


Figure 4.10 Parity plot for ΔUTS at the 180° location vs. Equation 4.2.

4.1.2.3 Effect of Strain Aging on $\Delta YS/TS$

The quantitative analysis method undertaken on the effect of aging variables on $\Delta YS/TS$ for the longitudinal samples is similar to that for ΔYS (Section 4.1.2.1) and ΔUTS (Section 4.1.2.2).

4.1.2.3.1 Analysis of $\Delta YS/TS$ – ANOVA Table

The reduced analysis of variance (ANOVA) data for $\Delta YS/TS$ is shown in Table 4-4. Judging from the p-values, the significant variables determining the value of $\Delta YS/TS$ are P and C/Nb ratio. The effects of temperature (p-value = 0.41) and time (p-value = 0.36) were deemed to be not statistically significant for the test conditions examined.

Table 4-4 Reduced ANOVA Data of 4-factor BBD for $\Delta YS/TS$ of Longitudinal Samples

Source	DF	SS	MS	F-Value	p-Value	Coefficient
Model	4	0.018	0.004	24	<0.001	
P	1	0.003	0.003	16	0.001	-0.016
C/Nb	1	0.004	0.004	22	<0.001	-0.018
P^2	1	0.004	0.004	19	<0.001	0.024
$(C/Nb)^2$	1	0.005	0.005	27	<0.001	-0.028
Lack-of-Fit	20	0.004	<0.001			
Pure Error	2	0	0			
R^2	0.81					

4.1.2.3.2 $\Delta YS/TS$ Aging Response – Model

The response surface model for predicting the change in $\Delta YS/TS$ is as follows:

$$\Delta YS/T = 0.053 - 0.016 \cdot P - 0.018 \cdot \frac{C}{Nb} + 0.024 \cdot P^2 - 0.028 \cdot \left(\frac{C}{Nb}\right)^2 \quad (4.3)$$

To assess the validity of the quadratic model for describing the measured data, a parity plot comparing the measured $\Delta YS/TS$ values (Table 3-1) and predicted values (Equation 4.3) are shown in Figure 4.11a. The measured and predicted data match each other relatively well with only one result (Steel B - ID) which shows a qualitatively large difference. The lowest $\Delta YS/TS$ value was measured and predicted for Steel C at the CL position, while the highest $\Delta YS/TS$ value was obtained for Steel B at the ID location. The additional aging data for the 90° location was used to generate the parity plot in Figure 4.11b. The data fits well with the model and confirms its accuracy, except for one point (Steel A - ID).

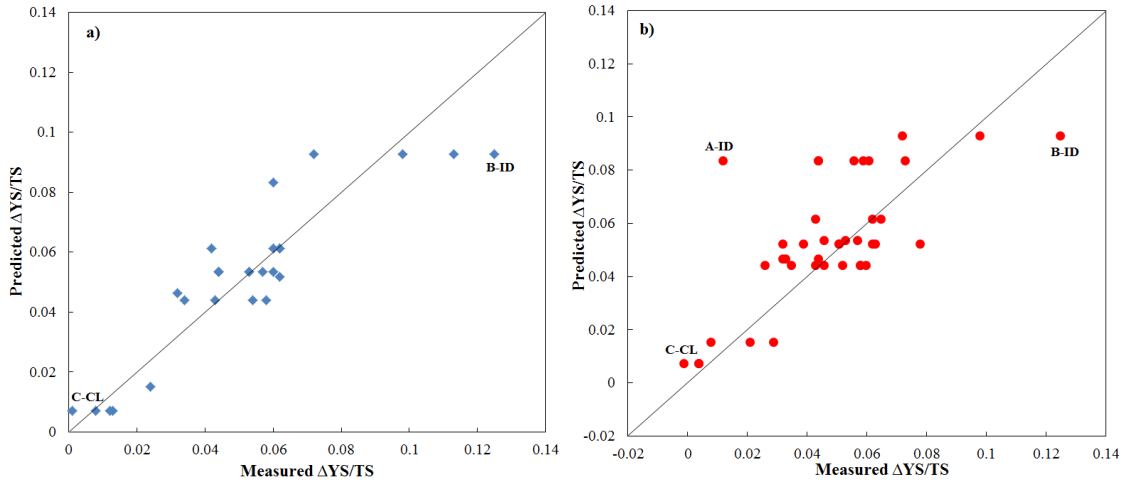


Figure 4.11 Parity plot for $\Delta YS/TS$ at the 90° location using a) BBD data (Table 4-1) and b) additional aging data.

4.1.2.3.3 $\Delta YS/TS$ Aging Response – Response Surface

The response surface plot for $\Delta YS/TS$ as a function of P and C/Nb ratio is shown in Figure 4.12. Similar to ΔYS , $\Delta YS/TS$ for Steel B is higher than the $\Delta YS/TS$ values for Steel A and C for any position. $\Delta YS/TS$ for samples from CL position is lower than that for the ID and OD positions.

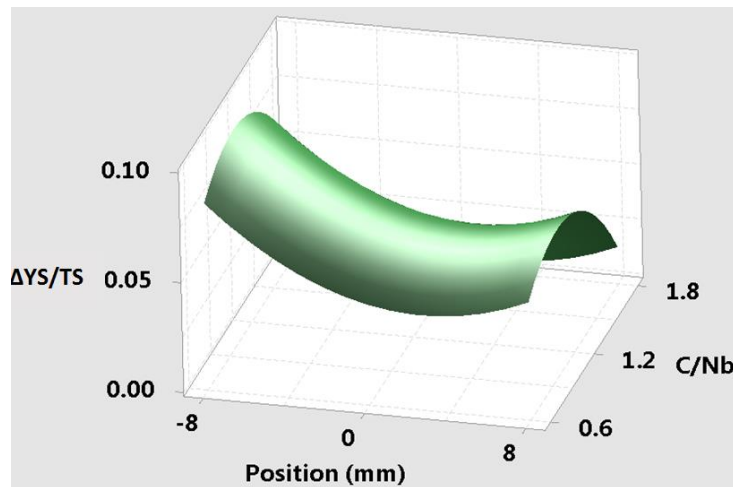


Figure 4.12 Response surface for $\Delta YS/TS$ vs. C/Nb and P.

4.1.2.3.4 $\Delta YS/TS$ Aging Response – Effect of Location

Equation 4.3 was applied to the aging data obtained at the 180° location. The parity plot for this location is shown in Figure 4.13. As with the other mechanical properties (YS and UTS), there is significant scatter between the measured and predicted data.

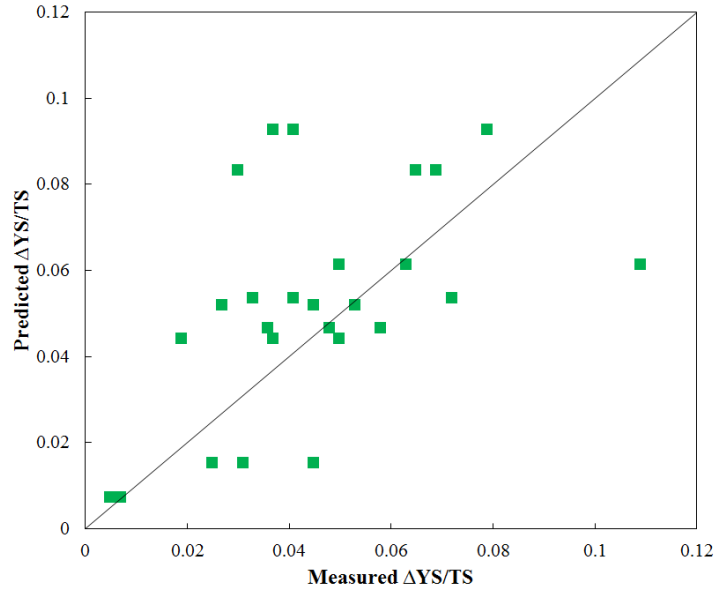


Figure 4.13 Parity plot for $\Delta YS/TS$ at the 180° location vs Equation 4.3.

4.1.3 Strain Hardening Exponent of Longitudinal Samples

The strain hardening exponents of as-received and aged (for different conditions) Steel A, B and C at 90° locations and different through wall thickness positions are summarized in Figure 4.14, Figure 4.15 and Figure 4.16, respectively. The strain hardening exponent of the CL is higher than that of the ID and OD positions for all three steels. A similar effect for the through wall thickness position on the strain hardening exponent is also observed for steel samples located 180° to the weld (Figure 0.6). The effect of aging on the strain hardening exponent is relatively negligible.

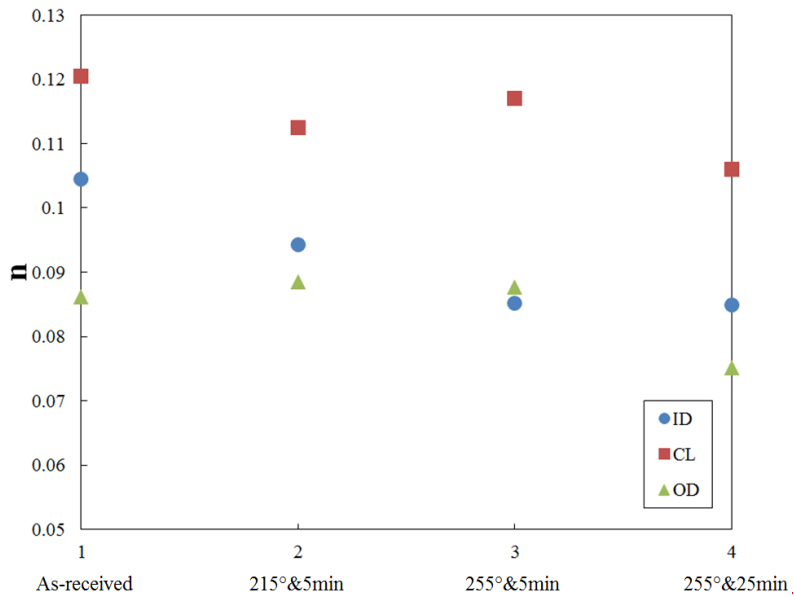


Figure 4.14 Strain hardening exponents for Steel A1 in the longitudinal orientation.

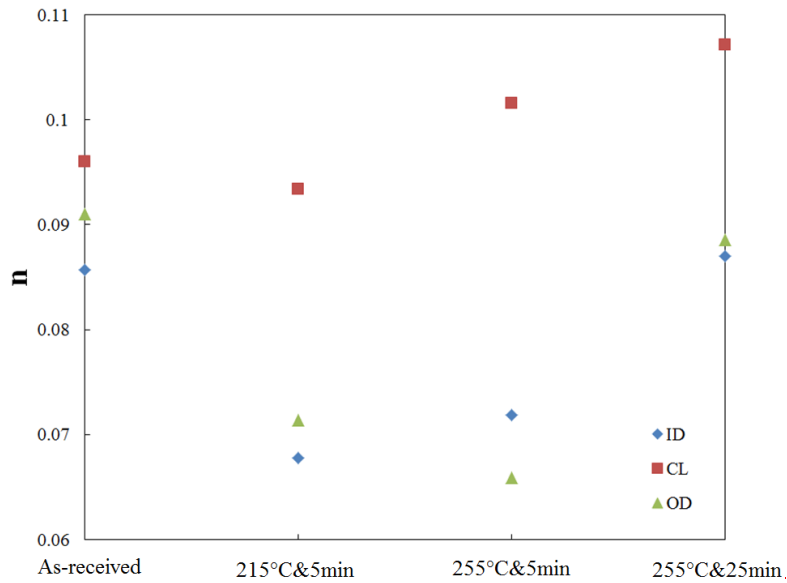


Figure 4.15 Strain hardening exponents for Steel B1 in the longitudinal orientation.

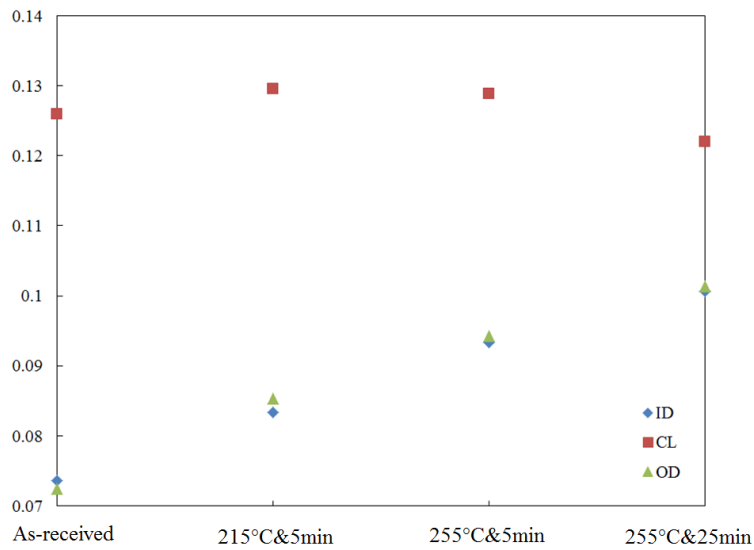


Figure 4.16 Strain hardening exponents for Steel C1 in the longitudinal orientation.

4.2 Transverse Tensile Properties

Tensile properties of transverse samples (i.e., YS, UTS YS/TS and strain hardening exponent) are presented in this section. Quantitative analysis on these properties affected by aging is also undertaken based on the BBD using the statistical software Minitab 17. The aging variables are aging temperature, aging time and C/Nb ratio. The other variable is imposed plastic strain rather than through wall thickness position, as shown in Table 3-6.

4.2.1 Transverse Tensile Properties of As-received Steels

The transverse tensile curves for Steel A, B and C extracted from the 180° location and CL position are shown in Figure 4.17. The yield stress is determined using the stress corresponding to 0.5% elongation. Similar to the longitudinal tensile samples, transverse samples from Steel A and B exhibit round-house yielding, while Steel C exhibits slight Luders strain in the stress-strain curves. The differences may result from microstructural differences between the steels (to be discussed in Chapter 6). The stress increase at a strain of 3% is caused by a sudden increase in strain rate from 1.563 mm/min to 12.5 mm/min. The sharply increased strain rate was used to improve data collection efficiency.

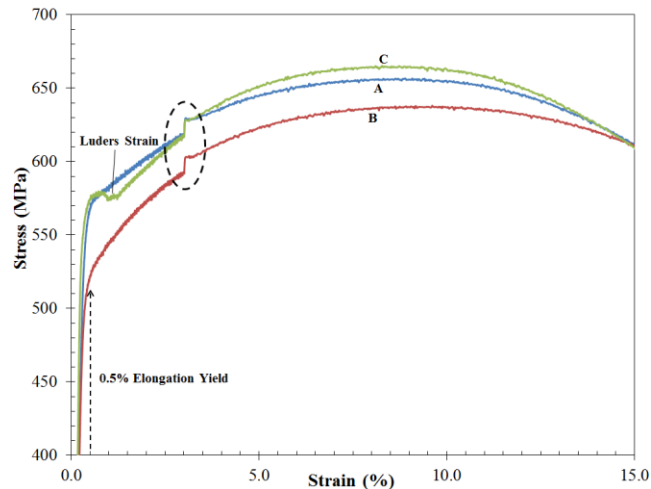


Figure 4.17 Transverse stress-strain curves for as-received pipe samples from the CL position for Steel A, B and C.

4.2.2 Transverse Tensile Properties of Pre-strained Steels

The stress-strain curves for as-received and pre-strained Steel A specimens are shown in Figure 4.18. The YS and UTS of Steel A increase with increasing plastic deformation. The transverse YS, UTS and YS/TS values for Steel A, B and C are summarized in Figure 4.19a, Figure 4.19b and Figure 4.19c, respectively. An increase in all three properties with increasing pre-strain occurs for all steels.

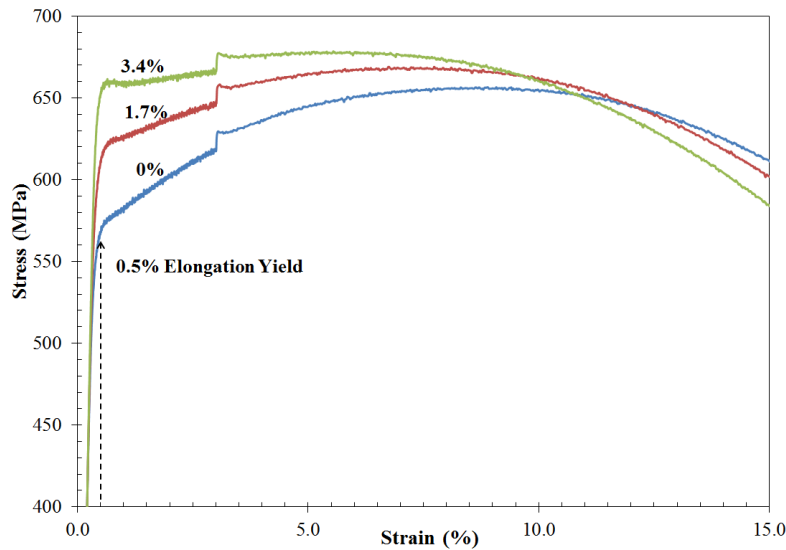


Figure 4.18 Transverse stress-strain curves for as-received, 1.7% pre-strained and 3.4% pre-strained samples from the CL position of Steel A.

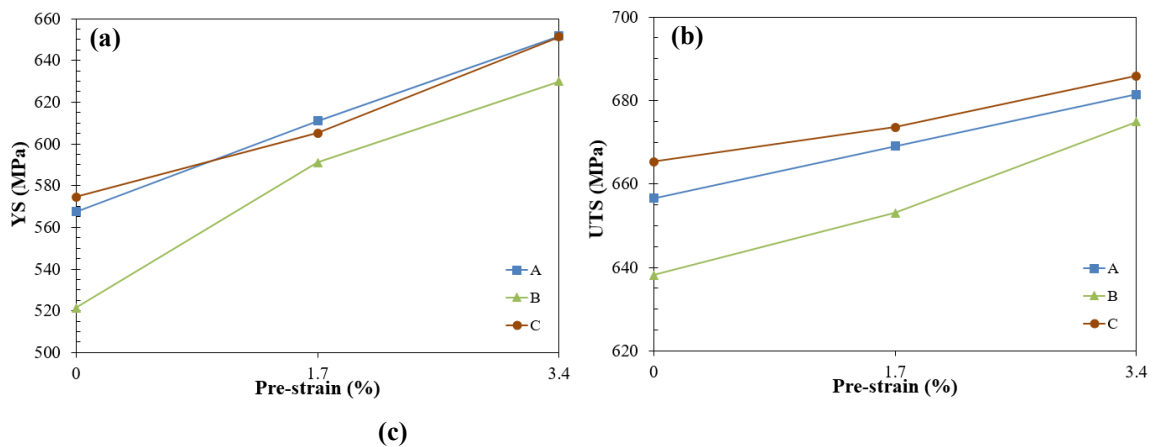


Figure 4.19 (a) YS, (b) UTS and (c) YS/TS for as-received, 1.7% pre-strained and 3.4% pre-strained transverse samples from the CL position of Steel A, B and C.

4.2.3 Transverse Tensile Curves of Strain-aged Steels

The tensile curves for pre-strained (1.7%) and after strain-aging (at 255°C for 5 minutes) samples from Steel A, B and C are shown in Figure 4.20a, Figure 4.20b and Figure 4.20c, respectively. Compared with the unaged pre-strained samples, an increase in the yield stress and a transition from a round-house type to a plateau type of yielding occur for the strain-aged steels. Especially for Steel A, a sharp return of the upper yield point followed by Luders strain appears after the aging treatment. The UTS of strain-aged Steel A is attained at the upper yield stress, rather than through subsequent work hardening. No distinct lower yield point and work hardening are observed in Figure 4.19a. The reason for such phenomenon will be discussed in Section 6.1.1. This is not observed in all tensile curves for the aged longitudinal steel samples. Although apparent Luders strain also

appears in the tensile curves for strain-aged Steel B and C, the sudden drop of stress following the upper yield point is not observed and the UTS is attained during work hardening.

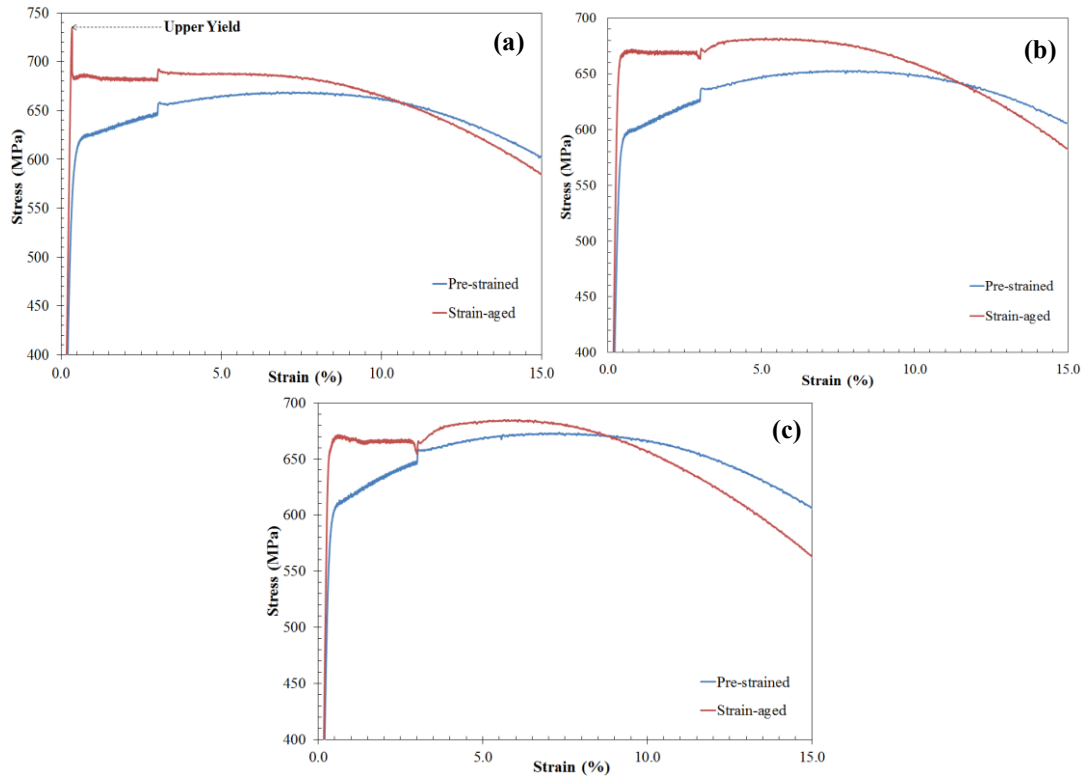


Figure 4.20 Transverse stress-strain curves for 1.7% pre-strained and subsequently aged at 255°C for 5 minutes samples for (a) Steel A, (b) Steel B and (c) Steel C.

4.2.4 Quantitative Analysis (4-factor BBD) of Transverse Tensile Properties Affected by Strain-aging

Table 4-5 summarizes all 27 tests undertaken based on the BBD using the variables and levels shown in Table 3-6. Also included in Table 4-5 are the measured changes in the yield stress (ΔYS), ultimate tensile strength (ΔUTS) and the yield to strength ratio ($\Delta YS/TS$), as a result of each aging treatment. Minitab 17 was used to develop a quadratic model with an analysis of variance (ANOVA) table. Parity plots were used to assess the overall fit of the empirical equation. Response surfaces were also plotted to show the effect of different variables on each mechanical property change.

Table 4-5 Four-factor BBD Test Matrix and Results for Transverse Samples

Temp	Time	Pre-strain	C/Nb	Δ YS (MPa)	Δ UTS (MPa)	Δ YS/TS
0	-1	0	-1	66.6	28.6	0.058
0	0	-1	-1	68.3	9.6	0.089
0	1	0	-1	69.6	42.4	0.041
0	0	1	-1	58.1	34.9	0.035
-1	0	0	-1	55.7	11.1	0.067
1	0	0	-1	72.3	30.9	0.061
1	0	1	0	82.7	50.5	0.050
0	-1	-1	0	59.2	12.1	0.076
0	0	0	0	59.8	15.7	0.068
-1	0	-1	0	45.5	7.0	0.062
0	0	0	0	61.9	23.5	0.060
-1	0	1	0	32	7.7	0.037
0	-1	1	0	47	28.7	0.029
0	1	-1	0	74.1	17.6	0.091
1	1	0	0	79.1	41.1	0.061
-1	1	0	0	41	26.2	0.026
0	1	1	0	61.6	18.1	0.065
1	-1	0	0	77.6	29.1	0.075
1	0	-1	0	88.6	29.2	0.097
-1	-1	0	0	22.6	8.3	0.023
0	0	0	0	69.6	42.3	0.045
0	0	1	1	46.4	15.7	0.045
0	1	0	1	53.9	3.2	0.076
-1	0	0	1	36.8	-3.2	0.060
0	0	-1	1	3	-6.0	0.012
0	-1	0	1	50	2.1	0.072
1	0	0	1	63.9	11.4	0.079

4.2.4.1 Effect of Strain Aging on Δ YS

Based on the information provided in Table 4-5, an ANOVA table suggesting the statistical significance of each variable affecting Δ YS, along with the quadratic model, was generated using the software Minitab 17. In addition, a parity plot was used to validate the empirical equation. Response surfaces are plotted to illustrate the influence of statistically significant factors on Δ YS.

4.2.4.1.1 Δ YS Aging Response - ANOVA Table

The reduced ANOVA data for Δ YS is shown in Table 4-6. The selected variables, squared terms and combination of variables are those with p-values lower than 0.05. Aging temperature, C/Nb ratio and pre-strain are statistically significant aging variables for Δ YS. The presence of $\epsilon \cdot (C/Nb)$ indicates that interaction of pre-strain with C/Nb ratio

affects the ΔYS and that the response surface is non-linear over the range of these variables. Time was not considered as a significant variable because the p-value reached 0.237.

Table 4-6 Reduced ANOVA Table of 4-factor BBD for ΔYS of Transverse Samples

Model	DF	SS	F-Value	p-Value	Coefficient
T	1	4431	36	<0.001	19.2
C/Nb	1	1555	13	0.002	-11.4
$\varepsilon \cdot (C/Nb)$	1	718	6	0.024	13.4
Lack-of-Fit	15	2376	3	0.073	
Pure Error	8	453			
R^2	0.70				

4.2.4.1.2 ΔYS Aging Response – Model

The response surface model for predicting the change in YS resulting from aging is as follows:

$$\Delta YS = 57.3 + 19.2 \cdot T - 11.4 \left(\frac{C}{Nb} \right) + 13.4 \varepsilon \cdot \left(\frac{C}{Nb} \right) \quad (4.4)$$

To assess the validity of the model (Equation 4.4), a parity plot (Figure 4.21) is used to compare the measured and predicted ΔYS . The BBD data and additional test data are plotted in Figure 4.21a and Figure 4.21b, respectively. Figure 4.21a shows that most values match each other well, despite the presence of one significant outlier where the difference between the measured and predicted values is over 20 MPa. The smallest value of ΔYS was measured for Steel C (without pre-strain), while the largest ΔYS was measured for Steel B (without pre-strain and with 1.7% pre-strain). The additional aging test data was used to generate the parity plot shown in Figure 4.21b. Except for 2 data points, where the model over predicts the measured data by over 20 MPa, the additional test data fits reasonably well with the model and supports the validity of the model in predicting the values of ΔYS due to strain aging.

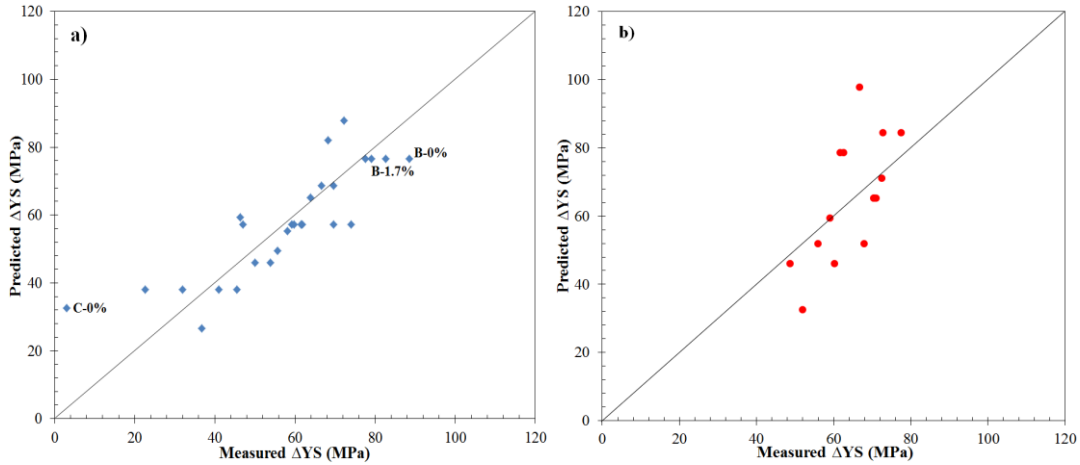


Figure 4.21 Parity plots based on Equation 4.4 for ΔYS of transverse samples using (a) BBD data and (b) additional aging test data.

4.2.4.1.3 ΔYS Aging Response – Response Surface

The response surface plots (i.e., graphing of Equation 4.4) for ΔYS vs. T and C/Nb ratio and ΔYS vs. ϵ and C/Nb ratio are shown in Figure 4.22a and Figure 4.22b, respectively. In Figure 4.22a, the ΔYS for all three steels increases with increasing aging temperature. Generally, the predicted ΔYS for Steel C is lower than that for Steel A and B, which is consistent with the measured results (Figure 4.21a). The effect of pre-strain on ΔYS varies for different pipe steels (Figure 4.22b). With tensile pre-strain increasing from 0% to 3.4%, ΔYS increases for Steel C. In contrast ΔYS decreases for Steel A.

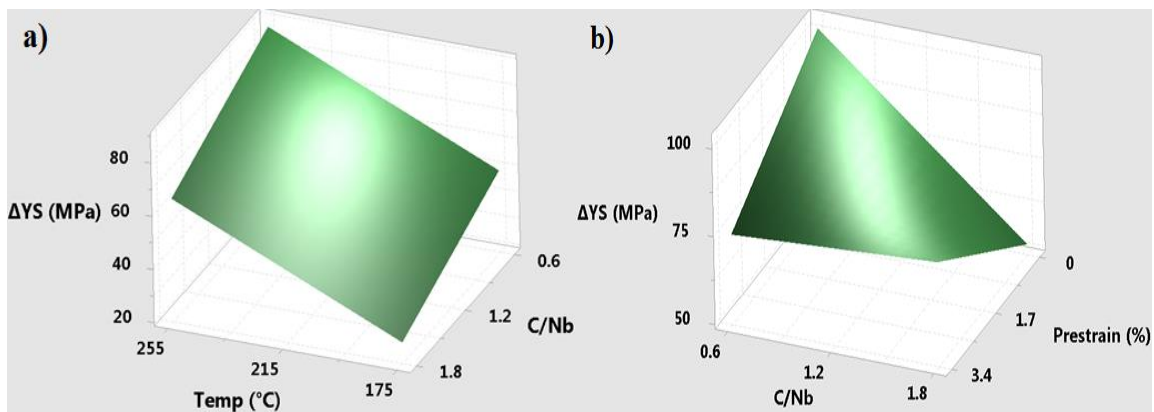


Figure 4.22 Response surface plots for transverse samples for a) ΔYS vs. C/Nb and T , $\epsilon = 1.7\%$ and b) ΔYS vs. C/Nb and ϵ , $T = 255^\circ C$.

4.2.4.2 Effect of Strain Aging on ΔUTS

The quantitative analysis method undertaken on the effect of aging variables on ΔUTS for the longitudinal samples is similar to that for ΔYS of transverse samples (Section 4.2.4.1).

4.2.4.2.1 Δ UTS Aging Response – ANOVA Table

The reduced ANOVA data for Δ UTS is shown in Table 4-7. Aging temperature (T), pre-strain (ϵ) and C/Nb ratio are significant variables affecting the Δ UTS value. The presence of the squared term $(C/Nb)^2$ indicates that the response surface for Δ UTS is nonlinear over the range of these variables studied in this work. The p-value for time is 0.26; hence, it is not statistically significant in this model.

Table 4-7 Reduced ANOVA Table of 4-factor BBD for Δ UTS of Transverse Samples

Model	DF	SS	MS	F-Value	p-Value	Coefficient
Temp	1	1521	1521	21	<0.001	11.3
Pre-strain	1	618	618	9	0.008	7.2
C/Nb	1	1503	1503	21	<0.001	-11.2
$(C/Nb)^2$	1	510	510	7	0.014	-8.8
Lack-of-Fit	14	802	57	1	0.813	
Pure Error	8	773	97			
R^2	0.73					

4.2.4.2.2 Δ UTS Aging Response – Model

The response surface model for predicting the change in Δ YS resulting from aging is as follows:

$$\Delta UTS = 23.8 + 11.3 \cdot T + 7.2 \cdot \epsilon - 11.2 \cdot \left(\frac{C}{Nb}\right) - 8.8 \cdot \left(\frac{C}{Nb}\right)^2 \quad (4.5)$$

According to Equation 4.5, Δ UTS increases with increasing aging temperature and pre-strain. A parity plot (Figure 4.23a) comparing the measured Δ UTS (Table 4-5) and predicted Δ UTS (Equation 4.5) is used to assess the validity of the model. The measured and modelled data match with each other well without the presence of any significant outliers. The highest value of Δ UTS is observed for Steel B (3.4% pre-strained), while the lowest value is observed for Steel C (as-received and 1.7% pre-strained). In contrast, the parity plot (Figure 4.23b) based on additional aging test data does not shown good correlation between predicted and measured Δ UTS values.

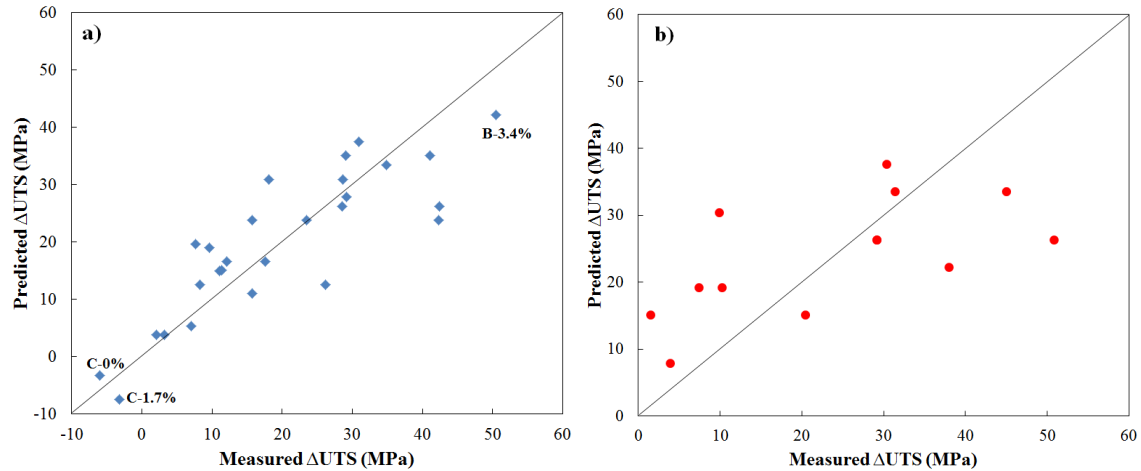


Figure 4.23 Parity plots based on Equation 4.5 for Δ UTS of transverse samples using a) BBD data and b) additional aging test data.

4.2.4.2.3 Δ UTS Aging Response – Response Surface

Response surface plots (i.e., graphing of Equation 4.5) for Δ UTS vs. aging temperature (T) and C/Nb and Δ UTS vs. pre-strain (ϵ) and C/Nb are shown in Figure 4.24a and Figure 4.24b. Δ UTS increases with increasing aging temperature and pre-strain. The predicted Δ UTS of Steel C is lower than that of Steel A and B, which is consistent with the measured results Figure 4.23a).

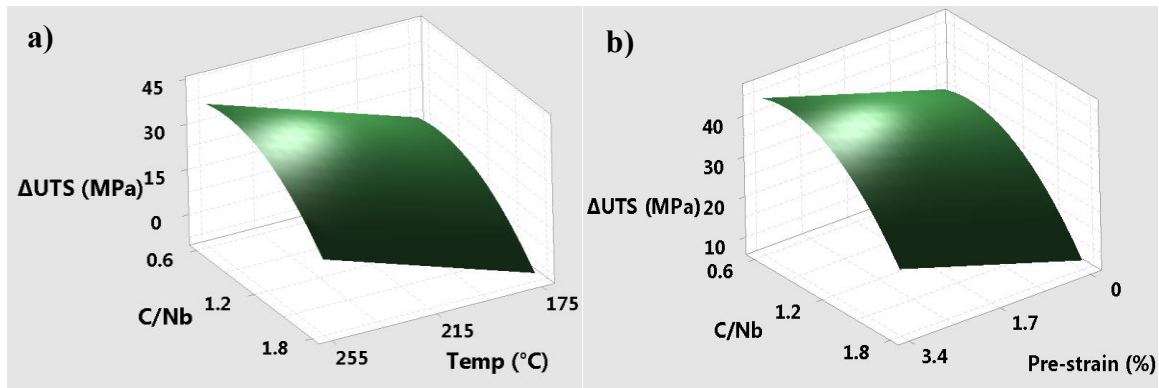


Figure 4.24 Response surface plots of transverse samples for a) Δ UTS vs. C/Nb and T, $\epsilon = 1.7\%$ and b) Δ UTS vs. C/Nb and ϵ , T = 255°C.

4.2.4.3 Effect of Strain Aging on Δ YS/TS

The quantitative analysis method undertaken on the effect of aging variables on Δ YS/TS for the longitudinal samples is similar to that for Δ YS (Section 4.2.4.1) and Δ UTS (Section 4.2.4.2).

4.2.4.3.1 $\Delta YS/TS$ Aging Response – ANOVA Table

The reduced ANOVA data for $\Delta YS/TS$ is shown in Table 4-8. Similar to ΔYS and ΔUTS , aging temperature (T), pre-strain (ϵ) and C/Nb ratio are significant variables for $\Delta YS/TS$. The term “C/Nb” (p-value = 0.916) is included in the expression to make the model match well with the experimental results. The presence of $\epsilon \cdot (C/Nb)$ indicates that the interaction of pre-strain with C/Nb ratio affects the $\Delta YS/TS$ and that the response surface is non-linear over the range of these variables. Time was not considered as a significant variable because the p-value reached 0.73.

Table 4-8 Reduced ANOVA Table of 4-factor BBD for $\Delta YS/TS$ of Transverse Samples

Model	DF	SS	MS	F-Value	p-Value	Coefficient
T	1	0.0018	0.0018	6.4	0.019	0.0123
ϵ	1	0.0023	0.0023	8.1	0.010	-0.0138
C/Nb	1	<0.0001	<0.0001	<0.1	0.906	-0.0006
$\epsilon \cdot (C/Nb)$	1	0.0019	0.0019	6.7	0.017	0.0218
Lack-of-Fit	20	0.0060	0.0003	2.2	0.359	
Pure Error	2	0.0003	0.0001			
R^2	0.49					

4.2.4.3.2 $\Delta YS/TS$ Aging Response – Model

The response surface model for predicting the change in YS/TS due to aging is as follows:

$$\Delta YS / TS = 0.0578 + 0.0123 \cdot T - 0.0138 \cdot \epsilon - 0.0006 \cdot \frac{C}{Nb} + 0.0218 \cdot \epsilon \cdot \frac{C}{Nb} \quad (4.6)$$

According to Equation 4.6, $\Delta YS/TS$ increases with increasing aging temperature and decreasing pre-strain. A parity plot (Figure 4.25) comparing the measured $\Delta YS/TS$ (Table 4.8) and predicted $\Delta YS/TS$ (Equation 4.6) is used to assess the validity of the model. Compared with other mechanical properties, there is significant scatter between the measured data and predicted values, which is in accordance with the low R^2 value ($R^2 = 0.49$ for $\Delta YS/TS$ vs. $R^2 = 0.70$ for ΔYS and $R^2 = 0.73$ for ΔUTS). The highest value of $\Delta YS/TS$ is observed for as-received samples from Steel A and Steel B.

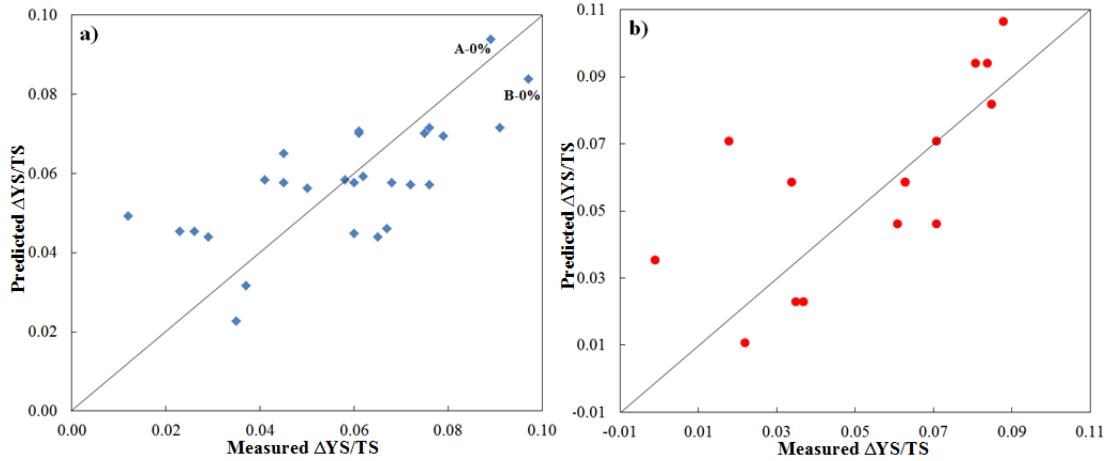


Figure 4.25 Parity plots based on Equation 4.6 for $\Delta YS/TS$ of transverse samples using a) BBD data and b) additional aging test data.

4.2.4.3.3 $\Delta YS/TS$ Aging Response – Response Surface

Response surface plots (i.e., graphing of Equation 4.6) for $\Delta YS/TS$ vs. aging temperature and C/Nb and ΔUTS vs. pre-strain and C/Nb are shown in Figure 4.26a and Figure 4.26b. According to Figure 4.26a, an increase in aging temperature plays a more important role in increasing the $\Delta YS/TS$ value. Figure 4.26b illustrates the interaction between the effect of C/Nb ratio and pre-strain. Similar to the change in ΔYS , $\Delta YS/TS$ decreases with increasing pre-strain in Steel A and increases with increasing pre-strain in Steel C.

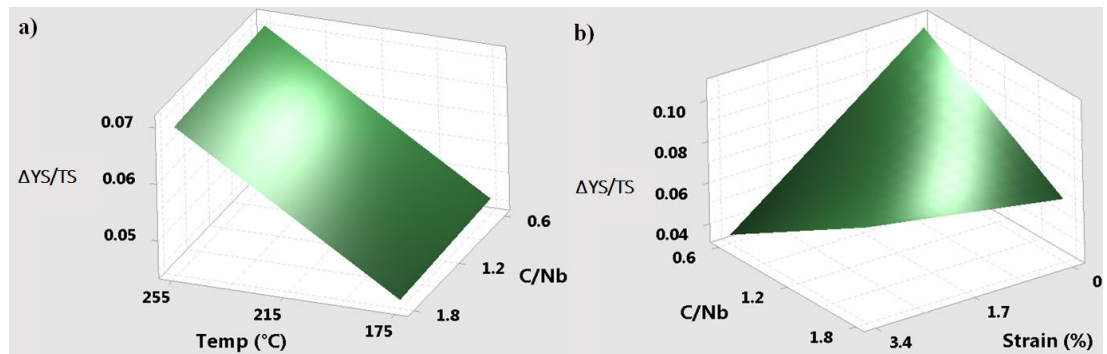


Figure 4.26 Response surface plots of transverse samples for a) $\Delta YS/TS$ vs. C/Nb and T, $\epsilon = 1.7\%$ and b) $\Delta YS/TS$ vs. C/Nb and ϵ , T = 255°C.

4.2.5 Quantitative Analysis (3-factor BBD) of Transverse Tensile Properties of Steel A Affected by Strain-aging

Due to the presence of significant outliers where the difference between the measured and predicted ΔYS (through 4-factor BBD) is over 20 MPa ($R^2 = 0.70$), a 3-factor BBD (performed only on Steel A) was created to explore whether a model may yield a better result using only the variables aging temperature, time and pre-strain compared to the 4-factor BBD presented in Section 4.2.4.1.1. This is because the variable C/Nb represents

the differences in all three steels; these could include chemical composition, microstructure and initial strain.

Table 4-9 summarized all 15 tests undertaken based on BBD using the variables and levels shown in Table 3-6. Also included in Table 4-9 are the measured changes in the yield stress (ΔYS) as a result of each aging treatment.

Table 4-9 Three-factor BBD Test Matrix and Results for Transverse Steel A

Test	Temp	Time	Pre-strain	ΔYS (MPa)
1	0	-1	1	56.0
2	0	1	-1	62.7
3	-1	1	0	60.4
4	1	-1	0	72.9
5	1	1	0	77.7
6	-1	-1	0	48.8
7	0	0	0	71.2
8	0	1	1	68.1
9	-1	0	-1	59.1
10	0	-1	-1	61.8
11	1	0	-1	66.8
12	0	0	0	70.5
13	-1	0	1	52.1
14	0	0	0	70.5
15	1	0	1	72.6

4.2.5.1 ΔYS Aging Response - ANOVA Table

The reduced ANOVA data for ΔYS is shown in Table 4-10 for Steel A with the transverse direction samples. Note that by focusing this analysis to one steel the C/Nb is no longer a variable and is constant. The dependent variables evaluated are T, t and ϵ . The selected variables, squared terms and combination of variables are those with p-values lower than 0.05. It can be seen that aging temperature, aging time and pre-strain all become statistically significant aging variables for ΔYS . Since C/Nb is not a variable in this BBD, other variables contribute more to ΔYS and the aging time, t, contributes significantly to ΔYS . Recall, that in the 4-factor BBD, time was not found to be significant. Thus the differences in the steels appear to have a greater effect on ΔYS than t. Also t is partly included with the variable T through the mechanism of diffusion. The presence of the squared term T^2 , t^2 and ϵ^2 indicates that the response surface for ΔYS is nonlinear over the range of these variables studied in this work. The presence of $T \cdot \epsilon$ and $t \cdot \epsilon$ indicates the interaction of aging temperature and time with pre-strain.

Table 4-10 Reduced ANOVA Table of 3-factor BBD for ΔYS of Transverse Steel A

Source	DF	SS	F-Value	p-Value	Coefficient
T	1	606	119	<0.001	8.7
t	1	108	21	0.002	3.7
T ²	1	26	5	0.059	-2.6
t ²	1	36	7	0.032	-3.1
ε^2	1	109	22	0.002	-5.4
T· ε	1	41	8	0.025	3.2
t· ε	1	31	6	0.042	2.8
Lack-of-Fit	5	35	43	0.023	
Pure Error	2	0			
R ²	0.96				

4.2.5.2 ΔYS Aging Response – Model

The response surface model for predicting the change in ΔYS resulting from aging is as follows:

$$\Delta YS = 70.7 + 8.7T + 3.7t - 2.6T^2 - 3.1t^2 - 5.4\varepsilon^2 + 3.2T \cdot \varepsilon + 2.8t \cdot \varepsilon \quad (4.7)$$

To assess the validity of the model (Equation 4.7), a parity plot (Figure 4.27) is used to compare the measured and predicted ΔYS . The BBD data and additional test data are plotted in Figure 4.27a and Figure 4.27b, respectively. Obviously, both figures show that the measured and modelled data match very closely with each other without the presence of any significant outliers. The improved validity of this model is also supported by the higher R² value (R² = 0.96 for Equation 4.7 vs. R² = 0.70 for Equation 4.4). The smallest change in YS was measured for the 3.4% pre-strained sample aged at 175°C, while the largest ΔYS was measured for the 1.7% pre-strained sample aged at 255°C.

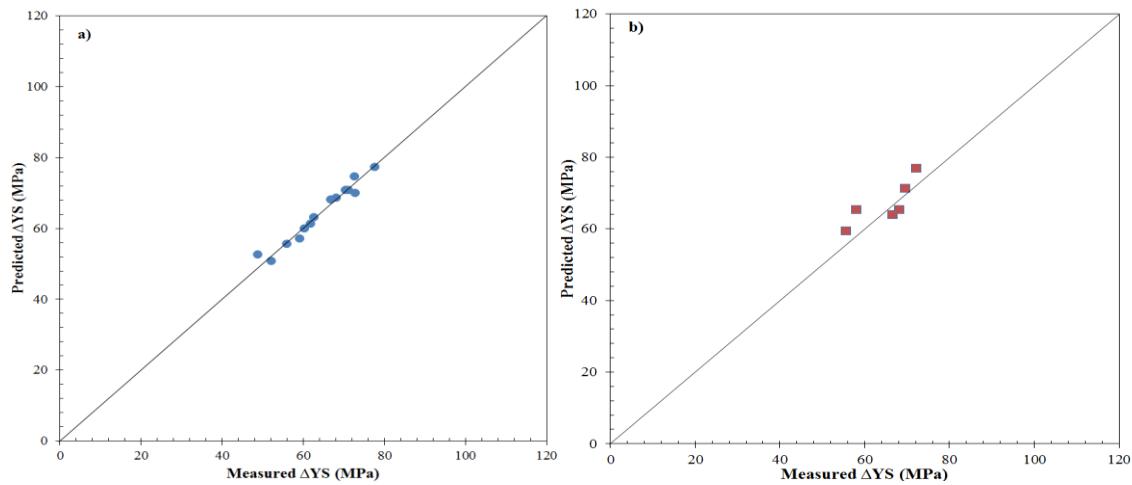


Figure 4.27 Parity plots based on Equation 4.7 for ΔYS of transverse Steel A samples using (a) BBD data and (b) additional aging test data.

4.2.5.3 Δ YS Aging Response – Response Surface

Response surface plots (i.e., graphing of Equation 4.7 or Δ YS vs. aging temperature and time and Δ YS vs. aging temperature and pre-strain) are shown in Figure 4.28a and Figure 4.28b, respectively. Figure 4.28a shows that Δ YS increases with both increasing aging temperature and time, although the rate of increase is higher as the temperature rises. The pre-strain values contributing to the largest Δ YS range from 0.8% to 1.7% (Figure 4.28b).

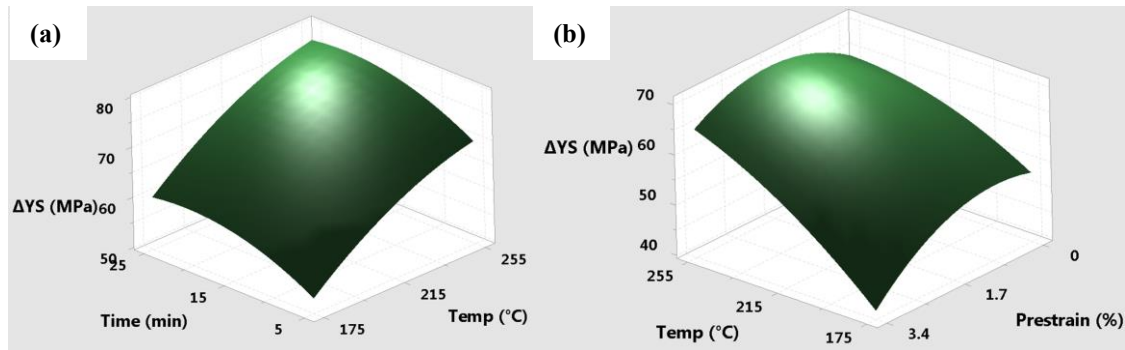


Figure 4.28 Response surface plots of transverse Steel A samples for (a) Δ YS vs. T and t, $\epsilon = 1.7\%$ and (b) Δ YS vs. T and ϵ , t = 5 min.

4.2.6 Strain Hardening Exponent of Transverse Samples

The measured strain hardening exponents (n) of as-received and pre-strained (1.7% and 3.4%) samples of Steel A, B and C are shown in Figure 4.29. For all three steels, the strain hardening exponents decrease with increasing applied pre-strain. The n values of aged transverse steel samples are not presented because of the presence of a remarkable upper yield point followed by a sudden drop in stress. The reason will be discussed in Section 6.1.1.

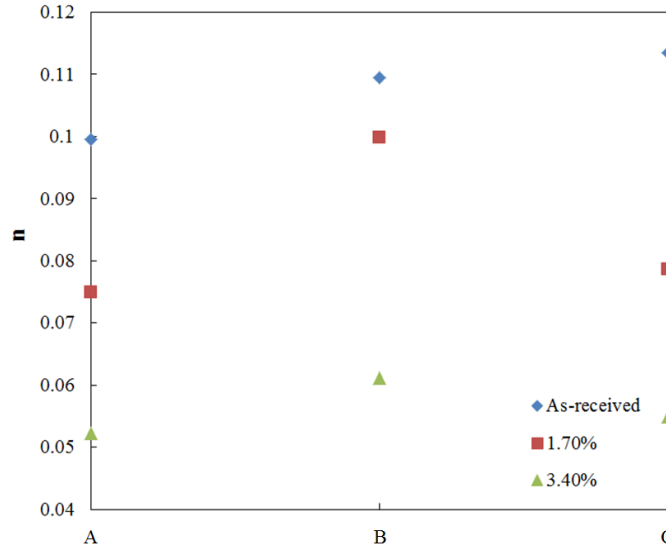


Figure 4.29 Strain hardening exponent for as-received and pre-strained transverse samples from Steel A, B and C.

4.3 Micro-hardness

The hardness of as-received and aged samples from ID, CL and OD positions (located 90° to the weld) from Steel A, B and C was measured using a micro-hardness tester.

4.3.1 Micro-hardness of As-received and Aged Steel A

The average micro-hardness values of as-received and aged samples from Steel A are shown in Figure 4.30. The standard deviation was obtained based on 20 replicate test results from the same sample. The hardness values from different positions increase with increasing aging temperature and time. Compared with Vickers hardness values of as-received samples, the change in HV due to aging (ΔHV) is higher for the ID ($\Delta HV_{255^{\circ}C\&25min} = 11.9$) and OD ($\Delta HV_{255^{\circ}C\&25min} = 13.4$) positions than that from the CL ($\Delta HV_{255^{\circ}C\&25min} = 8.3$) position.

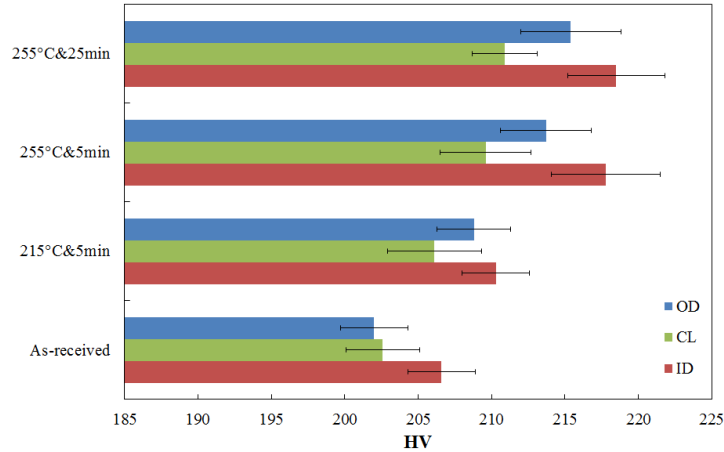


Figure 4.30 Micro-hardness of as-received and aged Steel A samples. The error bars in the figure represent the standard deviation on 20 measurements taken per sample.

4.3.2 Micro-hardness of As-received and Aged Steel B

The average Vickers hardness values of as-received and aged samples from Steel B are shown in Figure 4.31. As with Steel A, the hardness values from different positions increase with increasing aging temperature and time. The change in HV is higher for the ID ($\Delta HV_{255^{\circ}\text{C}\&25\text{min}} = 18.9$) and OD ($\Delta HV_{255^{\circ}\text{C}\&25\text{min}} = 15.2$) positions than that of the CL ($\Delta HV_{255^{\circ}\text{C}\&25\text{min}} = 10.2$) position.

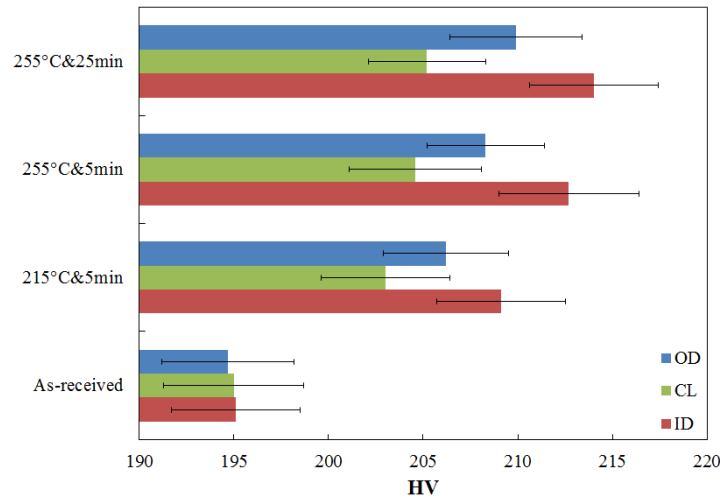


Figure 4.31 Micro-hardness of as-received and aged Steel B samples. The error bars in the figure represent the standard deviation on 20 measurements taken per sample.

4.3.3 Micro-hardness of As-received and Aged Steel C

The average hardness values of as-received and aged samples from Steel C are shown in Figure 4.32. Hardness values for the ID and OD positions are about 20 HV higher than

those of the CL position. Similar to Steels A and B, the hardness values from different positions increase with increasing aging temperature and time. The change in HV is much higher for the ID ($\Delta HV_{255^\circ\text{C}\&25\text{min}} = 10.1$) and OD ($\Delta HV_{255^\circ\text{C}\&25\text{min}} = 7.9$) positions than that of the CL ($\Delta HV_{255^\circ\text{C}\&25\text{min}} = 2.3$) position. ΔHV for CL position does not change much after aging treatment.

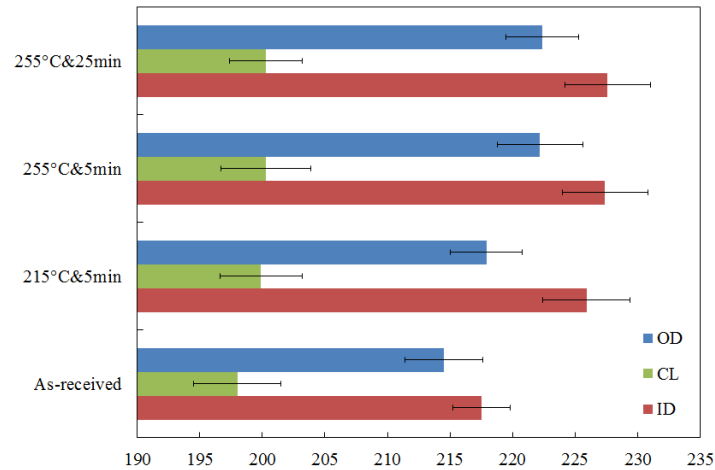


Figure 4.32 Micro-hardness of as-received and aged Steel C samples. The error bars in the figure represent the standard deviation on 20 measurements taken per sample.

4.4 Charpy Impact Toughness

The measured Charpy impact toughness (i.e., absorbed energy) of as-received and aged Steel A samples from the ID and OD positions are plotted in Figure 4.33 and Figure 4.34, respectively. For samples from both the ID and OD positions, the Charpy impact toughness increased slightly after aging at 215°C/255°C for 5 min. However, the toughness of samples aged at 255°C for 25 min is lower than that of as-received samples. Generally, the presence overlapping error bars in Figure 4.33 and Figure 4.34 indicates that the effect of aging on toughness is relatively small.

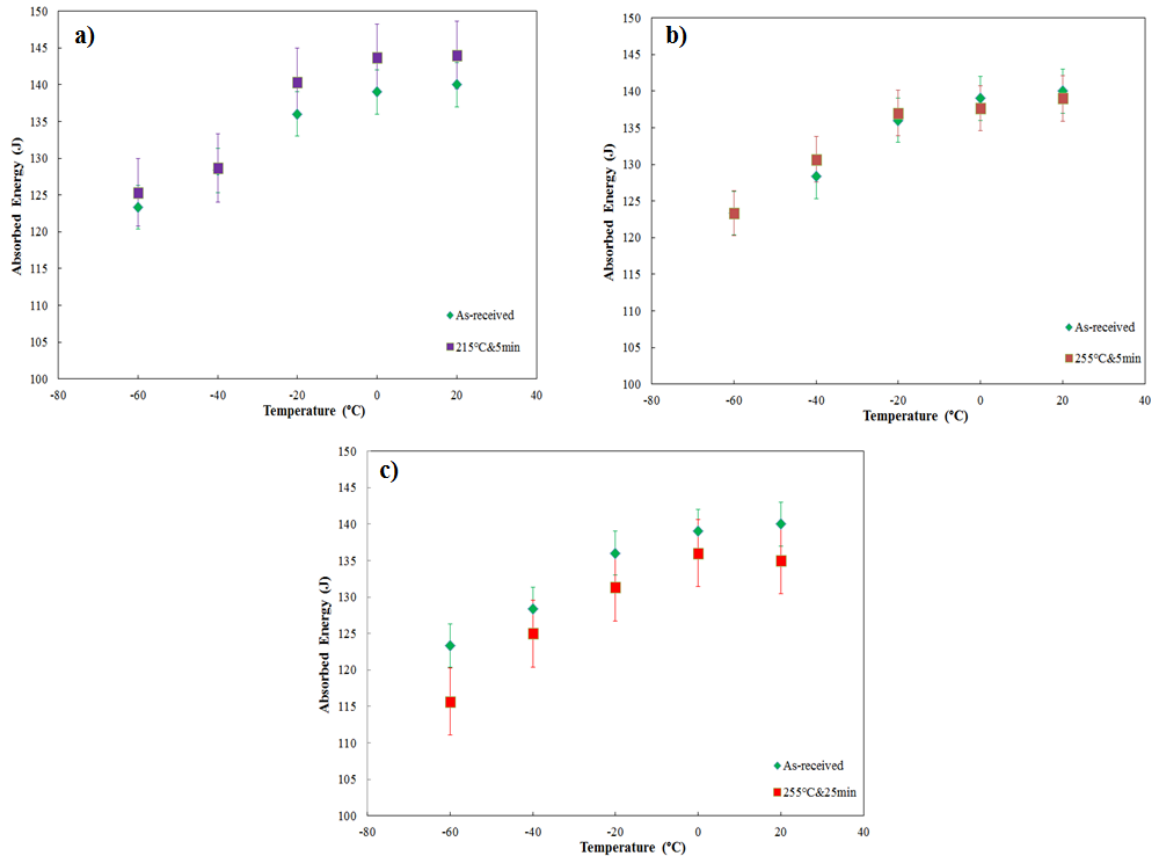


Figure 4.33 Absorbed energy of as-received and aged (a) at 215°C for 5 min, (b) at 255°C for 5 min and (c) at 255°C for 25 min Steel A samples from the ID position. The error bars in the figure represent the standard deviation on 5 measurements taken per sample.

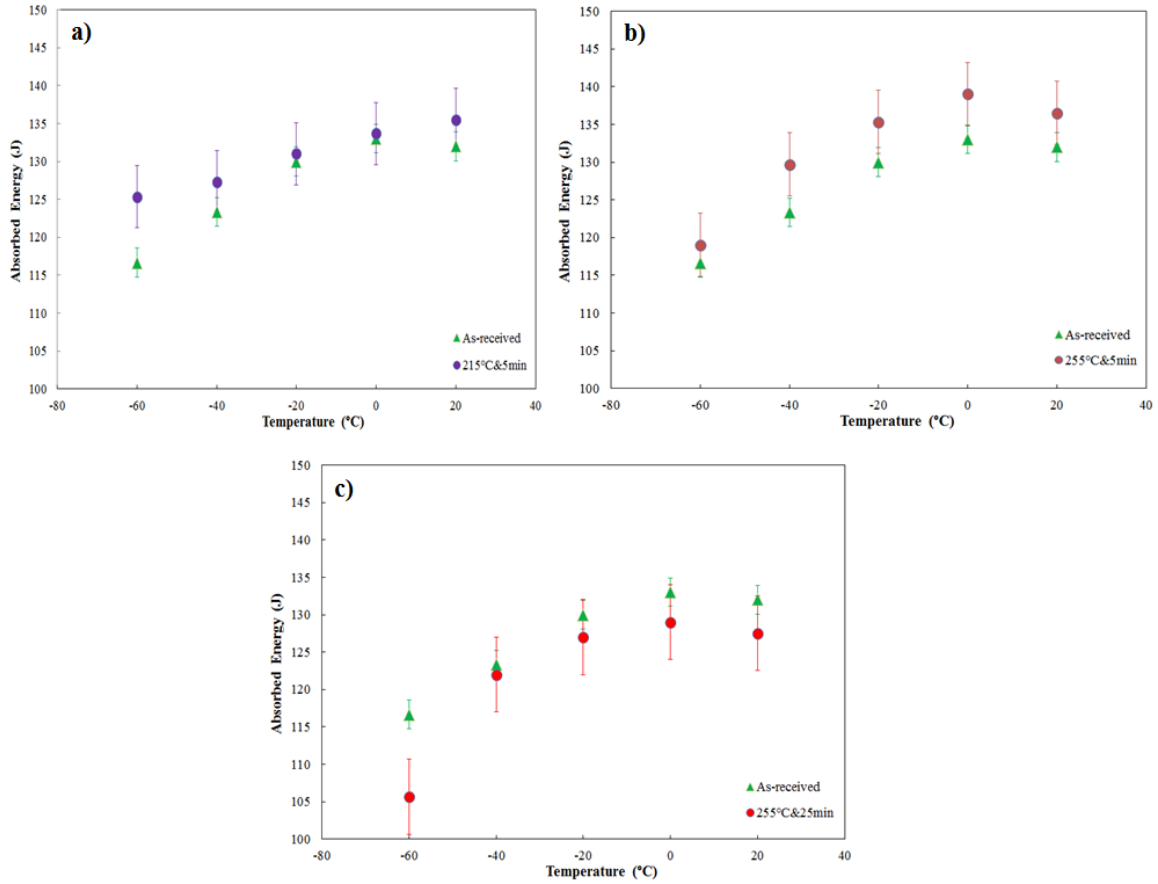


Figure 4.34 Absorbed energy of as-received and aged (a) at 215°C for 5 min, (b) at 255°C for 5 min and (c) at 255°C for 25 min Steel A samples from the OD position. The error bars in the figure represent the standard deviation on 5 measurements taken per sample.

4.5 Summary of the Effect of Strain Aging on Mechanical Properties

The statistically significant aging variables affecting longitudinal and transverse tensile properties are summarized in Table 4-11. Aging time is not considered as a significant factor in the 4-factor BBD for both longitudinal and transverse properties. In a 3-factor BBD, all the variables studied (temperature, time and pre-strain) are statistically significant.

Table 4-11 Statistically Significant Aging Variables Affecting Tensile Properties

	Longitudinal (4-Factor)	Transverse (4-Factor)	Transverse (3-Factor)
ΔYS	T, P, P ² , C/Nb, (C/Nb) ²	T, C/Nb, $\epsilon \cdot (C/Nb)$	T, T ² , t, t ² , ϵ^2 , T· ϵ , t· ϵ
ΔUTS	T, P, P ² , T·P	T, ϵ , C/Nb, (C/Nb) ²	
$\Delta YS/TS$	P, P ² , C/Nb, (C/Nb) ²	T, ϵ , $\epsilon \cdot (C/Nb)$	

Compared with the change in tensile properties (especially ΔYS), the changes in micro-hardness (ΔHV) and impact toughness (ΔCVN) are relatively small.

Chapter 5 Microstructure Analysis

This chapter includes optical microscopy (OM) and scanning electron microscopy (SEM) images for metallographic analysis. The microstructures of Steel A, B and C at the ID, CL and OD positions are quantitatively analyzed using ImageJ software. EBSD is also used for measuring the grain size distributions of Steel A, B and C from different through wall thickness positions.

5.1 OM and SEM Analysis

Metallographic images for all the three as-received steels from the ID, CL and OD positions (located 90° relative to the weld) observed in the longitudinal direction (Figure 3.9a) are shown in Figure 5.1. The corresponding OM images for the transverse direction (Figure 3.9b) are shown in Appendix B. SEM images for Steel A, B and C from the CL position are shown in Figure 5.2, Figure 5.3 and Figure 5.4, respectively.

The microstructure of Steel A is relatively uniform through the wall thickness and consists of acicular ferrite (AF in Figure 5.1 and Figure 5.2), ferrite (F in Figure 5.1) and a small amount of pearlite. Similarly, Steel B consists primarily of acicular ferrite and ferrite and the microstructure is also uniform through the wall thickness. Unlike Steel A and B, the microstructure of Steel C primarily consists of ferrite and pearlite (Figure 5.1 and Figure 5.4). The microstructure is less uniform through the wall thickness and exhibits a larger grain size at the CL position. The microstructures at the 180° location, for all three steels, are similar to those at the 90° location (Appendix B: Figure 0.10, Figure 0.11 and Figure 0.12).

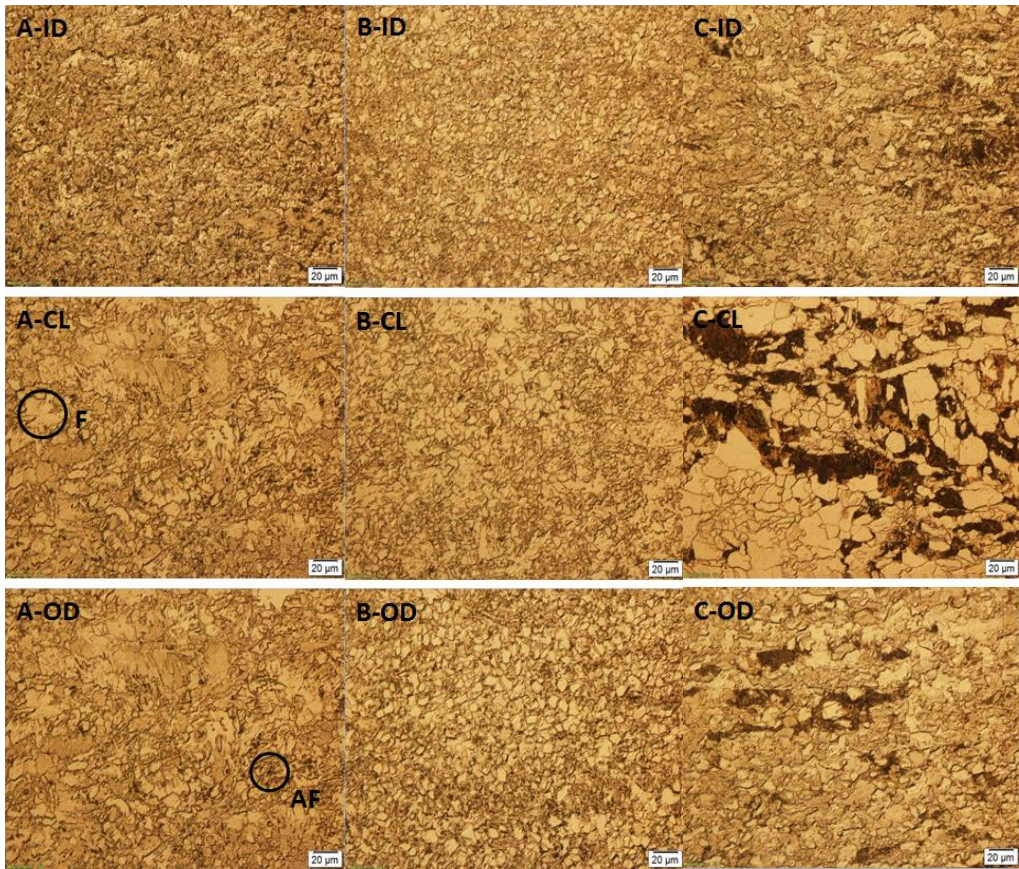


Figure 5.1 OM images of longitudinal surface (Figure 3.9a) for Steel A, B, C located 90° to the weld at the ID, CL and OD positions.

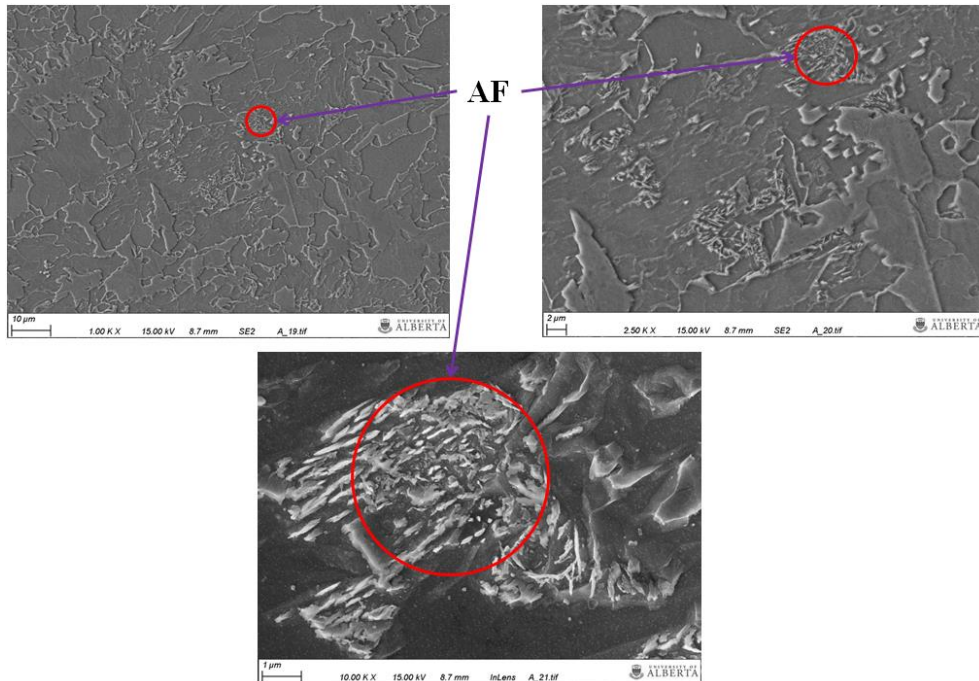


Figure 5.2 SEM SE images for Steel A at the CL position.

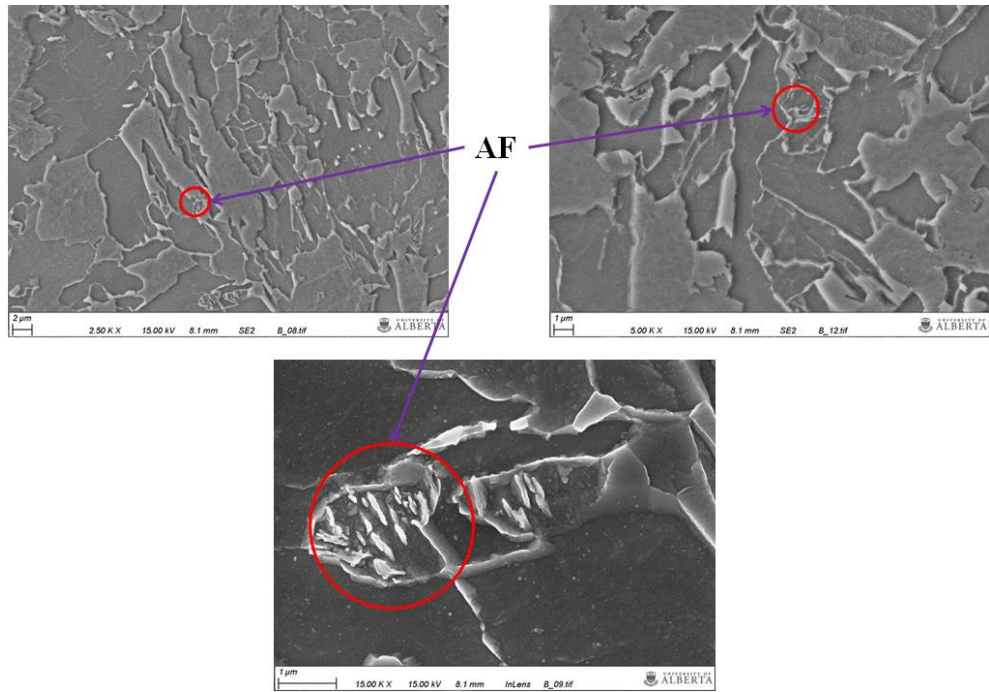


Figure 5.3 SEM SE images for Steel B at the CL position.

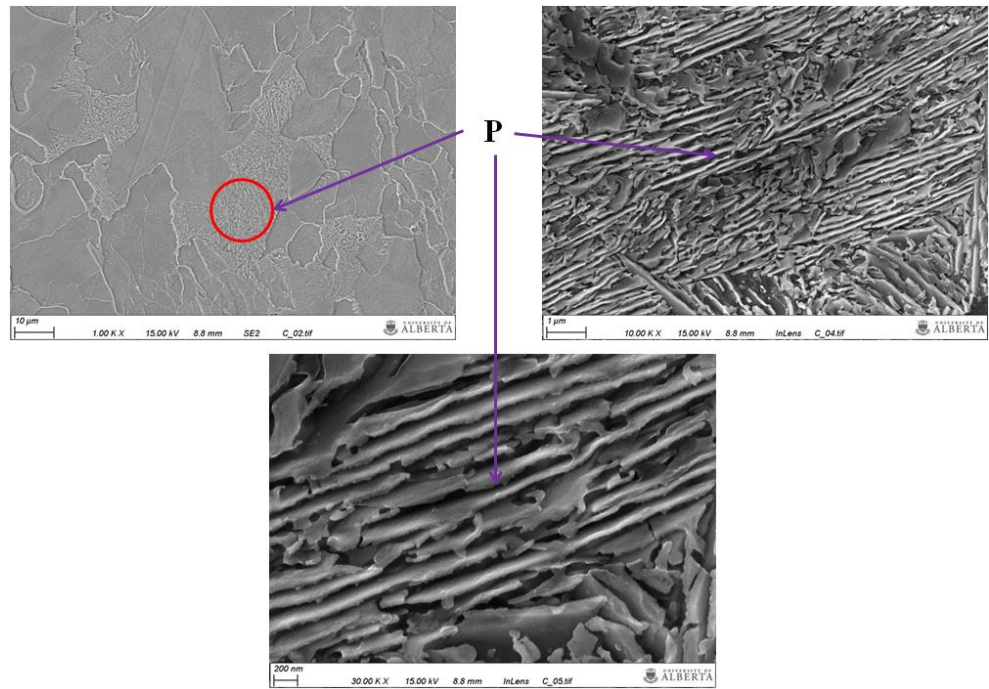


Figure 5.4 SEM SE images for Steel C at the CL position.

5.2 Grain Size Measurement

The average grain size of the steel was measured using the circular intercept method on OM images. Grain size distribution was obtained from EBSD maps.

5.2.1 Interception Method

The average grain sizes measured using the circular interception method for all three steels at the ID, CL and OD positions are summarized in Table 5-1 and plotted in Figure 5.5. Steel C has a larger grain size at all through wall thickness positions than either Steel A or B, which can also be observed qualitatively in Figure 5.1. Compared with Steel A and B, whose average grain size is uniform at different positions through the thickness, Steel C has a non-uniform grain size through thickness with 16.4 μm at CL, 9.8 μm at ID and 10.7 μm at OD positions. These results will be compared with the EBSD grain size measurements in the next section.

Table 5-1 Average Grain Size of As-received Steel A, B and C Located 90° to the Weld Measured by Circular Intercept method using OM Images

Grain Size	ID		CL		OD	
	Average (μm)	StDev (μm)	Average (μm)	StDev (μm)	Average (μm)	StDev (μm)
A	8.3	0.5	7.9	0.3	7.6	0.6
B	5.8	0.5	7.0	0.5	6.7	0.3
C	9.8	0.8	16.4	0.9	10.7	0.5

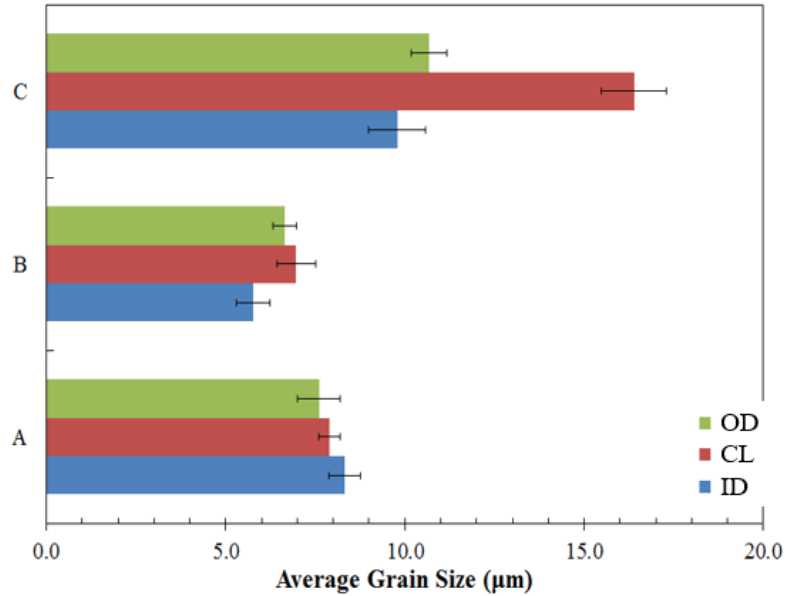


Figure 5.5 Grain size for as-received steels located 90° to the weld measured by circular interception method using OM images. The error bars in the figure represent the standard deviation on five measurements taken per sample.

5.2.2 EBSD Map Method

EBSM maps for longitudinal surfaces (Figure 3.9a) of Steel A, B and C at different through thickness positions are shown in Figure 5.6. The grain size measured using EBSD post-processing software CHANNEL5 is summarized in Table 5-2. The method used here to measure grain size has been presented in Section 3.6.1.2.

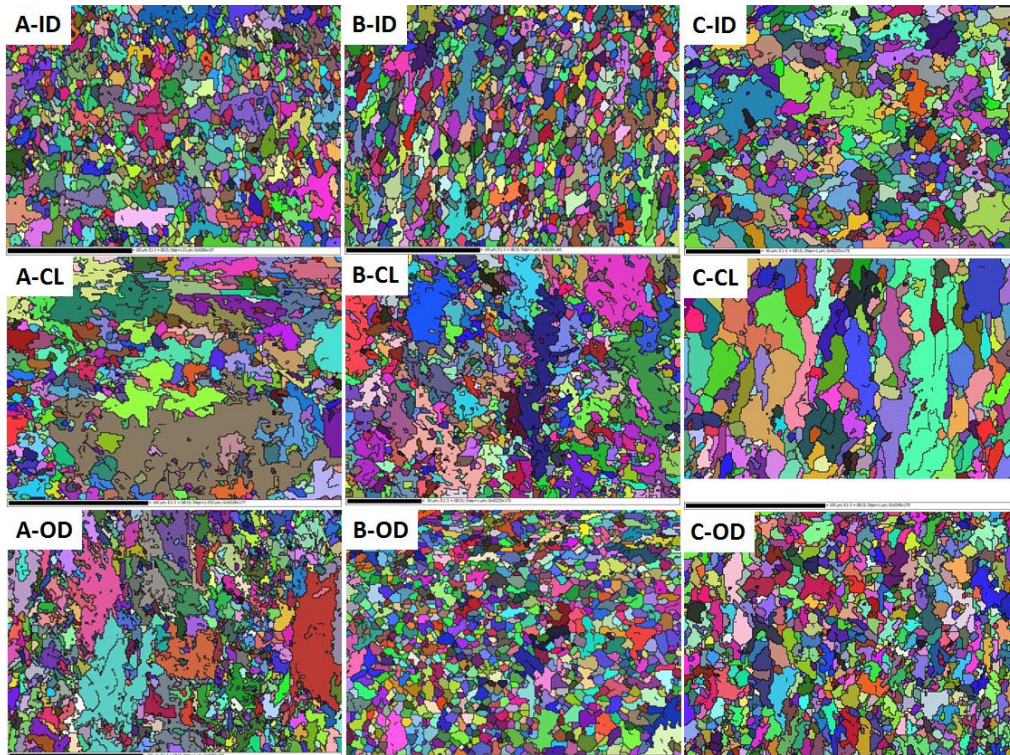


Figure 5.6 EBSD maps for Steel A, B and C at the ID, CL and OD positions.

Table 5-2 Average Grain Size of As-received Steel A, B and C at ID, CL and OD Positions Located 90° to the Weld Measured using EBSD Maps

Average Grain Size (μm)	ID	CL	OD
Steel A	4.2	4.6	4.0
Steel B	4.1	4.3	4.1
Steel C	5.3	6.1	4.7

The grain size distributions measured using EBSD for Steels A, B and C are illustrated in Figure 5.7, Figure 5.8 and Figure 5.9, respectively. In these figures, a higher area percentage of smaller grain sizes is observed for the ID and OD positions compared to the CL position for all steels. Larger grains are more frequently found for steels at the CL positions than the ID and OD positions. It is surprising to find grain sizes $>30 \mu\text{m}$ at any position for any steel as reported by the EBSD measurements as these were not observed in either OM or SEM images. The reason for this is likely due to the fact that there could be grains adjacent to each other but with similar orientations or with misorientations $<15^\circ$. Such a scenario will yield a result of these grains being counted as one grain using the EBSD analysis. However, as can be seen in Table 5-2, the average grain sizes from EBSD are small indicating that the contribution of grain size values $>30 \mu\text{m}$ are much smaller than those $<30 \mu\text{m}$.

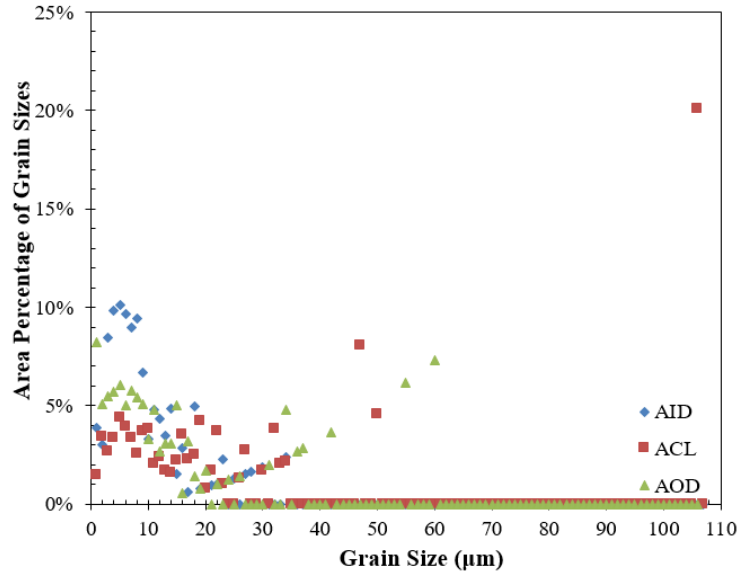


Figure 5.7 Area percentage of grain size for Steel A located 90° to the weld from ID, CL and OD positions.

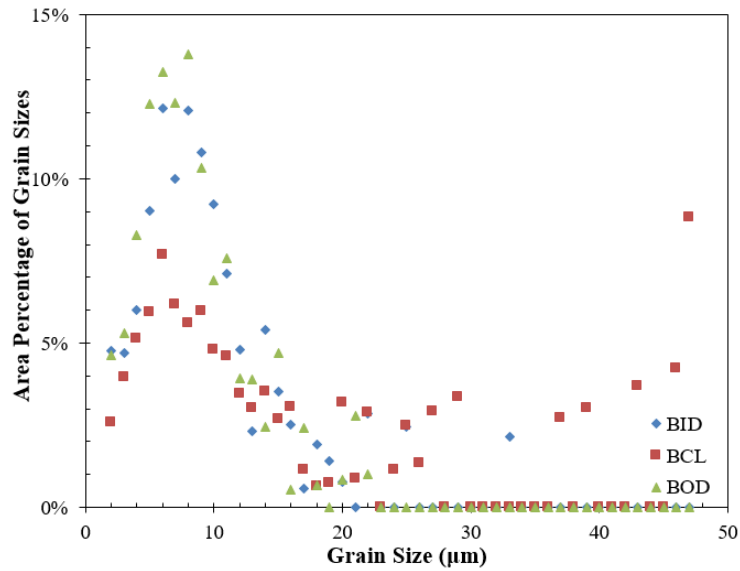


Figure 5.8 Area percentage of grain size for Steel B located 90° to the weld from ID, CL and OD positions.

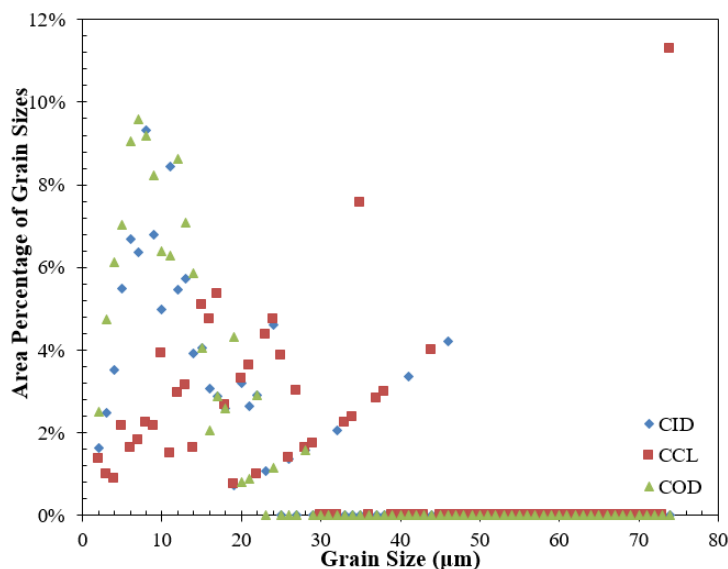


Figure 5.9 Area percentage of grain size for Steel C located 90° to the weld from ID, CL and OD positions.

Comparing the average values in Table 5-2 with those in Table 5-1, the average grain size values measured by the EBSD map method are smaller than the average values measured using OM. This is because in OM images, some grain boundaries are not revealed by the etchant so that some small grains cannot be detected. Furthermore, for the OM measurements, the presence of sub-boundaries in some grains can lead to differences with the EBSD measurements. For the EBSD measurements, these are based on the grain misorientation criterion of $\geq 15^\circ$ as well as the assumption that grains are approximated by the equivalent circle diameter. These factors will lead to errors in both measurements. However, the trends in grain sizes are consistent using both techniques. The grain sizes through the thickness of Steels A and B are nearly the same. Steel C clearly has larger grain sizes than Steels A and B, whose grain sizes are similar. Furthermore, in Steel C the grain size in the CL is the largest when compared to the ID and OD of Steel C.

5.3 Volume Fraction of Microconstituents

Using the method shown in Figure 3.21, the measured volume fractions of each microconstituent for all the three steels are summarized in Table 5-3. Steel C has a higher volume percentage of pearlite than Steel A and B, especially at the CL position (22%). This result is consistent with Figure 5.1. The combined effect of a variation in grain size and a higher volume percentage of pearlite for Steel C at the ID, CL and OD positions may be responsible for the variation in through thickness mechanical properties observed for the as-received tensile samples (Figure 4.2).

Table 5-3 Measured Volume Percentage of Phases for As-received Steel A, B and C
Located 90° to the Weld

	ID			CL			OD		
Steel	(% of phase)			(% of phase)			(% of phase)		
	AF	F	P	AF	F	P	AF	F	P
A	59	35	6	54	44	2	63	35	2
B	64	36	<1.0	40	60	<1.0	59	41	<1.0
C	67	21	12	0	78	22	59	31	10

Chapter 6 Discussion

In Chapter 4, it was found that the mechanical properties (tensile properties, hardness and Charpy impact toughness) of UOE X70 steel pipe are significantly affected by aging temperature, through thickness position (or pre-strain) and the C/Nb ratio. These important variables and their effects will be examined in terms of both the mechanism of strain aging and, where applicable, their relation to the microstructural features measured.

6.1 Effect of Aging Temperature

As was shown in Chapter 4, an increase in aging temperature gives rise to a larger increase in the YS, UTS, YS/TS and hardness. For both longitudinal and transverse tensile curves, the upper yield point and Luders strain may appear after aging at relatively higher temperatures. However, the strain hardening exponent of steels only changes slightly with increasing aging temperature or time. Also, the effect of temperature and time on the Charpy impact toughness of aged samples is negligible.

6.1.1 Effect of Aging Temperature on ΔYS

Since strain age hardening is primarily caused by C and/or N diffusion to dislocations and the subsequent “locking” effect, an increase in either temperature or time gives rise to the increase in ΔYS , as shown in Figure 4.28a. The diffusion distance of C during a period of time can be estimated using Equation 6.1 and Equation 6.2.

$$L = \sqrt{D \cdot t} \quad (6.1)$$

$$D = D_0 \cdot e^{\frac{-Q}{RT}} \quad (6.2)$$

where L is the diffusion distance of interstitial carbon, D is the diffusion coefficient, D_0 is the pre-exponential constant, Q is the activation energy, R is the gas constant, T is the absolute temperature and t is time. Based on Equation 6.1 and Equation 6.2, more C atoms diffuse to dislocations as temperature and/or time are increased, so that a higher degree of strain aging will occur. As shown in Figure 6.1, the diffusion distance of C ranges from 0.18 μm to 2.37 μm for the testing conditions. There is an increase in the estimated diffusion distance of free C atoms with increasing aging temperature for each aging time. Based on studies in the literature, the dislocation density for Nb microalloyed pipeline steels ranges from $1.3 \times 10^{13} \text{ m/m}^3$ to $5.0 \times 10^{14} \text{ m/m}^3$ [111] [112]. Assuming that the dislocations are uniformly placed in the microstructure, the average distance between the dislocations ranges from 0.04 μm to 0.28 μm . According to the free C content in the steels (Figure 6.30), the average distance between interstitial C atoms ranges from 0.04 μm to 0.14 μm . Therefore, the C atoms are able to diffuse to the

dislocations. Higher temperature gives rise to higher probability that C atoms can diffuse to dislocations and pin them.

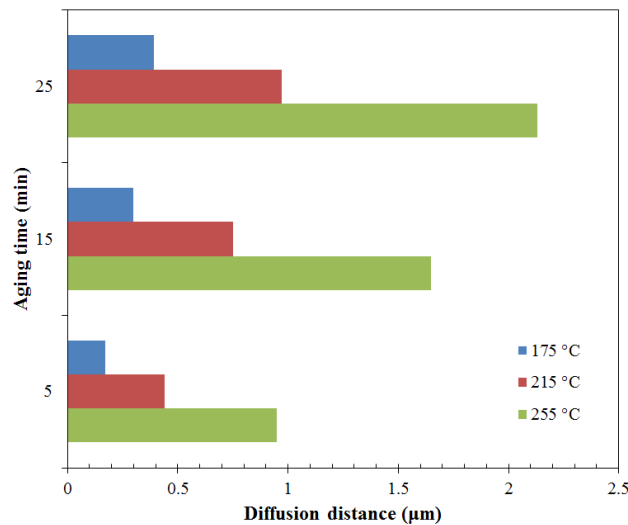


Figure 6.1 Diffusion distance of C atoms for each tested temperature and time combinations estimated using Equation 6.1 and Equation 6.2.

According to the response surfaces for both longitudinal and transverse ΔYS (Figure 4.6b and Figure 4.22), ΔYS increases as the aging temperature increases for the BBD testing conditions (from 175°C to 255°C). However, Figure 6.2 shows that a further increase in temperature (i.e., 300°C and 350°C) contributes to smaller ΔYS for Steel A. The blue brittleness temperature is around 300°C because the surface of the sample turns blue after aging at 300°C for 15 minutes (Figure 3.11). When the aging temperature is higher than the blue brittleness temperature, over-aging in microalloyed steels will occur because finely dispersed precipitates can form on dislocations [84] and weaken the steel. Thus, the quadratic models Equation 4.1 and Equation 4.4 used for predicting ΔYS are not applicable for relatively high aging temperatures (over 300°C).

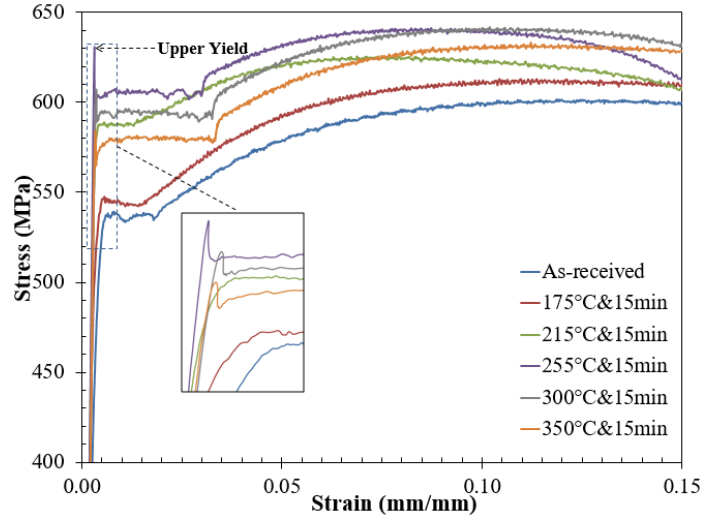


Figure 6.2 Stress-strain curves for as-received and aged longitudinal Steel A samples from the ID position.

In Equation, the diffusion ratio (i.e., $(\frac{D}{T})^{2/3}$, as shown in Section 2.3.1), is proportional to the number of dislocations locked by interstitial C atoms during the aging process. Plots of the ratio of this term relative to the values calculated for Steel A samples in the longitudinal direction are shown in Figure 6.3a and Figure 6.3b. The linear change in the ratio value over the test temperature range indicates that aging temperature is linearly related to the number of dislocations pinned by free C atoms due to aging. This may be the reason for the linear response of ΔYS to aging temperature in the BBD model (Equation 4.1 and Equation 4.4).

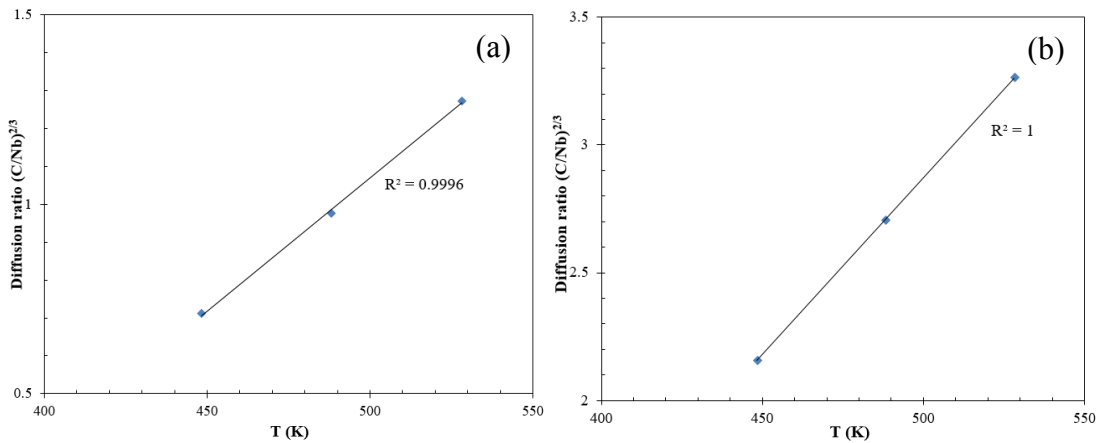


Figure 6.3 Plot of diffusion ratio vs. temperature for Steel A at the (a) ID and OD positions and (b) CL position.

Equation 4.1 and Equation 4.4 show that the aging coefficients for T are 10.43 and 19.22 for the longitudinal and transverse samples, respectively. The distributions of MS (mean of squares) for different variables affecting ΔYS of the longitudinal and transverse

samples are plotted in Figure 6.4a and Figure 6.4b. A larger distribution percentage of MS indicates higher significance of a variable in determining the ΔYS . The higher coefficient and distribution percentage (10% for longitudinal samples vs. 66% for transverse samples) for aging temperature suggest that temperature plays a more important role in affecting ΔYS for transverse samples than for the longitudinal samples. This may be due to the additional artificial plastic strain applied to the transverse samples. The imposed plastic strain in the transverse samples results in a higher dislocation density in the steels and magnifies the effect of aging temperature (i.e., diffusion of C and/or N atoms), because an increasing number of dislocations could be locked by the interstitial atoms.

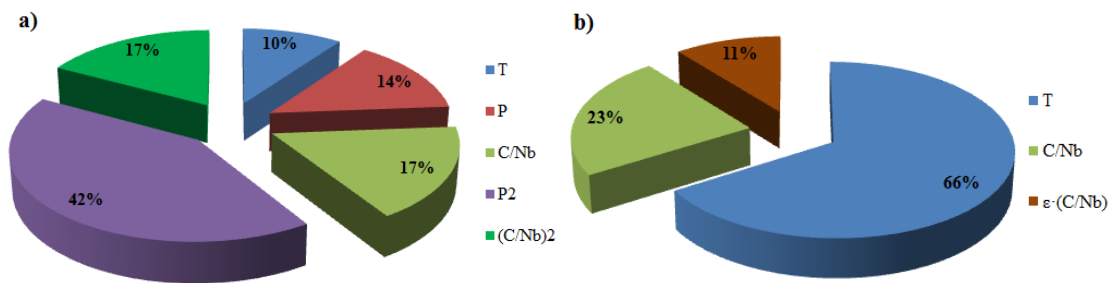


Figure 6.4 Distribution percentages of MS (means of squares) for different variables affecting ΔYS for a) longitudinal and b) transverse samples.

Figure 6.2 and Figure 6.5 show the stress-strain curves of longitudinal and transverse Steel A samples (unaged and aged at different temperatures), respectively. In Figure 6.2, although a plateau type of yielding appears for the as-received samples and those samples aged at lower temperatures (175°C to 215°C), the upper yield point is not apparent. In contrast, an upper yield point, followed by a sudden drop in stress, and Luders strain appear for the samples aged at higher aging temperatures (255°C to 350°C). Likewise, as shown in Figure 6.5, the tensile curve of the unaged 1.7% pre-strained transverse Steel A sample shows a round-house type of yielding, while an increasing trend towards discontinuous yielding featured by an upper yield point appears as the aging temperature increases.

The appearance of discontinuous yielding (i.e., upper yield point) is attributed to the formation of Cottrell atmospheres, where the mobile dislocations are pinned by interstitial C atoms. If the steel sample is aged at higher temperatures, an increasing number of C atoms will absorb enough kinetic energy to migrate to the dislocations and subsequently lock them. Thus, a larger force applied to the steel sample is required to tear the dislocations from the Cottrell atmospheres. After escaping the C atoms, the dislocations become highly mobile and generate rapid plastic flow under lower stresses. This is the reason why apparent discontinuous yielding (i.e., large difference between upper yield stress and lower yield stress) is observed for high aging temperatures (e.g., 255°C or even higher) for the test conditions. For the 1.7% pre-strained transverse Steel A sample aged at the highest temperature (255°C), the UTS is attained at the upper yield

stress, rather than through subsequent work hardening. No distinct lower yield point and work hardening are observed in the curve. The apparent upper yield point occurs because the increase in aging temperature contributes to an increase in the number of mobile dislocations pinned by C atoms. Meanwhile, since the sample has been plastically deformed and then aged, its work hardenability (i.e., uniform elongation) is reduced [70] and the increase in the tensile stress from the lower yield point is negligible.

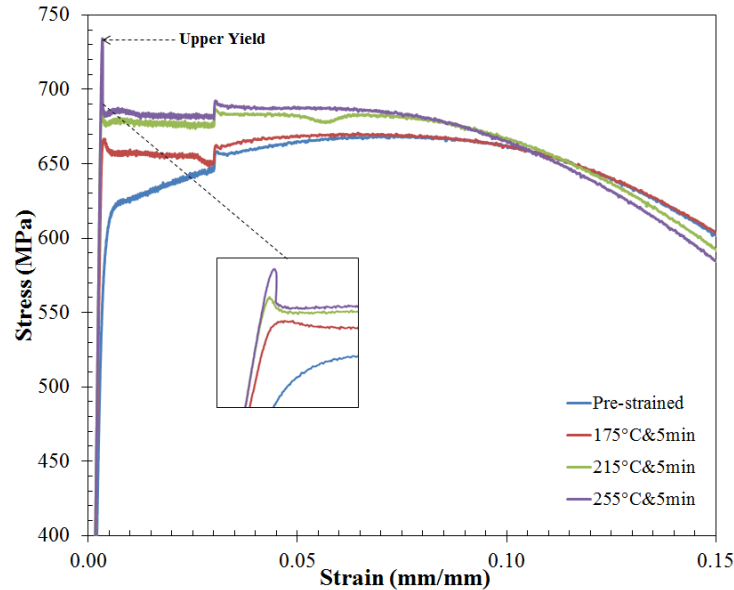


Figure 6.5 Stress-strain curves for 1.7% pre-strained and subsequently aged transverse Steel A samples.

6.1.2 Effect of Aging Temperature on Δ UTS

Equation 4.2 and Equation 4.5 show that Δ UTS increases with increasing aging temperature for both the longitudinal and transverse samples. The increase in UTS due to aging is mainly caused by the formation of solute clusters and precipitate growth when dislocation locking is completed [62]. This process results in an increase in the work hardenability of the steels and, thus, increases the UTS values. The distribution pie charts (Figure 6.6) show that the significance of aging temperature for longitudinal samples (28%) and transverse samples (37%) is similar.

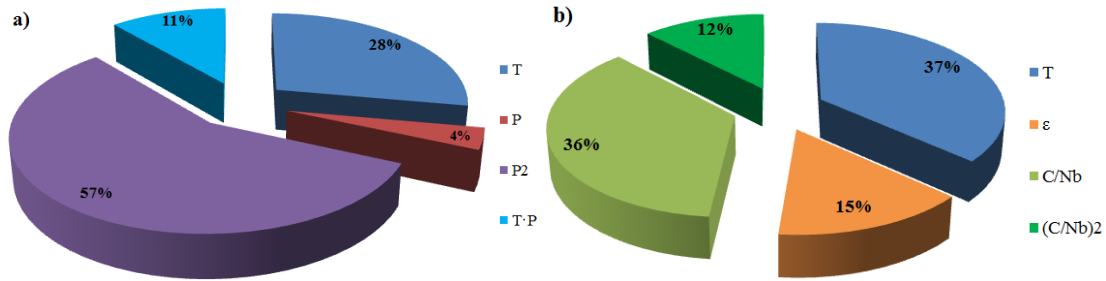


Figure 6.6 Distribution percentages of MS (means of squares) for different variables affecting ΔUTS for (a) longitudinal and (b) transverse samples.

The change in YS and UTS for steels at different positions through the pipe wall thickness caused by aging (at 255° for 25 min) is plotted in Figure 6.7. ΔUTS is lower than ΔYS for all the samples, especially for Steel A and B. The same trend is also observed in Table 4-1 and Table 4-5 for the longitudinal and transverse samples used for BBD. This is because the primary strain aging mechanism (i.e., diffusion of free C and N atoms) results in most of the mechanical property changes in microalloyed steels. The change in tensile properties caused by other mechanisms is relatively small.

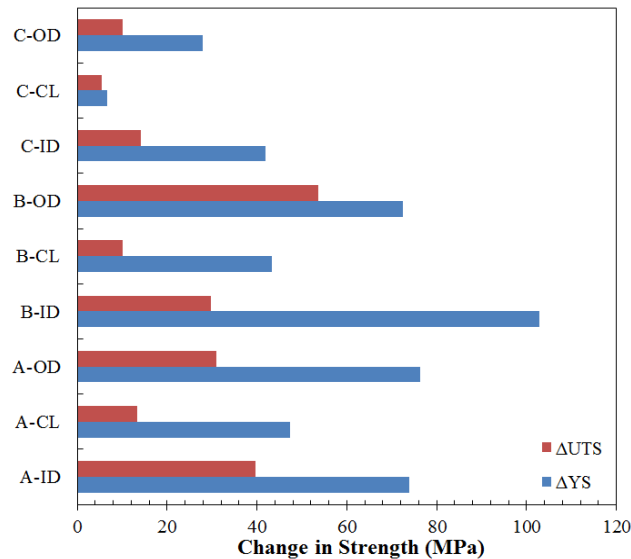


Figure 6.7 Change in YS and UTS after aging (at 255°C for 25 min) for steels located 90° relative to the weld at the ID, CL and OD positions.

6.1.3 Effect of Aging Temperature on $\Delta YS/TS$

Figure 6.8 shows the relationship between ΔYS and $\Delta YS/TS$ for all steels located 90° relative to the weld. A positive correlation between ΔYS and $\Delta YS/TS$ is observed, especially for the longitudinal samples ($R^2 = 0.79$). This suggests that variables influencing ΔYS (i.e., C/Nb ratio (type of steel), position (P), pre-strain and aging temperature) have similar effects on $\Delta YS/TS$.

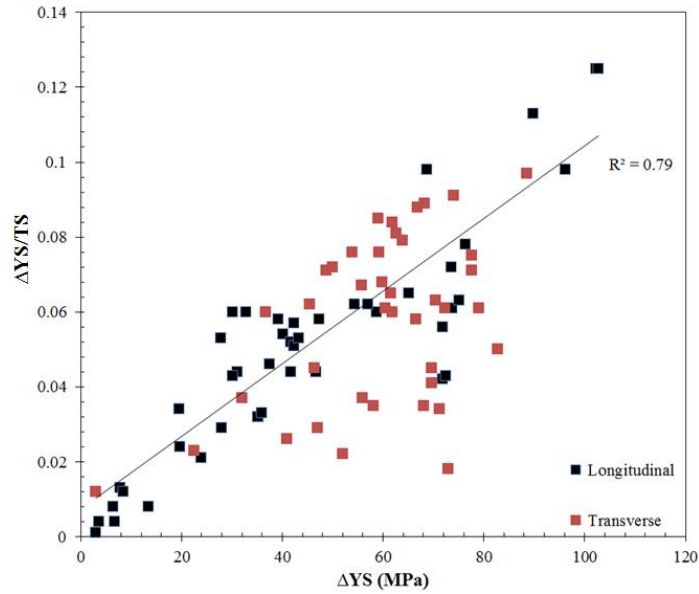


Figure 6.8 Plot of ΔYS vs. $\Delta YS/TS$ for all steels located 90° relative to the weld.

Although ΔYS and ΔUTS exhibit a linear dependence with aging temperature (Equation 4.1 and Equation 4.2) for the longitudinal samples, aging temperature does not exhibit a statistically significant effect on $\Delta YS/TS$. This suggests that an increase in aging temperature for the test conditions does not have a significant effect on the safety of the steels against failure (i.e., the capacity for plastic deformation). In contrast, temperature has a statistically significant effect on $\Delta YS/TS$ for the transverse samples, as shown in Table 4-8 and Figure 6.9. The remarkable increase in YS/TS due to the increase in aging temperature can be attributed to the imposed plastic strain that may give rise to a larger number of dislocations in the microstructure. The significant effect of plastic strain on strain aging effects will be discussed in Section 6.4.

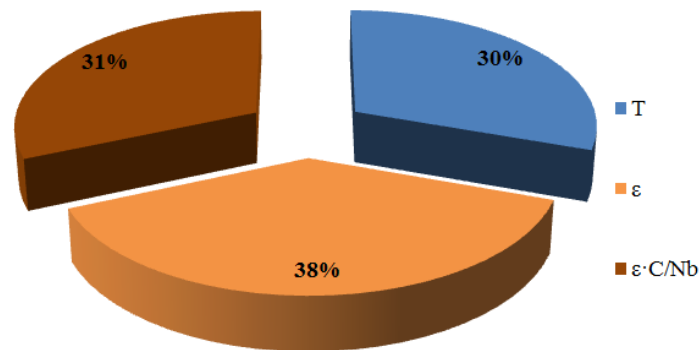


Figure 6.9 Distribution percentages of MS (means of squares) for different variables affecting $\Delta YS/TS$ of transverse steel samples.

6.1.4 Effect of Aging Temperature on ΔHV

As shown in Figure 4.30, Figure 4.31 and Figure 4.32, the micro-hardness values for all three steels at different through wall thickness positions increase slightly with increasing aging temperature. However, compared with ΔYS due to aging, the ΔHV values are much lower when the error bars are considered. This suggests that dislocation locking does not have a significant effect on the hardness of microalloyed steels.

6.1.5 Effect of Aging Temperature on CVN Toughness

According to Figure 4.33, the effect of aging on the Charpy V-notch impact toughness of Steel A at the ID position located 90° relative to the weld is relatively small, considering the presence of overlapping absorbed energy values for the aged and unaged samples. Also, the fracture surfaces for all the Charpy samples show 100% ductile fracture. The transition from ductile to brittle fracture is not observed even for the samples aged at the highest temperature (255°C) and cooled down to -60°C prior to the Charpy testing. Similar results are also found for Steel A at the OD position (Figure 4.34). This indicates that the effect of dislocation locking due to the aging treatment (for the test conditions) on the impact toughness is not as strong as the effect on tensile properties.

6.2 Effect of Aging Time

Figure 4.28a shows that ΔYS increases more rapidly with increasing temperature than with increasing time. All the empirical equations predicting the change in properties based on the 4-factor BBD show that aging time is not a statistically significant variable affecting strain aging. In addition, Figure 6.10 compares the YS of the three steels aged at 255°C for 5 minutes and 25 minutes. It shows that the changes in YS due to increasing aging time from 5 to 25 minutes are negligible. Thus, aging time plays a less important role in determining the aging response than the temperature does. This can be explained by the exponential relationship between L^2 and T, compared with the linear relationship between L^2 and t. Through Equation 6.1 and Equation 6.2, it can be calculated that an aging treatment at 255°C for 5 minutes is equivalent to an aging treatment at 175°C for 130 minutes (more than 25 minutes). Although time is considered as an important factor affecting ΔYS for the transverse direction in Steel A in a 3-factor BBD, the percent of the mean of squares (MS) of time (11%) is much lower than that of temperature (63%), as shown in Figure 6.11. Thus, aging time (from 5 min to 25 min) has a negligible effect on the property changes due to strain aging. Previous experimental results showing the effect of aging time were obtained by using much larger aging time intervals (from 35 min to 10,000 min) [61].

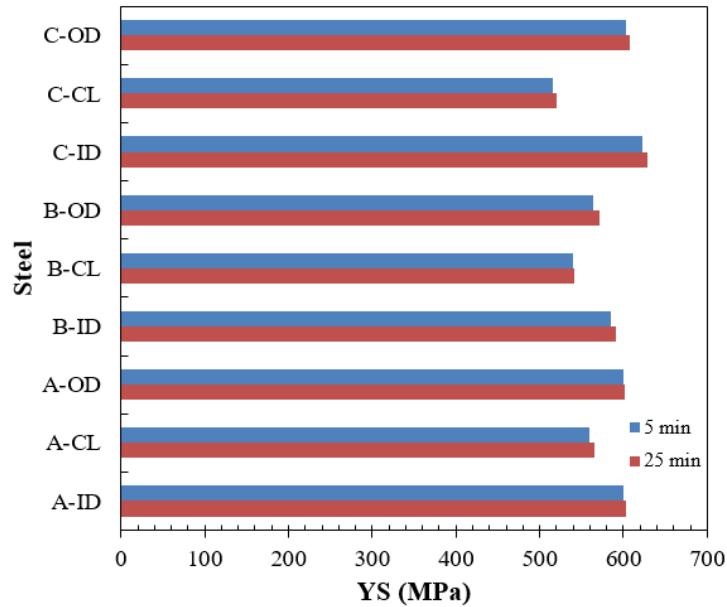


Figure 6.10 Yield strength for Steel A1, B1 and C1, at different through wall thickness positions, aged at 255°C for 5 minutes and 25 minutes.

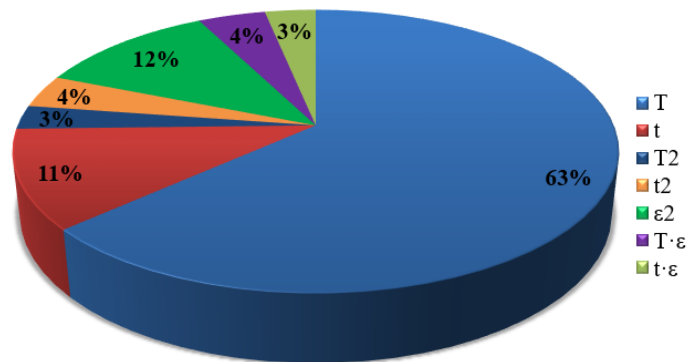


Figure 6.11 Distribution percentages of MS for different variables affecting ΔYS of Steel A in the transverse direction.

The effect of aging on the CVN impact toughness is relatively small when the error bars are considered (Figure 4.33 and Figure 4.34). There is a slight increase in absorbed energy for the samples aged at 215°C or 255°C for 5 minutes. The measured energy for the samples aged at 255°C for 25 minutes tends to be lower than that for the as-received samples. The slight increase in toughness can be attributed to the increase in the crack propagation energy. The increased YS and UTS during the aging process strengthen the matrix and impede the void coalescence in the microstructure of Steel A. The decrease in toughness after aging at 255°C for 25 minutes may be caused by the reduced ductility of the steel. Since toughness is a good combination of strength and ductility, the decrease in toughness can be attributed to the slightly reduced strain hardening rate (Figure 4.14), which is an estimate of uniform elongation [114].

6.3 Effect of Position

The effect of through wall thickness positions (ID, CL and OD) on mechanical properties for the three steels was studied for longitudinal samples. In the most simplistic case, the ID and OD of the pipe will experience the largest plastic strain – additional compressive strain for ID and tensile strain for OD. In addition, the larger values for the strain hardening exponent for the CL position (versus the ID and OD positions) of Steel A, B and C (Figure 4.14, Figure 4.15 and Figure 4.16) indicates higher work hardening. However, due to the complicated strain histories that can occur during UOE pipe forming and the difficulty in quantifying these strains, the effective amount of plastic strain at the ID, CL and OD positions is unknown.

6.3.1 Effect of Position on ΔYS

As shown in Figure 6.4a, position plays the most important role in determining ΔYS (14% for P plus 42% for P²). As both C/Nb ratio and aging temperature have significant effects on ΔYS , the effect of position can only be ascertained from aging tests in which these variables are held constant. Figure 6.12 shows the ΔYS values for Steel A, B and C aged at 255°C (time is not constant) as a function of position. It is shown that the increase in YS is larger at both the ID and OD positions for all the three steels, compared with that at the CL position. This is also shown in the response surface (Figure 4.6). The as-received mechanical properties (Figure 4.2, Figure 4.3 and Figure 4.4) and microstructure (Table 5-1 and Figure 5.1) are relatively uniform through the thickness for Steel A and B. Thus, the lower values of ΔYS at the CL position likely result from a difference in the through thickness forming strains imposed during UOE pipe production. Higher dislocation density is expected for the ID and OD positions, so that more mobile dislocations can be locked by the interstitial C and/or N atoms in the steels. For Steel C, the minimum in ΔYS at the CL position (lower than 10 MPa) may be attributed to differences in pipe forming strains and microstructure (larger grain size at the CL position).

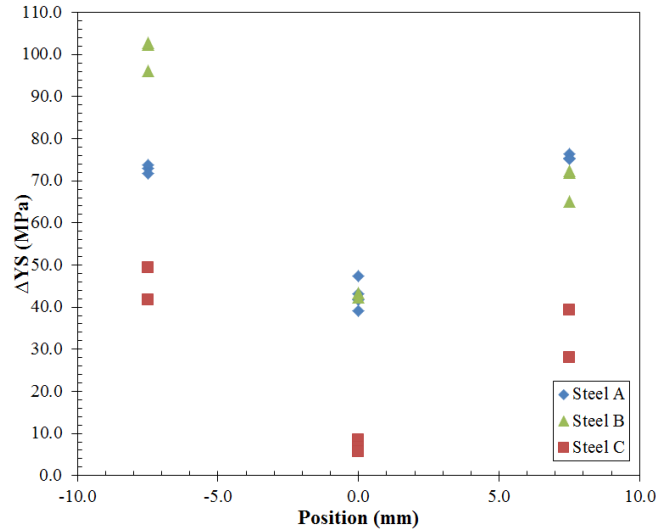


Figure 6.12 Plot of ΔYS vs. position for Steel A1, B1 and C1 aged at 255°C.

6.3.2 Effect of Position on ΔUTS

As shown in Figure 6.6a, position plays the most important role in determining ΔUTS (28% for P plus 57% for P²). Figure 6.13 shows the ΔUTS values for Steel A, B and C aged at 255°C (time is not constant) as a function of position. As with ΔYS , the increase in UTS is larger at both the ID and OD positions for all three steels, compared with that at the CL position. This trend is also shown in the response surface plot (Figure 4.9). Similarly, the variation in the magnitude of plastic strain (i.e., dislocation density) imposed during forming may be responsible for the lower ΔUTS values at the CL position for all three steels.

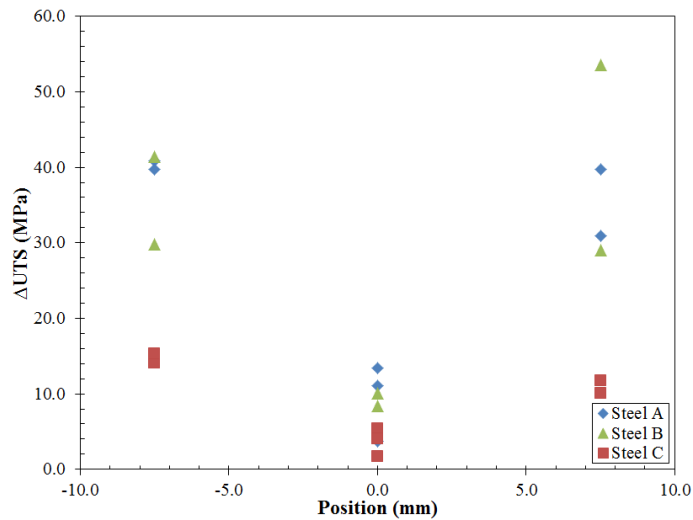


Figure 6.13 Plot of ΔUTS vs. position for Steel A1, B1 and C1.

6.3.3 Effect of Position on $\Delta YS/TS$

As discussed in Section 6.1.3, factors affecting ΔYS , such as C/Nb ratio and position, also have a similar effect on $\Delta YS/TS$. Figure 6.14 shows the $\Delta YS/TS$ values for Steel A, B and C aged at 255°C (time is not constant) as a function of position. Similar to ΔYS and ΔUTS , $\Delta YS/TS$ for the CL position tends to be lower than that for the ID and OD positions, despite the presence of two outliers for Steel B. This trend is also illustrated in the response surface plot (Figure 4.12). The minimum $\Delta YS/TS$ is observed for the CL position of Steel C (including a negative value), which may be attributed to its unique microstructural features (remarkably larger grain sizes and large fraction of pearlite). The effect of microstructure will be discussed in detail in Section 6.5.

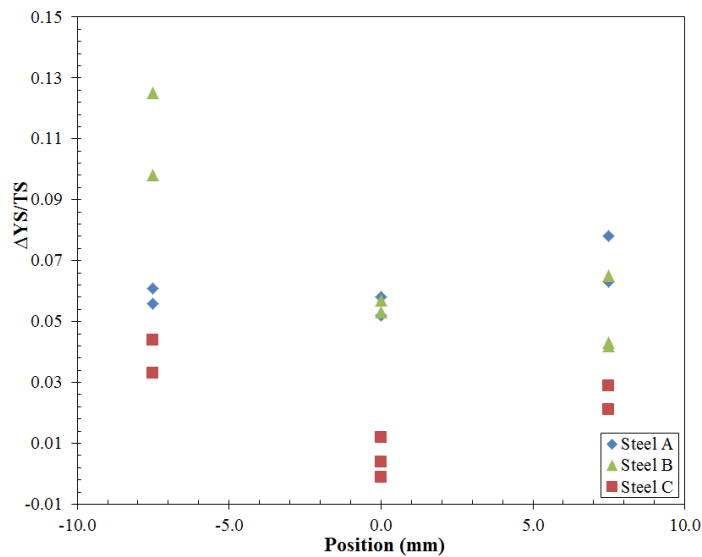


Figure 6.14 Plot of $\Delta YS/TS$ vs. position for Steel A1, B1 and C1 aged at 255°C.

6.3.4 Effect of Position on ΔHV

Although the change in the hardness values for the steels is relatively small, it can be seen in Figure 6.15 that the ΔHV is higher at the ID and OD positions than that at the CL position. This is also attributed to the difference in the amount of plastic strain at through wall thickness positions. Figure 6.16 shows that ΔHV is proportional to ΔYS for all three steels studied ($R^2 = 0.91$).

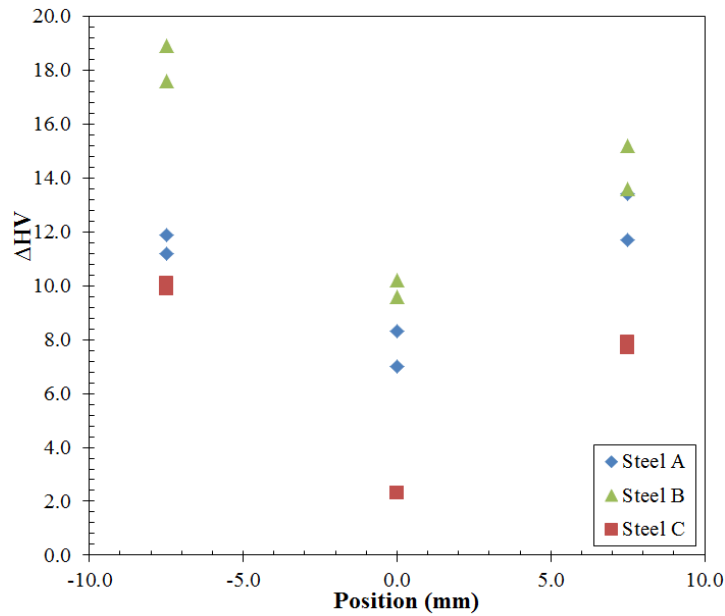


Figure 6.15 Plot of ΔHV vs. position for Steel A1, B1 and C1 aged at 255°C.

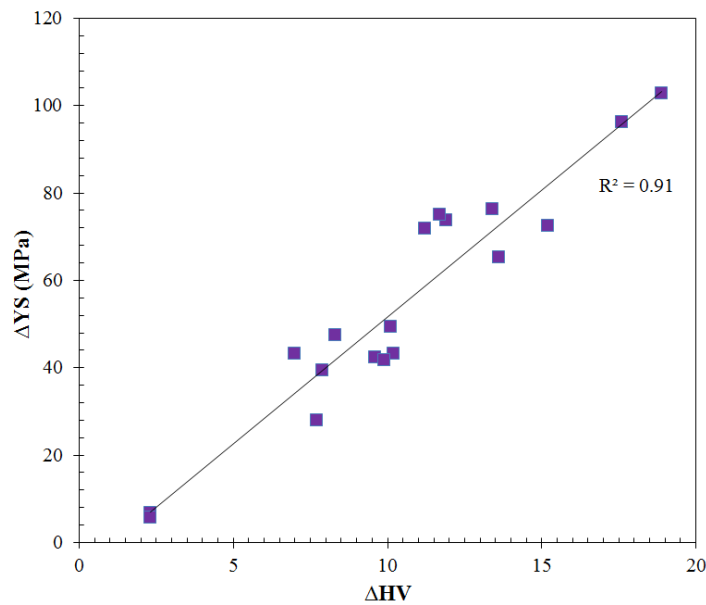


Figure 6.16 Plots of ΔYS vs. ΔHV for steels (located 90° to the weld) aged at 255°C.

6.4 Effect of Pre-strain

As shown in Figure 4.19, YS, UTS and YS/TS for all three steels are increased with increasing magnitude of pre-strain. The steels are strengthened by plastic deformation because of work hardening, which can be quantified by the increase in the number of dislocations [115]. Pre-strain of 1.70% is used to simulate the tensile strain due to pipe forming at the OD position, which can be estimated using the equation:

$$\varepsilon = \frac{t}{D} \quad (6.3)$$

where ε is the plastic strain imposed by UOE forming, t is the effective thickness of the pipe ($t = 15.6$ mm because the surface of the pipe was ground off) and D is the outer diameter of the pipe ($D = 914$ mm). A pre-strain of 3.40% was used for the BBD and to study the effect of a higher magnitude of strain on the strain aging phenomenon.

6.4.1 Effect of Pre-strain on ΔYS

As shown in Equation 4.4, the effect of pre-strain on ΔYS depends on C/Nb ratio (i.e., type of steel). Figure 4.21b shows that the increase in the magnitude of pre-strain leads to higher ΔYS for Steel C. However, a maximum ΔYS is not observed at a pre-strain of 3.40% for Steel A and B. The models with better estimation (based on 3-factor BBD where $R^2 = 0.96$ for Steel A and $R^2 = 0.99$ for Steel B) were used to analyze the effect of pre-strain on ΔYS . The 2D contour plots of ΔYS for Steel A and B are shown in Figure 6.17 and Figure 6.18, respectively.

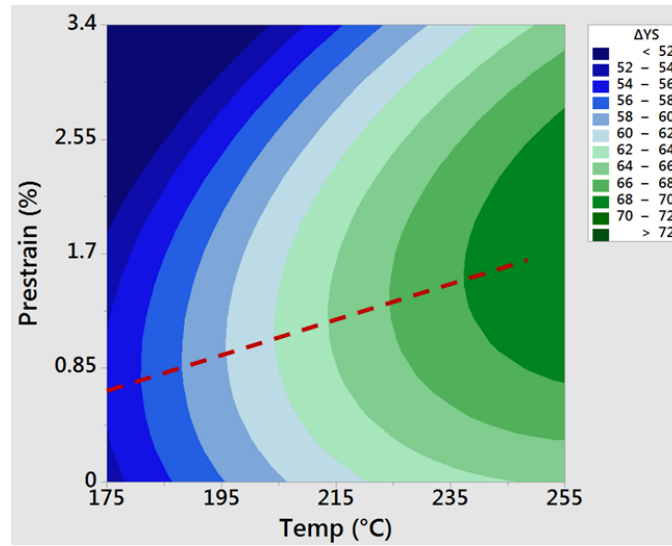


Figure 6.17 Contour plot of ΔYS vs. T and ε for Steel A ($t = 5$ min).

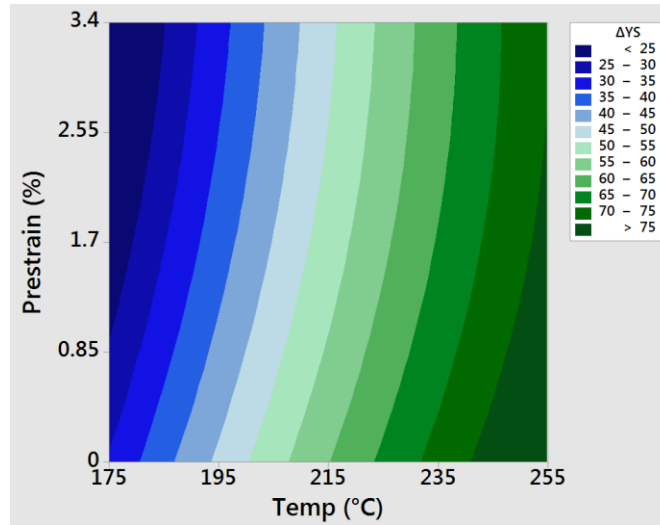


Figure 6.18 Contour plot of ΔYS vs. T and ϵ for Steel B ($t = 5$ min).

In Figure 6.17, the pre-strain (ϵ_m) contributing to the highest increase in YS of Steel A (at a given aging temperature) ranges from 0.75% to 1.70% (marked by the red dotted line). This trend is also presented in Figure 6.19. For Steel B, as shown in Figure 6.18, ΔYS decreases with increasing pre-strain (from 0% to 3.40%). Figure 6.20, however, shows an increasing trend of ΔYS for Steel C as the imposed strain increases. The decrease in ΔYS at high pre-strain (3.40%) is negligible.

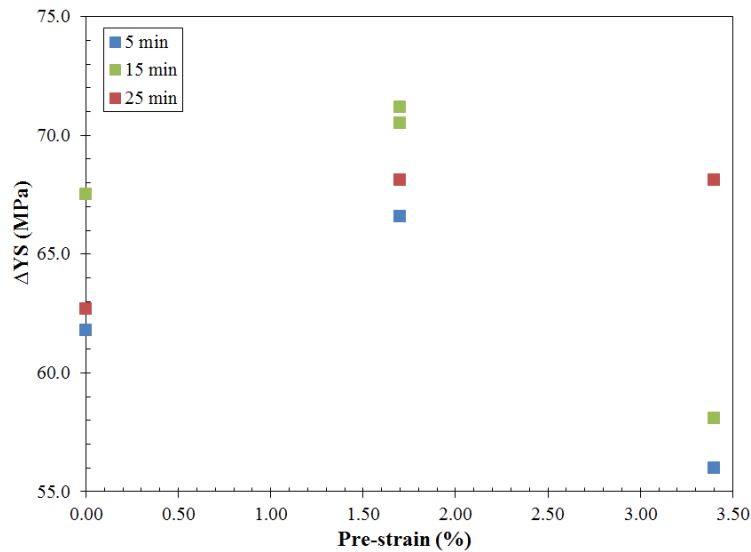


Figure 6.19 Plot of ΔYS vs. pre-strain for Steel A aged at 215°C.

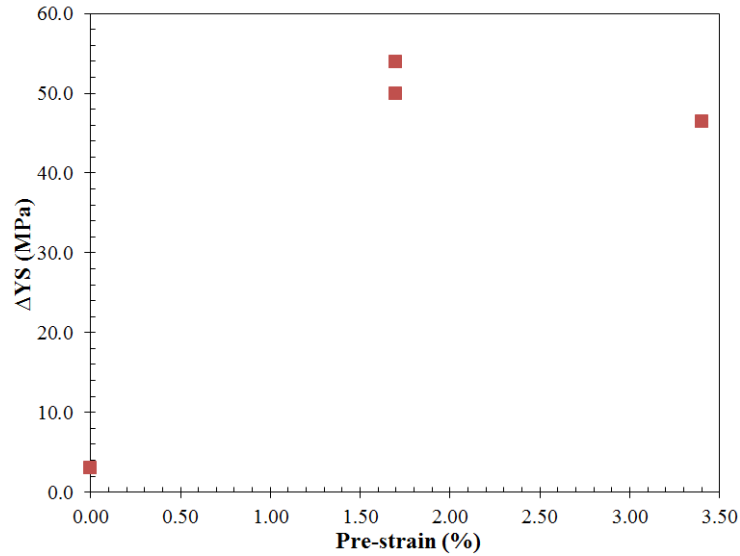


Figure 6.20 Plot of ΔYS vs. pre-strain for Steel C aged at 215°C.

When the imposed pre-strain increases from 0 to ϵ_m , ΔYS increases to the peak value because of the increase in the number of mobile dislocations within the microstructure of Steel A. The average distance between interstitial atoms and dislocations is reduced and, thus, the C or N atoms can diffuse to the dislocations more easily. However, when the pre-strain exceeds ϵ_m , new dislocations are still generated during work hardening, but the interactions between the dislocations (e.g., dislocation tangles) may reduce the mobility of the dislocations [116]. Previous research, including TEM analysis of dislocations over a range of pre-strains (from 0% to 8%) showed lower mobile dislocation density at a higher pre-strain (8%) than at a low pre-strain (4%) [117]. ΔYS experiences a decreasing trend because a further increase in dislocation density may result in stronger interaction between mobile dislocations (e.g., dislocation tangles) in the crystal structure of the steel [116]. Therefore, a higher magnitude of pre-strain would reduce the number of mobile dislocations and lessen the pinning effect of free C and N atoms.

The different aging response for Steel A, B and C can be explained by the difference in their initial dislocation density and microstructural features. As mentioned in Section 4.1.1, Steel A and B are expected to have a higher initial dislocation density than Steel C. This is also suggested by the difference in the strain hardening exponents ($n_C > n_A > n_B$) for the three steels, as shown in Figure 6.21. The higher ΔYS of both 1.70% and 3.40% pre-strained Steel C can be attributed to the better work hardenability (i.e., lower initial dislocation density and higher work hardening rate) of as-received sample. In stark contrast, Steel B (with the lowest strain hardening exponent) experiences a decrease in ΔYS because its initial dislocation density is already high enough to generate dislocation interactions that overshadow the dislocation pinning effect.

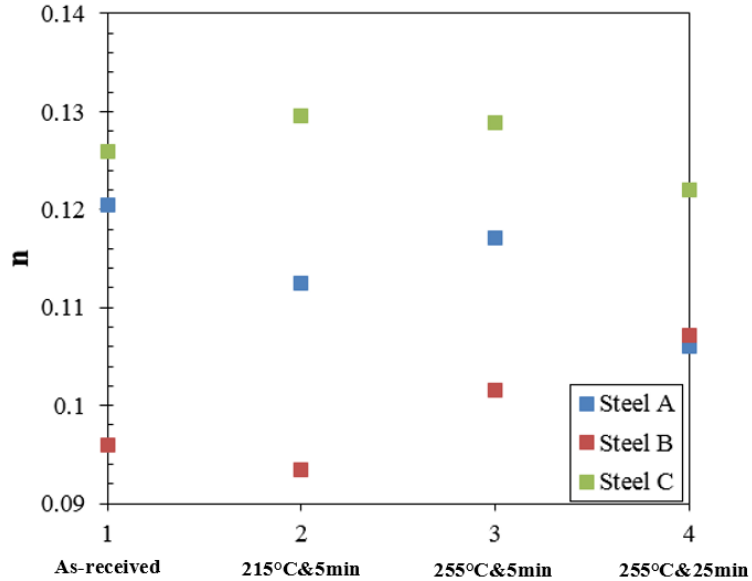


Figure 6.21 Strain hardening exponent for transverse samples of Steel A, B and C samples at the CL position.

6.4.2 Effect of Pre-strain on Δ UTS

The response surface plots and contour plots for Δ UTS of Steel A and B are shown in Figure 6.22 and Figure 6.23, respectively. The plot of Δ UTS as a function of pre-strain for Steel C is shown in Figure 6.24. An increasing trend in Δ UTS values due to aging with increasing pre-strain is observed for all three steels. For Steel A and B, a slight drop in Δ UTS occurs for lower aging temperatures (<235°C). Similar to the effect of pre-strain on Δ YS, this can be attributed to the decreased number of mobile dislocations at higher pre-strains. However, Δ UTS keeps increasing with increasing pre-strain at higher temperatures (>235°C). This is because Δ UTS due to aging is mainly caused by the solute clusters and precipitates formed along the dislocation when atmosphere locking is completed. The increment in work hardening capacity due to precipitation is sensitive to the amount of prestrain and increases with increasing dislocation density [62]. The small decrease in Δ UTS is not observed for Steel C because of its lower initial dislocation density.

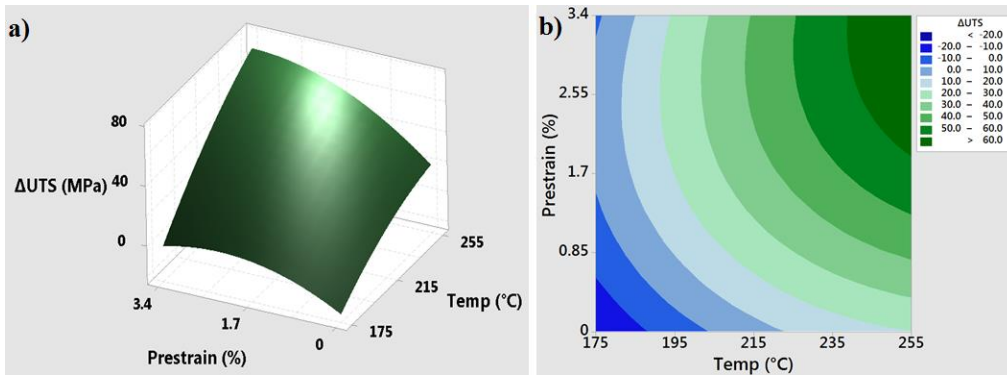


Figure 6.22 (a) Response surface plot and (b) contour plot of ΔUTS as a function of aging temperature and pre-strain for Steel A aged for 5 min.

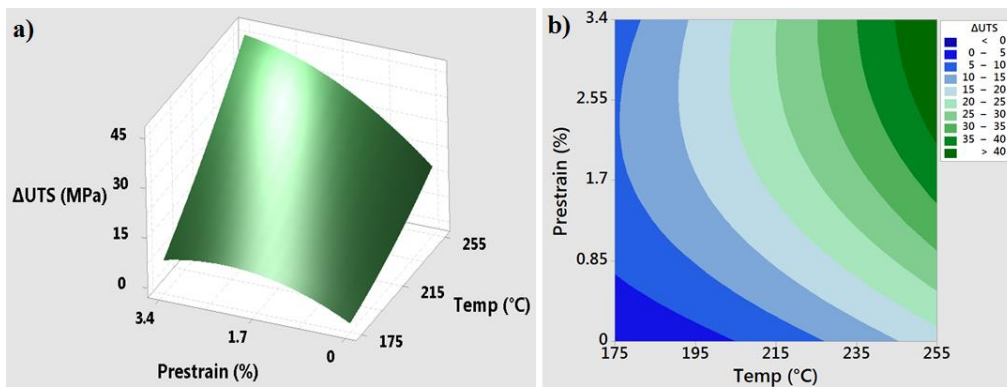


Figure 6.23 (a) Response surface plot and (b) contour plot of ΔUTS as a function of aging temperature and pre-strain for Steel B aged for 5 min.

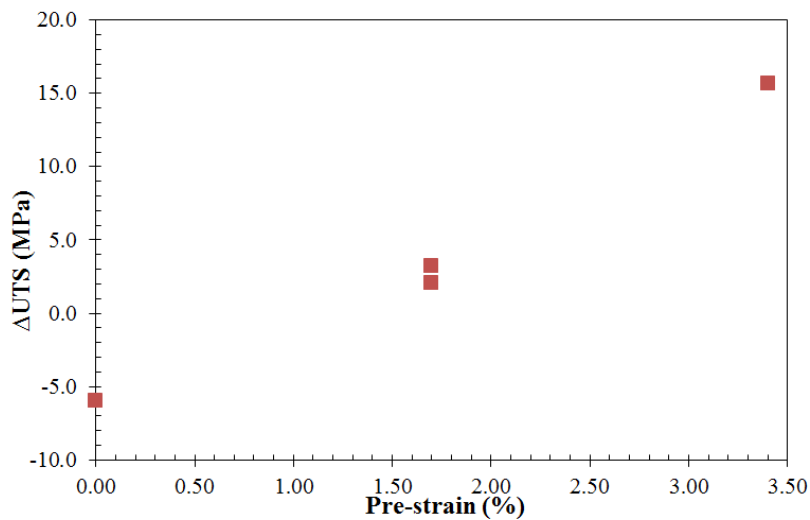


Figure 6.24 Plot of ΔUTS vs. pre-strain for Steel C aged at 215°C.

6.4.3 Effect of Pre-strain on $\Delta YS/TS$

The response surface plots along with the contour plots for $\Delta YS/TS$ of Steel A and B are shown in Figure 6.25 and Figure 6.26, respectively. The plot of $\Delta YS/TS$ as a function of pre-strain for Steel C is shown in Figure 6.27. Figure 6.25 and Figure 6.26 show that the $\Delta YS/TS$ values of Steel A and B decrease with increasing magnitude of pre-strain, which is attributed to the strong interaction between dislocations in the microstructure. However, as shown in Figure 6.26, there is still an increase in $\Delta YS/TS$ for Steel C before the pre-strain exceeds 1.7%. The difference in the response to pre-strain for Steel C can be attributed to its larger strain hardening exponent compared with Steel A and Steel B (as discussed in Section 6.4.1). With increasing pre-strain (i.e., work hardening), more dislocations are generated in Steel C than Steel A and B. This is the reason why the $\Delta YS/TS$ for Steel C is larger at higher magnitudes of pre-strain.

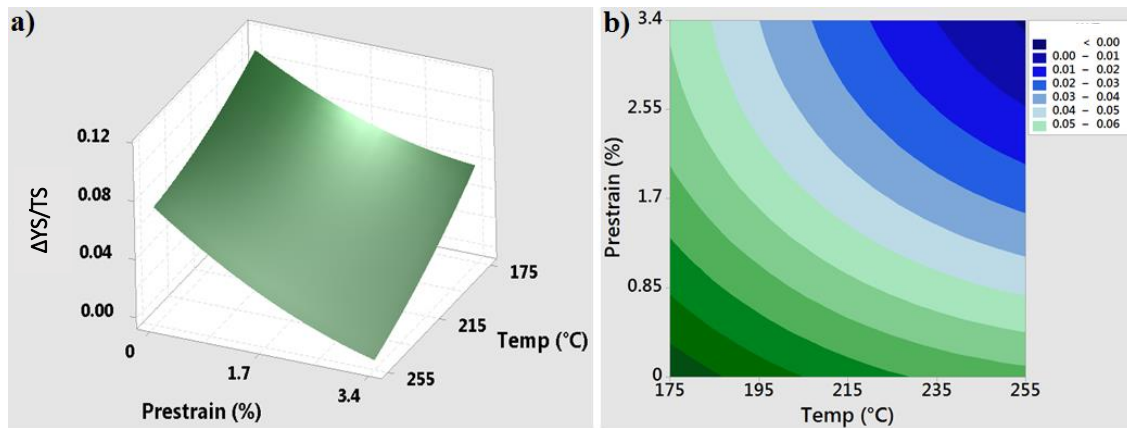


Figure 6.25 (a) Response surface plot and (b) contour plot of $\Delta YS/TS$ as a function of aging temperature and pre-strain for Steel A aged for 5 min.

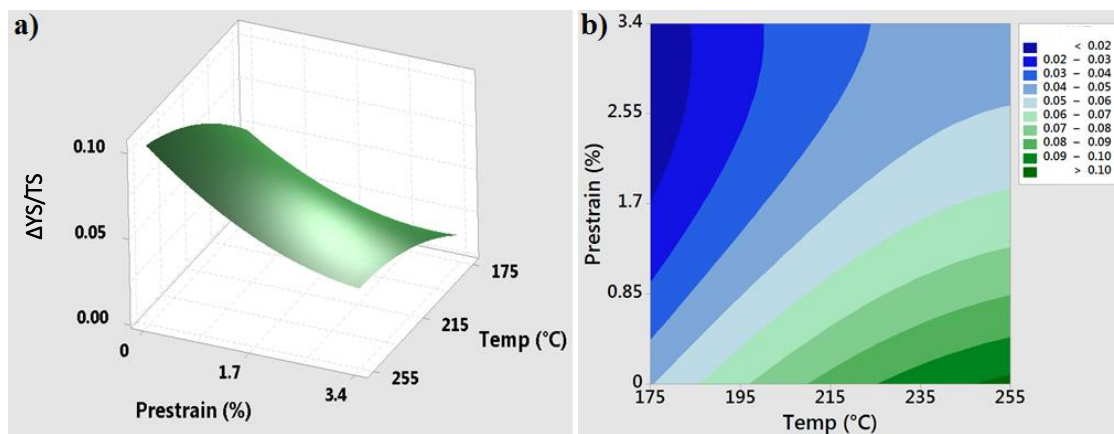


Figure 6.26 (a) Response surface plot and (b) contour plot of $\Delta YS/TS$ as a function of aging temperature and pre-strain for Steel B aged for 5 min.

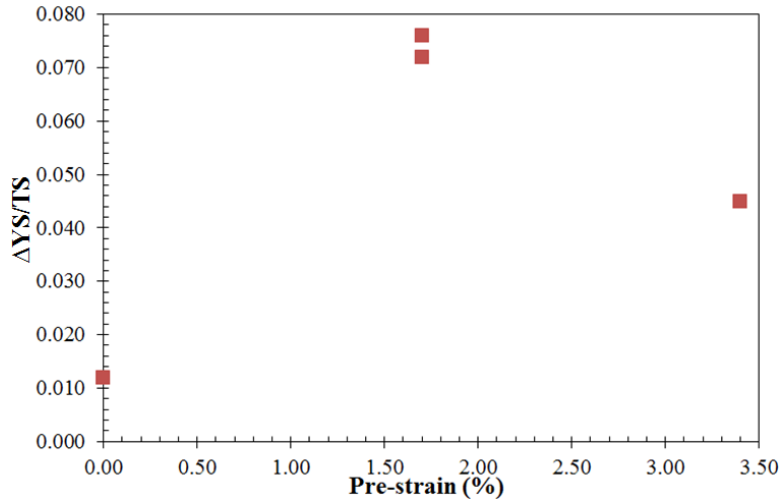


Figure 6.27 Plot of $\Delta YS/TS$ vs. pre-strain for Steel C aged at 215°C.

6.5 Effect of Microstructure

As is noted in Chapter 5, the microstructures of Steel A, B and C are qualitatively and quantitatively different. The microstructures of Steel A and B are relatively uniform through the wall thickness, compared with that of Steel C. The effects of both C/Nb ratio and through wall thickness position on the mechanical properties are considered in terms of the microstructural features of the three steels.

6.5.1 Effect of Microstructure on ΔYS

The near absence of pearlite in Steel B and its fine grain size (5.8 - 7.0 μm) suggest that the Hall-Petch effect (grain boundary strengthening) is the primary strengthening mechanism for this steel. The grains with smaller grain size strengthen the steel by generating more grain boundaries that impede dislocation movement. Conversely, Steel C has a much larger grain size (16.4 μm at the CL position) and a larger volume fraction of pearlite (22% at the CL position). For this steel, the YS can be attributed to competing factors of grain size and pearlite strengthening [118] [119]. Steel A has a microstructure somewhere between Steel B and C (closer to B). As shown in Figure 4.1 and Figure 4.17, the shapes of the tensile curves (especially during yielding) of longitudinal and transverse samples of Steel A are similar to those of Steel B.

According to Table 5-2 Average Grain Size of As-received Steel A, B and C at ID, CL and OD Positions Located 90° to the Weld Measured using EBSD Maps, the grain sizes measured using EBSD maps is higher for the CL position than those from the ID and OD positions for Steel A, B and C. In addition, Figure 5.7, Figure 5.8 and Figure 5.9 present a higher percentage of large grains (>10 μm) at the CL position for all three steels. This may result from steel processing where the cooling rate for the CL position is expected to be lower than that of the ID and OD positions. The finer grain size at the ID and OD

position maybe another contributor to the higher ΔYS because grain boundaries act as sources of dislocation during the pipe forming process [66] [67].

Figure 6.28 shows the change in ΔYS (using the longitudinal values measured at the 90° location) as a function of grain size. Since the grain size is related to C/Nb (i.e., type of steel) and through wall thickness position, aging temperature (the other important aging variable) is fixed to determine the relationship between ΔYS and grain size. It is shown that for each aging temperature, ΔYS increases with decreasing grain size. Particularly, the CL position of Steel C exhibits the smallest change in ΔYS . This may primarily be attributed to a difference in the initial dislocation densities of the finer grained steels (Steel A and B) versus the coarser grained Steel C, as discussed in Section 6.4.1. The high dislocation density in Steel A and B is in accordance with the fact that dislocation density for a given strain is proportional to the reciprocal of the grain size [120] [121]. Besides, the highest volume percentage of pearlite (as shown in Table 5-3) is at the CL position of Steel C, which may be another reason for the small change in YS because more carbon atoms combine with Fe atoms to form cementite. Although Steel C has the highest C/Nb ratio, it may not have a higher amount of interstitial carbon atoms than Steel A and B.

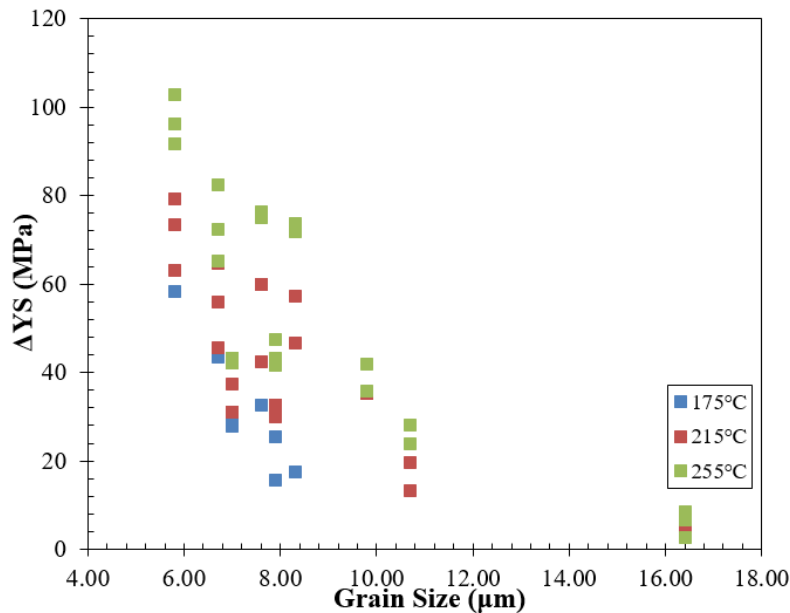


Figure 6.28 Plot of ΔYS for longitudinal samples aged at different temperatures vs. grain size.

According to Table 5-3, the volume percentages of pearlite for Steel A, B and C at different through wall thickness positions are plotted in Figure 6.29. Assuming that except for interstitial C atoms, all other C atoms are used to form NbC and cementite (Fe_3C), the estimated amounts of free C atoms are shown in Figure 6.30.

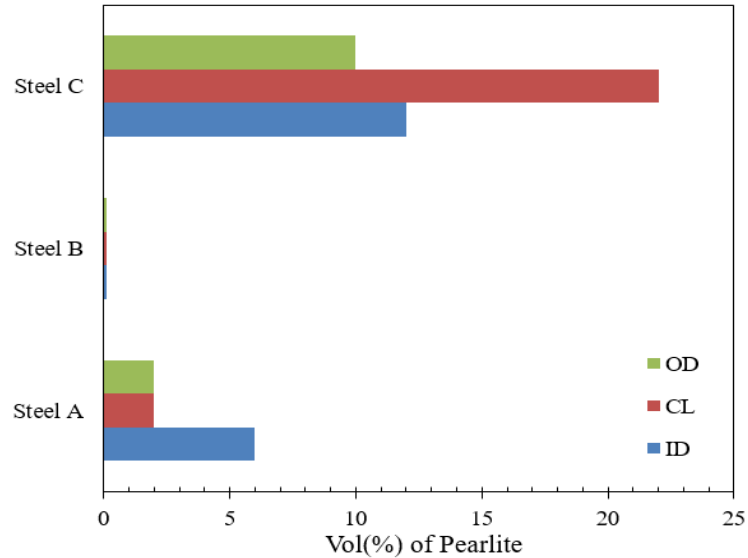


Figure 6.29 Measured volume percentage of pearlite for Steel A, B and C at OD, CL and ID positions located 90° to the weld.

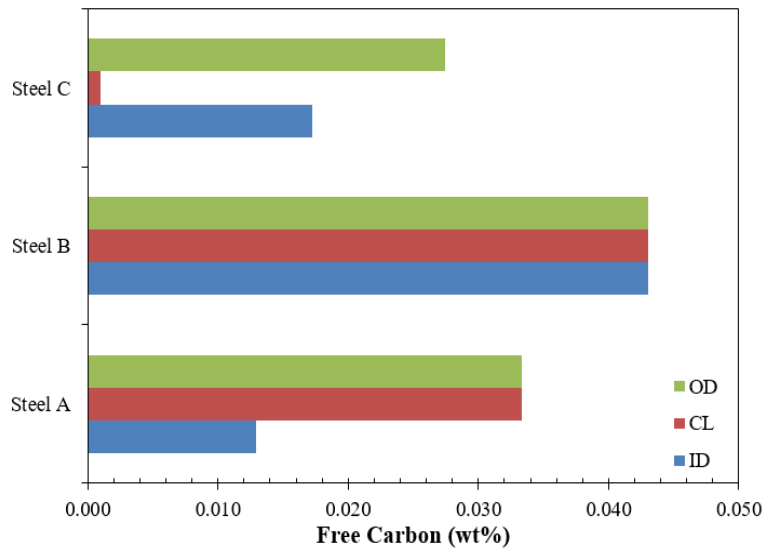


Figure 6.30 Estimated free carbon content for Steel A, B and C at the OD, CL and ID positions located 90° to the weld.

Figure 6.30 shows although Steel C has the highest weight percentage of C (0.09%, as shown in Table 3-1), the amount of free C atoms is relatively low (only 0.001% at the CL position). In contrast, Steel B has higher free C content than Steel A and C. This can be another reason why Steel B (with the smallest grain size) gives rise to the largest ΔYS .

According to Figure 4.7, the model used for predicting the ΔYS of the steels located 90° to the weld overestimates the ΔYS values for the 180° location. Since the microstructures of the steels from different macro pipe locations are similar to each other (Appendix B:

Figure 0.10, Figure 0.11 and Figure 0.12), the overestimation of predicted values is attributed to the different strain history at different locations.

Tensile curves for longitudinal and transverse samples of Steel A (Figure 6.2 and Figure 6.5) show apparent upper yield points followed by the Luders strain. In stark contrast, the curves of aged longitudinal Steel B are characterized by the round-house type of yielding (Figure 6.31a). Although Luders strain appears on the tensile curves of transverse Steel B samples, the upper yield points are not obvious (Figure 6.31b). Stress-strain curves of longitudinal and transverse Steel C samples are illustrated in Figure 6.32a and Figure 6.32b, in which an upper yield point followed by a slight drop in stress is observed.

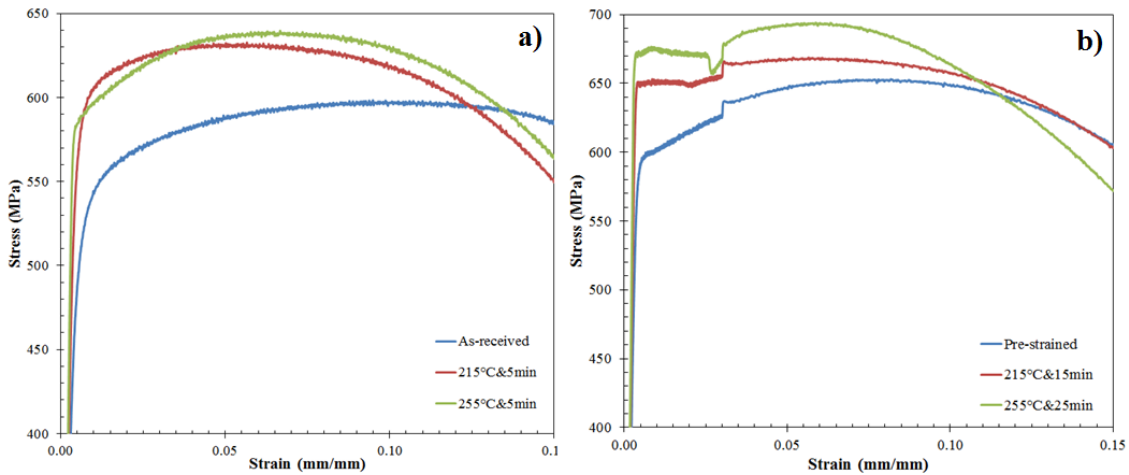


Figure 6.31 Stress-strain curves for Steel B: (a) longitudinal samples at the ID position and (b) transverse, 1.7% pre-strained samples.

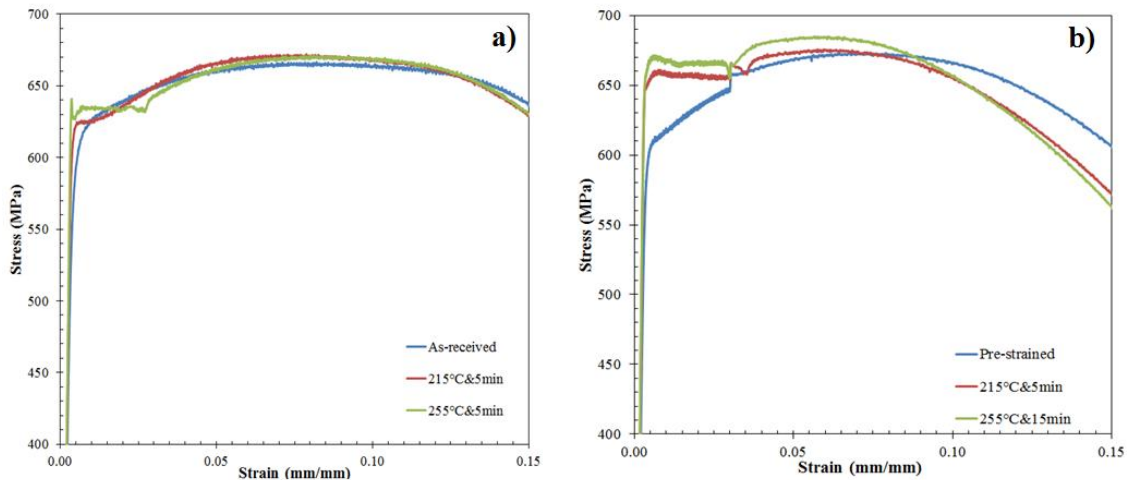


Figure 6.32 Stress-strain curves for Steel C: (a) longitudinal samples at the ID position and (b) transverse, 1.7% pre-strained samples.

The absence of the upper yield point for Steel B can be attributed to its higher initial dislocation density (as discussed in Section 6.4.1), due to the steel processing and pipe forming process. The strong interactions between dislocations in Steel B reduce the overall mobility of dislocations and overshadow the locking and unlocking effects caused by free C and/or N atoms.

6.5.2 Effect of Microstructure on Δ UTS

Figure 6.33 illustrates the change in Δ UTS for all three steels (using the longitudinal values measured at the 90° location) as a function of grain size. The correlation between Δ UTS and grain size is not as good as that for Δ YS. Neither an increasing trend nor a decreasing trend for Δ UTS with a change in grain size is observed in this figure. This indicates that other microstructure variables may be responsible for the change in Δ UTS during aging, such as the magnitude of plastic strain (i.e., dislocation density) imposed during UOE pipe forming. Equation 4.2 indicates that through wall thickness position, instead of the C/Nb ratio, plays a more important role in determining Δ UTS.

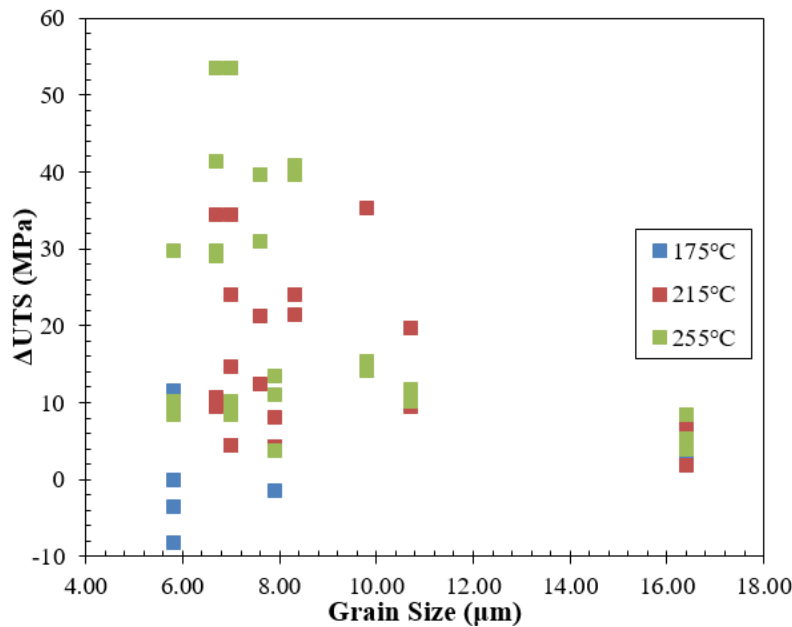


Figure 6.33 Plot of Δ UTS for longitudinal samples aged at different temperatures vs. grain size.

On examination of Figure 4.10, the equation used for predicting the Δ UTS of the steels located 90° to the weld overestimates the Δ UTS values for the 180° location. Since the microstructural features of the steels from different macro pipe locations are similar to each other (Appendix B: Figure 0.10, Figure 0.11 and Figure 0.12), the overestimation of predicted Δ UTS is also attributed to the difference in the strain history at different locations.

6.5.3 Effect of Microstructure on $\Delta YS/TS$

As shown in Equation 4.3, both the C/Nb ratio and position through wall thickness have significant influences on $\Delta YS/TS$. Figure 6.8 shows a positive correlation between ΔYS and $\Delta YS/TS$ for all three steels. Figure 6.34 shows $\Delta YS/TS$ as a function of grain size. As with ΔYS , $\Delta YS/TS$ also increases with decreasing grain size. The smallest change in $\Delta YS/TS$ is also observed for Steel C from the CL position (with the largest grain size). This can also be attributed to the difference in dislocation density and formation of cementite (i.e., reduction in the amount of free C atoms) in the microstructure.

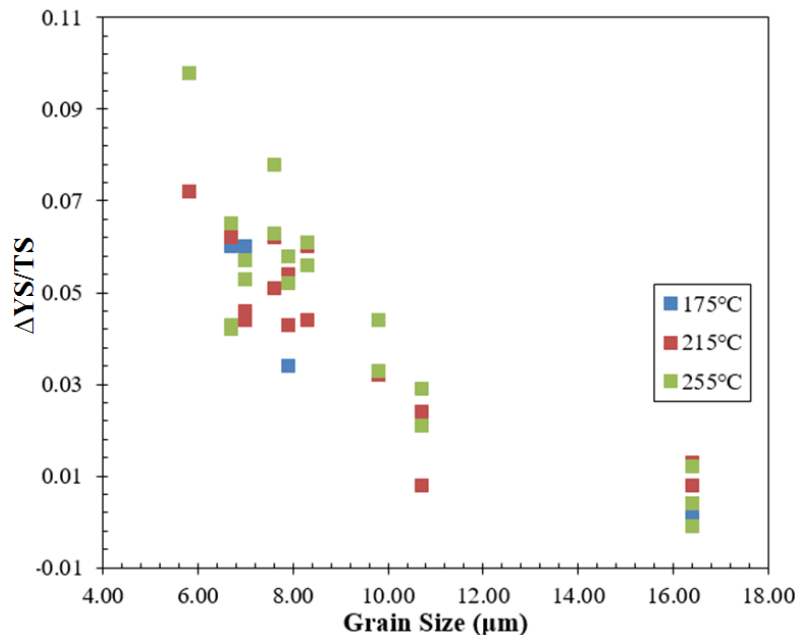


Figure 6.34 Plot of $\Delta YS/TS$ for longitudinal steel samples aged at different temperatures vs. grain size.

6.5.4 Effect of Microstructure on ΔHV

Figure 6.35 shows the change in ΔHV due to aging at 255°C as a function of grain size. For each through wall thickness position, ΔHV increases with decreasing grain size and decreasing volume percentage of pearlite. Due to the good linear correlation between ΔHV and ΔYS (Figure 6.16), the difference in initial dislocation density ($B > A > C$) and the formation of cementite in Steel C are also responsible for the result.

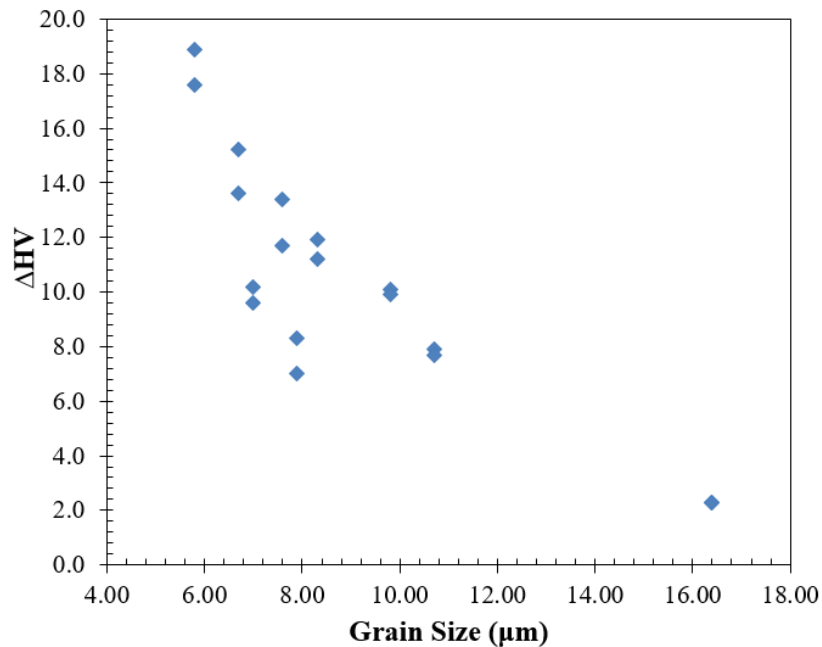


Figure 6.35 Plot of ΔHV due to aging at 255°C for steels from the 90° location vs. grain size.

6.6 Effect of Sample Direction

The effects of strain aging on ΔYS for longitudinal and transverse steel samples are compared and analyzed in this section. The longitudinal and transverse ΔYS values for all three steels from the CL positions aged at 215°C are illustrated in Figure 6.36. The average ΔYS values of aged longitudinal Steel A and B samples are significantly larger than the ΔYS values of aged samples in the transverse direction. This may be attributed to the difference in the plastic strain for the longitudinal and transverse directions. The similar and relatively small ΔYS values for the longitudinal and transverse Steel C samples may be due to its larger grain size and lower free C content (as discussed in Section 6.4.1 and Section 6.5.1).

The samples from the OD position correspond to the transverse samples from the CL position with pre-strain of 1.70% (Equation 6.3). Both the strain induced in longitudinal samples due to pipe forming and the artificially imposed plastic strain on transverse samples are perpendicular to the rolling direction. Their average ΔYS values are compared in Figure 6.37. Larger ΔYS values for the transverse samples (compared with the ΔYS values for the longitudinal samples) for Steel C are observed. This may be caused by stress concentration of cylindrical samples in the transverse direction. Due to the slightly reduced cross-section diameter in the middle of the samples, as shown in Figure 3.6, stress would concentrate at the location where the samples would break. Therefore, the imposed plastic strain at the fracture location would be higher than 1.70%,

which is the average pre-strain value through the gage length. The higher plastic strain applied to the fracture locations of the transverse samples, than that of the longitudinal samples, leads to the higher ΔYS for Steel C. For Steel A and B, although the transverse ΔYS values are still higher than the longitudinal ones, their difference is much smaller (<10 MPa). As shown in Figure 6.21, the strain hardening exponents for Steel A and B are smaller than that for Steel C. Thus, the increase in the number of dislocations in Steel A and B, due to an increase in plastic strain, would be smaller than that in Steel C. This is the reason why the longitudinal ΔYS is similar to the transverse ΔYS for both Steel A and B.

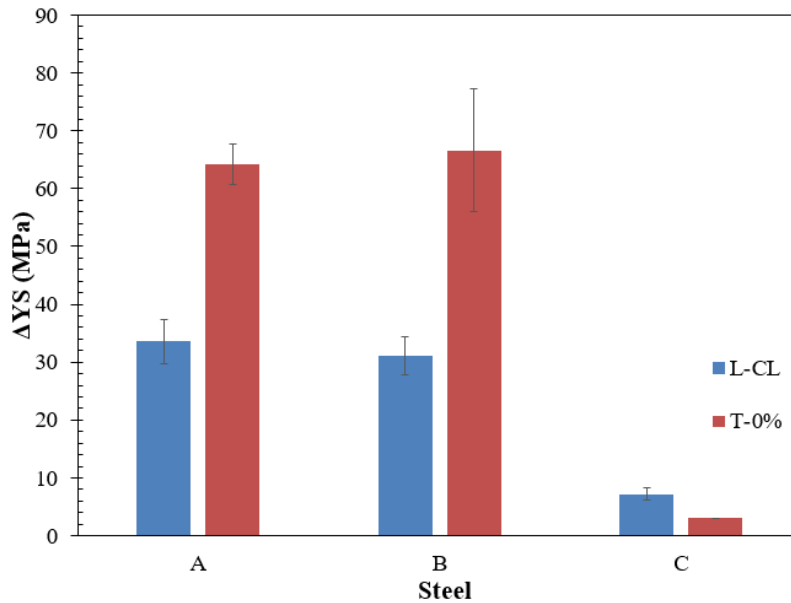


Figure 6.36 Average ΔYS for longitudinal and transverse steel samples from the CL position aged at 215°C.

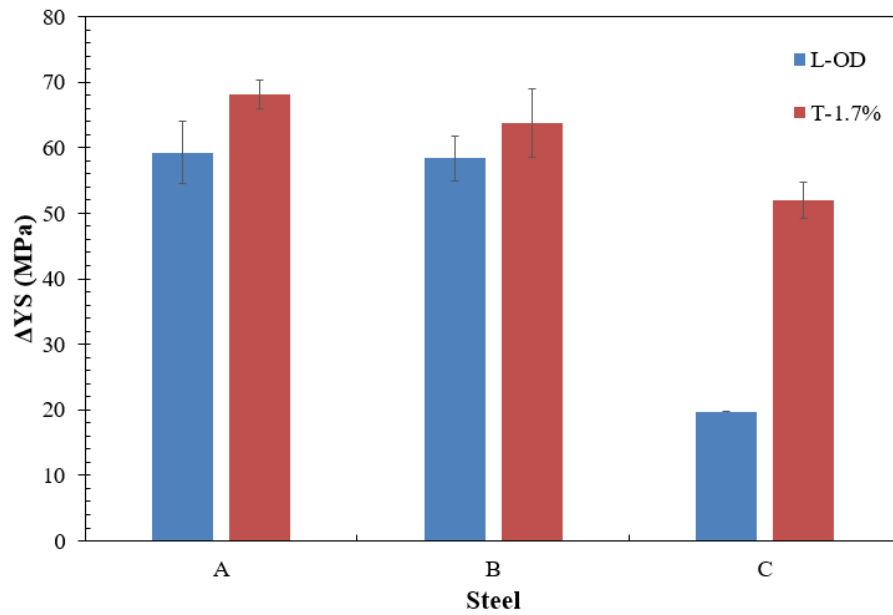


Figure 6.37 Average ΔYS for longitudinal steel samples from the OD position and transverse 1.70% pre-strained steel samples aged at 215°C.

Chapter 7 Conclusions, Recommendations and Future Work

This chapter summarizes the important findings in this work on the effect of strain aging on the mechanical properties of microalloyed pipeline steels. Recommendations and future work are suggested.

7.1 Conclusions

The effects of strain aging variables (i.e., aging temperature, aging time, position through wall thickness, imposed plastic strain and steel composition/microstructure) on the changes in the longitudinal and transverse tensile properties, micro-hardness and Charpy impact toughness of microalloyed steel (X70) UOE pipes are investigated in this research work. Three types of steel pipes from different manufacturers (named Steel A, Steel B and Steel C) are used in this work. The diameter and wall thickness of the pipes, as well as the Mn, Ti and N compositions, are similar for all three steels. The main differences between the steels are the C and Nb contents. The C/Nb ratio varies from 0.6 in A to 1.2 in B to 1.8 in C.

The statistically significant strain aging variables affecting the change in the longitudinal and transverse yield strength (ΔYS) for the test conditions examined are aging temperature, C/Nb ratio, position through wall thickness (affecting longitudinal ΔYS) and imposed plastic strain (affecting transverse ΔYS).

The statistically significant strain aging variables affecting the change in the longitudinal ultimate tensile strength (ΔUTS) are aging temperature and position through the wall thickness. C/Nb ratio is not considered as an important factor. The significant variables affecting transverse ΔUTS are temperature, imposed plastic strain and C/Nb ratio.

The statistically significant strain aging variables affecting change in the longitudinal yield to tensile strength ratio ($\Delta YS/TS$) are steel type (i.e., C/Nb ratio) and position through wall thickness. Aging temperature is not considered as an important factor. The significant variables affecting transverse $\Delta YS/TS$ are temperature, imposed plastic strain and C/Nb ratio.

A good linear correlation between ΔHV and longitudinal ΔYS affected by strain aging is found for all the steels tested. However, the level of change in ΔHV is lower than that for the changes in tensile properties.

The levels of changes in ΔYS , $\Delta YS/TS$ and ΔHV are influenced by the microstructure of the steels, where a greater increase in ΔYS is observed with decreasing grain size and to a lesser extent a decreasing volume percentage of pearlite.

The effect of through wall thickness position on the longitudinal ΔYS is attributed to both differences in microstructure (i.e., grain size and microconstituents) at different positions through wall thickness and the variation in plastic strain (i.e., dislocation density) through the thickness of the pipe associated with the steel processing and pipe forming. ΔYS , ΔUTS , $\Delta YS/TS$ and ΔHV are larger at the ID and OD positions than at the CL position.

The effect of the imposed plastic strain on the transverse tensile properties varies for different types of steels. For Steel C in this work, ΔYS increases with increasing magnitude of pre-strain. For Steel A and B, the increase in the magnitude of pre-strain gives rise to a decrease in ΔYS .

The macro pipe location (relative to the weld) affects the strain aging phenomena. The longitudinal tensile property changes (i.e., ΔYS , ΔUTS and $\Delta YS/TS$) due to aging for the 180° location were less than those at the 90° location. The microstructures at both locations are virtually the same and, thus, the difference is attributed to the difference in strain history imposed at each location during the UOE forming process.

The yielding type in the microalloyed steels is affected by aging. An increase in aging temperature contributes to the transition from continuous yielding to discontinuous yielding or a larger difference between the upper yield stress and lower yield stress. The appearance of the upper yield points is significantly affected by the microstructure of the microalloyed steels.

The effect of strain aging on Charpy impact toughness of the microalloyed steel is relatively small. The lowest toughness values for the steel were obtained for the steel aged at the highest temperature for the longest time for the test conditions.

7.2 Industrial Application

In North America, high internal operating pressure and severe environmental issues (e.g. ground movement) give rise to additional strain applied on the pipe walls. The pre-strain, along with the high temperature introduced during FBE coating application and sufficient service time period, potentially contributes to strain aging of pipeline steels [122]. In this work, the anti-corrosion coating application is simulated by using the same ranges of temperature and time. Although strain aging can strengthen the microalloyed steel pipes, it also contributes to an increase in YS/TS , a measure of the margin of safety against failure by plastic collapse. Therefore, strain aging poses a threat to the ability of a pipe to experience plastic deformation before failure.

For the test conditions, aging temperature plays a more important role than time in affecting strain aging of steel pipes. An increase in the aging temperature effectively accelerates the aging process and reduces the life of steel pipes. Thus, the effect of aging on the mechanical properties can be reduced by using a lower-temperature coating system.

Because of the difference in the mechanical property changes through the wall thickness of the pipes, the comprehensive properties of the pipes could be compromised.

Fundamentally, strain aging of steels involves the diffusion of free C and/or N atoms to mobile dislocations. Due to the considerable effect of pre-strain (affecting the dislocation density) on the transverse tensile properties of the pipes, the amount of free C and/or N is considered to be sufficient in all the three steels studied. Thus, further efforts on improving the strain aging resistance of the microalloyed (X70) steels could be focused on decreasing the dislocation density.

Grain size refinement can be achieved during the TMCP of microalloyed steels. It is found in this work that steels with smaller grains are more susceptible to strain aging. This should be considered for optimizing the parameters of TMCP.

7.3 Recommendations and Future Work

The strain aging mechanism mainly involves the diffusion of interstitial C and/or N atoms to dislocations. In this work, the interstitial C content is predicted based on steel composition and microstructural features. The variation in dislocation density is predicted based on tensile properties, such as the stress-strain curves and strain hardening exponents. Further research on quantifying the amount of free C (e.g., using atom probe tomography (APT)) and dislocation density (using TEM) in different steel samples is suggested to support the predictions in this work. In this work, the amount of N in different types of steel was relatively small and similar to each other. However, since the activation energy for diffusion of N is lower than that of C, the diffusion of N to dislocations is of interest.

The increase in UTS due to aging is believed to be caused by the formation of solute clusters and precipitates. Thus, the formation of carbides and nitrides during the aging process are of interest. TEM analysis of the size and distribution of precipitates (e.g., NbC) is suggested in future work.

In this work, the mechanical properties of aged steel samples from different through wall thickness positions (ID, CL and OD) were measured. Further study on the effect of strain aging on the mechanical properties of steel samples with full through wall thickness is recommended for industrial application.

Reference

- [1] M. D. Herynk and S. Kyriakides, "Effect of the UOE/UOC Pipe Manufacturing Processes on Pipe Collapse Pressure," *International Journal of Mechanical Sciences*, vol. 49, no. 5, pp. 533-553, 2007.
- [2] Q. Ren, T. Zou, D. Li, D. Tang and Y. Peng, "Numerical study on the X80 UOE pipe forming process," *Journal of Materials Processing Technology*, vol. 215, pp. 264-277, 2015.
- [3] T. R. Walker and R. J. Pick, "Developments in the geometric modelling of an ERW pipe skelp," *Journal of Materials Processing Technology*, vol. 25, no. 1, pp. 35-54, 1991.
- [4] J. D. Baird, "The effects of strain-ageing due to interstitial solutes on the mechanical properties of metals," *Metallurgical Reviews*, vol. 16, no. 1, pp. 1-18, 1971.
- [5] A. H. Cottrell and B. A. Bilby, "Dislocation theory of yielding and strain ageing of iron," *Proceeding of the Physical Society A*, vol. 62, no. 1, pp. 49-62, 1949.
- [6] B. A. Bilby, "On the interaction of dislocations and solute atoms," *Proceedings of the Physical Society A*, vol. 63, no. 3, pp. 191-200, 1950.
- [7] G. I. Taylor, "The mechanism of plastic deformation of crystal. Part I. Theoretical," *Proceedings of the Royal Society of London. Series A*, vol. 145, no. 855, pp. 362-387, 1934.
- [8] P. McConnell and E. B. Hawbolt, "A strain age study of acicular ferrite X-70 pipeline steels," *Journal of Materials for Energy Systems*, vol. 1, no. 2, pp. 25-31, 1979.
- [9] S. Lou and D. O. Northwood, "Effect of strain aging on the strength coefficient and strain-hardening exponent of construction-grade steels," *Journal of Materials Engineering and Performance*, vol. 3, no. 3, pp. 344-349, 1994.
- [10] L. B. Pfeil, "The change in tensile strength due to aging of cold-drawn iron and steel," *Journal of Iron and Steel Institute*, vol. 118, pp. 167-194, 1928.
- [11] E. S. Davenport and E. C. Bain, "The aging of steel," *Transactions, American Society for Metals*, vol. 23, pp. 1068-1093, 1935.
- [12] D. V. Wilson, "Grain-size dependence of discontinuous yielding in strain-aged steels," *Acta Metallurgica*, vol. 16, pp. 743-753, 1968.
- [13] A. K. De, S. Vandeputte and B. C. De Cooman, "Static strain aging behavior of ultra low carbon bake hardening steel," *Scripta Materialia*, vol. 41, pp. 831-837, 1999.
- [14] W. Zhao, M. Chen, S. Chen and J. Qu, "Static strain aging behavior of an X100 pipeline steel," *Materials Science and Engineering A*, vol. 550, pp. 418-422, 2012.

- [15] G. Liang, X. Peng, E. s. Juan and Y. F. Cheng, "Strain aging of X100 steel in service and the enhanced susceptibility of pipelines to stress corrosion cracking," *Journal of Materials Engineering and Performance*, vol. 22, no. 12, pp. 3778-3782, 2013.
- [16] P. Matthews, *Design of Experiments with Minitab*, ASQ Quality Press, 2005.
- [17] H. Abrams, G. N. Maniar, D. A. Nail and H. D. Solomon, "Optimization of processing, properties and service performance through microstructural control," in *ASTM International*, 1979.
- [18] J. G. Speer, J. R. Michael and S. S. Hansen, "Carbonitride precipitation in niobium/vanadium microalloyed steel," *Metallurgical Transaction A*, vol. 18A, pp. 211-222, 1987.
- [19] D. Q. Bai, I. A. Bettendorf, M. A. Cooke, I. A. Davenport, J. Asante, J. Dorricott and I. L. Aurora, "Process for making high strength micro-alloy steel". US Patent 6682613 B2, 2004.
- [20] K. Nishioka and K. Ichikawa, "Progress in thermomechanical control of steel plates and their commercialization," *Science and Technology of Advanced Materials*, vol. 13, no. 2, pp. 1-21, 2012.
- [21] T. Hirose, K. Shiba, T. Sawai, S. Jitsukawa and M. Akiba, "Effects of heat treatment process for blanket fabrication on mechanical properties of F82H," *Journal of Nuclear Materials*, vol. 329, pp. 324-327, 2004.
- [22] D. Liu, Q. Li and T. Emi, "Microstructure and mechanical properties in hot-rolled extra high-yield-strength steel plates for offshore structure and shipbuilding," *Metallurgical and Materials Transactions A*, vol. 42, no. 5, pp. 1349-1361, 2011.
- [23] M. Zhao, K. Yang and Y. Shan, "The effects of thermo-mechanical control process on microstructures and mechanical properties of a commercial pipeline steel," *Materials Science and Engineering A*, vol. 335, no. 1, pp. 14-20, 2002.
- [24] C. Ouchi, "Advances in physical metallurgy and processing of steels. Design of ferritic creep-resistant steels.," *ISIJ International*, vol. 335, no. 1, pp. 14-20, 2001.
- [25] W. Tan, B. Han, S. Wang, Y. Yang, C. Zhang and Zhang Y, "Effect of TMCP parameters on microstructure and mechanical properties of hot rolled economical dual phase steel in CSP," *Journal of Iron and Steel Research International*, vol. 19, no. 6, pp. 37-41, 2012.
- [26] H. Tamehiro, N. Yamada and H. Matsuda, "Effect of the thermo-mechanical control process on the properties of high-strength low alloy steel," *Transactions of the Iron and Steel Institute of Japan*, vol. 25, no. 1, pp. 54-61, 1985.
- [27] S. Shanmugam, N. K. Ramiseti, R. D. Misra, T. Mannering, D. Panda and S. Janstro, "Effect of cooling rate on the microstructure and mechanical properties of Nb-microalloyed steels," *Materials Science and Engineering A*, vol. 460, pp. 335-343, 2007.

- [28] M. Katsumi and N. Yutaka, "Manufacturing processes and products of steel pipes and tubes in JFE steel," JFE Technical Report 7, 2006.
- [29] L. B. Godefroid, L. C. Candido, R. V. B. Toffolo and L. H. S. Barbosa, "Microstructure and mechanical properties of two API steels for iron ore pipelines," *Materials Research*, vol. 17, pp. 114-120, 2014.
- [30] A. P. Institute, in *API 5L: Specification for Line Pipe, 44th Edition*, American Petroleum Institute, 2008.
- [31] R. Ren, T. Zou, D. Li, D. Tang and Y. Peng, "Numerical study on the X80 UOE pipe forming process," *Journal of Materials Processing Technology*, vol. 215, pp. 264-277, 2015.
- [32] M. D. Herynk, S. Kyriakides, A. Onoufriou and H. D. Yun, "Effects of the UOE/UOC pipe manufacturing processes on pipe collapse pressure," *International Journal of Mechanical Sciences*, vol. 49, pp. 533-553, 2007.
- [33] "Fusion Bonded Epoxy Powder Coating," Shaw Pipe, 2016. [Online]. Available: <http://www.shawpipe.ca/spp/solutions/fbe.html>.
- [34] R. Noecker, N. Nissley, N. Ma, N. Thirumalai, P. Wojtulewicz and M. Hukle, "Strain aging of C-Mn line pipe steels: an analytical approach to compare strain aging heat treatments," in *ASME 2011 30th International Conference on Ocean, Offshore and Arctic Engineering*. American Society of Mechanical Engineers, 2011.
- [35] W. D. Callister and D. G. Rethwisch, *Materials Science and Engineering: An Introduction*, New York: Wiley, 2009.
- [36] B. Ma, J. Shuai, D. Liu and K. Xu, "Assessment on failure pressure of high strength pipeline with corrosion defects," *Engineering Failure Analysis*, vol. 32, pp. 209-219, 2013.
- [37] K. G. Budinski and M. K. Budinski, *Engineering Materials Properties and Selection*, Prentice Hall, 1999.
- [38] "Vickers Test," Instron, 2016. [Online]. Available: <http://www.instron.us/en-us/our-company/library/test-types/hardness-test/vickers-test>.
- [39] "Design of the Week: DIY Material Testing Machine," Fabbaloo, 16 June 2014. [Online]. Available: <http://www.fabbaloo.com/blog/2014/6/15/design-of-the-week-diy-material-testing-machine>.
- [40] Y. N. Osetsky and D. J. Bacon, "Void and precipitate strengthening in a-iron: what can we learn from atomic-level modelling?," *Journal of Nuclear Materials*, vol. 323, pp. 268-280, 2003.
- [41] D. McLean, *Mechanical Properties of Metals*, New York-London: John Wiley & Sons, Inc..
- [42] F. Yoshida, Y. Kaneda and S. Yamamoto, "A plasticity model describing yielding-point phenomena of steels and its application to FE simulation of temper rolling," *International Journal of Plasticity*, vol. 24, pp. 1792-1818, 2008.

- [43] E. O. Hall, *Yield Point Phenomena in Metals and Alloys*, Plenum Press, 1970.
- [44] G. Krauss, "Martensite in steel: strength and structure," *Materials Science and Engineer A*, vol. 273, pp. 40-57, 1999.
- [45] W. Mason, "The Luders' lines on mild steel," *Proceedings of the Physical Society of London*, vol. 23, no. 1, pp. 305-333, 1910.
- [46] A. W. McReynolds, "Plastic deformation waves in aluminum," *Transactions of the American Institute of Mining and Metallurgical Engineers*, vol. 185, no. 1, pp. 32-45, 1949.
- [47] A. H. Cottrell, "Report on the strength of solids," in *Proceedings of Physical Society of London*, 1948.
- [48] J. L. Snoek, "Effect of small quantities of carbon and nitrogen on the elastic and plastic properties of iron," *Physica*, vol. 8, pp. 711-733, 1941.
- [49] W. S. Gorsky, "Theory of elastic after effect in unordered mixed crystals (elastic after effect of the second kind)," *Zeit. Phys. Soviet. U*, vol. 8, pp. 457-471, 1935.
- [50] G. I. Taylor, "The mechanism of plastic deformation of crystals. Part I. Theoretical," *Proceedings of the Royal Society of London A*, vol. 145, no. 855, pp. 362-387, 1934.
- [51] B. A. Bilby, "On the interaction of dislocations and solute atoms," *Proceedings of the Physical Society A*, vol. 63, no. 3, pp. 191-200, 1950.
- [52] E. O. Hall, "The deformation and ageing of mild steel: III discussion of results," *Proceedings of the Physical Society B*, vol. 64, no. 9, pp. 747-753, 1951.
- [53] A. W. Cocharde, G. Schoek and H. Wiedersich, "Interaction between dislocations and interstitial atoms in body-centered cubic metals," *Acta Metallurgica*, vol. 3, pp. 533-537, 1955.
- [54] T. Vreeland and D. S. Wood, "A comparison between dislocation theory and experimental measurements of delayed yield in steel," Technical Report, California Institute of Technology, Pasadena, 1954.
- [55] F. R. Nabarro, "Report on Strength of Solids," *Proceeding of the Physical Society of London*, pp. 38-40, 1948.
- [56] J. L. Snoek, "Tetragonal martensite and elastic after effect in iron," *Physica*, vol. 9, pp. 862-864, 1942.
- [57] A. B. Greninger and A. R. Alexander, "The mechanism of martensite formation," *Transactions of American Institute of Mining and Metallurgical Engineers*, vol. 185, no. 9, pp. 590-598, 1949.
- [58] N. F. Mott, *Imperfections in Nearly Perfect Crystals* (W. Shockley et al. eds.), New York: John Wiley & Sons, 1952.
- [59] B. B. Hundy, "The strain-age hardening of mild steel," *Metallurgica*, vol. 53, pp. 203-211, 1956.

- [60] D. V. Wilson and B. Russell, "Stress induced ordering and strain-ageing in low carbon steels," *Acta Metallurgica*, vol. 7, pp. 628-631, 1959.
- [61] D. V. Wilson and B. Russell, "The contribution of atmosphere locking to the strain-ageing of low carbon steels," *Acta Metallurgica*, vol. 8, pp. 36-45, 1960.
- [62] D. V. Wilson and B. Russell, "The contribution of precipitation to strain ageing in low carbon steels," *Acta Metallurgica*, vol. 8, pp. 468-479, 1960.
- [63] H. Conrad and G. Schoech, "Cottrell locking and the flow stress in iron," *Acta Metallurgica*, vol. 8, pp. 791-796, 1960.
- [64] N. J. Petch, "The fracture of metals," *Progress in Metal Physic*, vol. 5, pp. 1-52, 1954.
- [65] A. H. Cottrell, "Theory of brittle fracture in steel and similar metals," *Transactions of the American Institute of Mining and Metallurgical Engineers*, vol. 212, pp. 192-203, 1958.
- [66] D. V. Wilson, "Role of grain boundary in the discontinuous yielding of low-carbon steels," *Metal Science Journal*, vol. 1, pp. 40-47, 1967.
- [67] D. V. Wilson, "Grain-size dependence of discontinuous yielding in strain-aged steels," *Acta Metallurgica*, vol. 16, pp. 743-753, 1968.
- [68] H. S. Park, J. S. Kang, J. Y. Yoo and C. G. Park, "In-situ TEM and APT analysis on the dislocations associated with solute carbons in strain-aged low carbon pipeline steels," *Materials Science Forum*, vol. 654, pp. 122-125, 2010.
- [69] J. Z. Zhao, A. K. De and B. C. De Cooman, "Kinetics of Cottrell atmosphere formation during strain aging of ultra-low carbon steels," *Materials Letter*, vol. 44, no. 6, pp. 374-378, 2000.
- [70] M. S. Rashid, "Strain-aging of vanadium, niobium or titanium-strengthened high-strength low-alloy steels," *Metallurgical Transactions A*, vol. 6A, pp. 1265-1268, 1975.
- [71] M. S. Rashid, "Strain aging kinetics of vanadium or titanium strengthened high-strength low-alloy steel," *Metallurgica Transactions A*, vol. 7A, pp. 497-503, 1976.
- [72] P. McConnell and E. B. Hawbolt, "A strain age study of acicular ferrite X-70 pipeline steels," *Journal of Materials for Energy Systems*, vol. 1, pp. 25-31, 1979.
- [73] D. V. Wilson and Y. A. Konnan, "Work hardening in a steel containing a coarse dispersion of cementite particles," *Acta Metallurgica*, vol. 12, pp. 617-628, 1964.
- [74] A. B. Arabei, V. M. Farber, I. Y. Pyshmintsev, V. A. Khotimov, O. V. Selivanova, N. V. Lezhnin and M. A. Valov, "Influence of strain aging on the ductility of 05 [Gamma] 2 [Phi] δ steel in controlled rolling and accelerated cooling," *Steel in Translation*, vol. 42, pp. 776-780, 2012.
- [75] J. Y. Yoo, D. H. Seo, S. S. Ahn and K. B. Kang, "Development of X80/X100 linepipe steels with high strain aging resistance," *The Eighteenth International Offshore and Polar Engineering Conference, International Society of Offshore and Polar Engineers*, pp. 21-26, 2008.

- [76] C. Timms, D. DeGeer and M. McLamb, "Effect of a thermal coating process on X100 UOE line pipe," *ASME 2005 24th International Conference on Offshore Mechanics and Arctic Engineering, American Society of Mechanical Engineers*, pp. 557-561, 2005.
- [77] Q. Chi, L. Ji, P. Wang, Y. Li and L. Qi, "Effect of cold bending process and strain-age on properties of X80 linepipe," *International Conference on Pipelines and Trenchless Technology*, pp. 1317-1327, 2012.
- [78] A. K. De, S. Vandeputte and B. C. De Cooman, "Static strain aging behavior of ultra low carbon bake hardening steel," *Scripta Materialia*, vol. 41, pp. 831-837, 1999.
- [79] A. K. De, S. Vandeputte and B. C. De Cooman, "Effect of dislocation density on the low temperature aging behavior of an ultra low carbon bake hardening steel," *Journal of Alloys and Compounds*, vol. 310, pp. 405-410, 2000.
- [80] S. Hartley, "Strain-ageing in tantalum," *Acta Metallurgica*, vol. 14, pp. 1237-1246, 1966.
- [81] C. Wert and C. Zener, "Interstitial atomic diffusion coefficients," *Physical Review*, vol. 76, pp. 1170-1175, 1949.
- [82] J. R. Hammerle, L. H. de Almeida and S. N. Monteiro, "Lower temperatures mechanism of strain aging in carbon steels for drawn wires," *Scripta Materialia*, vol. 50, pp. 1289-1292, 2004.
- [83] S. Gunduz, "The effect of the pre-straining and aging on tensile behavior of microalloyed steels," *Journal of Engineering Science*, vol. 11, no. 1, pp. 147-152, 2005.
- [84] I. E. Dolzhenkov, "The nature of blue brittleness of steel," *Metal Science and Heat Treatment*, vol. 13, no. 3, pp. 220-224, 1971.
- [85] T. O. Souza and V. T. L. Buono, "Optimization of the strain aging resistance in aluminum killed steels produced by continuous annealing," *Materials Science and Engineering A*, vol. 354, pp. 212-216, 2003.
- [86] S. N. Ghali, H. S. El-Faramawy and M. M. Eissa, "Influence of boron additions on mechanical properties of carbon steel," *Journal of Minerals and Materials Characterization and Engineering*, vol. 11, pp. 995-999, 2012.
- [87] H. Duzcukoglu and S. Cetinterk, "Effect of boron addition on mechanical properties of 60SiCr7 Steel," *International Journal of Materials, Mechanical and Manufacturing*, vol. 3, pp. 117-120, 2015.
- [88] J. F. B. Pereira, *Kinetics of static strain aging in a low carbon steel with small additions of P, Si and Mn*, Belo Horizonte, MG: M.Sc. Thesis, Federal University of Minas Gerais, 1986, p. 131.
- [89] C. P. Stroble, "Precipitate morphology in MnS-AlN-inhibited high permeability grain oriented silicon steel," *IEEE Transactions on Magnetics*, vol. 12, pp. 861-863, 1976.

- [90] A. J. P. Gater, G. Fourlaris, S. G. R. Brown and L. J. Baker, "Strain aging of titanium-vanadium ultralow carbon strip steels," *Iron & Steelmaking*, vol. 39, no. 3, pp. 216-221, 2012.
- [91] E. V. Pereloma, V. Bata, R. I. Scott and R. M. Smith, "Effect of Cr and Mo on strain ageing behaviour of low carbon steel," *Materials Science and Engineering A*, vol. 527, pp. 2538-2546, 2010.
- [92] I. S. Golovin, M. S. Blanter and L. B. Magalas, "Diffusion and Defect Data. Part A: Defect and, Diffusion Forum," Trans Tech Publications, 2001, pp. 73-78.
- [93] W. Zhang, Y. Li, Q. Xiong and L. Ji, "Effect of prestrain and aging on mechanical properties of X100 pipeline steels," in *ICPTT 2013 Trenchless Technology*, ASCE, 2013.
- [94] B. Koohbor, D. Ohadi, S. Serajzadeh and J. M. Akhgar, "Effect of rolling speed on the occurrence of strain aging during and after warm rolling of a low-carbon steel," *Journal of Materials Science*, vol. 45, pp. 3405-3412, 2010.
- [95] D. Yang, R. Kulkarni, R. J. Behme and P. N. Kotiyan, "Effect of the melt granulation technique on the dissolution characteristics of griseofulvin," *International Journal of Pharmaceutics*, vol. 329, pp. 72-80, 2007.
- [96] G. E. P. Box and K. B. Wilson, "On the experimental attainment of optimum conditions," *Journal of the Royal Statistical Society B (Methodological)*, vol. 13, no. 1, pp. 1-45, 1951.
- [97] Y. Cheng, *The response surface methodology*, M.Sc. Thesis, Indiana University South Bend, 2009.
- [98] G. E. P. Box and D. W. Behnken, "Some new three level designs for the study of quantitative variables," *Technometrics*, vol. 2, no. 4, pp. 455-475, 1960.
- [99] G. E. P. Box and D. W. Behnken, "Simplex-sum designs: a class of second order rotatable designs derivable from those of first order," *The Annals of Mathematical Statistics*, vol. 31, no. 4, pp. 838-864, 1960.
- [100] *ASTM E8/E8M-13a, Standard Test Method for Tensile Testing Metallic Materials*, 2013.
- [101] *ASTM E23-05, Standard Test Methods for Notched Bar Impact Testing of Metallic Materials*, 2005.
- [102] J. S. Robinson, R. L. Cudd, D. A. Tanner and G. P. Dolan, "Quench sensitivity and tensile property inhomogeneity in 7010 forgings," *Journal of Materials Processing Technology*, vol. 119, pp. 261-267, 2001.
- [103] *ASTM E112-13, Standard Test Methods for Determining Average Grain Size*, 2014.
- [104] *ASTM E562-11, Standard Test Method for Determining Volume Fraction by Systematic Manual Point Count*, 2011.
- [105] W. L. Bragg, "The diffraction of short electromagnetic waves by a crystal," *Proceedings of the Cambridge Philosophical Society*, vol. 17, no. 43, p. 4, 1913.

- [106] S. Zaefferer, "On the formation mechanisms, spatial resolution and intensity of backscatter Kikuchi patterns," *Ultramicroscopy*, vol. 107, no. 2, pp. 254-266, 2007.
- [107] G. Nolze, "Characterization of the fcc/bcc orientation relationship by EBSD using pole figures and variants," *Zeitschrift für Metallkunde*, vol. 95, no. 9, pp. 744-755, 2004.
- [108] "Pattern formation," Oxford Instruments, 2016. [Online]. Available: <http://www.ebsd.com/ebsd-explained/basics-of-ebsd/pattern-formation>.
- [109] "Automated indexing and orientation measurement," Oxford Instruments, 2015. [Online]. Available: <http://www.ebsd.com/ebsd-explained/basics-of-ebsd/automated-indexing-and-orientation-measurement>.
- [110] F. J. Humphreys, "Grain and subgrain characterisation by electron backscatter diffraction," *Journal of Materials Science*, vol. 36, pp. 3833-3854, 2001.
- [111] X. Li, *Quantitative Characterization of Microstructure in High Strength*, Edmonton, Alberta: University of Alberta, 2009.
- [112] A. G. Kostyrychev, *Bauschinger effect in Nb and V microalloyed line pipe steels*, Birmingham: University of Birmingham, 2009.
- [113] M. Koyama, T. Sawaguchi and K. Tsuzaki, "Influence of dislocation separation on dynamic strain aging in a Fe-Mn-C austenitic steel," *Materials Transactions*, vol. 53, no. 3, pp. 546-552, 2012.
- [114] S. Kalpakjian and S. Schmid, *Manufacturing Processes for Engineering Materials (5th Edition)*, Pearson Education, 2008.
- [115] M. B. U. Messerschmidt, "Generation of dislocations during plastic deformation," *Materials Chemistry and Physics*, pp. 518-523, 2003.
- [116] B. Hutchinson and N. Ridley, "On dislocation accumulation and work hardening in Hadfield steel," *Scripta Materialia*, vol. 55, pp. 299-302, 2006.
- [117] L. Jin, W. Li and Y. Zhang, "Effects of solution carbon content and prestrain on strain aging behavior of ULC-BH steels," *Materials for Mechanical Engineering*, vol. 36, no. 12, pp. 37-44, December 2012.
- [118] T. Gladman, E. D. McIvor and F. B. Pickering, "Some Aspects of the Structure-Property Relationships in High-C Ferrite-Pearlite Steels," *Journal of the Iron and Steel Institute*, vol. 210, pp. 916-930, 1972.
- [119] F. B. Pickering and B. Garbarz, "Strengthening in pearlite formed from thermomechanically processed austenite in vanadium steels and implications for toughness," *Materials Science and Technology*, vol. 5, no. 3, pp. 227-237, 1989.
- [120] H. Conrad, S. Feuerstein and L. Rice, "Effects of grain size on the dislocation density and flow stress of niobium," *Materials Science and Engineering*, vol. 2, no. 3, pp. 157-168, 1967.
- [121] T. Narutani and J. Takamura, "Grain-size strengthening in terms of dislocation density measured by resistivity," *Acta Metallurgica et Materialia*, vol. 39, no. 8, pp. 2037-2049, 1991.

[122] F. Y. Cheng, "Strain Ageing of High-Strength Steels in the Northern Area and the Associated Technical Challenges in Development of High-Strength Steel Pipeline Technologies," in *Proceedings of the Twenty-third International Offshore and Polar Engineering*, Anchorage, Alaska, USA, 2013.

Appendix A Mechanical Property Results

The tensile property, micro-hardness and CVN impact toughness values of as-received and aged steel samples are included in this appendix.

Appendix A.1 Tensile Properties

The values of YS, UTS and YS/TS for as-received Steel A, B and C samples, in the longitudinal orientation at each through wall thickness position and each location relative to the weld, are summarized in Table A-1.

Table A-1 Summary of As-received Tensile Test Results

Steel	Position	Location (°)	YS (MPa)	UTS (MPa)	YS/TS
A	ID	90	528.7	601.6	0.879
A	CL	90	517.9	619.8	0.835
A	OD	90	525.5	601.3	0.874
A	ID	180	525.9	609.9	0.862
A	CL	180	529.7	619.3	0.855
A	OD	180	551.7	621.4	0.888
B	ID	90	488.5	598.3	0.816
B	CL	90	497.3	620.8	0.801
B	OD	90	499.0	596.9	0.836
B	ID	180	513.8	610.2	0.842
B	CL	180	500.8	622.7	0.804
B	OD	180	514.4	619.0	0.831
C	ID	90	587.4	656.8	0.894
C	CL	90	513.5	619.1	0.829
C	OD	90	579.2	646.2	0.896
C	ID	180	573.9	654.9	0.876
C	CL	180	510.5	617.5	0.827
C	OD	180	563.8	648.4	0.870

The values of YS, UTS and YS/TS for aged Steel A, B and C samples, in the longitudinal orientation at each through wall thickness position and each location relative to the weld, are summarized in Table A-2.

Table A-2 Summary of Aged Tensile Test Results

Steel	Position	Location (°)	Aging Condition	YS (MPa)	UTS (MPa)	YS/TS
A	ID	90	215°C&5min	575.4	623.1	0.923
A	ID	90	255°C&5min	600.5	642.4	0.935
A	ID	90	255°C&25min	602.5	641.3	0.94
A	ID	180	215°C&5min	557.9	625.3	0.892
A	ID	180	255°C&5min	588.5	635	0.927
A	ID	180	255°C&25min	592.6	636.3	0.931
A	CL	90	215°C&5min	548	624	0.878
A	CL	90	255°C&5min	559.6	630.9	0.887
A	CL	90	255°C&25min	565.3	633.2	0.893
A	CL	180	215°C&5min	551.2	630.5	0.874
A	CL	180	255°C&5min	564.7	633.1	0.892
A	CL	180	255°C&25min	582.7	644.1	0.905
A	OD	90	215°C&5min	567.9	613.8	0.925
A	OD	90	255°C&5min	600.6	641	0.937
A	OD	90	255°C&25min	601.8	632.2	0.952
A	OD	180	215°C&5min	577.2	630.8	0.915
A	OD	180	255°C&5min	610.6	654.4	0.933
A	OD	180	255°C&25min	613	651.5	0.941
B	ID	90	215°C&5min	562	632.7	0.888
B	ID	90	255°C&5min	584.7	639.7	0.914
B	ID	90	255°C&25min	591.3	628.1	0.941
B	ID	180	215°C&5min	539.1	610.2	0.883
B	ID	180	255°C&5min	547.4	622.7	0.879
B	ID	180	255°C&25min	583.5	633.5	0.921
B	CL	90	215°C&5min	534.8	631.5	0.847
B	CL	90	255°C&5min	539.6	629.2	0.858
B	CL	90	255°C&25min	540.6	630.9	0.854
B	CL	180	215°C&5min	517.3	617.8	0.837
B	CL	180	255°C&5min	528.4	625.2	0.845
B	CL	180	255°C&25min	566.5	646.3	0.876
B	OD	90	215°C&5min	544.5	606.4	0.898
B	OD	90	255°C&5min	564.2	625.9	0.901
B	OD	90	255°C&25min	571.4	650.5	0.879
B	OD	180	215°C&5min	544.5	617.9	0.881
B	OD	180	255°C&5min	548.7	613.6	0.894
B	OD	180	255°C&25min	599.1	637.5	0.94
C	ID	90	215°C&5min	622.6	671.9	0.926
C	ID	90	255°C&5min	623.3	672.1	0.927
C	ID	90	255°C&25min	629.2	670.9	0.938

Continued

Table A-2 Summary of Aged Tensile Test Results (Continued)

C	ID	180	215°C&5min	603.6	662.1	0.912
C	ID	180	255°C&5min	620.4	671.4	0.924
C	ID	180	255°C&25min	628.3	672.6	0.934
C	CL	90	215°C&5min	517.2	621	0.833
C	CL	90	255°C&5min	516.2	623.1	0.828
C	CL	90	255°C&25min	520.2	624.5	0.833
C	CL	180	215°C&5min	514.7	618	0.833
C	CL	180	255°C&5min	516.7	619.5	0.834
C	CL	180	255°C&25min	519.9	624.9	0.832
C	OD	90	215°C&5min	592.6	655.7	0.904
C	OD	90	255°C&5min	603.2	657.9	0.917
C	OD	90	255°C&25min	607.2	656.3	0.925
C	OD	180	215°C&5min	584.4	653.2	0.895
C	OD	180	255°C&5min	584.6	648.6	0.901
C	OD	180	255°C&25min	594.4	649.6	0.915

To qualitatively study the effect of strain aging on the longitudinal tensile properties of steel samples from different positions through the wall thickness and with respect to the location relative to the weld, each sample of a certain steel and from a certain position was heat treated at three different conditions: 1) at 215°C for 5 minutes; 2) at 255°C for 5 minutes and 3) at 255°C for 25 minutes. The YS values of steel samples located 90° relative to the weld aged at different conditions are illustrated in Figure 0.1, Figure 0.2 and Figure 0.3. The YS increases with increasing aging temperature and time for the test conditions. The increase in YS due to aging is higher for the steel samples (especially Steel C) from the ID and OD positions than those from the CL position. This is also observed for the samples located 180° to the weld (Figure 0.4, Figure 0.5 and Figure 0.6). Table A-2 shows the YS, UTS and YS/TS for the aged steels at both the 90° and 180° locations. Both UTS and YS/TS for each type of steel also tend to increase with either increasing aging temperature or increasing time.

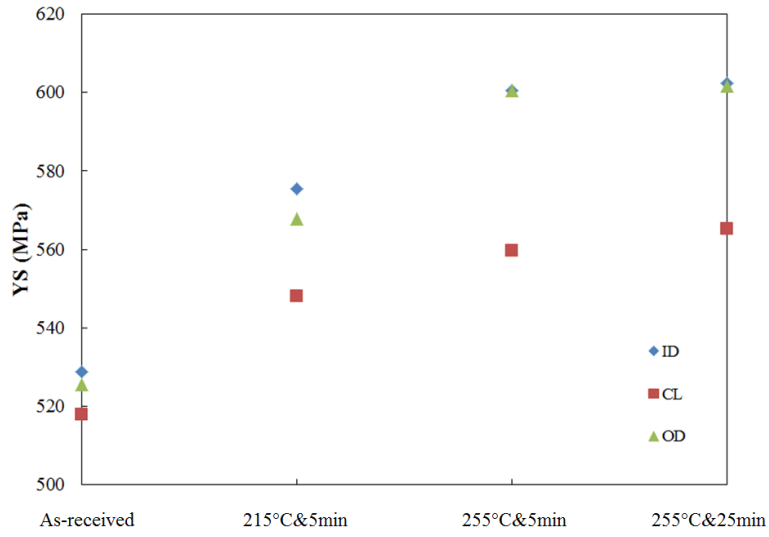


Figure 0.1 YS vs. aging conditions for Steel A1.

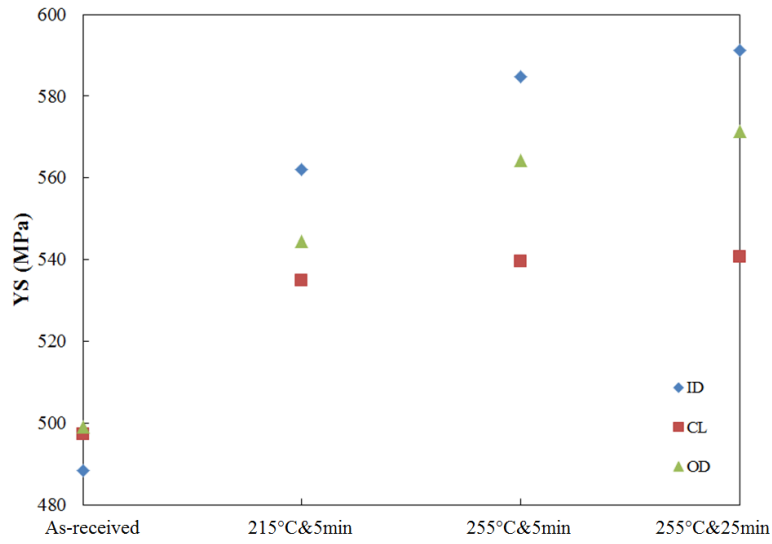


Figure 0.2 YS vs. aging conditions for Steel B1.

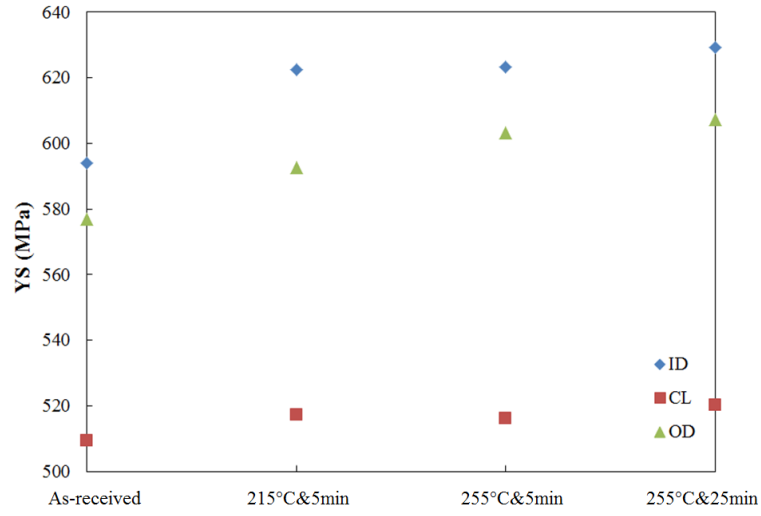


Figure 0.3 YS vs. aging conditions for Steel C1.

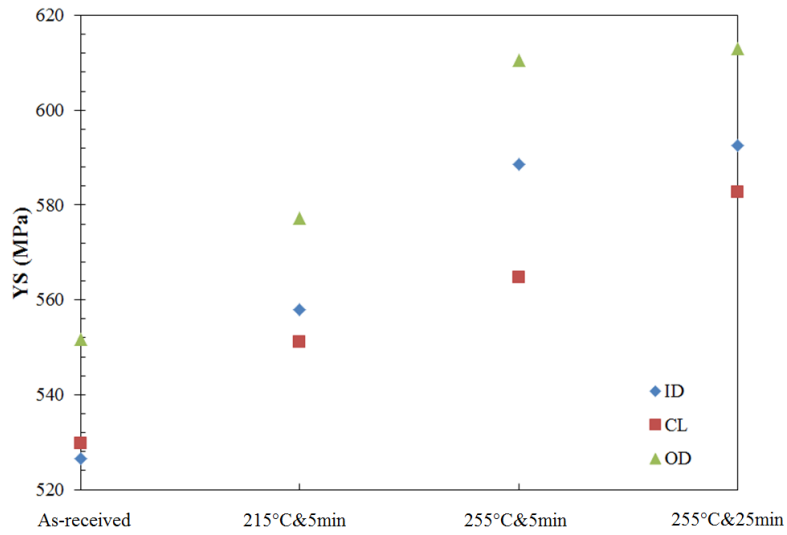


Figure 0.4 YS vs. aging conditions for Steel A2.

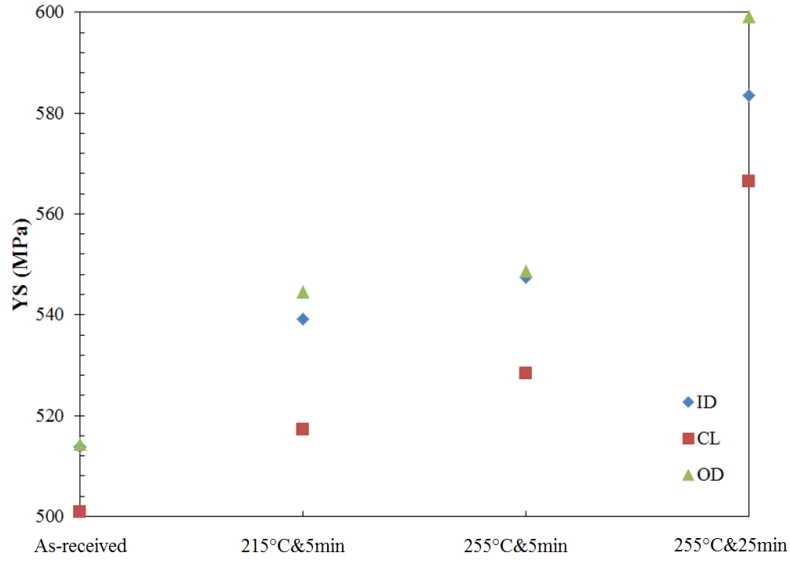


Figure 0.5 YS vs. aging conditions for Steel B2.

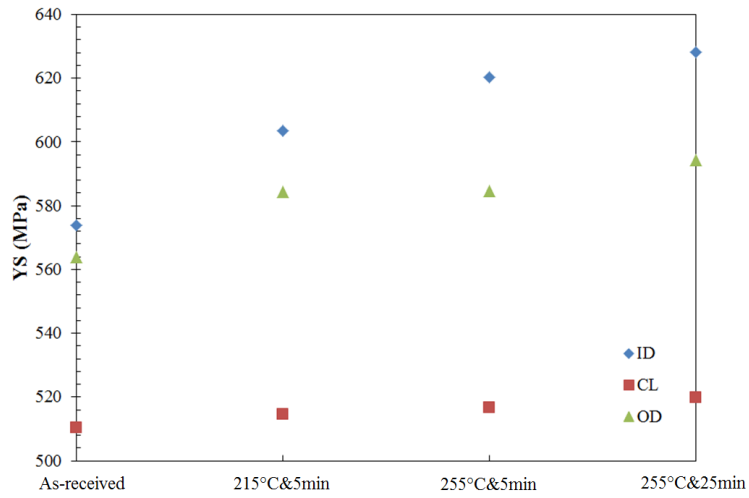


Figure 0.6 YS vs. aging conditions for Steel C2.

The strain hardening exponent (noted as n), which is a material constant used in calculations for stress-strain behavior associated with work hardening, was measured using the formula

$$\sigma_T = K \cdot \varepsilon_T^n \quad (A1)$$

where σ_T is the true stress acting on the steel, ε_T is the true strain acting on the steel and K is the strength coefficient. On a logarithmic scale, the exponential function was mapped onto a linear relationship

$$\lg \sigma_T = \lg K + n \lg \varepsilon_T \quad (A2)$$

where the slope is equal to the strain hardening exponent (n) and the intercept corresponding to a true strain value of 1 is the strength coefficient (K). The measurement of the strain hardening exponent for as-received Steel A from the CL position located 90° relative to the weld is shown in Figure 0.7 $\lg\sigma_T$ vs. $\lg\epsilon_T$ for longitudinal as-received Steel A1 (as-received, CL position), where n is equal to 0.1045. Since all the data fit very well with the regressive line and the R^2 value (0.9993) is very close to 1, the n value estimated in this method is believed to be accurate. The n values for other steels are measured using the same method. The measured n values of as-received Steel A, B and C at 180° locations are shown in Figure 0.8. Like the steels at 90° location, the n values at the CL tend to be larger than those at the ID and OD positions for all the steels.

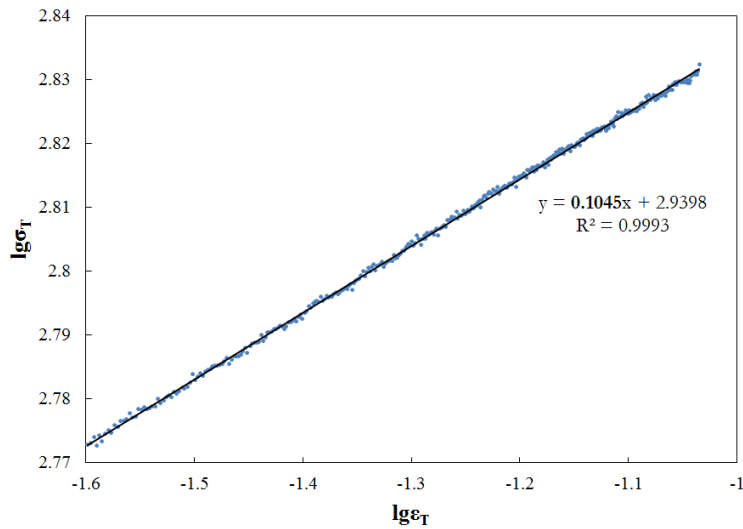


Figure 0.7 $\lg\sigma_T$ vs. $\lg\epsilon_T$ for longitudinal as-received Steel A1 (as-received, CL position).

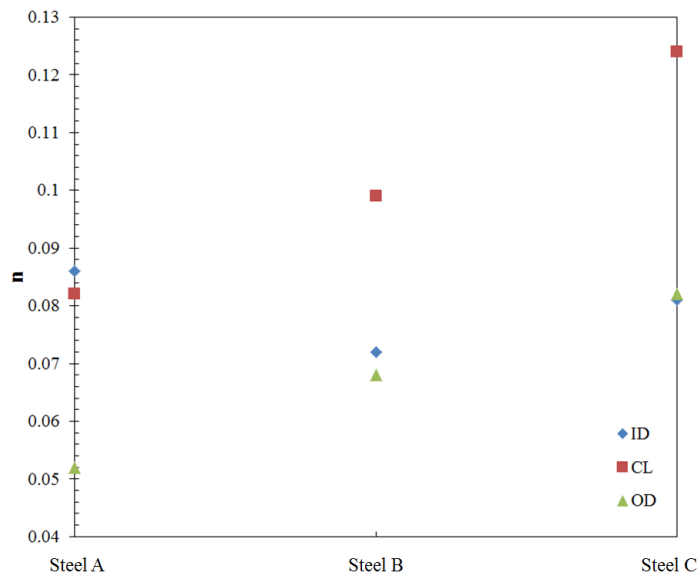


Figure 0.8 Strain hardening exponents for Steel A2, B2 and C2, in the longitudinal orientation, at the ID, CL and OD positions.

The YS, UTS and YS/TS values for as-received and pre-strained Steel A, B and C samples are summarized in Table A-3.

Table A-3 As-received and Pre-strained Tensile Properties

Steel	Pre-strain (%)	YS (MPa)	UTS (MPa)	YS/TS
A	0	567.6	656.6	0.86
A	1.7	611.0	669.1	0.91
A	3.4	651.7	681.4	0.96
B	0	521.4	638.1	0.82
B	1.7	591.1	653.0	0.91
B	3.4	630.0	674.9	0.93
C	0	574.6	665.3	0.86
C	1.7	605.2	673.6	0.90
C	3.4	651.3	685.9	0.95

Appendix A.2 Micro-hardness

The average micro-hardness values of as-received and aged Steel A, B and C samples are summarized in Table A-4, Table A-5 and Table A-6 below. The Vickers hardness testing was conducted on the longitudinal surfaces (Figure 3.9a) of the samples.

Table A-4 Micro-hardness of As-received and Aged Steel A

Sample Position	ID		CL		OD	
	HV	StDev	HV	StDev	HV	StDev
As-received	206.6	2.3	202.6	2.5	202	2.3
215°C&5min	210.3	2.3	206.1	3.2	208.8	2.5
255°C&5min	217.8	3.7	209.6	3.1	213.7	3.1
255°C&25min	218.5	3.3	210.9	2.2	215.4	3.4

Table A-5 Micro-hardness of As-received and Aged Steel B

Aging treatment	ID		CL		OD	
	HV	StDev	HV	StDev	HV	StDev
As-received	195.1	3.4	195.0	3.7	194.7	3.5
215°C&5min	209.1	3.4	203.0	3.4	206.2	3.3
255°C&5min	212.7	3.7	204.6	3.5	208.3	3.1
255°C&25min	214.0	3.4	205.2	3.1	209.9	3.5

Table A-6 Micro-hardness of As-received and Aged Steel C

Aging treatment	ID		CL		OD	
	HV	StDev	HV	StDev	HV	StDev
As-received	217.5	2.3	198.0	3.5	214.5	3.1
215°C&5min	225.9	3.5	199.9	3.3	217.9	2.9
255°C&5min	227.4	3.4	200.3	3.6	222.2	3.4
255°C&25min	227.6	3.4	200.3	2.9	222.4	2.9

Appendix A.3 CVN Impact Toughness

The measured Charpy impact toughness (i.e., absorbed energy) for as-received and aged Steel A samples from both the ID and OD positions are summarized in Table A-7 and Table A-8.

Table A-7 Absorbed Energy for Steel A Charpy Samples from the ID Position

Absorbed energy (J)	Test temperature (°C)									
	-60		-40		-20		0		20	
	Average	StDev	Average	StDev	Average	StDev	Average	StDev	Average	StDev
As-received	123.3	1.5	128.3	5.0	136.0	7.2	139.0	14.7	140.0	1.4
215°C&5min	125.3	3.2	128.7	7.4	140.3	10.6	143.7	5.7	144.0	4.2
255°C&5min	123.3	9.3	130.7	10.8	137.0	8.0	137.7	11.2	139.0	5.7
255°C&25min	115.7	11.0	125.0	9.6	131.3	12.1	136.0	8.9	135.0	4.2

Table A-8 Absorbed Energy for Steel A Charpy Samples from the OD Position

Absorbed energy (J)	Test temperature (°C)									
	-60		-40		-20		0		20	
	Average	StDev	Average	StDev	Average	StDev	Average	StDev	Average	StDev
As-received	116.7	4.2	123.3	1.5	130.0	6.0	133.0	1.7	132.0	5.7
215°C&5min	125.3	3.2	127.3	7.4	131.0	5.0	133.7	12.2	135.5	14.8
255°C&5min	119.0	4.6	129.7	11.9	135.3	7.4	139.0	6.0	136.5	12.0
255°C&25min	105.7	16.4	122.0	10.0	127.0	10.1	129.0	9.8	127.5	3.5

Appendix B Microstructure Analysis

Compared with Figure 5.1, Figure 0.9 shows that the grains become elongated when observed from the transverse surface (perpendicular to the rolling direction). Elongation is caused by the rolling process during TMCP.

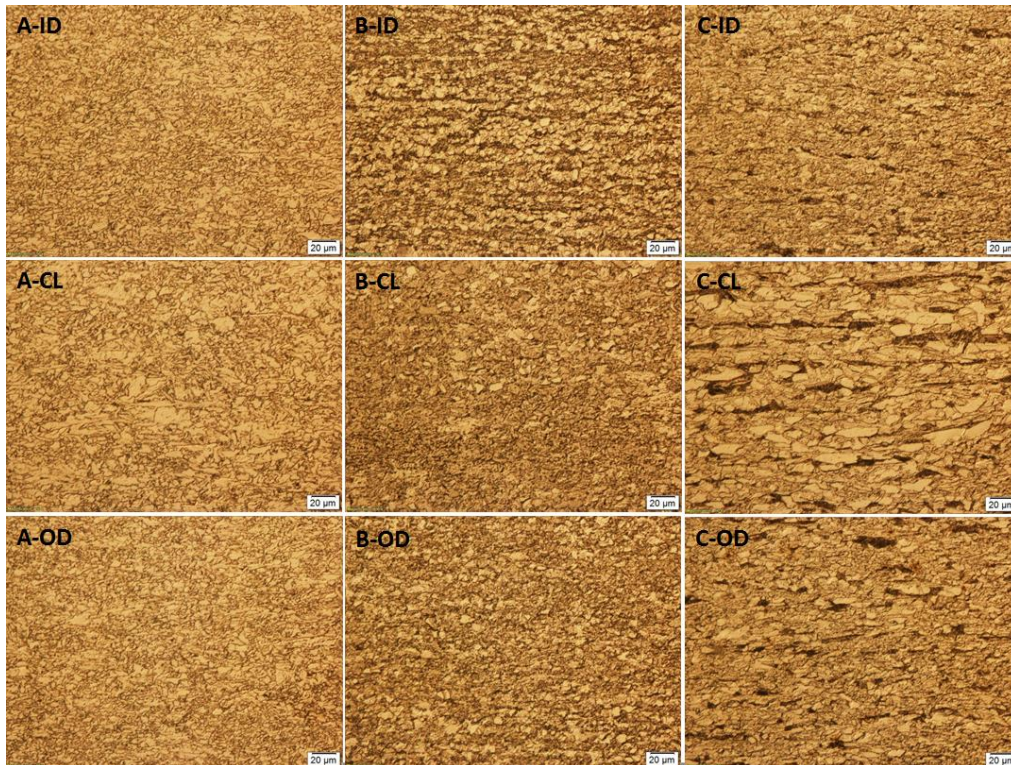


Figure 0.9 OM images of the transverse surface (Figure 3.9b) for Steel A, B, C located 90° to the weld at the ID, CL and OD positions.

The microstructures for steel samples from the ID and CL positions located 180° relative to the weld were also observed optically. The comparisons between the microstructures of Steel A, B and C for different locations relative to the weld are shown in Figure 0.10, Figure 0.11 and Figure 0.12, respectively. The microstructures at the 180° location, for all the three steels, are similar to those at the 90° location.

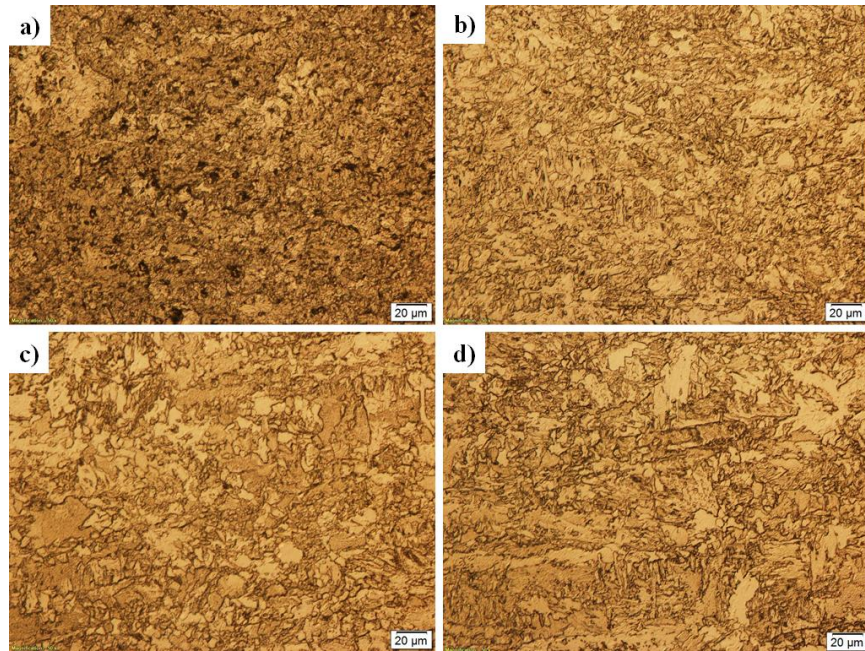


Figure 0.10 OM images of the longitudinal surface (Figure 3.9b) for Steel A: a) from the ID position at the 90° location; b) from the ID position at the 180° location; c) from the CL position at the 90° location; d) from the CL position at the 180° location.

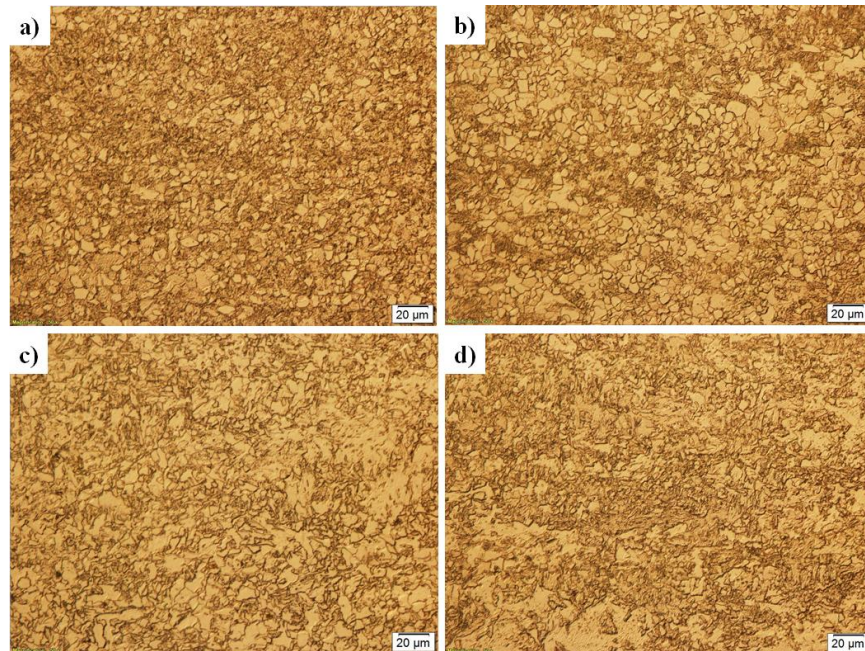


Figure 0.11 OM images of the longitudinal surface (Figure 3.9b) for Steel B: a) from the ID position at the 90° location; b) from the ID position at the 180° location; c) from the CL position at the 90° location; d) from the CL position at the 180° location.

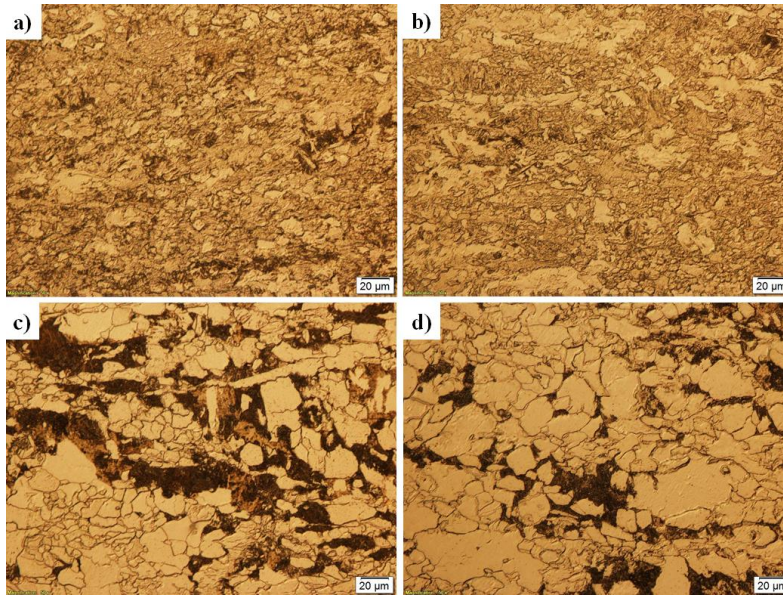


Figure 0.12 OM images of the longitudinal surface (Figure 3.9b) for Steel C: a) from the ID position at the 90° location; b) from the ID position at the 180° location; c) from the CL position at the 90° location; d) from the CL position at the 180° location.

As shown in Figure 0.13 and Figure 0.14, the average grain size measured using the circular interception method and volume percentage of microconstituents for the 90° and 180° locations are very close to each other for all the three steels.

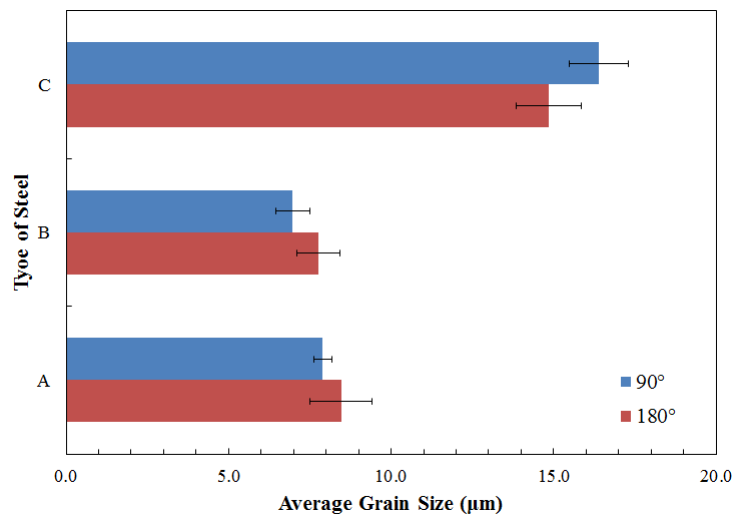


Figure 0.13 Measured average grain size for Steel A, B and C from the CL position located 90° and 180° to the weld.

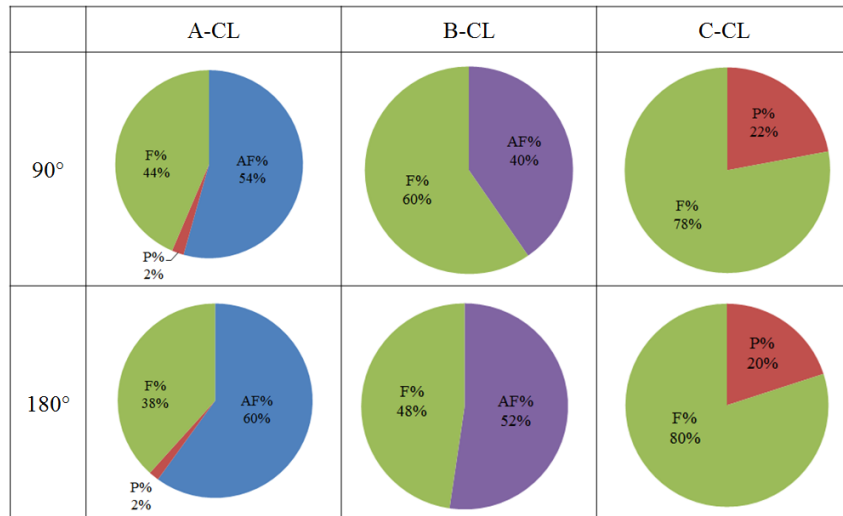


Figure 0.14 Measured volume fraction of microconstituents for Steel A, B and C from the CL position located 90° and 180° to the weld.

Appendix C Full ANOVA Tables for Box-Behnken Designs

As mentioned in Section 4.1.2.1.1, the full ANOVA data including all the independent variables are presented in this appendix.

The full ANOVA table of 4-factor BBD for Δ YS of longitudinal samples is presented in Table C-9. All the linear, quadratic and interaction terms are shown in the table. The terms with p-values not more than 0.05 are considered to be statistically significant aging variables for Δ YS and are summarized in Table 4-2. Compared with Table C-9, the p-values in Table 4-2 tend to be smaller. Since the insignificant aging variables are not included in the reduced ANOVA table, the statistically significant factors contribute more to Δ YS of longitudinal samples.

Table C-9 Full ANOVA Table of 4-factor BBD for Δ YS of Longitudinal Samples

Source	DF	SS	MS	F-Value	p-Value	Coefficient
Model	14	13756	983	19	<0.001	
T	1	1304	1304	26	<0.001	20.9
t	1	104	104	2	0.176	5.9
P	1	334	334	7	0.024	-10.6
C/Nb	1	2241	2241	44	<0.001	-27.3
T ²	1	72	72	1	0.256	7.3
t ²	1	79	79	2	0.234	7.7
P ²	1	5181	5181	103	<0.001	62.3
(C/Nb) ²	1	1514	1514	30	<0.001	-33.7
T·t	1	3	3	0	0.820	1.7
T·P	1	8	8	0	0.705	2.8
T·(C/Nb)	1	50	50	1	0.341	-7.1
t·P	1	14	14	0	0.607	-3.8
t·(C/Nb)	1	19	18	0	0.556	-4.3
P·(C/Nb)	1	48	48	1	0.347	-7.0
Lack-of-Fit	10	606	61			
Pure Error	2	0	0			
R ²	0.96					

The full ANOVA tables of 4-factor BBD for Δ UTS and Δ YS/TS of longitudinal samples are presented in Table C-10 and Table C-11, respectively. Likewise, the terms with p-values not more than 0.05 are considered to be statistically significant and summarized in Table 4-3 and Table 4-4, respectively. Compared with the full ANOVA data, the p-values in Table 4-3 and Table 4-4 tend to be smaller. Since the insignificant aging variables are not included in the reduced ANOVA table, the statistically significant factors contribute more to Δ UTS and Δ YS/TS.

Table C-10 Full ANOVA Table of 4-factor BBD for Δ UTS of Longitudinal Samples

Source	DF	SS	MS	F-Value	p-Value	Coefficient
Model	14	3596	257	3	0.038	
T	1	935	935	10	0.007	17.7
t	1	4	4	0	0.835	1.2
P	1	125	125	1	0.262	-6.4
C/Nb	1	91	91	1	0.335	-5.5
T ²	1	0	0	0	0.981	0.2
t ²	1	0	0	0	0.983	-0.2
P ²	1	1439	1439	16	0.002	32.9
(C/Nb) ²	1	38	38	0	0.529	-5.3
T·t	1	11	11	0	0.738	-3.3
T·P	1	378	378	4	0.063	19.5
T·(C/Nb)	1	11	11	0	0.738	-3.3
t·P	1	60	60	1	0.430	7.8
t·(C/Nb)	1	7	7	0	0.781	-2.7
P·(C/Nb)	1	13	13	0	0.707	-3.7
Lack-of-Fit	10	1079	108			
Pure Error	2	0	0			
R ²	0.77					

Table C-11 Full ANOVA Table of 4-factor BBD for Δ YS/TS of Longitudinal Samples

Source	DF	SS	MS	F-Value	p-Value	Coefficient
Model	14	0.0193	0.0014	7.1	0.001	
T	1	0.0001	0.0001	0.7	0.411	0.0068
t	1	0.0002	0.0002	0.9	0.358	0.0077
P	1	0.0029	0.0029	15.2	0.002	-0.0313
C/Nb	1	0.0041	0.0041	21.1	0.001	-0.0368
T ²	1	0.0003	0.0003	1.4	0.254	0.0144
t ²	1	0.0002	0.0002	1.3	0.279	0.0137
P ²	1	0.0039	0.0039	20.2	0.001	0.0542
(C/Nb) ²	1	0.0031	0.0031	16.3	0.002	-0.0486
T·t	1	<0.0001	<0.0001	0.0	0.916	0.0015
T·P	1	0.0005	0.0005	2.6	0.132	-0.0225
T·(C/Nb)	1	<0.0001	<0.0001	0.2	0.649	-0.0065
t·P	1	0.0004	0.0004	2.2	0.166	-0.0205
t·(C/Nb)	1	<0.0001	<0.0001	0.1	0.833	-0.0030
P·(C/Nb)	1	<0.0001	<0.0001	0.1	0.725	-0.0050
Lack-of-Fit	10	0.0023	0.0002			
Pure Error	2	0	0			
R ²	0.89					

The full ANOVA table of 4-factor BBD for ΔYS of transverse samples is presented in Table C-12. Similarly, the terms with p-values not more than 0.05 are considered to be statistically significant aging variables for ΔYS and summarized in Table 4-6. Compared with Table C-12, the p-values in Table 4-6 tend to be smaller. Also, since the insignificant aging variables are not included in the reduced ANOVA table, the statistically significant factors contribute more to ΔYS of transverse samples.

Table C-12 Full ANOVA Table of 4-factor BBD for ΔYS of Transverse Samples

Source	DF	SS	MS	F-Value	p-Value	Coefficient
Model	14	7512	537	3	0.026	
T	1	4431	4431	26	0.000	38.4
t	1	264	264	2	0.234	9.4
ϵ	1	10	10	0	0.813	-1.8
C/Nb	1	1555	1555	9	0.010	-22.8
T ²	1	7	7	0	0.842	-2.3
t ²	1	2	2	0	0.920	-1.2
ϵ^2	1	136	136	1	0.386	-10.1
(C/Nb) ²	1	324	324	2	0.191	-15.6
T·t	1	71	71	0	0.527	-8.5
T· ϵ	1	14	14	0	0.775	3.8
T·(C/Nb)	1	28	28	0	0.693	5.3
t· ϵ	1	0	0	0	0.991	-0.2
t·(C/Nb)	1	0	0	0	0.973	0.5
ϵ ·(C/Nb)	1	718	718	4	0.061	26.8
Lack-of-Fit	10	1968	197	7	0.125	
Pure Error	2	53	27			
R ²				0.79		

The full ANOVA tables of 4-factor BBD for ΔUTS and $\Delta YS/TS$ of transverse samples are presented in Table C-13 and Table C-14, respectively. Likewise, the terms with p-values not more than 0.05 are considered to be statistically significant and summarized in Table 4-7 and Table 4-8, respectively. Compared with the full ANOVA data, the p-values in Table 4-7 and Table 4-8 tend to be smaller. The statistically significant factors contribute more to ΔUTS and $\Delta YS/TS$ because the insignificant aging variables are not included in the reduced ANOVA table,

Table C-13 Full ANOVA Table of 4-factor BBD for Δ UTS of Transverse Samples

Source	DF	SS	MS	F-Value	p-Value	Coefficient
Model	14	4627	330	4	0.016	
T	1	1521	1521	17	0.002	11.3
ε	1	618	618	7	0.023	7.2
C/Nb	1	1503	1503	16	0.002	-11.2
t	1	131	131	1	0.255	3.3
T^2	1	11	11	0	0.736	-1.4
ε^2	1	106	106	1	0.303	-4.5
$(C/Nb)^2$	1	534	534	6	0.033	-10.0
t^2	1	1	1	0	0.923	-0.4
T· ε	1	106	106	1	0.303	5.2
T·(C/Nb)	1	7	7	0	0.791	-1.3
T·t	1	9	9	0	0.763	-1.5
ε ·(C/Nb)	1	3	3	0	0.854	-0.9
ε ·t	1	65	65	1	0.417	-4.0
(C/Nb)·t	1	40	40	0	0.520	-3.2
Lack-of-Fit	10	727	73	0	0.875	
Pure Error	2	374	187			
R^2	0.81					

Table C-14 Full ANOVA Table of 4-factor BBD for Δ YS/TS of Transverse Samples

Source	DF	SS	MS	F-Value	p-Value	Coefficient
Model	14	0.0067	0.0005	1.0	0.496	
T	1	0.0018	0.0018	3.9	0.072	0.0247
t	1	0.0001	0.0001	0.1	0.725	0.0045
ε	1	0.0023	0.0023	4.9	0.047	-0.0277
C/Nb	1	<0.0001	<0.0001	0.0	0.927	-0.0012
T^2	1	<0.0001	<0.0001	0.0	0.948	0.0013
t^2	1	<0.0001	<0.0001	0.0	1.000	0.0000
ε^2	1	<0.0001	<0.0001	0.0	0.948	-0.0013
$(C/Nb)^2$	1	<0.0001	<0.0001	0.0	0.979	0.0005
T·t	1	0.0001	0.0001	0.2	0.702	-0.0085
T· ε	1	0.0001	0.0001	0.3	0.621	-0.0110
T·(C/Nb)	1	0.0002	0.0002	0.3	0.574	0.0125
t· ε	1	0.0001	0.0001	0.2	0.636	0.0105
t·(C/Nb)	1	0.0001	0.0001	0.2	0.636	0.0105
ε ·(C/Nb)	1	0.0019	0.0019	4.0	0.068	0.0435
Lack-of-Fit	10	0.0054	0.0005	3.9	0.220	
Pure Error	2	0.0003	0.0001			
R^2	0.54					

The full ANOVA tables of 3-factor BBD for ΔYS of transverse Steel A and B samples are presented in Table C-15 and Table C-16, respectively. Similarly, the terms with p-values not more than 0.05 are considered to be statistically significant aging variables for ΔYS and summarized in Table 4-10. Compared with Table C-15, the p-values in Table 4-10 tend to be smaller. Besides, Figure 6.18 was plotted using Table C-16.

Table C-15 Full ANOVA Table of 3-factor BBD for ΔYS of Transverse Steel A

Source	DF	SS	MS	F-Value	p-Value	Coefficient
Model	9	950	106	22	0.002	
T	1	606	606	128	<0.001	17.4
t	1	108	108	23	0.005	7.4
ε	1	0	0	0	0.805	-0.4
T^2	1	26	26	5	0.067	-5.3
t^2	1	36	36	8	0.039	-6.3
ε^2	1	109	109	23	0.005	-10.9
T·t	1	12	12	2	0.179	-3.4
T· ε	1	41	41	9	0.032	6.4
t· ε	1	31	31	7	0.050	5.6
Lack-of-Fit	3	23	8	48	0.021	
Pure Error	2	0	0			
R^2	0.98					

Table C-16 Full ANOVA Table of 3-factor BBD for ΔYS of Transverse Steel B

Source	DF	SS	MS	F-Value	p-Value	Coefficient
Model	9	5166	574	42	<0.001	
T	1	4371	4371	320	<0.001	46.8
t	1	305	305	22	0.005	12.4
ε	1	244	244	18	0.008	-11.1
T^2	1	44	44	3	0.131	-6.9
t^2	1	101	101	7	0.042	-10.4
ε^2	1	14	14	1	0.362	3.9
T·t	1	71	71	5	0.071	-8.5
T· ε	1	14	14	1	0.357	3.8
t· ε	1	0	0	0	0.969	-0.2
Lack-of-Fit	3	15	5	0	0.897	
Pure Error	2	53	27			
R^2	0.99					